UNIVERSITÉ
LAVAL

Dielectric barrier discharges: A promising tool for the fabrication of anti-fogging coatings

Thèse

Ivan Rodriguez Duran

Doctorat en génie des matériaux et de la métallurgie
Philosophiæ doctor (Ph. D.)

Québec, Canada

Dielectric barrier discharges: A promising tool for the fabrication of anti-fogging coatings

Thèse

Iván Rodríguez Durán

Sous la direction de :

Gaétan Laroche, directeur de recherche

Résumé

La « vue floue » typique des surfaces embuées peut être extrêmement frustrante. Des exemples tels que les lunettes qui s'embuent pendant l'activité physique, la condensation qui se forme à l'intérieur des fenêtres pendant l'hiver ou les miroirs qui se couvrent de buée pendant la douche le démontrent. En outre, la présence de buée sur les surfaces cause des effets néfastes dans certains secteurs d'activité comme l'industrie automobile (pare-brise et rétroviseurs), l'industrie optique (objectifs, caméras, télescopes et capteurs), l'industrie solaire (modules photovoltaïques), l'industrie alimentaire (emballages d'aliments) et le secteur médical (lunettes et endoscopes). Au cours de la dernière décennie, l'application de revêtements (super)hydrophiles a suscité un intérêt croissant, en raison de leur capacité d'atténuer les effets de la buée. Leur principe de fonctionnement repose sur l'utilisation de matériaux interagissant avec les gouttes d'eau pour en modifier leur morphologie, générant une couche mince d'eau sur la surface. Ainsi, la lumière incidente n'est pas dispersée et les effets de la buée sont amoindris.

Jusqu'à présent, la plupart des techniques de dépôt explorées pour produire des revêtements (super) hydrophiles sont inaccessibles à la production de masse en raison de leur nature multi-étape. Pour cette raison, l'exploration de techniques adaptées à ce type de production, telles que les décharges à barrière diélectrique à pression atmosphérique (AP-DBD), un type de procédé de dépôt chimique en phase vapeur assisté par plasma (AP-PECVD), est cruciale afin d'élargir l'utilisation des revêtements antibuée au-delà du laboratoire. Dans un procédé AP-PECVD contrôlé par des barrières diélectriques (AP-DBD), certains précurseurs inorganiques ou organométalliques (e.g., $TiCl_4$, TiN, SiH_4, $Si_2O(CH_3)_2$) sont introduits entre deux électrodes parallèles avec un gaz vecteur (e.g., N_2, Ar, He) à la pression atmosphérique, où ils se fragmentent à la suite d'interactions avec les espèces du plasma. Les fragments résultants réagissent les uns avec les autres ou avec le substrat afin de produire les espèces réactives requises au dépôt du revêtement. Les caractéristiques structurelles et fonctionnelles des revêtements PECVD (e.g., la rugosité de surface, la biocompatibilité, les propriétés

optiques et de mouillage) dépendent des certains paramètres de dépôt, tels que la puissance dissipée dans la décharge, le type de décharge, la concentration de précurseurs et le débit de gaz.

La possibilité de se procurer des échantillons de verre dotés de la propriété antibuée via AP-PECVD a été démontrée dans cette thèse. En contrôlant les paramètres de dépôt, les revêtements antibuée ont été préparés en utilisant du 1,3,5,7-tétraméthylcyclotétrasiloxane ($Si_4O_4H_4(CH_3)_4$) et de l'oxyde nitreux (N_2O) au moyen d'une DBD fonctionnant en N_2 à la pression atmosphérique. Dans le cas des revêtements fabriqués dans des conditions statiques (aucun mouvement entre l'échantillon de verre et les électrodes), l'évaluation quantitative de la résistance à la buée (ASTM F 659-06) a révélé que les revêtements obtenus avec un rapport $[N_2O]/[TMCTS] \geq 30$ ou avec une puissance dissipée $\geq 0{,}25\ W\ cm^{-2}$ sont antibuée (transmittance > 80%) en raison de leur nature hydrophile. La quantité de précurseur et d'oxydant injectée dans la décharge, exprimée par la somme « $[N_2O] + [TMCTS]$ », n'agissait que peu sur la performance antibuée. En l'absence de changements significatifs dans la rugosité de surface (R_{rms} et R_a étant compris entre 3 et 6 nm), l'origine de la performance antibuée a été attribuée à la chimie de surface. Couplé aux rapports O/Si (résultats XPS), un paramètre arbitraire, appelé « rapport d'embuage » a été défini en considérant les résultats FTIR pour expliquer les performances antibuée observées. On a pu constater qu'un rapport O/Si $\geq 2{,}3$ couplé à un rapport d'embuage dans l'intervalle de 0-0,10, résultant de la présence de fonctionnalités hydrophiles, telles que les groupes silanol, hydroxyle, carboxyle or ester à la surface étaient nécessaires pour atteindre la propriété antibuée. Par ailleurs, les revêtements préparés dans des conditions dynamiques utilisant trois autres précurseurs aux structures différentes quant à la présence d'un cycle et au nombre de groupes Si-H et Si-CH_3 (l'octaméthylcyclotétrasiloxane, le 1,1,3,3-tétraméthyldisiloxane et l'hexaméthyldisiloxane) n'étaient pas antibuée. Ce résultat porte à croire que la structure cyclique du TMCTS et la forte réactivité des liaisons Si-H est à l'origine de la formation de ces fonctionnalités hydrophiles et par conséquent, à la performance antibuée observée dans les verres traités en injectant du TMCTS dans la décharge plasma.

Abstract

Experience shows that the "blurred view" typical of fogged surfaces can be incredibly frustrating. Eyewear fogging up during physical activity, condensation forming on the inside of windows during the winter, or bathroom mirrors steaming up when taking a shower are some obvious examples. In addition to being upsetting, the fogging of surfaces has been reported to cause adverse effects on sectors of activity as diverse as the automotive industry (e.g., windshield glass and rearview mirrors), the optical industry (e.g., lenses, cameras, telescopes, and sensors), the solar industry (e.g., photovoltaic modules), the food industry (e.g., food packaging), and medicine (e.g., goggles and endoscopes). Over the last decade, interest has been growing in the application of hydrophilic and superhydrophilic coatings, as they can efficiently mitigate the effects of fogging by changing the morphology of fog drops. The working principle of a (super)hydrophilic surface is based on the use of materials producing a thin film of water on the solid surface on interaction with fog drops. As a result, incident light transmits without being scattered and the effects of fogging are minimized.

Unfortunately, most of the deposition techniques used thus far for the fabrication of (super)hydrophilic coatings involves multiple steps, thus making their integration into mass production a challenging task. For this reason, the exploration of deposition techniques adapted for large-scale production is crucial to broaden the range of application of anti-fogging coatings beyond the laboratory. In this regard, numerous studies on the use of dielectric barriers in plasma enhanced chemical vapor deposition at atmospheric pressure (AP-PECVD) are strongly emerging to address this issue. In a typical AP-PECVD controlled by dielectric barriers, inorganic or organometallic precursors (e.g., $TiCl_4$, TiN, SiH_4, $Si_2O(CH_3)_2$) are introduced between two parallel electrodes along with a carrier gas (e.g., N_2, Ar, He) at atmospheric pressure where, on interaction with plasma species, undergo fragmentation. The resulting fragments can react with the substrate or with each other to produce short-lived species required for coating deposition. The structural and functional features of PECVD coatings (e.g., surface roughness, biocompatibility, wetting and optical

properties) depend on several deposition parameters, including the power dissipated in the discharge, type of plasma discharge, precursor concentration, and the flow rate of gases.

With this in mind, the feasibility of conferring fogging resistance to commercial glass samples via AP-PECVD has been demonstrated in this doctoral thesis. By appropriately controlling the deposition parameters, anti-fogging coatings were prepared using 1,3,5,7-tetramethylcyclotetrasiloxane ($Si_4O_4H_4(CH_3)_4$) and nitrous oxide (N_2O) by a dielectric barrier discharge operated in N_2 at atmospheric pressure (AP-DBD). When coating deposition was conducted in static conditions, that is, with no relative movement between the glass sample and the electrodes, quantitative assessment of the fogging resistance (ASTM F 659-06 standard) revealed that coatings obtained under $[N_2O]/[TMCTS]$ ratios ≥ 30 or under a dissipated power $\geq 0.25 \, W \, cm^{-2}$ endowed glass samples with the anti-fogging property (transmittance $> 80\%$), because of their hydrophilic nature. In terms of the $[N_2O] + [TMCTS]$ sum, the amount of TMCTS and N_2O injected into the discharge did not appear to have a great impact on the anti-fogging performance. Indeed, as no significant changes in surface roughness were observed (R_{rms} and R_a were between 3 and 6 nm), the origin of the anti-fogging performance was attributed to the surface chemistry. To this end, an arbitrary parameter, called "fogging ratio", was defined considering FTIR results to account for, along with O/Si ratios (XPS results), the observed anti-fogging performance. Fogging ratios in the 0–0.10 range coupled with O/Si ratios ≥ 2.3, resulting from the presence of hydrophilic functionalities, such as silanol (Si-OH), hydroxyl (C-OH) carboxyl (COOH), and ester (COOR) groups at the coating surface were necessary to attain the anti-fogging property. Interestingly, coatings prepared in dynamic conditions using three other precursors with different structures and different number of Si-H and Si-CH$_3$ groups; namely, octamethylcyclotetrasiloxane (OMCTS), 1,1,3,3-tetramethyldisiloxane (TMDSO), and hexamethyldisiloxane (HMDSO) were not fogging-resistant. This result leads us to believe that the cyclic structure of TMCTS in conjunction with the high reactivity of Si-H bonds is behind the formation of the above-mentioned hydrophilic functionalities, and thus the anti-fogging performance of TMCTS-coated glasses.

Table of contents

List of tables

List of figures

List of symbols and constants

Symbol	Description	Units
A	Area	m^2
c	Speed of light in vacuum (2.9979×10^8)	$m\ s^{-1}$
C_i	Concentration of element i	at.%
d	Inter-electrode distance	mm
d_p	Depth of penetration	μm
e	Charge of the electron (1.6022×10^{-19})	C
E	Kinetic energy	eV
E	Electric field	$V\ m^{-1}$
E_F	Fermi level	eV
E_V	Energy level of vacuum	eV
E/p	Total reduced electric field	$V\ m^{-1}\ Torr^{-1}$
$f(E)$	Energy distribution function	-
F	Force	N
h	Planck constant (6.626×10^{-34})	$m^2\ kg\ s^{-1}$
g_i	Partition function of the state i	-
I	Current	A
k	Force constant/spring constant	$N\ m^{-1}$
k_B	Boltzmann constant (1.3806×10^{-23})	$m^2\ kg\ s^{-2}\ K^{-1}$
l	Sampling length	m
L	Characteristic reaction dimension	m
m	Particle mass	kg
m_e	Electron mass (9.1094×10^{-31})	kg
n	Particle number density, plasma density	m^{-3}
n_i	Refractive index of medium i	-
N_D	Plasma parameter	-
P	Pressure	Torr
T	(Particle) temperature	eV
V	Applied voltage	V
V_{br}	Breakdown voltage	V
α	Townsend's first ionization coefficient	m^{-1}
α_i	Degree of ionization	-
δ_c	Cantilever deflection	m
ε_0	Permittivity of free space (8.854×10^{-12})	$F\ m^{-1}$
ε	Electrical permittivity of a medium	$F\ m^{-1}$
ε_i	Ionization energy	eV
η	Electron attachment coefficient	m^{-1}
ϕ	Work function	eV
ϕ_i	Sensitivity factor of the element i	-
θ	Contact angle/Incident angle	°
θ_c	Critical angle	°
γ	Secondary electron emission coefficient	-

Symbol	Description	Units
λ_D	Debye length	m
λ	Mean free path length/wavelength	m/nm
μ	Reduced mass	m
μ	Bond dipole moment	C m
μ	Particle mobility	$m^2\ V^{-1}\ s^{-1}$
ν	Collision frequency	s^{-1}
ρ	Mass density	$kg\ m^{-3}$

List of abbreviations

Abbreviation	Definition
AFM	Atomic force microscopy
APGD	Atmospheric pressure glow discharge
APCAs	Apparent contact angles
AP-DBD	Atmospheric pressure dielectric barrier discharge
ASTM	American society for testing and materials
ATR-FTIR	Attenuated total reflectance – Fourier transform infrared spectroscopy
BE	Binding energy
CA	Contact angle
CAH	Contac angle hysteresis
CHI	Chitosan
CLA	Center-average line
CMC	Carboxymethyl cellulose
CNTs	Carbon nanotubes
CNRS	Centre national de recherche scientifique
CQMF	Centre québécois sur les matériaux fonctionnels
CR-39	Allyl diglycol carbonate
CSH	Calcium silicate hydrates
CTAB	Cetyltrimethylammonium bromide
CTE	Complete thermodynamic equilibrium
CVD	Chemical vapor deposition
DBD	Dielectric barrier discharge
DC	Direct current
DFT	Discrete Fourier transform
DLIL	Direct laser interference lithography
DSHNs	Double-shell hollow nanospheres
DZ	Faujasitic nanozeolites
EEDF	Electron energy distribution function
ESCA	Electron spectroscopy for chemical analysis
FAS	Fluoroalkylsilane molecules
FAS-17	Heptadecafluorodecyltripropoxysilane
FDBD	Filamentary dielectric barrier discharge
FQRNT	Fonds québécois de la recherche sur la nature et les technologies
GLID	Glycerol monolauric acid monoitaconic acid diester
GIARC	Gradient-index anti-reflection coating
HA	Hyaluronic acid
HMDA	1H, 1H, 2H, 2H-heptadecafluorodecyl methacrylate
HDBD	Homogeneous dielectric barrier discharge
HMDSO	Hexamethyldisiloxane
HRXPS	High-resolution x-ray photoelectron spectroscopy
HSNs	Hollow silica nanoparticles
IR	Infrared
ISO	International organization for standardization
ITO	Indium tin oxide

Abbreviation	Definition
KE	Kinetic energy
L	Liquid phase
LAPLACE	Laboratoire plasma et conversion d'énergie
LbL	Layer-by-layer deposition
LED	Light emitting diode
LLDPE	Linear low-density polyethylene
LIS	Laboratoire d'ingénierie de surface
LTE	Local thermodynamic equilibrium
LVDT	Linear variable differential transformer
MA	Maleic anhydride
MMGD	Monostearic acid monomaleic acid glycerol
MPSNPs	Mesoporous silica nanoparticles
MTMS	Methyltrimethoxysilane
NSERC	Natural sciences and engineering research council of Canada
MW	Micro wave
NB	Norbornene
NF	Nanoflowers
NP	Nanoparticles
NS	Nanosheets
OCA	Oil contact angle
OPD	Optical path difference
PAA	Polyacrylic acid
PAM	Polyacrylamide
PC	Polycarbonate
PDDA	Polydiallyldimethylammonium chloride
PDMAEMA	Polydimethylaminoethyl methacrylate
PDMS	Polydimethylsiloxane
PE	Polyethylene
PECVD	Plasma enhanced chemical vapor deposition
PEG	Polyethylene glycol
PEGDA	Polyethylene glycol diacrylate
PEGDMA	Polyethylene glycol dimethacrylate
PEGMA	Polyethylene glycol methacrylate
PFOS	Perfluorooctanesulfonic acid potassium salt
PEI	Polyethylenimine
PET	Polyethylene terephthalate
PFPE	Perfluoropolyether polymers
PFTOES	1H, 1H, 2H, 2H-perfluorooctyltriethoxysilane
PFTOS	1H, 1H, 2H, 2H-perfluorodecyltriethoxysilane
PHEA	Poly (2-hydroxyethyl acrylate)
PHEMA	Poly (2-hydroxyethyl methacrylate)
PLA	Polylactic acid
PMAA	Polymethacrylic acid
PMMA	Polymethyl methacrylate

Abbreviation	Definition
PP	Polypropylene
PPMM	Polyether pentaerythritol monomaleate
pSBMA	Polysulfobetaine methacrylate
pSBVI	Polysulfobetaine vinylimidazole
PS	Polystyrene
PSS	Sodium poly(4-styrenesulfonate)
PTFE	Polytetrafluoroethylene
PVA	Polyvinyl alcohol
PVAc	Polyvinyl acetate
PVC	Polyvinyl chloride
PVD	Physical vapor deposition
PVDF	Polyvinylidene fluoride
PVP	Poly vinylpyrrolidone
QC	Quaternized cellulose
RE	Rare earth
RIE	Reactive ion etching
RF	Radio frequency
RGO	Reduced graphene oxide
RH	Relative humidity
ROS	Reactive oxidizing species
S	Solid phase
SA	Sliding angle
SBSi	Sulfobetaine silane
Sccm	Standard cubic centimeter per minute
SEM	Scanning electron microscopy
SIPN	Semi-interpenetrating polymer networks
SLAN	Sacrificial layer-mediated nanoimprinting
SN2	Substitution nucleophilic bimolecular
SPM	Scanning probe microscopies
SSNPs	Solid silica nanoparticles
SWSs	Subwavelength structures
TD	Townsend discharge
TDBD	Townsend dielectric barrier discharge
TEOS	Tetraethoxysilane
TFAA	Trifluoroacetic acid allyl ester
TMCTS	1,3,5,7-tetramethylcyclotetrasiloxane
TMDSO	1,1,3,3-tetramethyldisiloxane
TNB	Titanate nanobelts
TPCL	Triple phase contact line
OMCTS	Octamethylcyclotetrasiloxane
UHV	Ultra-high vacuum
V	Vapor phase
WCA	Water contact angle
XPS	X-ray photoelectron spectroscopy

Acknowledgements

À travers ces lignes, je souhaite exprimer ma sincère et profonde gratitude à toutes les personnes qui, avec leur soutien scientifique et humain, ont collaboré à la réalisation de ce travail de thèse.

Tout d'abord, je tiens à remercier les membres du jury Luc Stafford, Émile J. Knystautas et Sylvain Coulombe d'avoir accepté de lire et d'évaluer cette longue thèse, et pour tous les commentaires pertinents, les précieuses suggestions et remarques qui en ont découlés. Je voudrais exprimer ma gratitude à mon directeur de recherche, le professeur Gaétan Laroche, pour le dévouement et le soutien qu'il a apporté à ce travail, pour le respect de mes suggestions et idées ainsi que pour la direction et la rigueur qu'il a maintenue tout au long du processus d'élaboration de ma thèse. Je le remercie pour la confiance et l'accueil depuis mon arrivée à Québec. Merci beaucoup à Luc Stafford pour ses conseils et la patience dont il a fait preuve envers moi dans le cadre du cours de physique de plasmas. Sa contribution à cette thèse est très considérable.

Je remercie mes collègues du département de Génie des mines, de la métallurgie et des matériaux, et tout particulièrement Geoffroy Rouget et Geneviève Bruneau qui m'ont toujours apporté un grand soutien moral et humain, nécessaires dans les moments difficiles durant le doctorat, en plus des nombreux litres de café tant appréciés.

Merci à tous mes collègues (amis) du laboratoire d'Ingénierie de Surface (LIS) : Morgane Laurent, Caroline Royer, Laurence Padioleau, Natalia Milaniak, Nawel Ghribi, Souhaila Ghadhab, Saeideh Shokrollahi, Amna Amri, Laurine Martocq, Andrée-Anne Guay-Bégin et Ibrahim Bilem. Le soutien et la joie que vous m'avez transmis au cours de cet ardu chemin me sont très chers. Je vous embrasse fort.

Un gros merci, aussi, à tous mes collègues (amis) du laboratoire des biomatériaux et de bioingénierie (LBB) : Carolina Bartolan, Leticia Marin, Clayton Campello, Dimitria

Camasão, Sergio Loffredo, Francesco Copes, Gabriel Morand, Samira Ravanbakhsh, Sergio Piraña, Vanessa Montaño, Linda Bonilla, Daniele Pezzoli, Nina Bono, Lucie Levesque, Caroline Loy… et le *big chef*, le professeur Diego Mantovani—merci de m'avoir donné la chance de t'assister dans le cours de matériaux de l'ingénieur, entre autres choses ☺.

À mon cher collègue Carlo Paternoster. Merci pour ton savoir-être, merci d'avoir partagé avec moi tes réflexions sur la vie, sur ce que l'avenir nous réserve, sur la façon dont la vie peut être parfois injuste, etc. Tu ne sais pas à quel point nos conversations au bureau vont me manquer. En ta compagnie, les aléas et les malheurs deviennent bons, la tristesse prend la forme de la joie et la solitude disparaît. Bonne continuation mon ami.

Je ne pourrais pas faire mes remerciements sans dédier quelques mots à mon amie Stéphanie. Ce fût un vrai plaisir de travailler avec toi. Le jour où je t'ai rencontrée, je me suis dit que nous allions très bien nous entendre. Je ne m'étais pas trompé; le temps m'a donné raison. J'espère que nous garderons notre belle amitié à vie.

Un travail de recherche est toujours le résultat des idées et des efforts de personnes qui gravitent autour de nous. Pour cette raison, je remercie sincèrement Jacopo. Je lui suis très reconnaissant pour sa gentillesse, son temps, ses idées et d'avoir facilité la fin de cette thèse. *Grazie mille*.

À ma *beloved* Pascale. Qu'est-ce que j'aurais fait sans toi? Dis-moi. Je te remercie doublement—pour ton professionnalisme et pour tes qualités humaines. Merci pour tes conseils, tes suggestions, les belles discussions et ta présence lors de mes consultations sur le XPS, FTIR et AFM, entre autres. Sans aucun doute, tu as contribué à mon développement professionnel; tu m'as beaucoup appris. Merci pour ton soutien, tes encouragements, ton affection, pour avoir partagé avec moi de nombreux moments heureux et tristes, pour avoir su m'écouter. Bref, pour m'avoir donné de l'amour et de l'amitié depuis mon arrivée.

Un travail de recherche est également le résultat de la reconnaissance et du soutien vitaux offerts par les personnes qui nous accordent de la valeur, sans lesquelles nous n'aurions pas la force et l'énergie qui nous incitent à nous développer en tant qu'individus et en tant que professionnels.

Merci à mon cher Martin. Merci de m'avoir accueilli à bras ouverts à mon arrivée au Québec. Merci de m'avoir fait voir qu'il y a toujours des gens qui ont des valeurs, du cœur et qui sont capables du don de soi sans ne jamais rien attendre en retour. Tu as toujours été là, même si c'était pour m'entendre me plaindre du froid ou pour corriger mes textes en français. Tes réflexions et tes conseils demeurent avec moi.

Merci aux membres de ma famille, car malgré la distance, leurs encouragements, leur soutien et leur joie m'ont donné la force pour avancer et terminer. Javier, mon frère, même si nous sommes très différents, je sais que tu es aussi fier de moi que je peux l'être de toi. Je remercie spécialement ma mère. Je suis qui je suis grâce à toi. Il n'y a pas assez de mots pour décrire à quel point je t'admire. Merci pour ta patience, pour ta compréhension, pour le temps que tu as accordé pour m'encourager et me consoler quand je vivais de mauvais moments.

Une mention spéciale pour celles qui ne sont plus avec moi—ma tante Isabelle et ma grand-mère Marie. Je n'ai pas pu vous dire adieu. Votre absence m'a ramené et ancré plus les pieds sur la terre. Votre absence m'a fait réfléchir sur la fugacité de la vie, la fragilité de l'être humain, l'importance d'aimer et d'être aimé. Je tiens à partager mes pensées avec vous, c'est le moment, c'est mon moment, mon cœur me le demande.

Pendant la jeunesse, on ne pense que très peu au temps. Il n'y a pas de dates éloignées. Le temps n'expire pas. Tout est programmé : les jours, les semaines, les mois et les années. Il n'y a pas de conscience du temps. Il n'y a pas d'abîmes. Lorsqu'on vieillit la fugacité de la vie commence à avoir une signification tangible. Certaines personnes parlent de la fugacité de la vie. Celles qui le font le plus sont les aînés, les malades et les désillusionnés. Pour eux, la brièveté de la vie transforme le temps en conscience et en existence. Ils comprennent qu'on

ne peut pas reculer le temps. Tout ce qui semblait lointain devient soudainement proche. Ce qui semblait improbable devient palpable. L'impossibilité d'arrêter le temps devient évidente et les pertes deviennent encore plus douloureuses. La certitude qui accompagne l'aphorisme « les limites de la vie » quitte le terrain des mots et devient une réalité.

La fugacité est synonyme d'impuissance et de prélude à une réalité presque toujours triste, sombre et cruelle. L'éphémère n'est pas une condition du temps, c'est une condition de l'être humain et de la mort qui ne cesse jamais de mourir. La manque d'espoir, de joie, d'enthousiasme, de sentiment d'appartenance déterminent la cadence de la marche. Les pages des calendriers tombent très lentement. Le cours du temps n'est établi ni par le désir ni par la volonté; c'est le poids de la tristesse qui tient les rênes. Le temps devient ami ou ennemi, c'est selon.

On remarque la fugacité de la vie lorsque l'inclémence du temps frappe. Les aînés, les malades, les solitaires, et même les bohémiens essaient en vain d'appréhender le temps, car ils savent que le temps ne leur appartient que pour un temps. La phrase « le temps ne pardonne pas » est vraie. Face à la vie qui s'en va, l'impossibilité de capturer les instants devient évidente. Les petites certitudes qui construisent les significations de l'existence disparaissent. Il n'y a pas d'antidote contre la fugacité de l'existence. Il ne pouvait en être autrement: il en va de même avec la mort. Certains écrivent, d'autres peignent, certains dansent, d'autres essaient de dire quelque chose. Ces actions soulagent, tempèrent, mais sans plus.

À tous les jours, je me dis : « Iván la vie est fugace, elle glisse entre tes doigts, elle glisse entre tes mots, profites-en ».

Foreword

This doctoral project was conducted within the framework of a graduate program (PhD) in metallurgical and materials engineering at l'Université Laval (Department of Mining, Metallurgical, and Materials Engineering). This study focused on the deposition of anti-fogging coatings by atmospheric pressure dielectric barrier discharges (AP-DBDs) using 1,3,5,7-tetramethylcyclotetrasiloxane (TMCTS) and nitrous oxide (N_2O). Coating deposition and surface characterization were performed at the "Laboratoire d'Ingénierie de Surface" (LIS) at l'hôpital St-François d'Assise (Québec, Canada).

Headed by the professor Gaétan Laroche, **Laboratoire d'Ingénierie de Surface** has developed a significant expertise in surface characterization by X-ray photoelectron spectroscopy, infrared spectroscopy, atomic force microscopy, scanning electron microscopy, among other techniques; as well as in surface modification strategies for biomedical applications. These include the covalent immobilization of (bio)molecules on the surface of materials to promote cell adhesion and cell proliferation, and the functionalization of polymers by atmospheric pressure dielectric barrier discharges (AP-DBD).

The use of AP-DBD for the deposition of anti-fogging coatings made it possible to develop a collaboration (6-months traineeship) with the "Laboratoire Plasma et Conversion d'Énergie" (LAPLACE) at l'Université Paul Sabatier (Toulouse, France).

Laboratoire Plasma et Conversion d'Énergie has achieved international recognition in the use of plasmas for numerous applications (e.g., coting deposition, surface cleaning, gas purification) as well as in the chemical, physical, electrical characterization of low-pressure and atmospheric pressure plasmas. With the focus on understanding the mechanisms governing the dielectric barrier discharges operated at atmospheric pressure, this laboratory has become a global reference point in the field of plasma physics.

This doctoral project has a marked empirical and "literary" character and opens a new line of investigation on plasma-deposited anti-fogging coatings, as no research on this topic has thus far been conducted. Research and review articles included in this dissertation are the result of a close collaboration between colleagues, research assistants, post-doctoral researchers, and professors, mentioned below:

Université Laval: Pascale Chevallier (PhD in Chemistry, research assistant at l'hôpital St-François d'Assise), Stéphane Turgeon (PhD in Physics, research assistant at l'hôpital St-François d'Assise), and Gaétan Laroche (PhD in Chemistry, full professor in the Department of Mining, Metallurgical, and Materials engineering).

Université de Montréal: Jacopo Profili (PhD in Plasma Physics, postdoctoral researcher), Antoine Durocher-Jean (PhD in Plasma Physics), and Luc Stafford (PhD in Plasma Physics, full professor in the Department of Physics).

Université Paul Sabatier: Nicolas Gherardi (PhD in Electrical Engineering & Plasma Physics, CNRS researcher)

Experimental results and literature research are presented in the form of four articles, each of which has been integrated in the following chapters:

Chapter 1: "Water drop-surface interactions as the basis for the design of anti-fogging surfaces: Theory, practice, and applications trends"

Authors: Iván Rodríguez Durán and Gaétan Laroche

Article history:

Journal: Advances in Colloid and Interface Science (IF = 8.243 in 2018)

https://doi.org/10.1016/j.cis.2018.11.005

Submitted: July 2018

Accepted: November 2018

Published: November 2018

The authors identified the scope of this review article. Iván Rodríguez reviewed the literature and wrote the manuscript, under the supervision of Prof. Gaétan Laroche. The authors discussed the structure and edited the manuscript.

Because of its vast length (248 pages double spaced), a second review article on the current state of anti-fogging surfaces was not included in this dissertation.

The authors identified the scope of this review article. Iván Rodríguez reviewed the literature and wrote the manuscript, under the supervision of Prof. Gaétan Laroche. The authors discussed the structure and edited the manuscript.

Iván Rodríguez reviewed the literature, performed all experiments, analyzed the data, and prepared the manuscript, under the supervision of Prof. Gaétan Laroche. Prof. Gaétan Laroche and the rest of co-authors perused and edited the manuscript.

Chapter 5: "Anti-fogging coatings deposited by atmospheric pressure dielectric barrier discharges: A comprehensive structural and chemical analysis"

Authors: Iván Rodríguez Durán, Jacopo Profili, Luc Stafford, and Gaétan Laroche

Article history:

Proposed Journal: ACS applied materials & interfaces

Submitted: 18th July 2019

Accepted:

Published:

Iván Rodriguez reviewed the literature, performed all experiments excluding AFM analyses, which were performed by Jacopo Profili, and prepared the manuscript, under the supervision of Prof. Gaétan Laroche. Experimental data were analyzed by Iván Rodriguez. Prof. Gaétan Laroche and the rest of co-authors perused, discussed, and edited the manuscript.

Chapter 6: "Unveiling the origin of the anti-fogging performance of plasma-coated glass: Role of the structure and chemistry of siloxane precursors"

Authors: Iván Rodríguez Durán, Jacopo Profili, Luc Stafford, and Gaétan Laroche

Article history:

Proposed Journal: Chemistry of materials

Submitted: 18th July 2019

Accepted:

Published:

Iván Rodríguez reviewed the literature, designed and performed all experiments excluding AFM analyses, which were conducted by Jacopo Profili, and prepared the manuscript, under the supervision of Prof. Gaétan Laroche. Experimental data were analyzed by Iván

Rodríguez. Prof. Gaétan Laroche and the rest of co-authors perused, discussed, and edited the manuscript.

Introduction

Problem statement

Transparent materials such as glasses and some polymers play an essential role in our daily life. Indeed, it is well known that their application in mirrors, windows, automobile windshields, and eyewear make our day-to-day activities more comfortable. These examples aside, many more can also be found in several spheres of human activity, including such sectors as diverse and distinct as the medical, photovoltaic and food industry fields. Unfortunately, due to the unavoidable condensation of water vapor on solid surfaces, these materials undergo fogging under normal operating conditions.

Fogging can be defined as a natural phenomenon occurring when humid air condenses and transforms into small and discrete liquid drops on a solid surface whose temperature is less than or equal to the dew point [1]. The as-formed droplets create an irregular pattern that causes a blurred view because of the scattering of incident light in all directions [2]. As a result, optical properties such as the light-transmitting capabilities of transparent materials are severely compromised. Although condensation is not harmful, its occurrence can be upsetting, as it usually forms on items used in our daily lives, including bathroom mirrors, eyeglasses, swimming goggles, binoculars, glass lenses or camera lenses, to name a few [3–7].

Further to this, fogging causes serious problems in different spheres of activity where materials with excellent optical performance are required. For example, the presence of condensation has been reported to reduce the precision of analytical instruments such as gas chromatographs [8] and microscopes [9], while blurred vision is generally associated with safety concerns in the aeronautic and automotive sectors [10–13] as well as in certain surgical procedures (e.g., endoscopic surgery) [14–20]. In applications where we seek to maximize the solar energy input, as in greenhouse cladding materials, fogging can dramatically reduce

the light transmission, resulting in a decrease in crop yield [21–24]. Similarly, condensation reduces the efficiency of photovoltaic panels due to a decrease in the amount of light, i.e., incident photons, entering the solar cells [25,26]. In the food packaging industry, the presence of condensation on the inside of packed produce (e.g., freshly chopped vegetables) gives rise to esthetic and hygienic concerns [27–30].

How to prevent surfaces from fogging up?

Today, when selecting materials to fabricate elements dealing with condensation such as chiller cabinets, greenhouse claddings, food packaging, protective goggles, or aircraft windows, it is standard practice to incorporate some anti-fogging characteristics in their design. Over the last decade, various anti-fogging strategies have been applied to deter fogging and are generally grouped into two groups. The first group of anti-fogging strategies pertains to changes in certain environmental parameters including relative humidity, temperature, and surrounding air flow. Among these, the heating of materials (by applying an external voltage, for example) and the improvement of the air velocity are well-proven strategies to avoid or remove surface fog [10,20,31–36]. In the former case, fogging is prevented as the surface of the material is kept above the dew point on heating. In contrast, an increase in the air velocity enhances evaporation and ultimately minimizes condensation, as a result of the humidity drop at the vicinity of the solid surface. Although these practices are very effective in combating surface fog, it should not be forgotten that the energy consumption and, in some cases, the concerns related to the design of defogging equipment or to material selection, may account for their application in very specific cases.

As regards design issues, a paradigmatic example can be found in vehicle windshields. The windshield defrosting and defogging systems are ideally required to promptly melt ice or snow on the outer surface of the windshield while removing surface fog from its inner surface [37]. IR thermography has demonstrated, however, that the warm air ejected by the defrosting/defogging system does not extend over the entire windshield surface [11]. This limitation, due to the windshield's geometry, contributes to the emergence of "dead zones"

located at the corners and at the upper side of the windshield, where frost and surface fog persist [38].

On the other hand, the issues regarding transparent heaters for defrosting/defogging purposes pertain mostly to materials selection. An ideal defogger must rapidly remove condensation on application of a voltage as low as possible [39]. To this end, the working saturation temperature of the heater must be as high as possible to reduce the defogging time. It has been reported that the working saturation temperature relies on the convective heat loss at the solid-air interface, which is linked to the material's heat-transfer coefficient [34]. For this reason, the current trend in this field is to fabricate transparent heaters using materials with the lowest overall heat-transfer coefficient. In this regard, numerous studies on carbon nanotubes (CNTs) [40], graphene [34,41,42], graphene oxide [43], indium tin oxide (ITO) [44], Pt-decorated Ni micromesh [45], and silver/cupronickel wire mesh [33,46] are strongly emerging to address this issue. Even though these materials have amply demonstrated outstanding anti-fogging performance, their large-scale application remains far from a practical reality, for cost-effectiveness reasons.

In the case of anti-fogging strategies focusing on changing the morphology of water drops, the preparation of hydrophilic or superhydrophilic surfaces have generated significant interest because of their capacity to reduce light scattering via filmwise condensation (see "spreading mechanism" in **section 1.5.1**). In addition, these surfaces exhibit a higher evaporation rate than those featuring dropwise condensation, because of the greater radius of curvature of water drops [9]. As a result, beside the fact that filmwise condensation mitigates scattering events, superhydrophilic surfaces become fog-free more quickly than, for example, untreated ones, which are usually more hydrophobic.

In theory, surfaces with water-repellent properties also prevent the effects of condensation. That said, their use for anti-fogging purposes appears to have attracted less attention compared to that of the (super)hydrophilic surfaces. This fact is most likely motivated by two reasons. First, to prevent light scattering, these surfaces must be tilted to roll off water drops;

second, given that both small sliding angles and contact angle hysteresis are required (see "Cassie-air trapping state" in **section 1.4.2.2**), more sophisticated manufacturing processes are required to fulfill such requirements. Compared to the above-mentioned category (controlling external parameters), the second category of anti-fogging strategies represents a more interesting option because of their easier, more manageable nature and lower related energy costs.

With this in mind, the anti-fogging property can be attained either through the deposition of a thin film of a distinct material that is normally more hydrophilic than the substrate or by direct modification of the substrate's surface features (roughness or chemistry). The deposition of anti-fogging coatings has been broadly applied for both inorganic and organic substrates, while the modification of the substrate's surface features has been almost exclusive to polymeric films (**sections 1.6.3** and **1.6.4**). As in the case of anti-fogging strategies pertaining to changes in the environmental parameters, these procedures have proven to be effective in combating surface fog; that said, their integration into mass production is a challenging task. For example, the fabrication of anti-fogging coatings by conventional coating techniques, such as dip-coating, spin-coating, or layer-by-layer deposition, usually involves time-consuming multistep processes, and quite often, is not adapted to thermally sensitive substrates (e.g., polymers, composites), because of the application of post-thermal treatments. With all of these constraints, the use of these surfaces is restricted to the laboratory and is as yet not adapted for large-scale production, with the exception of the food industry and in very specific cases (e.g., protective eyewear).

Research purpose and objectives

The aim of this doctoral project is to develop a straightforward cost- and time-effective strategy to fabricate anti-fogging coatings with potential applicability in mirrors, eyeglasses, windows, swimming goggles, endoscope lenses, or photovoltaic modules, to name a few.

In this doctoral project, the feasibility of conferring anti-fogging characteristics to commercial glass substrates has been demonstrated. Glass samples were endowed with the anti-fogging feature through a plasma deposition process; specifically, by a dielectric barrier discharge (DBD) operated in N_2 at atmospheric pressure (Townsend discharges) in the presence of 1,3,5,7-tetramethylcyclotetrasiloxane (TMCTS) and nitrous oxide (N_2O). Surprisingly, the use of atmospheric pressure DBDs for the manufacture of anti-fogging coatings has thus far not been explored, despite their tremendous potential for integration into mass production. Indeed, plasma processing at atmospheric pressure eludes the constraints imposed by operation at low pressure, such as the need for vacuum systems, and allows for coating deposition at room or near to room temperature. The latter feature makes AP-DBDs suitable for the fabrication of anti-fogging coatings on "thermally sensitive" materials, such as polymers or polymer-based composite materials.

The following objectives define the scope of this doctoral project:

1. Study of the structure, chemistry, topography, and wetting behavior of plasma-deposited coatings.

To reach this objective, coatings were analyzed using several characterization techniques. The chemistry of coatings was characterized by X-Ray Photoelectron Spectroscopy (XPS) and Fourier Transform Infrared Spectroscopy (FTIR). Surface topography was characterized by Atomic Force Microscopy (AFM) and wetting behavior was assessed by means of the sessile drop method.

2. Correlation between the deposition conditions and the anti-fogging performance of coatings.

To reach this objective, the anti-fogging response (light transmission under fogging conditions) was correlated with the deposition parameters and discussed in terms of the chemistry and surface roughness of the coatings. The investigated deposition parameters were the $[N_2O]/[TMCTS]$ ratio ([X] indicates concentration of X), the $[N_2O] + [TMCTS]$

sum, and the power dissipated in the discharge. The optimal deposition conditions were identified.

3. Unveiling the origin of the anti-fogging performance.

To reach this objective, the (cyclic) structure and the chemistry (presence of Si-H and Si-CH$_3$ groups) of TMCTS were both questioned. Using the optimal deposition conditions, a comparative study involving three other precursors with different structure and chemistry, namely octamethylcyclotetrasiloxane (OMCTS), 1,1,3,3-tetramethyldisiloxane (TMDSO), and hexamethyldisiloxane (HMDSO), was conducted.

Dissertation organization

This dissertation consists of six chapters. **Chapter 1** provides a review of strategies toward anti-fogging property based on water drop/surface interactions. The core problems associated with the fogging of surfaces are detailed along with the most relevant theories of surface wetting. Strategies allowing for the fabrication of anti-fogging surfaces based on surface chemistry and/or roughness modification, including the deposition of organic, inorganic, and composite materials, and the application of surface modification techniques are discussed in length. A brief overview of the current state and future opportunities coupled with considerations for future research in the field of anti-fogging technology are also presented. **Chapter 2** provides theoretical notions of plasmas physics and addresses some aspects relevant to atmospheric pressure dielectric barrier discharges (AP-DBD). Electrical breakdown in gases is explained in detail and correlated with the operation modes of dielectric barrier discharges. A brief description of the interactions between the plasma species and the substrate occurring during coating deposition is also presented along with the use of TMCTS for coating deposition. The techniques used to characterize the plasma-deposited coatings are described in **chapter 3**. Experimental results are presented in **chapters 4**, **5**, and **6**. Finally, the lessons learned from this doctoral project, topics proposed for future research, and recommendations to move forward from the results presented here are summarized in general discussion and conclusions.

1 Water drop-surface interactions as the basis for the design of anti-fogging surfaces: Theory, practice, and application trends

Iván Rodríguez Durán[ab] and Gaétan Laroche[ab]

[a]Laboratoire d'Ingénierie de Surface, Centre de Recherche sur les Matériaux Avancés, Département de Génie des Mines, de la Métallurgie et des Matériaux, Université Laval, 1065 Avenue de la médecine, Québec G1V 0A6, Canada.
[b]Centre de Recherche du Centre Hospitalier Universitaire de Québec, Hôpital St-François d'Assise, 10 rue de l'Espinay, Québec G1L 3L5, Canada.

1.1 Résumé

Les matériaux à base de verre et de polymères sont devenus essentiels dans la fabrication d'une multitude d'éléments, notamment les lunettes, les pare-brise d'automobile, les miroirs, les serres et les emballages d'aliments, qui s'embuent malheureusement dans les conditions normales de fonctionnement. Loin d'être un phénomène inoffensif, la formation de minuscules gouttes d'eau à la surface nuit aux propriétés optiques (par exemple, la capacité de transmission de la lumière) et pose souvent des problèmes d'esthétique, d'hygiène et de sécurité. Dans ce contexte, il n'est pas surprenant que la recherche dans le domaine des surfaces antibuée gagne en popularité, en particulier depuis les dernières années, compte tenu du nombre croissant d'études consacrées à ce sujet. Ce chapitre aborde les avancées les plus pertinentes publiées à ce jour concernant les surfaces antibuée, avec une attention toute particulière pour certaines caractéristiques comme le dépôt des revêtements, la micro/nano structuration et fonctionnalisation des surfaces. Tout d'abord, une brève explication de la formation de buée sur les surfaces, les principaux problèmes d'intérêt liés au phénomène de formation de buée, les stratégies antibuée ainsi qu'une description des états de mouillage des surfaces antibuée sont présentés. Les mécanismes antibuée sont ensuite discutés en termes de la morphologie des gouttes d'eau, en poursuivant avec une description des principales techniques de fabrication des surfaces antibuée. Ce chapitre se termine en décrivant les perspectives actuelles et futures de l'utilité des surfaces antibuée pour plusieurs applications et en abordant certains défis toujours d'actualité dans le domaine.

1.2 Abstract

Glass- and polymer-based materials have become essential for the fabrication of a multitude of elements, including eyeglasses, automobile windshields, bathroom mirrors, greenhouses, and food packages, which unfortunately mist up under typical operating conditions. Far from being an innocuous phenomenon, the formation of minute water drops on the surface is detrimental to their optical properties (e.g., light-transmitting capability) and, in many cases, results in esthetical, hygienic, and safety concerns. In this context, it is therefore not surprising that the research in the field of fog-resistant surfaces is gaining in popularity, particularly in recent years, in view of the growing number of studies focusing on this topic. This chapter addresses the most relevant advances released thus far on anti-fogging surfaces, with a particular focus on coating deposition, surface micro/nanostructuring, and surface functionalization. A brief explanation of how surfaces fog up and the main issues of interest linked to fogging phenomenon, including common problems, anti-fogging strategies, and wetting states are first presented. Anti-fogging mechanisms are then discussed in terms of the morphology of water drops, continuing with a description of the main fabrication techniques toward anti-fogging property. This chapter concludes with the current and the future perspectives on the utility of anti-fogging surfaces for several applications and some remaining challenges in this field.

1.3 Introduction

Fogging is the naturally occurring phenomenon by which water vapor condenses on a solid surface whose temperature is less than the dew point of the surrounding air-water vapor mixture [47]. The dew point is the temperature at which water vapor in air must be cooled to reach saturation (relative humidity of 100%) [1]. From a physical point of view, the conversion of water vapor into liquid water in the presence of a solid surface involves two main stages, namely, formation of minute droplets with radii exceeding a critical value or "heterogeneous nucleation"; and drop growth [48]. That said, to fully address the fogging phenomenon, the contact angle of water drops must be taken into account as it determines whether the condensate will fog up the surface or not. Generally speaking, the higher the water contact angle, the more pronounced the effects of condensation [49]. The main reason for this lies in the fact that each droplet scatters the incident light in all directions because of the small radius of curvature at the drop water/air interface [22]. The interaction between light and water drops explains to a large extent, why transparent materials become blurry when exposed to hot and humid environments. This feature of fogged surfaces is commonly referred to in the literature as "breath figures" [50–52].

The fogging of surfaces has been shown to cause adverse effects on sectors of activity such as the medical, the automotive, or the photovoltaic. For example, the presence of condensation on optical elements as diverse as mirrors, lenses, and prisms decreases the precision of microscopes and chromatographs [8,9]. In the automotive and aeronautic sectors (e.g., train, vehicle, and aircraft), the fogging of windshields is quite often linked to safety concerns as it causes limited visibility and image distortion [10–13]. Fogging has also been reported to impair the visual field of endoscopes during surgical procedures [53] and lower the energy-conversion efficiency of solar cells [26]. In the food industry, condensation on greenhouse claddings limits the crop yield [54,55] and reduces the visual appearance of packaged food, which is perceived by consumers as a lack of freshness and quality [56].

Thus far, two anti-fogging strategies have amply demonstrated their effectiveness in preventing these situations from occurring. The first one involves changing the environmental parameters, namely, temperature, relative humidity, and surrounding air flow. Rear windshields, chiller cabinets, or swimming pool windows equipped with heat elements, are some examples of how to remove surface fog by simply changing temperature. The heating equipment is basically a conductive coating that keeps surface temperature above the dew point upon application of a voltage [39]. Quite a number of papers on electrothermal coatings based on oxides such as In_2O_3-SnO_2 [44] and graphene oxide [41,43], metals such as Ni, Ag, and Cu [33,45,46], and semimetals such as carbon nanotubes [40] and graphene [42], have been published in this regard. These materials make it possible to remove fogging with minimal energy consumption [57]. Increasing air flow velocity is another well-known approach to get rid of surface fog. In this instance, air mixing first, promotes water evaporation and diminishes the number of potential condensation points [31,32]. The way windshield defrosting/defogging systems operate is an eloquent illustration of this phenomenon [11,37,38]. The incorporation of moist adsorbents [58] or purging by dry air or inert gas [59,60] have also proven to be successful in preventing condensation in dual-panel lens and double-glazed windows, respectively.

The second category of anti-fogging strategies focuses on changing the morphology of water drops by tuning the wetting characteristics of the surface. The wetting behavior of any material can be tailored by adjusting its surface features, i.e., roughness and surface chemistry, either by direct modification or by deposition a coating of a distinct material on the surface. As detailed in the following sections, this practice has shown to be suitable to endow anti-fogging surfaces with additional features such as icing-delay, anti-reflective, anti-bacterial, or anti-fouling characteristics. Anti-fogging strategies based on the direct modification of the substrate's surface features can be divided into two families. The first one pertains to changes in surface chemistry through the creation of functional groups different from the ones originally found on the surface. In this case, the bulk properties and surface topography remain virtually unchanged. On the contrary, the second family of anti-fogging strategies involves either enhancing surface roughness or "carving" surface nano/micro features with well-defined geometries, by means of "bottom-up" processing.

Here, a rigorous control of topography is crucial, as surface features exceeding 100 nm have been shown to compromise the optical properties, mainly because of light scattering, and the resistance to scratching and wear [61,62]. On the other hand, the deposition of thin films by "top-down" processing has also proven to be as effective as "bottom-up" processing or surface treatments in endowing polymeric and ceramic substrates with the anti-fogging feature.

Given the above considerations, anti-fogging surfaces can be classified into four distinct groups according to their apparent contact angles (APCAs) [63]: more specifically, superhydrophilic, hydrophilic, superhydrophobic, and hydrophobic surfaces. Hydrophilic and superhydrophilic surfaces, with an APCA in the range of $10° < θ < 40–50°$ and $5° < θ < 10°$, respectively, are made of "water-loving" materials. According to Drelich and colleagues [64], complete drop spreading or "superhydrophilicity" is possible only in textured or/and structured surfaces (rough and/or porous) featuring a roughness factor, as defined by Wenzel equation, greater than one. Surfaces with water-attracting features make water drops spread over the surface, thus forming a thin water film that allows for incident light to pass through without being scattered. As a result, the surface remains optically clear, even under strong fogging conditions.

A water contact angle of 90° has been conventionally adopted as the cut-off value to differentiate hydrophilic surfaces from those repelling water, i.e., (super)hydrophobic surfaces [65,66]. That said, it is widely accepted that surfaces with water contact angles above 40–50° [22,49,67] are not able to mitigate the effects of condensation despite being hydrophilic; hence, the above-mentioned $10° < θ < 40–50°$ range. Hydrophobic and superhydrophobic surfaces, with an APCA in the range of $90° < θ < 150°$ and $150° < θ < 180°$, respectively, are the result of a nano/microtextured surface coated with an intrinsically water-repellent material.

The term "superhydrophobic" refers to a nearly non-wettable state characterized by very low contact angle hysteresis and sliding angles ($< 5–10°$) [68], and can formally be described by

the "Cassie air-trapping" or a closely related wetting state [63,69]. Contrary to (super)hydrophilic surfaces, the application of water repellency for anti-fogging purposes appears to have attracted less interest within the scientific community. The fact that (super)hydrophobic surfaces must be tilted to remove condensation; and that the combination of water repellency with the anti-fogging performance calls for more complex and more time-consuming manufacturing processes may account for this divergence.

A concise overview of common fogging concerns and the fundamental aspects of fogging occurrence are introduced in **section 1.3**. On this basis, wetting states depicting the interaction of water drops with solid surfaces are presented in **section 1.4**. Materials and anti-fogging mechanisms are described in **section 1.5**. In **section 1.6**, fabrication techniques toward anti-fogging property are discussed in detail and classified into "top-down" and "bottom-up" processing, and surface functionalization. Featured applications of anti-fogging surfaces in key sectors of activity such as the food and photovoltaic industries and medicine, are addressed in **section 1.7**. **Section 1.8** concludes with our personal standpoint based on remaining and forthcoming challenges, current trends, and potential promising breakthroughs in this field.

1.4   Wetting states of anti-fogging surfaces

Experience shows that condensation of water vapor on a solid surface can occur according to two distinct modes, namely dropwise and filmwise condensation [70–72]. In dropwise condensation, a myriad of small water droplets with high contact angles forms when water vapor condenses on a low energy surface. In this case, the effects of fogging materialize, even though the surface is not fully wetted. On the contrary, should condensation take place on a substrate with high energy surface, water drops will exhibit very low contact angles (filmwise condensation). Here, no fogging is observed, as a thin film of water, not greatly hindering light transmission, forms on the surface.

As can be inferred from what Mother Nature show us, the morphology of water drops has a key role in the optical properties of materials under fogging conditions. Thus, surface chemistry and topography must both be properly adjusted to change water drops shape, and in this way, design surfaces simultaneously meeting suitable wetting behavior and anti-fogging requirements. As detailed in the following section, several wetting states have been proposed to explain the wettability of solid surfaces, considering surface chemistry and topography in a straightforward way, in terms of contact angles and surface roughness.

1.4.1 Smooth surfaces

1.4.1.1 Young model

As depicted in **Figure 1.1**, water drops resting on a smooth surface can be characterized by the angle θ_0 between the surface and the tangent line drawn along the liquid/vapor interface from the point where solid, liquid, and vapor phases meet.
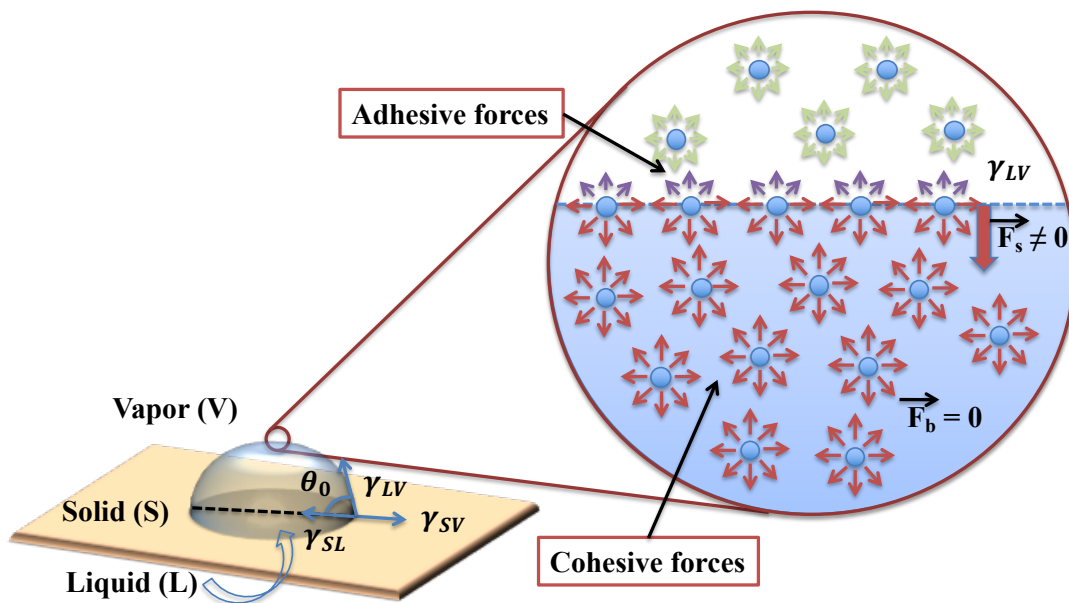
Figure 1.1: *Microscopic view of a water drop showing surface tensions at liquid/vapor, liquid/solid, and solid/vapor interfaces and forces acting on water molecules (adhesive and cohesive forces). Surface tension is the energy required to increase the surface area of a given phase by a unit of area (J m⁻²). F_s = forces between water molecules at the drop surface, and F_b = forces between water molecules within the bulk.*

In the early 19th century, Thomas Young [73] stated that the contact angle θ_0 is governed by the mechanical equilibrium resulting from surface tensions acting on the liquid drop/surface system, as follows:

$$\cos \theta_0 = \frac{\gamma_{SV} - \gamma_{SL}}{\gamma_{LV}} \tag{1.1}$$

where γ_{SL}, γ_{SV}, and γ_{LV} are the surface tensions solid/liquid, solid/vapor, and liquid/vapor, respectively, and θ_0 is the so-called "static contact angle".

Strictly speaking, **Equation 1.1** does not appear in Young's publication "An essay on the cohesion of fluids" [73]; however, there are two statements contained in it, namely, *for each combination of a solid and a fluid, there is an appropriate angle of contact between the surfaces of the fluid, exposed to the air, and the solid* and *We may therefore inquire into the conditions of equilibrium of the three forces acting on the angular particles, one in the direction of the surface of the fluid only, a second in that of the common surface of the solid and fluid, and the third in that of the exposed surface of the solid*, which substantiate that the contact angle can be defined in terms of the surface tensions γ_{SL}, γ_{SV}, and γ_{LV}.

Although the use of surface tensions rather than forces, as stated by Young, has been a subject of debate [74], theoretical derivation of **Equation 1.1** has recently been proven using thermodynamic arguments [75–78]. Despite this, Young's equation (**Equation 1.1**) does not adequately reflect the complexity of wetting phenomena, as it applies strictly to atomically flat and chemically homogeneous surfaces that neither dissolve nor react when in contact with the liquid. With all of these constraints, interpreting water contact angles measured on real surfaces, i.e., APCAs, calls for wetting states considering, not only surface chemistry (via surface tensions) but also surface roughness.

1.4.2 Rough surfaces

1.4.2.1 Wenzel equation

Following observation of contact angles on real surfaces, Wenzel [79,80] proposed an alternative to Young's equation including the effect of surface roughness on the wetting behavior, as follows:

$$\cos \theta_W = R_f \cos \theta_0 \qquad (1.2)$$

where θ_W is the "apparent contact angle" or the contact angle measured on a rough surface, R_f is the roughness factor, and θ_0 is the contact angle as described by **Equation 1.1**.

The roughness factor is defined as the ratio between the real surface area A_R (for a given surface topography, i.e., peaks and valleys) and the geometric area resulting from the projection of the rough surface onto a hypothetical planar surface A_P. Given that $A_R > A_P$, hydrophilicity and hydrophobicity are both enhanced with surface roughness. Indeed, an increase in roughness factor lowers θ_W when $\theta_0 < 90°$ yet enhances θ_W when $\theta_0 > 90°$. Regardless of the hydrophilicity/hydrophobicity of the surface, the wetting of a rough and chemically homogeneous surface results in two-phase solid-water interface with no air trapped within, namely the Wenzel wetting state (**Figure 1.2a**).

1.4.2.2 Cassie-Baxter equation

As reported in the preceding paragraph, Wenzel state presumes that rough surfaces are fully wettable. Nevertheless, it has been shown that liquid drops can eventually break Wenzel's assumption, and not displace the air trapped into the cavities [81,82].

Cassie and Baxter addressed this issue by assuming that such surfaces are composed of two distinct features, one with a fractional area φ_1 and Young's contact angle θ_1, and the other, with a fractional area φ_2 and Young's contact angle θ_2, with $\varphi_1 + \varphi_2 = 1$. The apparent contact angle, which can be regarded as a weighted average of static contact angles for each fraction, is given by the Cassie-Baxter equation:

$$\cos \theta_{CB} = \varphi_1 \cos \theta_1 + \varphi_2 \cos \theta_2 \qquad (1.3)$$

In this case, two wetting scenarios are possible: Cassie air-trapping and Cassie impregnating sates. The first wetting state considers water drops lying on the top of protrusions of the solid surface and air trapped underneath them (**Figure 1.2b**). This distinguishing feature of the Cassie air-trapping state has been attributed either to re-entrant geometries [83] or the combination of a hierarchical topography with a low surface energy material. On this basis, the first fraction φ_1 corresponds to the solid/liquid interface with a fractional area φ_{SL} and $\theta_1 = \theta_0$ (flat protrusions), and the second one φ_2, to the liquid/vapor interface with a fractional area $\varphi_{LV} = 1 - \varphi_{SL}$ and $\theta_2 = 180°$ (full water repellency). In light of these boundary conditions, **Equation 1.3** thus becomes [84,85]:

$$\cos \theta_{CA} = -1 + \varphi_{SL} (\cos \theta_0 + 1) \qquad (1.4)$$

Equation 1.4 represents the so-called "Cassie air-trapping wetting state" (**Figure 1.2b**). Here, the resulting three-phase solid-water-air interface is *a sine qua non* for a superhydrophobic anti-fogging surface to operate optimally. The term "optimally" refers to the situation in which water drops leave the surface upon rolling leaving no remnants behind. Conversely, if the surface is impregnated by water (water displaces air trapped in the cavities), Cassie-Baxter equation can be rewritten as follows:

$$\cos \theta_{CI} = 1 + \varphi_{SL} (\cos \theta_0 - 1) \qquad (1.5)$$

Equation 1.5 represents the so-called "Cassie impregnating wetting state" (**Figure 1.2c**) [69]. In both wetting states, φ_{SL} ranges from 0 to 1. When $\varphi_{SL} = 1$, the wetting behavior is described by Young's equation (flat surface), while $\varphi_{SL} = 0$ results in a non-wettable surface ($\theta = 180°$).
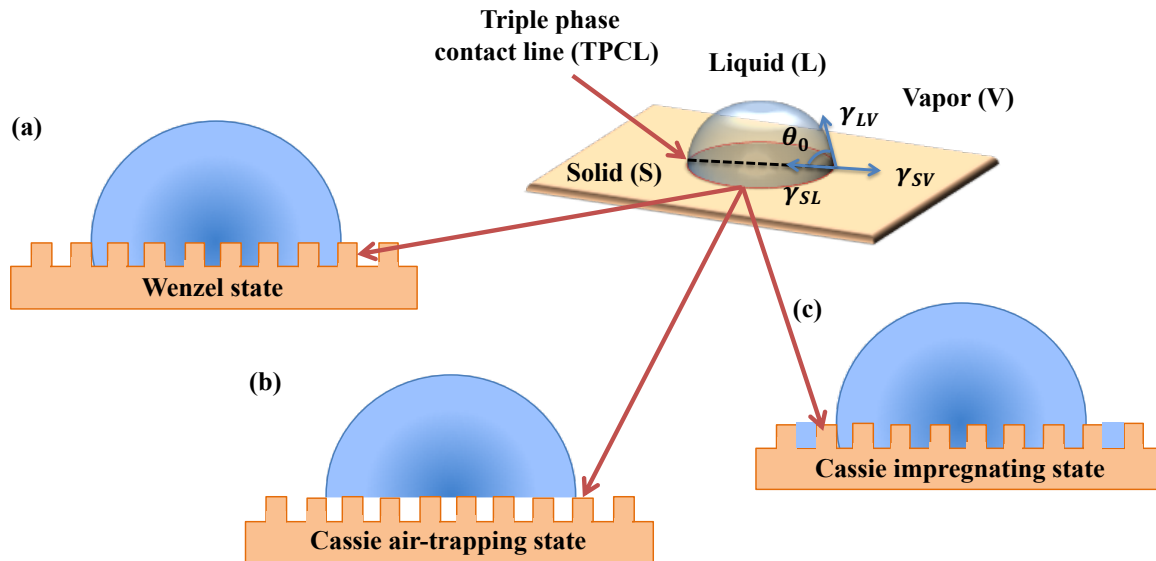
Figure 1.2: Wetting regimes. (a) Wenzel state, (b) Cassie air-trapping state, and (c) Cassie impregnating state. Solid, liquid, and vapor phases meet in an imaginary circular line known as the "triple phase contact line" (TPCL).

1.4.3 The issue of line tension in micro/nano droplets and contact angle hysteresis

According to Marmur [86], Wenzel and Cassie-Baxter equations do not adequately describe the wetting behavior of real surfaces, as they are built on the assumption that the contact angle does not depend on the size of the drop. Although appropriate for water drops sufficiently large compared with surface features (roughness), these equations do not take into account the non-negligible effects of line tension in nano- and micro-scaled sessile droplets [87–89], which also forms during condensation. In this context, Bormashenko [90]

recently reported a general formula describing the wetting behavior of rough surfaces including the effect of the tension line in minute droplets.

On the other hand, for a specific system water drop/surface, the combination of the triad γ_{SV}, γ_{LV}, and γ_{SL} with surface roughness must result in a unique contact angle. That said, the observed contact angles usually differ from those obtained using the above-mentioned equations, primarily because of the motion of the triple phase contact line (TPCL). The TPCL is defined as the imaginary circular line where solid, liquid, and vapor phases meet (**Figure 1.1**) [63]. A moving TPCL leads to a minimum value of the contact angle, or "receding angle" θ_{rec} and a maximum one, or "advancing angle" θ_{adv}, which can be assessed using two different methods, namely dynamic sessile drop method and tilting base method [65].

In the dynamic sessile drop method, a water droplet is dropped onto a horizontal surface from a syringe without losing contact with the needle. When water is removed from the drop, the contact angle decreases to a minimum value or the receding contact angle, θ_{rec}, before TPCL moves inward (**Figure 1.3a**). When liquid is added, TPCL reaches a stable state characterized by the advancing contact angle, θ_{adv}, that is, the contact angle measured just before TPCL moves outward (**Figure 1.3b**). The difference between advancing and receding contact angles ($\Delta\theta = \theta_{adv} - \theta_{rec}$) is called "contact angle hysteresis" (CAH) [68]. Adhesion hysteresis, chemical heterogeneities, and surface roughness have been reported as the main factors behind the contact angle hysteresis [77,91–94]. Nevertheless, the pinning of the TPCL is probably the most important source of CAH, as observed in silicon wafers [93] and extruded polymer [94] films, known for being atomically smooth and free of chemical heterogeneities.

In the tilting base method, a water droplet is placed on a horizontal surface as in the preceding method. In addition to the CAH, this approach allows for the assessment of contact angles when water drops meet a tilted or a moving surface (i.e., dynamic wettability). The difference with respect to the sessile droplet method is that the angle between the surface and the

horizontal plane is gradually tilted from 0° to a critical value α, also known as "sliding angle" (SA), triggering drop motion (**Figure 1.3c**) [95]. As will be seen later in **section 1.5**, the water contact angle (WCA), the contact angle hysteresis (CAH), and the sliding angle (SA) are key parameters requiring control to design anti-fogging surfaces featuring rolling-mechanism.
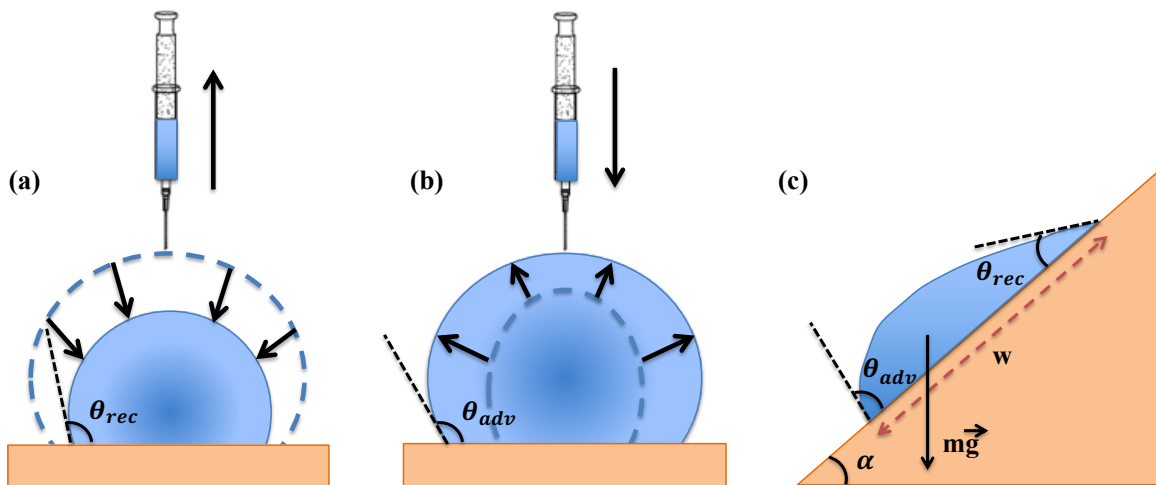
Figure 1.3: *Dynamic sessile drop method for the assessment of (a) receding $\boldsymbol{\theta_{rec}}$ and (b) advancing $\boldsymbol{\theta_{adv}}$ contact angles. (c) Tilting base method for the measurement of advancing and receding contact angles, and sliding angles. Adapted with permission from "Definitions for hydrophilicity, hydrophobicity, and superhydrophobicity: Getting the basics right", Law, K.-Y., J. Phys. Chem. Lett., Volume 5, Issue 4, 2014, Pages 686-688. Copyright 2018, American Chemical Society.*

1.5 How to prevent surfaces from fogging up: Anti-fogging strategies, mechanisms, and materials

Anti-fogging strategies explored thus far can be grouped into two broad categories. The first one aims at controlling the parameters external to the liquid/solid interface, that is, those involved in the nucleation of water drops (e.g., temperature, air flow, and relative humidity). Although this approach has proven to be very effective in avoiding or removing condensation, it is outside the scope of this chapter. The second category of anti-fogging strategies pertains to changes in the morphology of water drops either by directly tuning the substrate's surface features (chemistry and roughness) or by coating deposition. Compared

to the first category of anti-fogging strategies, the elaboration of surfaces endowed with the anti-fogging feature has generated more interest, in light of the numerous papers published in the last ten years. According to the most recent literature, the way these surfaces combat fogging can be explained by three different mechanisms:

1.5.1 (Super)hydrophilic anti-fogging surfaces: Spreading mechanism

Anti-fogging surfaces featuring spreading mechanism are mostly coatings made from hydrophilic or "water-loving" materials. These materials interact with water drops causing them to spread across the surface, and thus form a scattering-free water film (**Figure 1.4**).

$\theta = 90°$ $0° < \theta < 90°$ $\theta \approx 0°$

Time
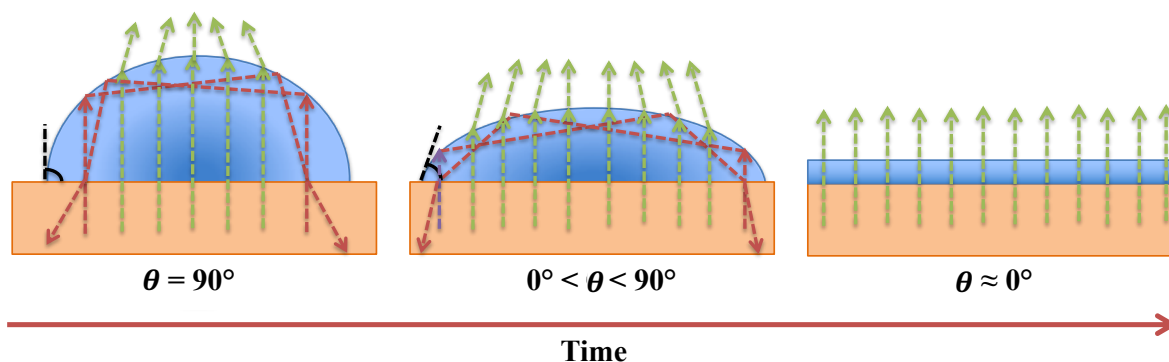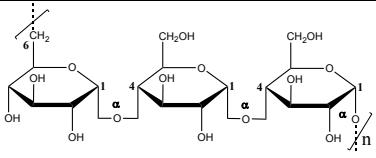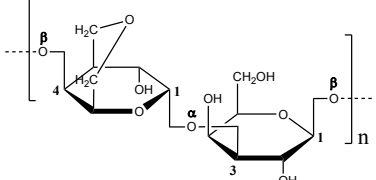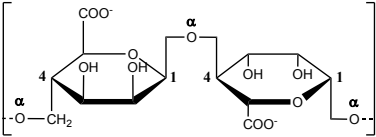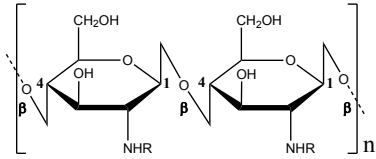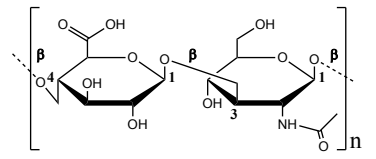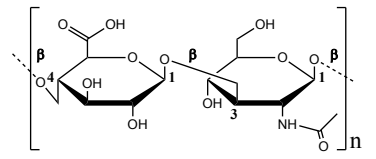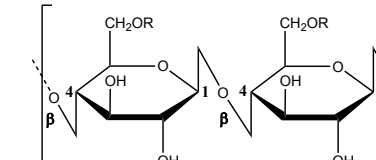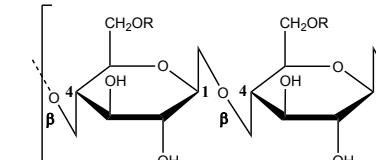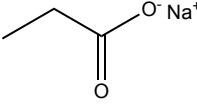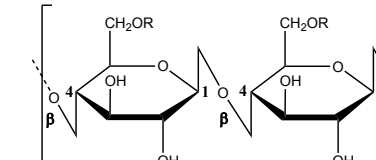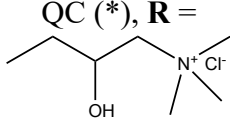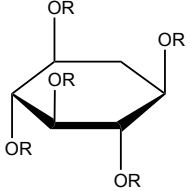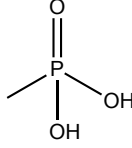
Figure 1.4: Illustration of the spreading mechanism. As water drops spread across the surface, total internal reflection (dashed red rays) become less prevalent while transmitted light (dashed green rays), increasingly less scattered, travel through the system water drop/surface. These surfaces are either hydrophilic (10° < θ < 40–50°) or superhydrophilic (5° < θ < 10°).

To date, there appears to be general agreement that wetted surfaces remain optically clear under aggressive fogging conditions, if the contact angle of water drops is less than 40–50° [22,49,67]. Generally speaking, these coatings can be made either from polymers and inorganic materials or from a mixture of both (composite materials). Polymers with pendant hydrophilic functionalities such as hydroxyl (OH), carboxyl (COOH), ester (COOR), amino (NH$_2$), amide (NHCOR), sulfonic (SO$_3$H), and dihydrogen phosphate groups (PO$_4$H$_2$) are materials of choice for anti-fogging coatings (**Table 1.1**).
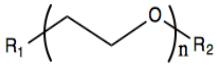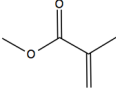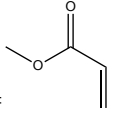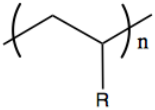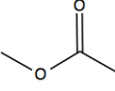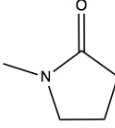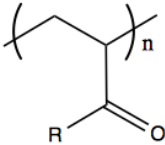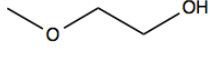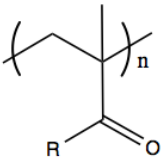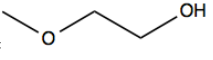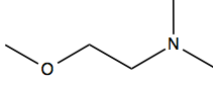
Table 1.1: *Repeating units of the main polymers of natural origin used in anti-fogging formulations. CMC: carboxymethyl cellulose, QC: quaternized cellulose. *Water-soluble. **Water-swellable. ***Water-insoluble.*

Kingdom of nature	Repeating unit	Anti-fogging polymer
Fungi		Pullulan (*)
Protista (Algae)		Agar-agar (*/**)
		Alginate (*)
Animalia (Animals)		Chitosan (*/***), **R** = H Chitin (***), **R** =
		Hyaluronic acid (***)
Plantae (Plants)	 	Cellulose (***), **R** = H CMC (*), **R** = QC (*), **R** = Phytic acid (*), **R** =

In this regard, the use of natural polymers has been receiving increasing attention in recent years because of their unique features, including the possibility of covering thermally sensitive materials, their easy availability, as well as their non-toxic and environmentally friendly nature. On the other hand, synthetic polymers have also been explored for anti-fogging purposes because of their unique features, including their availability and crosslinkable nature, low-cost, and tunable interaction with water drops. These macromolecules can be classified into four main families according to their chemical structure, namely, polyethers, polyvinyls, polyacrylates/polyacrylamides, and polymethacrylates (**Table 1.2**).

The criterion of either being naturally-sourced or not, appears not to apply when considering inorganic materials. As a matter of fact, most of the studies reported thus far on inorganic coatings with anti-fogging performance consider more suitable to classify them, according to their response to light, into two groups. The first one comprises intrinsically hydrophilic and non-photoresponsive materials, such as SiO_2, ZrO_2, In_2O_3-SnO_2 (ITO), MgO-Al_2O_3, and graphene oxide, while the second one is integrated by materials becoming superhydrophilic upon exposure to UV light, such as TiO_2, ZnO, and Bi_2O_3. These materials are typically covered with abundant hydroxyl (OH) groups per area unit. On the other hand, the combination of the photo-induced superhydrophilicity with the photocatalytic property allows for the use of TiO_2-based materials in applications where self-cleaning and anti-fogging characteristics are required. Without going into detail, photocatalysis is basically a set of reactions whereby a dirty TiO_2 surface gets cleaned at room temperature. For this to occur, TiO_2 must absorb UV light to yield "reactive oxidizing species" (ROS), such as superoxide and hydroxyl radicals, that decompose organic pollutants into CO_2 and H_2O [96]. Unfortunately, the fact that TiO_2 necessitates UV light to perform makes it challenging to design TiO_2-based anti-fogging coatings for indoor applications. Indeed, when stored in a dark place, an UV-irradiated TiO_2 surface (superhydrophilic) experiences a conversion toward a more hydrophobic state, which is normally less effective in combating surface fog. To remedy this situation, a growing number of studies have focused efforts not only on enhancing the anti-fogging performance of TiO_2 in the absence of UV light, but also on broadening its photocatalytic response to visible and near-IR regions.

Table 1.2: *Repeating units of the main synthetic polymers used in anti-fogging formulations.*
*Water-soluble. **Water-swellable. ***Water-insoluble.*

Family	Repeating unit	Anti-fogging polymer
Polyether		Poly (ethylene glycol) (PEG) (*) $R_1 = R_2 = H$ Poly (ethyleneglycol dimethacrylate) (PEGDMA) (*) $R_1 = R_2 =$ Poly (ethyleneglycol methacrylate) (PEGMA) (*) $R_1 = H$, R_2 as in PEGDMA Poly (ethyleneglycol diacrylate) (PEGDA) (*) $R_1 = R_2 =$
Polyvinyl		Poly (vinyl alcohol) (PVA) (*) $R = OH$ Poly (vinyl acetate) (PVAc) (***) $R =$ Poly (vinyl-N-pyrrolidone) (PVP) (*) $R =$
Polyacrylates & Polyacrylamides		Poly (acrylic acid) (PAA) (*) $R = OH$ Poly (2-hydroxyethyl acrylate) (PHEA) (*) $R =$ Poly (acrylamide) (PAM) (*) $R = NH_2$
Polymethacrylates		Poly (methacrylic acid) (PMAA) (*) $R = OH$ Poly (methyl methacrylate) (PMMA) (***) $R = O\text{-}CH_3$ Poly (2-hydroxyethyl methacrylate) (PHEMA) (**) $R =$ Poly (dimethylaminoethyl methacrylate) (PDMAEMA) (*) $R =$

Mixing with oxides, such as WO_3, ZnO, SiO_2, $ZnFe_2O_4$, and reduced graphene oxide [97–103]; doping with metals, such as Cu and Ag [104,105]; incorporating porogens, including PEG and cetyltrimethylammonium bromide (CTAB), coupled with a calcination treatment [106–110]; using "building blocks" with high surface-to-volume ratios (e.g., nanofibers, nanobelts, nanospheres) [111–117]; and increasing the surface roughness [118–122], have amply demonstrated to be suitable approaches to fabricate dual anti-fogging/self-cleaning TiO_2-based films, with no need for UV light to perform.

Despite not being implemented as widely as coating deposition, the direct modification of the substrate's surface features (chemistry and roughness) has amply proven its effectiveness in fabricating fog-resistant surfaces featuring spreading mechanism. In this regard, the anti-fogging performance can be met either by modifying surface topography (**section 1.6.2**) or by creating hydrophilic functionalities by means of surface treatments (**section 1.6.3**).

1.5.2 (Super)hydrophobic anti-fogging surfaces: Rolling mechanism

Contrary to those featuring spreading mechanism, surfaces with water-repellent characteristics must be tilted to a minimal angle α (sliding angle) to roll off water drops, and thus avoid the effects of surface fog (**Figure 1.5**).
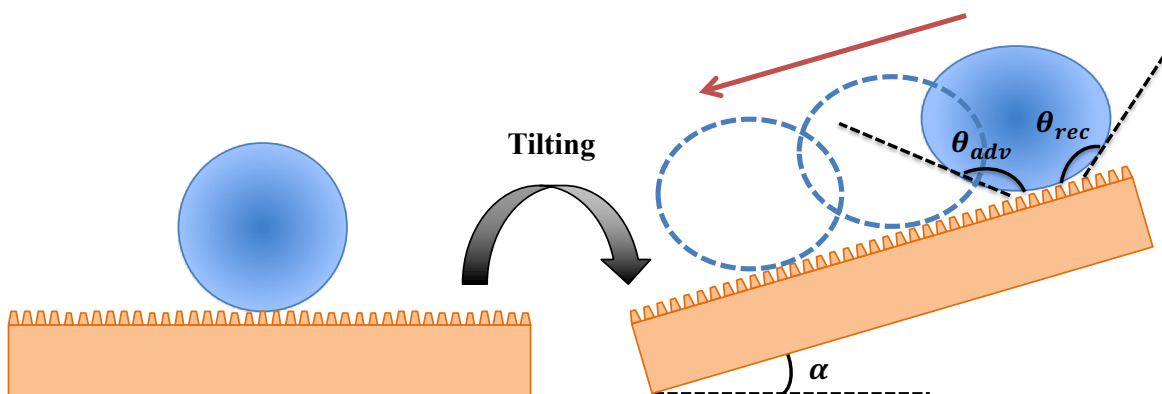
Figure 1.5: *Illustration of the rolling mechanism. Upon elevation of one side of the surface, water drops roll off easily, thereby preventing light scattering. These surfaces are either hydrophobic (150° > **θ** > 90°) or superhydrophobic (**θ** > 150°) and exhibit very low CAH and SA.*

There is general agreement among the scientific community that surface features required for a superhydrophobic anti-fogging surface to perform optimally are high contact angles (CA) coupled with low CA hysteresis and low slides angles (**Figure 1.6**). Surfaces displaying these characteristics fall into one of the following wetting states: Wenzel, Cassie air-trapping, Cassie impregnating (with a single level of hierarchy of roughness), and Lotus-like (with a double level of hierarchy of roughness, that is micro and nanoscale roughness).
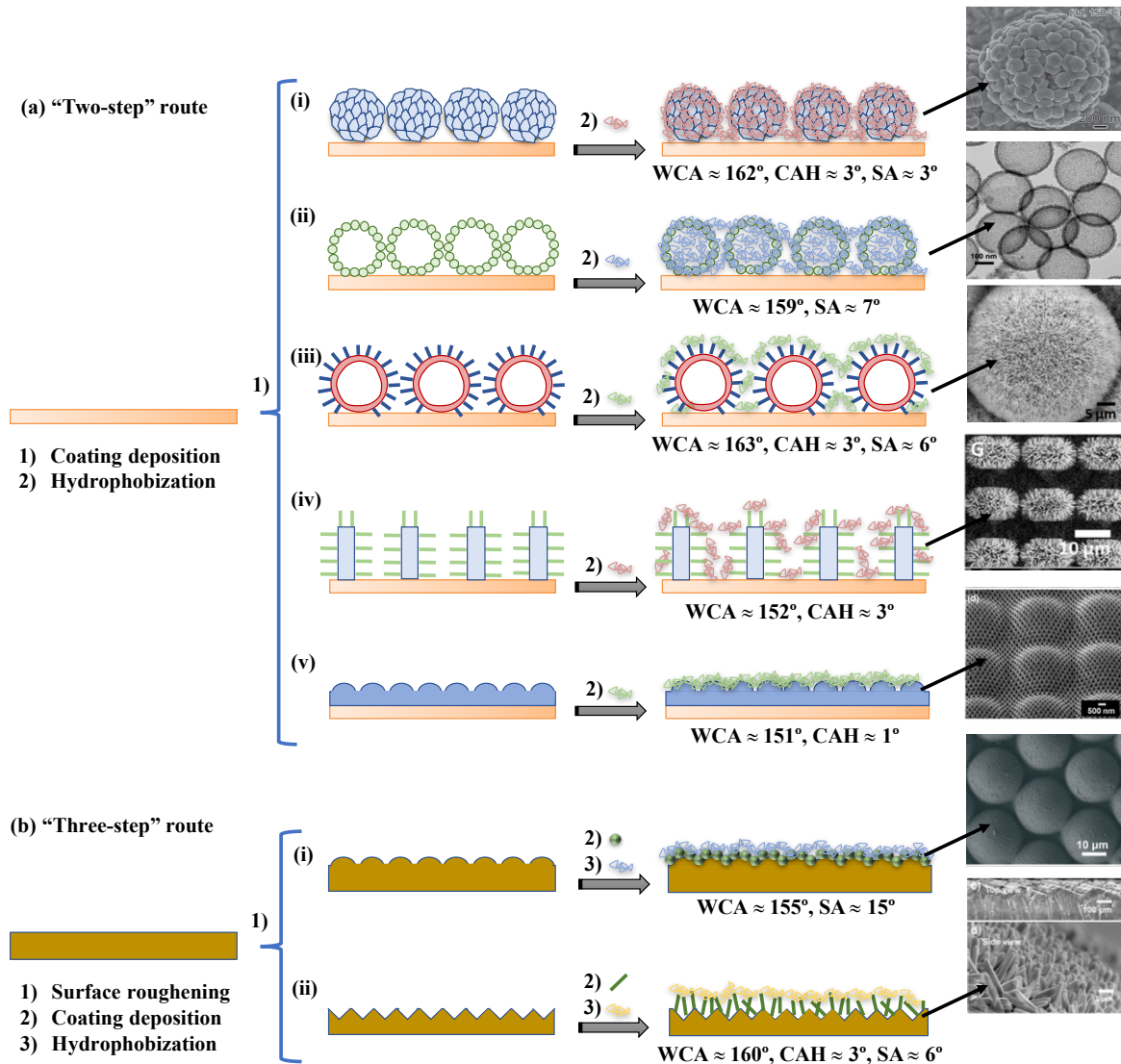
Figure 1.6: Routes toward water-repellency and anti-fogging performance. (a) The "two-step" route: deposition of a layer with high specific surface and hydrophobization. (i) Deposition of fly-eye bio-inspired ZnO nanostructures and treatment with 1H, 1H, 2H, 2H-perfluorooctyltriethoxysilane (PFOTES) [123]; (ii) deposition of raspberry-like SiO₂ nanospheres and hydrophobization with 1H,1H,2H,2H-perfluorodecyltriethoxysilane (PFOTS) [124]; (iii) deposition of dandelion-like ZnO microspheres and subsequent treatment with heptadecafluorodecyltripropoxysilane (FAS-17) [125]; (iv) deposition of

The rose petal-like state has not been considered here as it usually displays high contact angle hysteresis. Cassie air-trapping and Lotus-like wetting states are suitable for anti-fogging purposes as water drops roll off the surface leaving no others behind. In contrast, Wenzel and Cassie impregnating wetting states do not meet anti-fogging requirements. Here, drops remaining entrapped into the surface features, after the tilting of the surface, can be detrimental to the anti-fogging performance, as they scatter light as larger water drops do.

With this in mind, anti-fogging surfaces featuring rolling mechanism can be fabricated according to two different routes: the "two-step" and "three-step" routes. The "two-step" route (**Figure 1.6a**), which is typically applied to ceramic substrates, is based on the deposition of "building units" followed by a treatment with a low surface energy material [123–127], while the "three-step" route (**Figure 1.6b**) consists of surface microstructuring of a polymeric substrate by soft lithography (**section 1.6.2.2**), followed by coating deposition and hydrophobization [128,129].

1.5.3 Hydrophilic/oleophobic anti-fogging surfaces: Percolation mechanism

Anti-fogging surfaces featuring percolation mechanism are mainly coatings made of fluorosurfactants polymers, namely, perfluorinated polyethylene glycol polymers [130–137] (**Figure 1.7a**) and perfluoropolyether polymers (**Figure 1.7b**) [138,139], containing hydrophilic and oleophobic domains [140].

(a)

n = 6-18, m = 4-6

Linear fluorosurfactants
"FSN" and **"FSO"**

Y-shaped fluorosurfactant

(b)

m/n = 1

R = CF$_3$ **"Z-03"**

R =   OH   **"Zdol"**

R =   OH   **"Z-tetraol"**
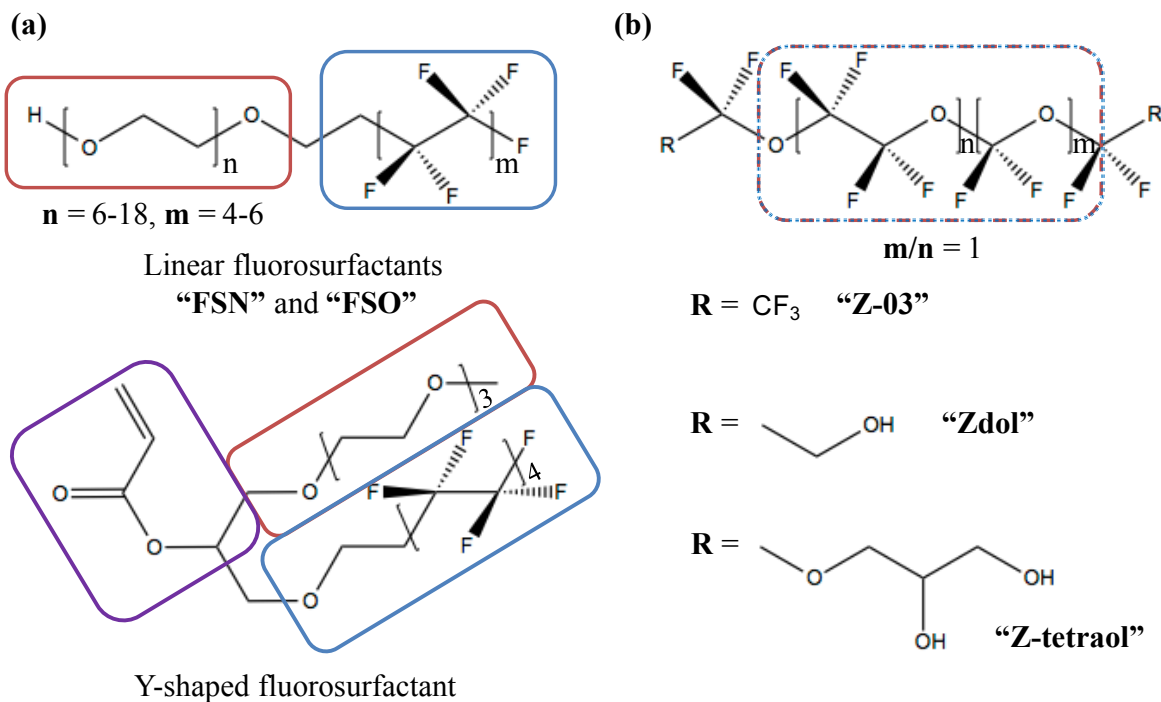
Figure 1.7: Fluorocarbon surfactants used in anti-fogging surfaces featuring percolation mechanism. (a) Linear and "Y-shaped" perfluorinated polyethylene glycol oligomers. Hydrophilic and oleophobic components are separated in the polymer chain. Depending on the hydrophilic domain, these molecules can be anionic, cationic, non-ionic, or amphoteric. (b) Family of perfluoropolyether polymers (PFPE): hydrophilic and oleophobic domains cannot be distinguished in the backbone. Red: hydrophilic domain, blue: hydrophobic domain, purple: a polymerizable vinyl group.

Due to this particular feature, these surfaces enable small molecules (e.g., water molecules) to penetrate the coating faster than do larger ones (e.g., hexadecane molecules). To date, two distinct mechanisms have been proposed to explain this striking behavior. The first one, at times referred to as the "flip-flop" mechanism, relies on the presence of "defects" of appropriate size in the coating [130,131,133,134,136,137]. In general, when fluorosurfactants are deposited on a substrate, perfluorinated chains are orientated outward (hydrophobic/oleophobic region) while polyethylene glycol- and hydroxyl-containing moieties are directed toward the surface (hydrophilic/oleophobic region). Considering that this configuration results in a low surface energy barrier repelling oil and water drops, right-sized defects in the fluorine-containing layer are then necessary to enable water drops to permeate and reach the interface coating/substrate (**Figure 1.8**).
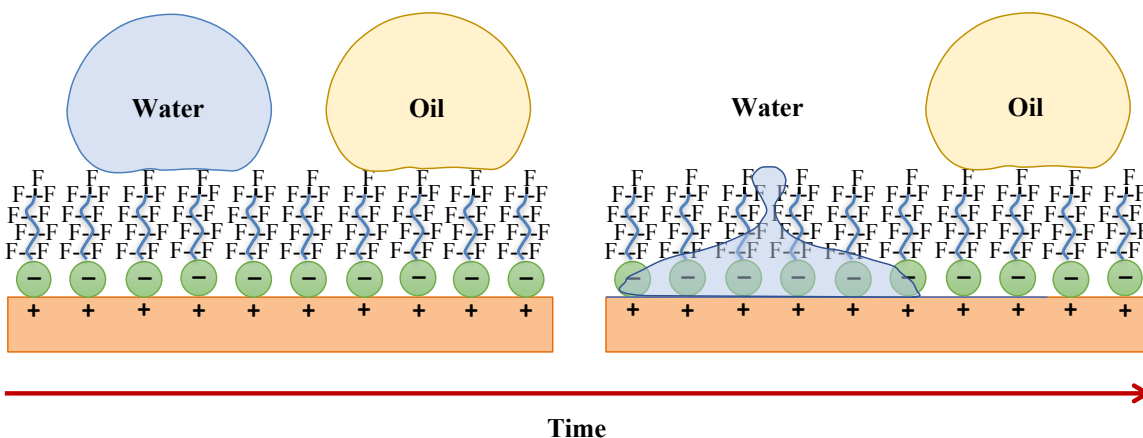
Figure 1.8: *Illustration of the "flip-flop" mechanism. The distinguishing feature of a oleophobic/hydrophilic coating is the tendency of water drops to permeate the coating, and thus eliminate the effects of condensations, while blocking or slowing down the passage of oily substances. Accordingly, oil contact angles (OCA) are greater than water contact angles (WCA). Adapted from "Bioinspired, roughness-induced, water and oil super-philic and super-phobic coatings prepared by adaptable layer-by-layer technique", Brown, P. S.; Bhushan, B.; Young, T.; et al., Sci. Rep., Volume 5, 2015, Page 14030. (Open access).*

Another proposed mechanism accounting for the simultaneous hydrophilicity/oleophobicity relies on the rearrangement of polymer chains when in contact with water or any other polar liquid [138,139]. Contrary to the preceding mechanism, the presence of defects in the fluorine-containing region is no longer necessary. Here, when a water drop meets the surface, perfluorinated chains rapidly rearrange inducing the formation of "channels" that allow for small water molecules to permeate quickly toward the hydrophilic region, while blocking or slowing down larger oil molecules. As in the case of TiO_2-based materials, surfaces with simultaneous hydrophilicity and oleophobicity are suitable for use in applications requiring anti-fogging performance with a certain degree of self-cleaning activity. Badyal's group [136] proposed a "switching parameter", defined as the difference between oil (hexadecane) and water static contact angles, to quantitatively assess the percolation mechanism. The higher the "switching parameter," the better these anti-fogging surfaces perform. In another study, Howarter et al. [133] demonstrated that an advancing WCA < 30° and a receding OCA > 67°, are necessary to meet simultaneous self-cleaning and anti-fogging properties. In either case, the strong affinity between water molecules and the surface enables water drops (the cleaning fluid) to wet the surface by displacing oily substances (the pollutant).

1.6 Fabrication techniques toward anti-fogging property

The above-illustrated mechanisms highlight the fact that a judicious combination of surface topography and surface chemistry is key to developing surfaces with fogging resistance. Bearing this in mind, a plethora of fabrication techniques aimed at adjusting the wetting behavior of water drops on solid surfaces has been thus far applied. The following sections present the most widely used techniques for the preparation of anti-fogging materials. To be consistent with the notions outlined above, these techniques have been classified into three distinct categories: bottom-up and top-down processing, and surface functionalization.

1.6.1 Bottom-up processing

Bottom-up processing involves the assembly of small "bricks" such as nanoparticles and polymers into more complex systems.

1.6.1.1 Dip-coating deposition

When vinyl/acrylic polymers such as PVA, PVP, and PAA, are used as starting materials, dip-coating deposition allows for the fabrication of anti-fogging coatings endowed with frost-resisting and even self-healing features [141–144]. In PET and PC substrates (eyeglasses) covered with PVA-Nafion complexes prepared by Sun et al. [145] a minimum thickness of 61 nm was required to prevent fogging effects at room temperature, while a thickness of 247 nm was necessary to ensure transparency over boiling water (**Figure 1.9a**). In addition to providing PC lenses free of frozen fog (**Figure 1.9b,c**), PVA/Nafion films were also found to be self-healable (**Figure 1.9d,e**). After five cycles of damage and healing tests, the transmittance of the coated PET fully recovered ($T_{average} \approx 99\%$ at 500 nm), as supported by the complete closing of the scratches (**Figure 1.9f,g**).
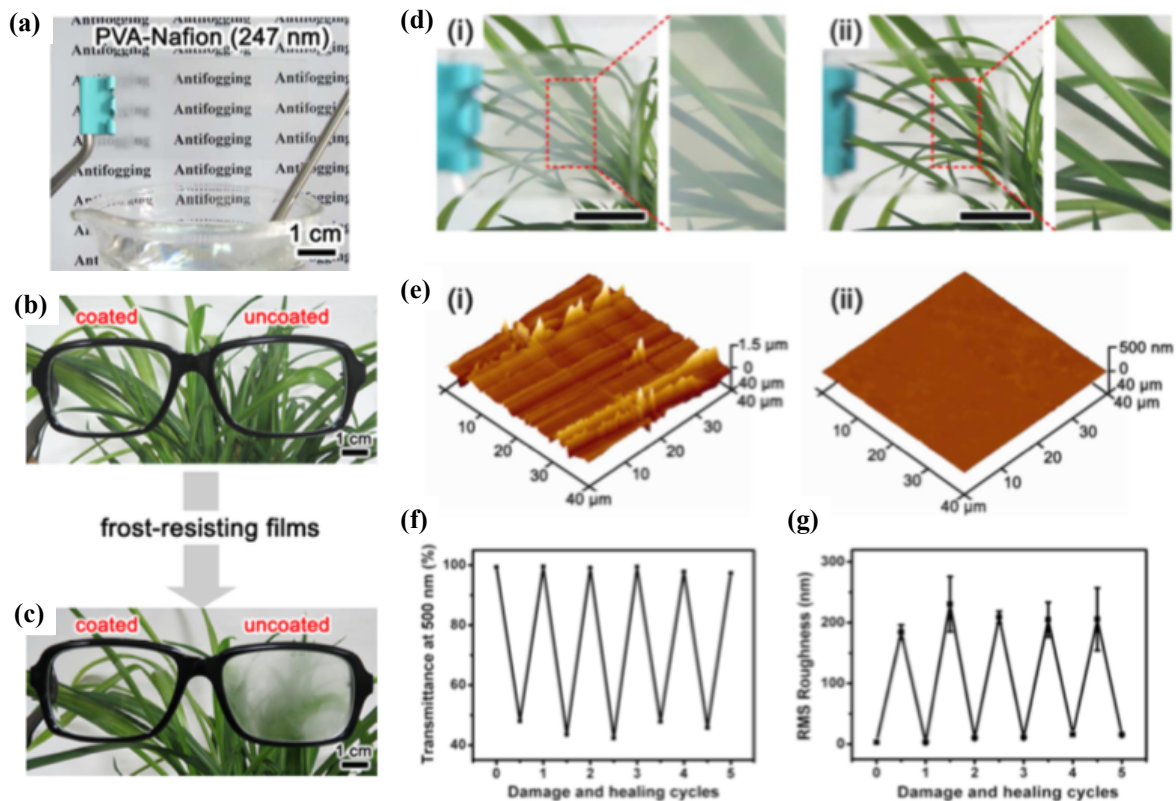
Figure 1.9: *(a) Anti-fogging properties of a PVA-Nafion film with thickness of ~247 nm, respectively. These films were first conditioned in a –20°C refrigerator for 1 h and then placed over boiling water (~50°C and ~100% RH). (b) Pair of polycarbonate eyeglasses, with the left-hand lens coated with PVA-Nafion films and the right-hand one uncoated. (c) Eyeglasses after being conditioned at –20°C for 1 h and then exposed to an ambient environment of ~20°C and ~40% RH. (d) Digital images of the PVA-Nafion film on a glass substrate that heals scratches. (i) Film scratched with sandpaper and (ii) scratched film from panel i after healing in water for 5 min. The scale bar is 1 cm. (e) AFM images of the scratched PVA-Nafion film before (i) and after (ii) healing in water. (f,g) Changes in transmittance at 500 nm and R_{rms} roughness, respectively, of the PVA-Nafion film during five cycles of the scratching-healing process. Reprinted with permission from "Highly transparent and water-enabled healable antifogging and frost-resisting films based on poly(vinyl alcohol)-nafion complexes", Li, Y.; Fang, X.; Wang, Y.; Ma, B.; and Sun, J., Chem. Mater., Volume 28, Issue 19, 2016, Pages 6975-6984. Copyright 2018, American Chemical Society.*

Although PEG-based coatings do not feature self-healability [146], hydrogels prepared by Molina et al. [147] using a PEG functionalized with 3-isocyanatopropyltriethoxysilane hold great promise for the manufacture of anti-fogging films with drug delivery capability, due to its water absorbing characteristics. Anti-fogging coatings made from isosorbide-based epoxy resin, a polymer containing epoxide groups, also exhibited potential applicability as drug

delivery system [148]. Different research groups have recently developed fog-resistant films containing sulfonic and phosphonic groups, well known for their high water-absorbing characteristics and underwater oleophobicity [149–152] (**Figure 1.10**).
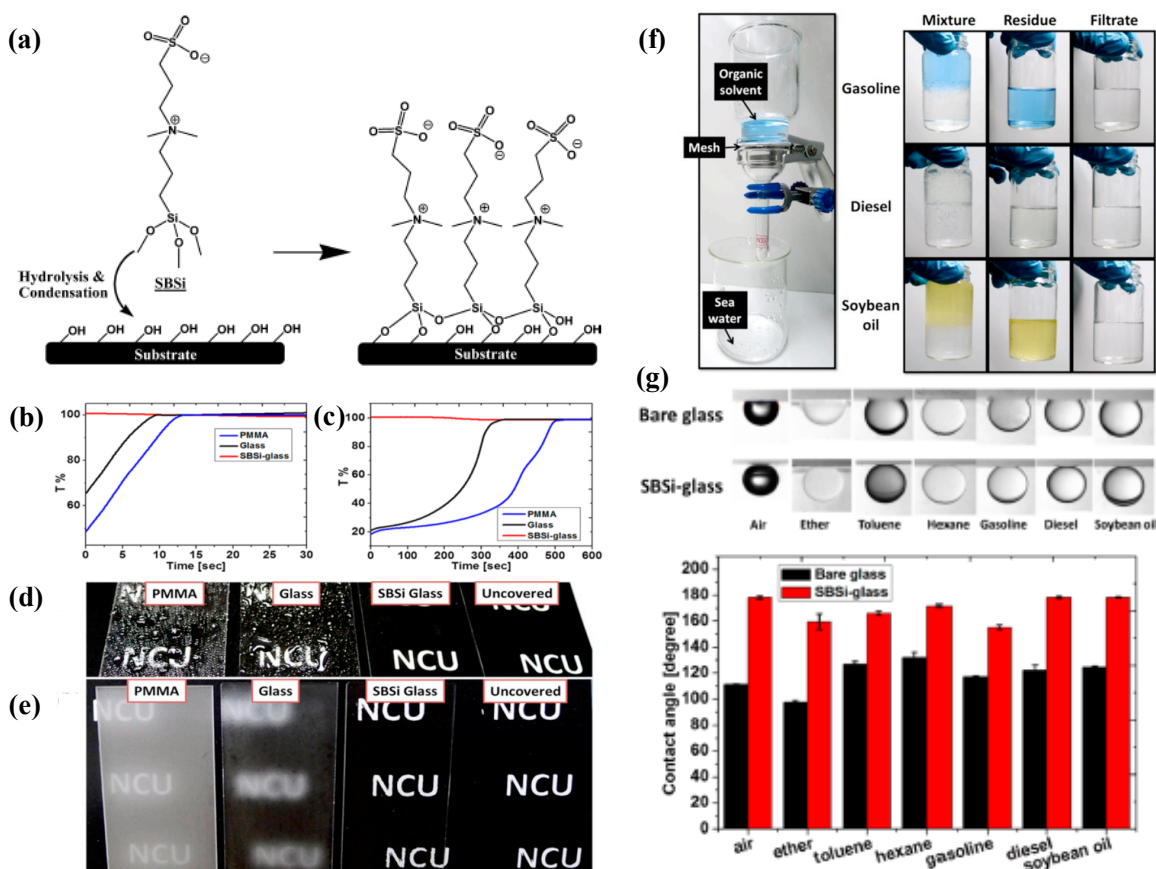
Figure 1.10: *(a) Chemical structure of SBSi and the formation of SBSi coatings on the oxidized substrate. Light transmission through the samples of PMMA, bare glass, and SBSi-glass after the treatments of (b) hot or (c) freezing at -20°C. (d) Water spray on samples of PMMA, bare glass, and SBSi-glass. (e) Anti-fogging test by treating the water steam to samples of PMMA, bare glass, and SBSi-glass. (f) Oil-water separation apparatus and images of oil-water mixtures, residues, and filtrates in vials before and after separation. The colors of organic fluids are original, without pigment added. (g) Optical images of the underwater-oil CA measurements for SBSi-glass performed with air bubbles, ether, toluene, hexane, gasoline, diesel, and soybean oil; and quantitative results of OCAs for bare and SBSi-glass samples. Reprinted with permission from "Surface modification for superhydrophilicity and underwater superoleophobicity: Applications in antifog", Huang, K.-T.; Yeh, S.-B.; and Huang, C.-J., ACS Appl. Mater. Interfaces., Volume 7, Issue 38, 2015, Pages 21021-21029. Copyright 2018, American Chemical Society.*

Ezzat and colleagues [153] fabricated anti-fogging glasses with extreme wettability (WCA < 5°) by anchoring zwitterionic poly(sulfobetaine methacrylate) (pSBMA) and poly(sulfobetaine vinylimidazole) (pSBVI) polymer brushes, while Huang et al. [154] deposited by dip-coating silanized zwitterionic sulfobetaine silane (SBSi) on glasses (**Figure 1.10a**). In the latter study, the coated glasses recovered up to 99% of the initial light transmission after being exposed to hot water, as well as cooled at –20°C (**Figure 1.10b,c**). This behavior was in agreement with the observed "see-through" property under different fogging scenarios (**Figure 1.10d,e**). Furthermore, a SBSi-coated stainless steel mesh selectively separated water from various oil/water mixtures and oil/water emulsions with high efficiency (> 99.5% and > 98.2%, respectively) (**Figure 1.10f,g**).

Oil/water separation efficiencies > 99.5% were also observed in a stainless steel wire mesh coated with anti-fogging formulations based on phytic acid and ferric ions (Fe^{III}) [155]; while fog-resistant coatings reported by Wu's group [156] were shown to not only repel oil underwater (OCA > 150°), but also to prevent bacterial adhesion (*E. coli* and *S. aureus*). Combining the dip-coating deposition with the *in situ* nanopressing technique (**Figure 1.11a**), Zhang and collaborators built on glass and PET samples bilayer configurations integrated either by solid silica nanoparticles (WCA = 33.1°) [157] (**Figure 1.11b**) or by hollow silica nanoparticles (WCA = 37.5°) [158] (**Figure 1.11c**) partly embedded in a thin film of thermally crosslinked PVA-PAA blends. The anti-reflective property observed in optimal SNs-HSNs/(PVA-PAA) configurations resulted in better light transmittance ($T_{average}$ > 93%) in the visible range when compared with that of uncoated substrates ($T_{average} \approx 85\text{–}90\%$).

Coatings with anti-fogging activity can also be prepared by immobilizing inorganic nanoparticles (typically SiO_2 and TiO_2) either in a network of hydrophilic polymers on the substrate (e,g., PVA, PVP, and PEGMA [159], glycidoxypropyltrimethoxysilane [160] or a catechol-conjugated polymer [161]) or on the substrate by direct deposition using sol-gel [25] or aqueous solutions [162].
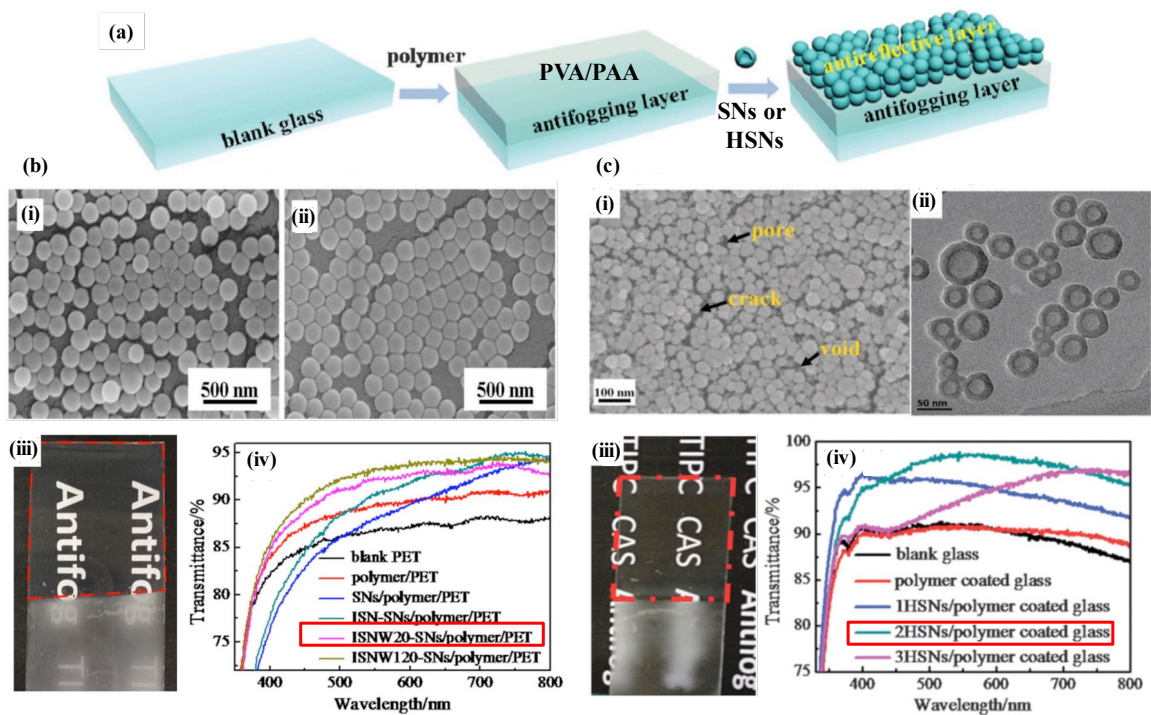
Figure 1.11: *(a) Schematic of the in situ nanopressing process. (b) SEM images of (i) SNs/polymer/PET, and (ii) ISNW20-SNs/polymer/PET, ISNW20: 20 washing cycles. (iii) Digital images exhibiting the antifogging property of blank (lower part) and ISNW20-SNs/polymer coated (upper part) PET, respectively; (iv) Transmission spectra of blank PET, polymer/PET, SNs/polymer/PET, ISN-SNs/polymer/PET, ISNW20-SNs/polymer/PET, and ISNW120-SNs/polymer/PET, respectively. (c) (i) SEM image of the 2HSNs/polymer thin film coated glass, (ii) TEM image of the HSNs. (iii) Digital images exhibiting the antifogging properties of 2HSNs/polymer coated glasses (upper part) and blank glasses (lower part). (iv) Transmission spectra of blank glass and glasses coated, respectively, by polymer, 1HSNs/polymer, 2HSNs/polymer, and 3HSNs/polymer. The best anti-fogging configuration is shown in a red rectangle. Figures and graphics reprinted with permission from references [157,158].*

The use of mesoporous silica nanoparticles (MPSNPs) [163,164], hollow silica nanospheres (HSNs) [165], double-shell hollow nanospheres of SiO_2/TiO_2 (DSHNs) [166], and solid silica nanoparticles (SSNPs) [167], among others, as building blocks allows for the fabrication of anti-fogging films with hierarchical roughness featuring spreading mechanism (high specific surface). Coatings made up of SSNPs deposited on $La(OH)_3$ nanorods prepared by You and colleagues [168] have proven remarkable capacity to alleviate surface fog (WCA ≈ 0°) and minimize light reflection under sun exposure. Cao et al. [169] employed very recently faujasitic nanozeolites (DZ) with an average size of 25–30 nm as assembly units to prepare on glass samples coatings with anti-reflective/anti-fogging features, while

Liu and colleagues [170] proposed a soft templating route combining *in situ* growth with a modified Stöber method to synthesize TiO$_2$/SiO$_2$ nanospheres directly on glass surfaces (**Figure 1.12a**). Upon calcination (500°C for 2 h), the resulting 500-nm-sized TiO$_2$/SiO$_2$ nanospheres conferred superhydrophilic property (WCA = 2°) suitable for anti-fogging purposes to glass samples (**Figure 1.12b,c**).

Figure 1.12: *(a) The in situ synthesis mechanism of TiO$_2$/SiO$_2$ nanospheres. (b) Contact angle of the blank substrate, substrate with SiO$_2$ particles, and substrate with TiO$_2$/SiO$_2$ nanospheres. (c) The anti-fogging property of the samples. "In situ growth of TiO$_2$/SiO$_2$ nanospheres on glass substrates via solution impregnation for antifogging", Liu, F.; Shen, J.; Zhou, W.; Zhang, S.; and Wan, L., RSC Adv., Volume 7, Issue 26, 2017, Pages 15992-15996. Published by The Royal Society of Chemistry.*

Several studies have proven, on the other hand, the feasibility of conferring anti-fogging performance to glass (WCA < 10°) by depositing silica or titania sols by dip-coating, followed by calcination [171,172] in the absence or presence of porogens (e.g., PEG [173], CTAB [174]). The removal of residual carbon-containing groups/porogens upon calcination led to an increase in surface roughness, which drove the surface toward a superhydrophilic state.

1.6.1.2 Spin-coating deposition

Spin-coating deposition makes it possible to prepare anti-fogging coatings based on semi-interpenetrating polymer networks (SIPNs) with frost-resistance [175] and even anti-bacterial/anti-viral activity [176]. For example, Zhao and colleagues [177] prepared SIPNs

based on random copolymers of poly(DMAEMA-co-MMA) within a network of UV-cured PEGDMA with anti-fogging/anti-bacterial features (**Figure 1.13**).
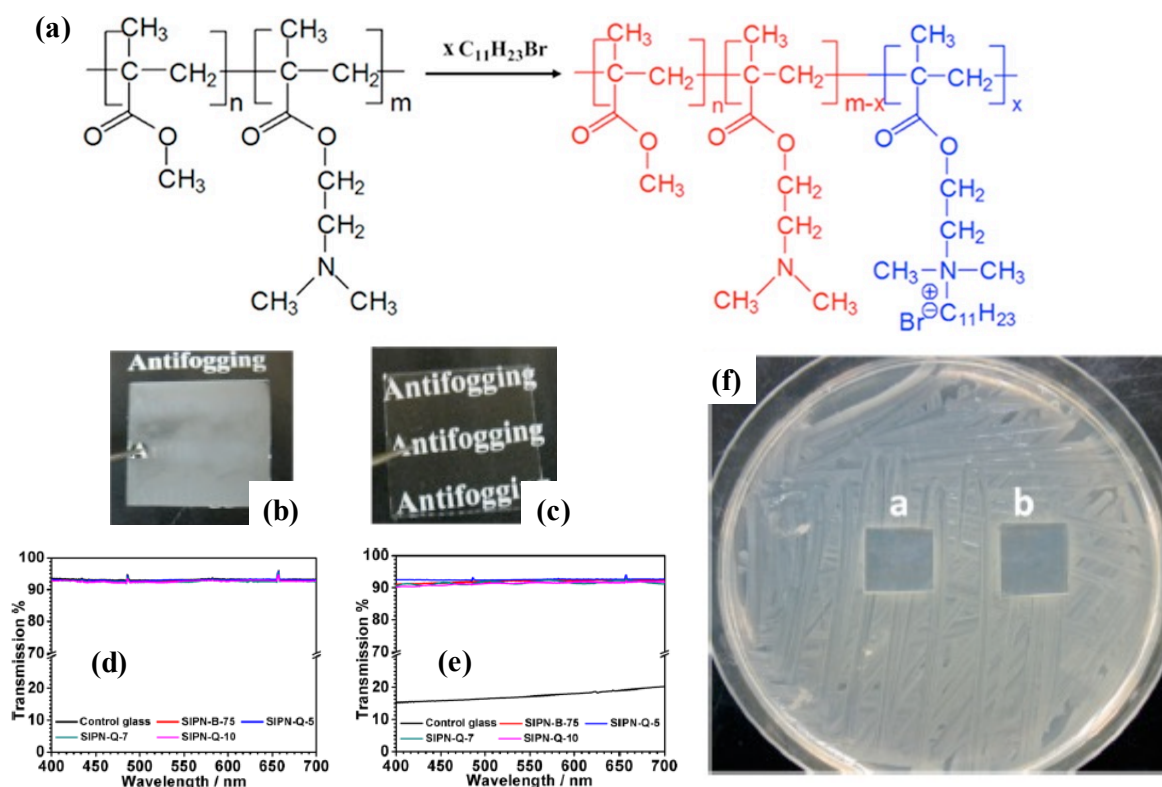
Figure 1.13: *(a) Schematic illustration of partial quaternization of poly(DMAEMA-co-MMA). Photos of different samples: (b) control glass and (c) SIPN-Q-5, which were first stored at -20°C for 30 min and then exposed for 5 s to ambient lab conditions (~20°C, 50% RH). Light transmittance at the normal incident angle for various samples: (d) as prepared and (e) 5 s under ambient condition (~20°C, 50% RH) after being stored at -20 °C for 30 min. (f) Zone-of-inhibition test result of (a) SIPN-Q-5 and (b) SIPN-Q-10 in a cultured lawn of E. coli. "SIPN-Q-X", X: x mol% in the copolymer of quaternized DMAEMA. Reprinted with permission from "Dual-functional antifogging/antimicrobial polymer coating", Zhao, J.; Ma, L.; Millians, W.; Wu, T.; and Ming, W., ACS Appl. Mater. Interfaces., Volume 8, Issue 13, 2016, Pages 8737-8742. Copyright 2018, American Chemical Society.*

Partial quaternization of DMAEMA via SN2 (substitution nucleophilic bimolecular) (**Figure 1.13a**) using 1-bromoundecane (5 mol% in the copolymer, "SIPN-Q-5") yielded coatings providing glass samples, not only with remarkable optical properties ($T_{average} > 90\%$,) and capacity to prevent surface fog (**Figure 1.13b**-e), but also with very high killing efficiency against *E. coli* and *S. epidermidis* (5-log reduction) (**Figure 1.13f**). Nam et al. [178] developed a two-step process consisting of deposition of functionalized PEG

containing polymers with pendent polymerizable norbornene (NB) groups by spin-coating, followed by immersion in a solution of Grubb's catalyst to fabricate optimal fog-resistant glasses (NB ≤ 30 mol%) with water-attracting features. Unlike SIPNs, no UV light nor heat was required to induce crosslinking. Anti-fogging composite coatings based on a bilayer configuration with enhanced mechanical properties can be fabricated by spin-coating deposition [179,180]. Films consisting of a bottom layer ("primer") of colloidal SiO_2 (30 wt%) embedded in cross-linked network of dipentaethritol hexaacrylate, and a top layer containing HEMA and "Tween-20" have shown encouraging results (**Figure 1.14a**) [181]. The addition of 10 wt% of "Tween-20" to the coating formulation, resulted in superhydrophilic coatings with fully adherence to PMMA substrates and long-lasting fog-free effect (> 1 year) (**Figure 1.14b**).
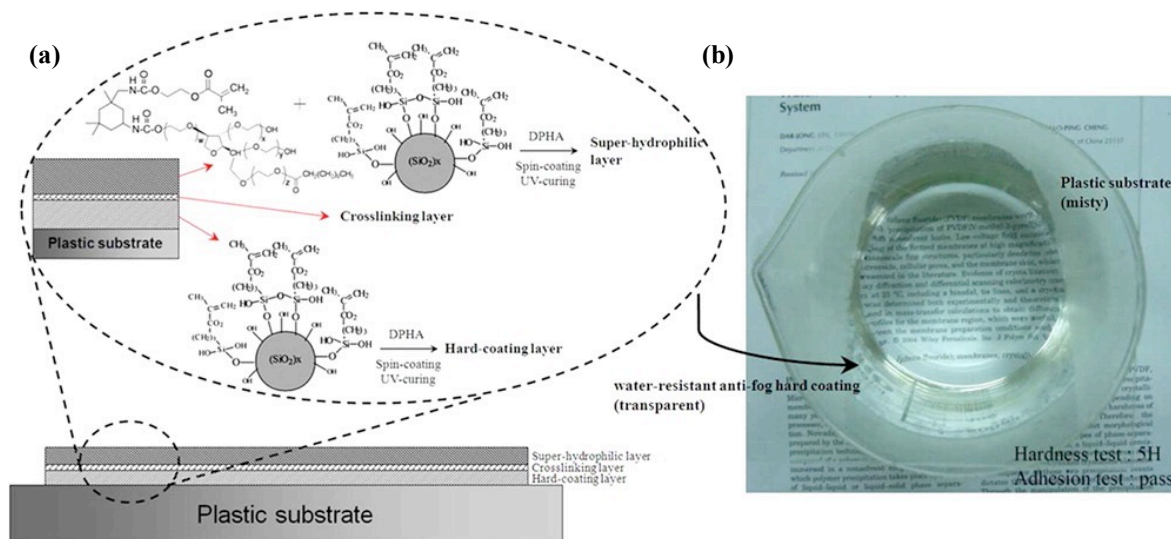
Figure 1.14: *(a) Bilayered anti-fogging coating. (b) Steam anti-fogging tests of coatings in AF10 after 1 year in service. Reprinted with permission from "Preparation of water-resistant antifog hard coatings on plastic substrate", Chang, C.-C.; Huang, F.-H.; Chang, H.-H.; Don, T.-M.; Chen, C.-C.; and Cheng, L.-P., Langmuir, Volume 28, Issue 49, 2012, Pages 17193-17201. Copyright 2018, American Chemical Society.*

As in dip-coating deposition, the spin-coating process provides a facile way to build up inorganic coating on flat substrates, employing "building bricks" such as solid and hollow nanoparticles, microspheres, and nanorods, among others [182]. Here, the idea is to procure anti-fogging activity by designing surfaces endowed with hierarchical topography. With this

goal in mind, Shan and colleagues [183] developed 400-nm-thick coatings made up of a thin film of Cu-Bi$_2$O$_3$ covered with MPSNPs, by combining the spin-coating technique with the sol-gel method. Anti-fogging MPSNPs/Cu-Bi$_2$O$_3$ films (Cu:Bi$_2$O$_3$ molar ratio = 5) performed adequately when exposed to humid air after being cooled in a freezer ($-18°C$) and were able to degrade methyl orange and stearic acid upon exposure to UV light (1 mW cm^{-2}).

Mesoporous SiO$_2$/Bi$_2$O$_3$/TiO$_2$ triple-layered thin films prepared on glass slides using a simple sol-gel/spin-coating approach showed similar results in terms of photocatalytic response and anti-fogging performance [184]. Silica- and titania-based coatings with enhanced wetting behavior can be prepared in ways other than those involving the deposition of building blocks. Similar to dip-coating deposition, particular emphasis has been placed on the *in situ* generation of nanopores upon calcination, for example, by using porogens [185] or surfactants [186]. Regardless of the adopted strategy, the principle is simple: the infiltration water drops into the nanoporous network drives the anti-fogging phenomenon (spreading mechanism). Alternatively, Budunoglu and collaborators [187] fabricated 135-nm-thick SiO$_2$ films with tunable porosity on glass samples using "ormosil" (organically modified silica) gels, which were prepared via hydrolysis and condensation of TEOS and methyltrimethoxysilane (MTMS). The pore size was tuned by changing the TEOS/MTMS volume ratio in the sol-gel mixture. A rational commitment between the "see-through" property, mechanical durability, and optical clarity (T$_{average}$ > 95%, in the visible range) was met for a TEOS/MTMS volume ratio of 3:2.

Despite the conceptual simplicity behind the spin-coating technique, the feasibility of fabricating anti-fogging coatings with hierarchical surface features similar to those observed in the compound eyes of insects have been recently demonstrated. For example, Sun and colleagues [123] designed fog-free surfaces by depositing on glass samples fly-eye bioinspired ZnO microspheres (**Figure 1.6ai**). Following hydrophobization with 1H, 1H, 2H, 2H-perfluorooctyltriethoxysilane, coated glasses prevented water drops from accumulating on the surface when placed in an artificial fogging chamber for 2 min at a tilting angle of 10° (WCA = 162.2° and SA ≈ 3°). Zhang and collaborators [188] reported a straightforward

method involving sol-gel process and spin-coating deposition to produce films with moth compound eye-like features using a mixture of MPSNPs containing surfactants and SiO_2 sol. Finally, Li's group [189] very recently reported on the fabrication of coatings with water- and oil-attracting features made of Cu_3SnS_4, a ternary semiconductor. Following annealing in N_2 at 500°C, spin-coated glasses ($R_{rms} = 0.432$ nm) displayed superamphiphilicity, as revealed by a WCA and OCA below 1°, and a band-gap (1.74 eV) compatible with applications in the field of photovoltaic cells (see **section 1.7.2**).

1.6.1.3 Layer-by-layer deposition

The layer-by-layer (LbL) deposition is a straightforward coating technique to build up multi-layer structures. This bottom-up approach involves sequential assembling of thin layers by dipping the sample into different solutions, followed by rinsing cycles. In general, the coating's robustness is ensured either by electrostatic interactions or by covalent and non-covalent interactions between adjacent layers, namely, hydrogen, hemiacetal, and ester bonds. In the last five years, various research groups have demonstrated that the incorporation of natural polymers, such as carboxymethyl cellulose (CMC), chitosan (CHI), and other polysaccharides [190–192]; and synthetic polymers, such as polyvinyl and polyacrylic compounds [193–197], into anti-fogging formulations can be successfully attained via LbL. For example, Spiroiu's group [198] fabricated anti-fogging layers with WCA exceeding 90°, based on self-assembled structures of CHI and sodium lauryl ether sulfate micelles, while Lee's group [199] developed zwitter-wettable coatings comprising a hydrophilic bottom layer of (CHI/CMC)$_{30}$ capped with three hydrophobic (CHI/Nafion) bilayers (WCA ≈ 110°). As did Shibraen's and Cohen's groups [192,193], these research groups considered the water-absorbing characteristics of these coatings to account for the observed anti-fogging performance and, in some cases, the frosting delay capacity (percolation mechanism) [193,194].

Sun and colleagues [200] designed anti-fogging films with oil-repellent features via the assembly of hyaluronic acid (HA) and branched poly(ethylenimine) (bPEI) and subsequent

hydrophobization with perfluorooctanesulfonic acid potassium salt (PFOS). It was found that glass and plastic lenses coated with PFOS-(HA/bPEI)$_{50}$ films were able to heal cuts of 80 μm in width after 5 min in water. Very recently, Shiratori et al. [201] demonstrated that films composed of multistacked layers of negatively charged PVA-PAA blends and positively charged PAH-PVA-PAA blends featured not only capacity to minimize fogging effects but also anti-reflective and anti-thrombogenic properties (**Figure 1.15**).
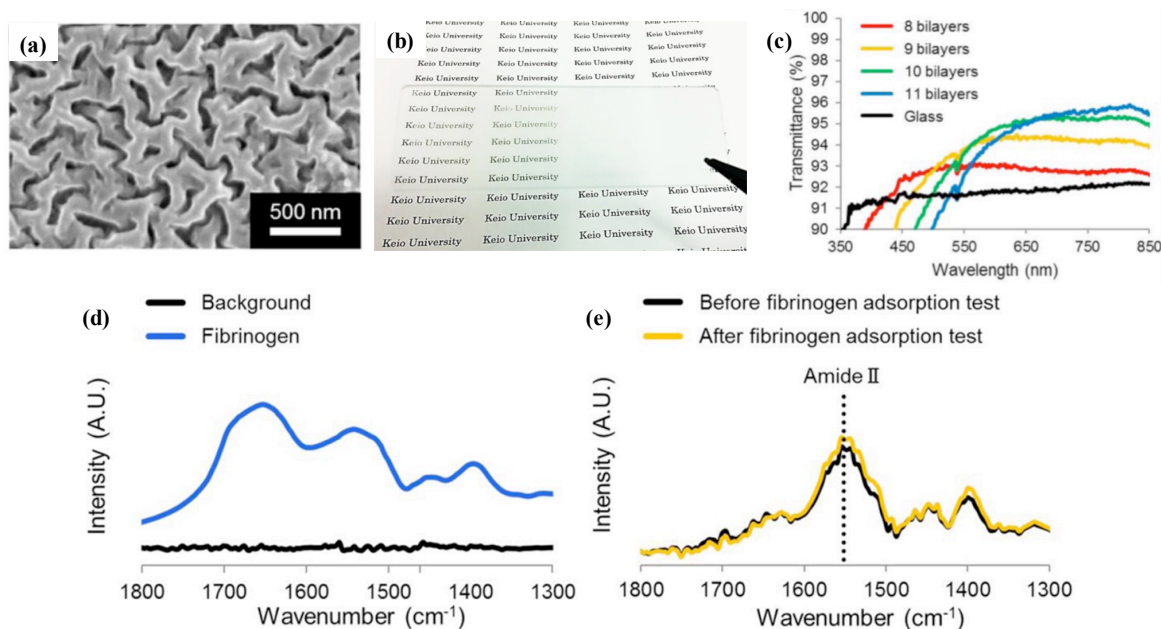
Figure 1.15: *(a) Scanning electron microscopy image of ((PAH-PVA-PAA)/(PVA-PAA))$_{10}$ films. (b) Transmittance of films with different numbers of bilayers on glass substrates. (c) Photography of a cooled glass slide with (left) and without (right) the coating in a high-humidity environment (90% RH) at 35°C after being cooled in a refrigerator to < 5°C. Fourier transform infrared spectra of (d) bare silicon wafer substrate and fibrinogen and (e) ((PAH-PVA-PAA)/(PVA-PAA))$_{10}$ films before and after contact with a fibrinogen solution. Reprinted with permission from "Antifibrinogen, antireflective, antifogging surfaces with biocompatible nano-ordered hierarchical texture fabricated by layer-by-layer self-assembly", Manabe, K.; Matsuda, M.; Nakamura, C.; Takahashi, K.; Kyung, K. H.; and Shiratori, S., Chem. Mater.,Volume 29, Issue 11, 2017, Pages 4745-4753. Copyright 2018, American Chemical Society.*

The hierarchical topography observed in ((PAH-PVA-PAA)/(PVA-PAA))$_{10}$-coated glasses coupled with abundant OH groups per area unit translated to extreme wetting behavior (WCA < 5°) (**Figure 1.15a**). Qualitative assessment of the anti-fogging performance

revealed that ((PAH-PVA-PAA)/(PVA-PAA))$_{10}$ coatings conferred noticeable visual characteristics to glasses when in contact with a moist environment at 35°C (**Figure 1.15b**). Furthermore, the light transmission values (T$_{average}$ ≈ 95%) were greater than those of a bare glass (T$_{average}$ ≈ 91%, in the 450–850 nm range) (**Figure 1.15c**). In view of the FITR results, these anti-fogging coatings prevented the adhesion of fibrinogen, thus revealing a potential application as "anti-anticlotting" material (**Figure 1.15d,e**).

Regarding inorganic anti-fogging layers, studies carried out by various research groups in the last seven years show that, solid and mesoporous SiO$_2$ nanoparticles, i.e., SSNPs and MPSNPs, can be assembled in three different ways [202–204]. The first one involves combining SSNPs with nanosheets (**Figure 1.16a**). In this context, worthy of mention are the studies conducted by Byeon and colleagues [205,206], who designed coatings with luminescent/anti-fogging features by assembling nanosheets of RE-doped gadolinium hydroxides (RE = Eu, Tb, and Dy) with SSNPs. Following annealing at 500–600°C, the resulting (Gd$_2$O$_3$:RE/SSNPs)$_n$ coatings (n = 7–9, 30) prevented fogging via spreading mechanism (WCA < 5°). Depending on the dopant, the coated glasses featured efficient red (Eu), green (Tb), and blue (Dy) light emissions when illuminated with light of 254 nm. In a similar manner, stacking of reduced graphene oxide (RGO) nanosheets with nanoparticles of SiO$_2$ [207] or TiO$_2$ [101] has also been used to produce fog-resistant coatings with high specific surface area.

The second way to prepare anti-fogging coatings with hierarchical porosity involves using "building blocks", such as raspberry-like [124,208–210] and mulberry-like [113,211,212] nanospheres, which are synthesized prior to the deposition process by a judicious assembly of nanospheres (**Figure 1.16c,d,f,g**).
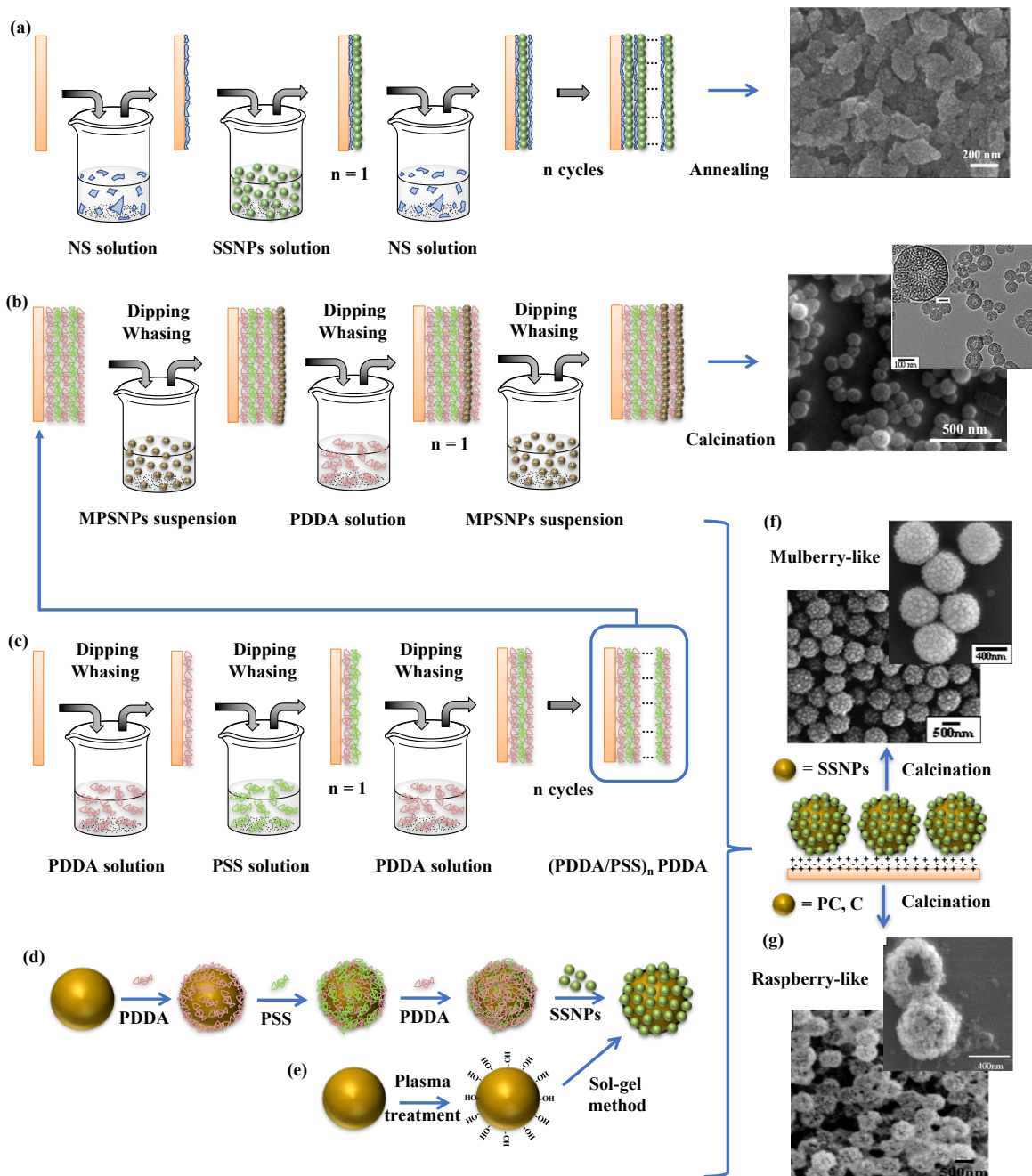
Figure 1.16: *LbL strategies for the deposition of inorganic materials used in anti-fogging coatings* [206,208,211,213]. *C: Carbon (template), MPSNPs: Mesoporous silica nanoparticles, NS: Nanosheets, PC: Polycarbonate (template), PDDA: Poly (diallyldimethylammonium chloride), PSS: Sodium poly(4-styrenesulfonate), SSNPs: Solid silica nanoparticles.*

Many other research groups have followed a protocol similar to that depicted in **Figure 1.16c,d,f** to fabricate super wettable surfaces with hierarchical roughness, using only

nanoparticles of SiO_2 [130,131,202,214], TiO_2 [98,112], ZrO_2 [215], $Al(OH)_3$-$Mg(OH)_2$ as building units or PDDA-sodium silicate complexes [216]. The third way to produce hierarchically rough anti-fogging surfaces is based on the assembly of mesoporous silica nanoparticles (MPSNPs) according to the protocol depicted in **Figure 1.16b** [213,217–219]. On the other hand, several studies have shown that anti-fogging activity comparable to the one obtained these ways can be attained, without the need for calcination or annealing post-treatments [220,221] coupled, in some cases, with a reduction in the number of deposition cycles. For example, Sun and collaborators [222] evidenced that only three deposition cycles of MPSNPs (~ 50 nm) alternating with PDDA sufficed to retain transparency when coated PC, CR-39 were exposed under very humid conditions. Analogously, Guo et al. [223] used the LbL assembly technique to produce fog-free films consisting of discrete layers of poly(ethylenimine) (PEI) and PSS containing clusters of calcium silicate hydrates (CSH). Interestingly, coatings integrated by multi-stacked layers of ZnO nanoparticles (NP)/nano-flowers (NF) and PAA proved to not only be effective in eliminating the effects of condensation but also in blocking UV light [224] and killing bacteria [203]. Notable capacity to block UV light was also noticed in a multistack configuration consisting of discrete layers of PEI and CMC-modified TiO_2 nanoparticles recently prepared by Li and collaborators [225]. Further to this, $(PEI/CMC@TiO_2)_{15}$ coatings were found to delay aging of PET substrates while conferring them anti-fogging performance (WCA < 5°).

1.6.1.4 Physical and chemical vapor deposition

Sputtering methods such as RF magnetron sputtering, and evaporation methods such as electron beam deposition has proven to be suitable to fabricate nanostructured anti-fogging inorganic coatings, with high deposition rates, excellent adhesion, and uniformity [226,227]. For example, Kwak and colleagues [228] reported a two-step process to fabricate ZnO-based anti-fogging coatings consisting of the deposition of a ZnO seed layer on glass samples by RF sputtering, and subsequent growth of ZnO nanorods using ammoniacal solutions of zinc nitrate hexahydrate. Because of a light transmission as high as bare glass (≈ 90% in the 400–700 nm range) and the ability to block light below 370 nm as in [203,224,225], these

surfaces hold promise for fenestration purposes. ITO nanorods prepared by RF magnetron sputtering, followed by in-air annealing at 250°C have shown to endow glass samples with satisfactory anti-fogging and self-cleaning properties [229] (**Figure 1.17a,b**). Coatings met extreme wettability (WCA < 1°) with sputtering times > 40 min, because of the increase in size of nanorods (**Figure 1.17c**). No fogging was observed in the samples treated for 60 min under an aggressive cold fog test a –20°C (**Figure 1.17d**). Following functionalization with 2H-perfluorodecyltrichlorosilane, the as-prepared surfaces were easy to clean, as a drop of green powder phosphor lying on the surface was easily removed when water was added, leaving no remnant (**Figure 1.17b**).
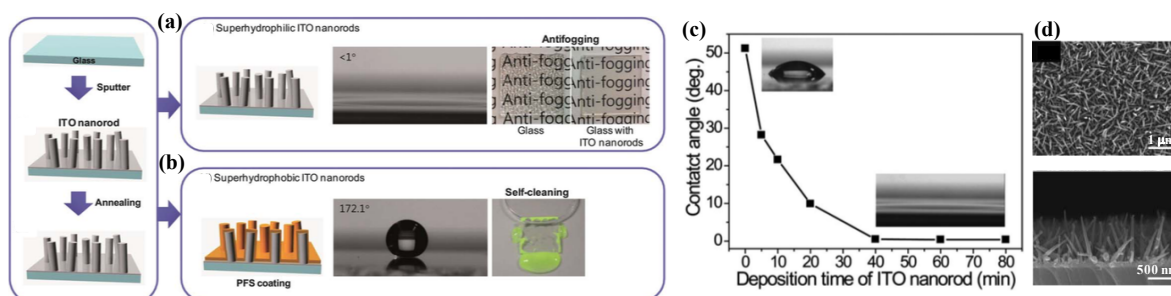
Figure 1.17: *Schematic illustration of the fabrication procedures for preparing a multifunctional ITO nanorod film: (a) superhydrophilic ITO nanorods (WCA <1°) displaying anti-fogging behavior when exposed to a humid environment (RH > 80%) after storage at -20°C, and (b) superhydrophobic ITO nanorods (WCA = 172.1°, SA ≈ 0°) featuring self-cleaning activity. (c) WCA of the post-annealed ITO nanorod films on glass substrates as a function of the growth time. The insets show the water CAs of a bare glass substrate and of an ITO nanorod film grown on a glass substrate for 60 min. (d) Top- and side view SEM images of the ITO nanorod film grown on a glass substrate for 60 min. Reproduced from "Fabrication and characterization of large-scale multifunctional transparent ITO nanorod films", Park, H. K.; Yoon, S. W.; Chung, W. W.; Min, B. K.; and Do, Y. R., J. Mater. Chem. A, Volume 1, Issue 19, 2013, Pages 5860-5867. Copyright 2018, with permission of The Royal Society of Chemistry.*

RF magnetron sputtering made it possible to build multifunctional TiO_2-based configurations showing tremendous potential in smart window applications, as observed in glasses covered with a TiO_2(anatase)/VO_2(monoclinic)/TiO_2(rutile) tri-layered film [230] or with a multi-stacked TiO_2(anatase)/Si/Ag(Cr)/TiN_x structure [231]. Using electron beam evaporation, Eshaghi and collaborators [232] developed a multistack configuration consisting of discrete layers of SiO_2 and TiO_2 that proved to be effective in preventing condensation effects on

glass. In the same vein, Palmisano and colleagues [233] demonstrated the feasibility of depositing smooth TiO_2 coatings with better anti-fogging and self-cleaning performances than the ones observed in a commercial anti-fogging glass (Pilkington Activ[TM] glass).

Using the CVD technique on glass samples, Chen and collaborators [234] deposited SiO_2 coatings with a regular convex nipple structure employing ammonia-catalyzed sol-gel solutions of TEOS. Even though all of the treated samples remained fog-free when placed over hot water or cooled at −18°C, the best optical properties ($T_{average} \approx 95\%$ in the 400–800 nm range) were noticed in glasses treated for 10 h. Shoji et al. [235] prepared silicon resin thin films on PC substrates with tunable hydrophobic/hydrophilic features using a low-pressure RF plasma. When plasma polymerization was performed in O_2/HCOOH atmosphere under a power input between 50 and 150 W, the coated PC displayed extreme wettability (WCA < 5°) and remained fog-free when exposed to steam, breath, and room conditions after cooling at lower temperature.

1.6.1.5 Electrochemical deposition

Meroni and colleagues [236] reported on the feasibility of an electrochemical method (potentiostatic deposition), similar to that employed by Patel et al. [237], to deposit several layers of TiO_2 on glass. Following application of 3.6 V for 60 s to a glass sample immersed in a TiO_2 sol, the resulting crack-free smooth TiO_2 coatings were fully wettable yet degraded transparency of glass substrates, as supported by a decrease in the average transmittance from 92% (uncoated glass) to approximately 75% in the visible region. In addition, the anti-fogging property was consistent, with a decrease in WCA from 40 to 0° following exposure to UV light (30 mW cm^{-2}). In contrast, TiO_2 coatings with nanofiber morphology fabricated by Tricoli's group [116] by electrospinning, displayed non-UV-activated anti-fogging features. Following thermal treatment at 500°C, the resulting TiO_2 nanofibers of 200 nm in thickness provided glasses with excellent capacity to avoid blurry view when exposed to vapor, because of the great amount of hydroxyl on the surface (specific area = 106 m^2 g^{-1}, WCA < 10°), as well as acceptable light transmission ($T_{max} \approx 93\%$) for incident light of 400

and 600 nm. Similarly, films composed of TiO_2 nanobelts were shown to be superhydrophilic with no previous UV exposure [117]. In this instance, titanate nanobelts (TNB), which were synthesized via a hydrothermal method, were deposited on ITO glass via electrophoretic deposition, and then functionalized with 1H,1H,2H,2H-perfluorooctyltriethoxysilane (FAS) (**Figure 1.18a,b**). When the functionalization time was 2 min, the resulting dynamic wetting behavior of the FAS-treated surfaces (WCA ≈ 156.2° and SA ≈ 8.6°) led to the easy cleaning against yellow nitrogen-doped titanate powder (**Figure 1.18c,d**). Upon calcination at 500°C, a drastic shifting toward a super wettable state (WCA ≈ 0°) was noticed, because of the removal of the hydrophobizing agent and the conversion of TNB into porous TiO_2 (anatase) (**Figure 1.18e**). Under fogging conditions, the TiO_2-coated glasses exhibited higher transmissivity than did uncoated ones (**Figure 1.18f**).
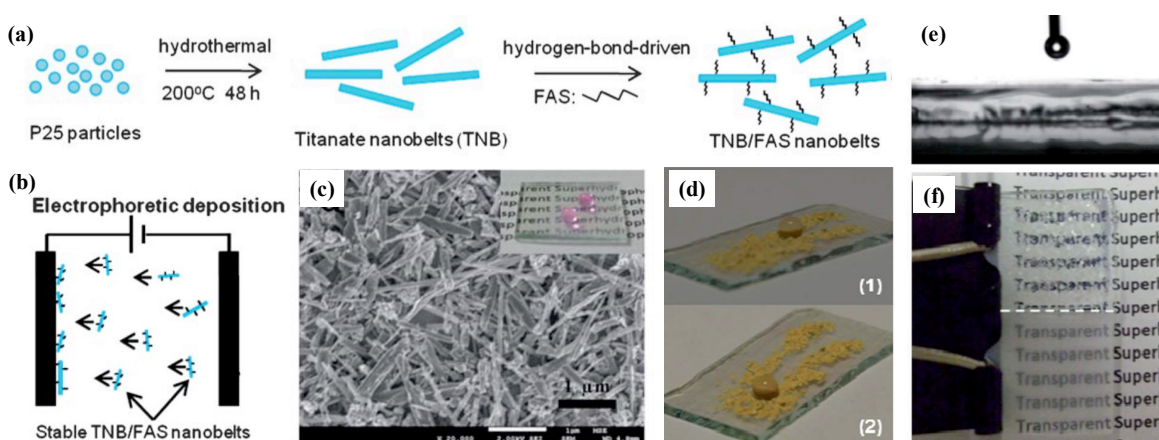
Figure 1.18: *(a) Schematic drawing of the synthesis and hydrogen-bond-driven stabilization of titanate nanobelts. (b) Schematic illustration of the electrophoretic deposition process to prepare a TNB/FAS film. (c) SEM image of the as-prepared superhydrophobic TNB/FAS film (2 min). The inset image shows water droplets on the transparent TNB/FAS film on ITO glass. (d) Time sequence of the self-cleaning process on the superhydrophobic coating with low water adhesion. (e) Water droplet on the superhydrophilic TiO_2 film. (f) Photograph of an ITO substrate deposited with superhydrophilic coatings (bottom) and a control ITO substrate without any coating deposition (upper) taken from a refrigerator (-4°C) to the humid laboratory air (ca. 50% RH). Reproduced from "Transparent superhydrophobic/superhydrophilic TiO_2-based coatings for self-cleaning and anti-fogging", Lai, Y.; Tang, Y.; Gong, J.; Gong, D.; Chi, L.; Lin, C.; Chen, Z.; Liu, M. J.; Zheng, Y. M.; Zhai, J.; et al., J. Mater. Chem., Volume 22, Issue 15, 2012, Pages 7420-7426. Copyright 2018, with permission of The Royal Society of Chemistry.*

1.6.1.6 Others

The techniques mentioned above cover the most common bottom-up approaches for producing anti-fogging surfaces; however, other not less important ones have not been addressed here. These include: solvent casting methods [238–240]; bar coating methods [27,241–245]; spray coating techniques [115,246–248]; and multi-step approaches [249,250].

1.6.2 Top-down processing

Top-down processing is based on the removal of material from a starting sample either to increase surface roughness or to create fine patterns, and thus drive the surface toward anti-fogging property.

1.6.2.1 Dry and wet etching methods

In dry etching, the sample is subjected to either high energy particles (e.g., electrons, X-rays), ions, or both; while in wet etching, the sample is dipped in an acid or in an alkaline solution for a certain period of time to "carve" the surface. In wet etching, the surface morphology, the material removal rate, and the resulting optical properties can be tailored, by varying certain experimental parameters, namely, temperature, the concentration of reactive species, and etching time [251–253]. In this regard, He et al. [251] designed dual anti-fogging/anti-reflective glasses (WCA = 4.3°), with nanoflake-like surface features using a liquid alkali etching (5 g L^{-1} of NaOH, 85°C). A similar approach was reported by Myoung and colleagues [252] (**Figure 1.19**).
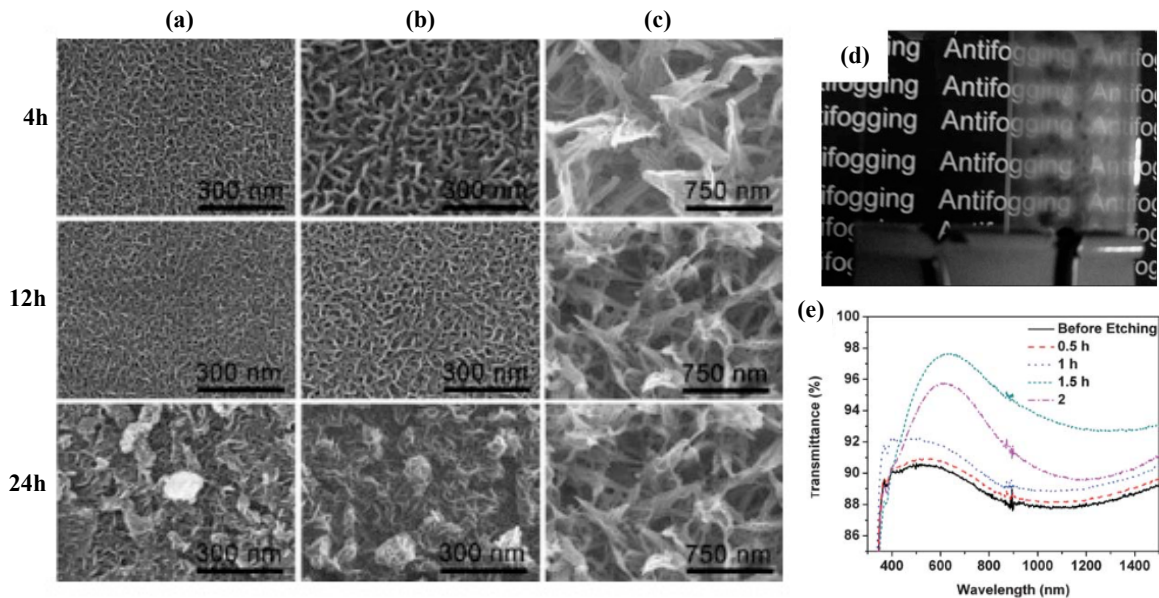
Figure 1.19: *SEM images of glasses etched for different periods of time (4, 12, and 24 h): (a) glass "A" (27.42 wt% of Na₂O), (b) glass "B" (24.08 wt% of Na₂O), and (c) glass "C" (0.35 wt% of Na₂O). (d) Transmittance spectra of glass A before and after etching (KOH 1M) at different etching times, and (e) anti-fogging performance of etched "A" glasses (4 h) when cooled at −10°C and exposed thereafter to steam (right: before etching and left: after etching). Reproduced from "A multifunctional nanoporous layer created on glass through a simple alkali corrosion process", Xiong, J.; Das, S. N.; Kar, J. P.; Choi, J.-H.; and Myoung, J.-M., J. Mater. Chem. Volume 20, Issue 45, 2010, Pages 10246-10252. Copyright 2018, with permission of The Royal Society of Chemistry.*

In this instance, glass samples with variable wt% of Na₂O were dipped in KOH solutions at 95°C for 4, 12, and 24 h (**Figure 1.19a-c**). Even though hydrophilicity was shown to increase with the etching time, at least 4 h of etching treatment were required to obtain "A" glasses with resistance to fogging (**Figure 1.19d**). Furthermore, this treatment increased the maximum transmittance of "A" glasses from ≈ 90 to 97.7% (at 630 nm) due to a concomitant variation in size of nanoflake-like structures (**Figure 1.19e**). Aqueous NaHCO₃ solutions have also shown an ability to "chisel" glass surfaces to yield sponge-like structures with a notable capacity to alleviate fogging effects [253]. Yao et al. [254] fabricated fog-free glasses in a sequential approach consisting in chemical dry etching using a H₂SiF₆-containing vapor (≤ 20°C), annealing at 720°C for 135 s, and low-pressure O₂ plasma treatment for 25 min. On the other hand, etching can be used to "activate" surfaces prior to coating deposition. Here, the goal is to ensure the adherence of anti-fogging coatings on the substrate to prevent

them from detaching when exposed to a humid environment or under normal cleaning practices. For example, Lam et al. [109] deposited TiO_2/SiO_2 bilayers on NaOH-etched and UV-irradiated PC, while Yao and collaborators [255] dipped glasses, which were previously treated following the above-mentioned protocol [254], in a SSNPs solution (20 nm) to ensure the "see-through" property. In another study, Di Mundo's group [256] conferred anti-fogging capability to PC films through a self-masked plasma etching and subsequent deposition of a superhydrophilic silica-like coating, using a low-pressure O_2/Ar plasma fed with hexamethyldisiloxane (HMDSO).

Evidence shows that the above-illustrated etching methods make it challenging to prepare surface structures with desired geometric order and well-defined shapes (e.g., subwavelength structures, SWSs). In this context, reactive ion etching (RIE) has proven to be a more suitable approach due to its unique ability to etch with finer resolution, and higher aspect ratio than isotropic etching does [257]. For example, Lee and colleagues [258] tailored the wettability of borosilicate glass substrates by means of a self-masked RIE operating under controlled conditions, namely, 50 W and CF_4:O_2 ratio of 4:1. When the etching time was 7 min, the glasses became hydrophilic (WCA = 12.5°) in response to a concurrent formation of tapered SWSs with aspect ratios in the 1.5–2 range. Both the low WCA and the high surface energy (87.8 mN m^{-1}) substantiated the observed fog-free effect when the etched glasses were exposed to steam. Alternatively, Xu et al. [259] built up tapered conical structures (aspect ratio of 2.8) by reactive ion etching (100 W and CHF_3:Ar ratio = 2), using a thin film of Ag nanoparticles as etching mask. As in the previous study, the judicious combination of the inherent hydrophilicity of SiO_2 and the nanohole egg-crate-like structure was behind the observed broadband optical transmissivity (400–1400 nm) as well as the anti-fogging performance (WCA $\approx$ 0°) of quartz slides. RIE in combination with bottom-up processing allows for the fabrication of nanostructured polymer-based anti-fogging coatings with outstanding optical performance. In this regard, it is worth highlighting the straightforward strategy reported by Suh and collaborators [260] involving the deposition of an UV-curable polyurethane acrylate by roll-pressing, and subsequent self-masked RIE to fabricate super wettable glasses (WCA < 5°). Following the same idea, Sim et al. [261] elaborated anti-fogging layers with graded roughness (gradient-index anti-reflection coating, GIARC) using

block copolymers of polystyrene (PS) and polydimethylsiloxane (PDMS) (i.e., PS-b-PDMS) as starting materials.
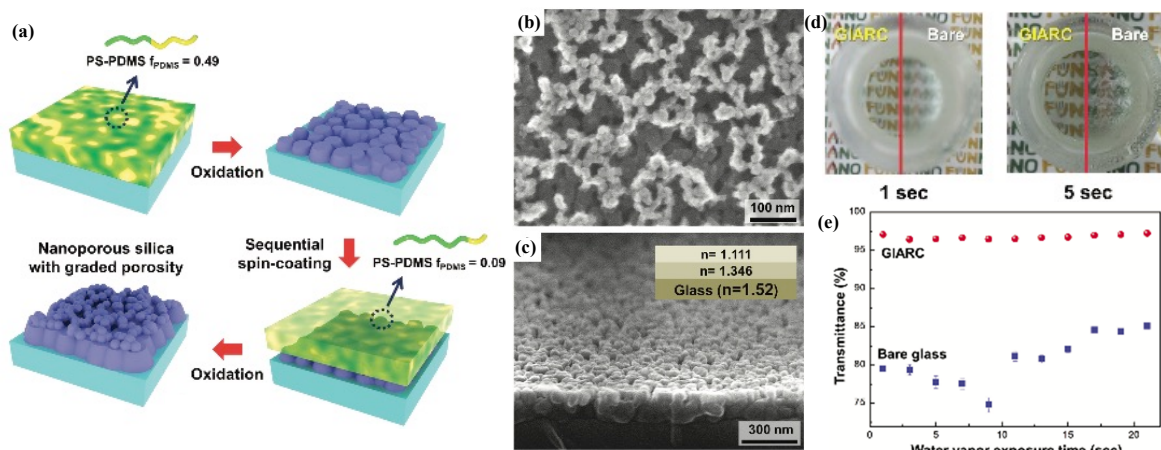
Figure 1.20: *(a) Facile solution-based procedure for the preparation of the gradient-index anti-reflection coating (GIARC) based on Si-containing block copolymers. SEM images of a double-layered GIARC consisting of (b) SD55k (f_{PDMS} = 0.091) and (c) SD43k (f_{PDMS} = 0.488). (d) Comparison of the anti-fogging properties of GIARC and a bare glass substrate. (e) Changes in transmittance with the exposure time to water vapor. Reprinted from "Ultra-high optical transparency of robust, graded-index, and anti-fogging silica coating derived from Si-containing block copolymers", Sim, D.; Choi, M.-J.; Hur, Y.; Nam, B.; Chae, G.; Park, J.; and Jung, Y., Adv. Opt. Mater. Volume 1, Issue 6, 2013, Pages 428-433. Copyright 2018, with permission from John Wiley and Sons.*

Briefly, glass substrates were first coated with PS-b-PDMS films and subjected thereafter to RIE to convert the copolymer into nano-structured SiO_2 (**Figure 1.20a**). Surface features such as roughness and porosity, as well as the optical properties of the resulting coating were found to depend on both the molecular weight of PDMS and its fraction in the copolymer (**Figure 1.20b,c**). Optimized nanoporous silica films "SD55k" (f_{PDMS} = 9.1%), enabled an easy legibility of the letters behind the coated glasses when exposed to super-saturated water vapor at 90°C (**Figure 1.20d**). This behavior was consistent with an average transmittance remaining almost unchanged at approximately 97% under the same conditions (**Figure 1.20e**).

1.6.2.2 Lithography

This top-down approach makes it possible to design subwavelength structures, SWSs (≤ 100 nm) with excellent precision and accuracy using photons, electrons, or ions. Park et al. [61] applied "orthogonal interference lithography" to fabricate periodic square arrays of tapered SWSs on silica samples with an aspect ratio of 5.5 and packing densities above 10^6 mm^{-2}. The resulting surfaces simultaneously met anti-fogging performance, with a WCA ≈ 0°, and minimal reflection over a wide range of incident angles (0 to 80°) in the visible and near-IR wavelengths. Mao and collaborators [262] very recently reported on the potential applicability of "direct laser interference lithography" (DLIL) for the manufacture of anti-fogging eyeglasses. A square periodic array of inverted nanocones made of polyurethane acrylate, which was fabricated in a sequential approach consisting in DLIL, dry etching, and UV replication process, has also generated worthwhile results [263]. Due to the superhydrophilicity (WCA ≈ 0°) conferred by the SWSs with an aspect ratio ≈ 4, no fogging was observed when the nanotextured glasses were placed over saturated steam. Moreover, such glasses displayed remarkable light transmission ($T_{average} > 95\%$, incidence angle of 0°) over the 350–1400 nm range. In another study, Duan and colleagues [264] combined a sol-gel/dip-coating method with DLIL to design non-UV-activated anti-fogging ZrO_2 coatings with a grooved or a mastoideus surface.

Soft lithography, on the other hand, allows for the preparation of polymer-based anti-fogging coatings with micro/nanostructured surface features using mechanical procedures, such as stamping and molding. In this regard, Zheng's group [129] fabricated anti-fogging surfaces with water-repellent and icing-delay characteristics by planting onto poly(vinylidene difluoride) microratchets, which were obtained by the heat-pressing pattern-transfer technique, nanohairs of ZnO (**Figure 6bii**). Following hydrophobization with heptadecafluorodecyltripropoxysilane (FAS-17), water drops remained in a non-freezable state at −5°C and rolled off the surface when exposed to breeze, due to the water-repellent properties of the surface (WCA ≈ 150°). Epoxy micropillars arrays covered with ZnO nanohairs fabricated by soft replication methods ("Bosch process") and crystal-growth

techniques have shown better results in terms of ice formation delay [126]. In this case, an icing delay time as high as 9839 s was noticed in the FAS-treated surfaces (an icing delay time of 7360 s at −10°C was reported in the previous study), even though the contact angle was virtually the same (WCA ≈ 152°) (**Figure 1.6aiv**).

Although lithography has great potential for the fabrication of intricate structures, surprisingly only a few research groups have focused their expertise toward developing anti-fogging films with topographical features similar to the ones found in insect's eyes [265–267]. For instance, moth eye-like nanostructures integrated by polydimethylsiloxane domes have been elaborated employing the lift-up soft-lithography technique (**Figure 1.6bi**) [128]. Following deposition of SSNPs and subsequent treatment with monolayers of self-assembled fluoroalkylsilane (FAS), the resulting hydrophobicity (WCA = 155° and SA = 15°) supported the rolling mechanism behind the observed anti-fogging activity. By means of sacrificial layer-mediated nanoimprinting (SLAN), Raut and collaborators [127] deposited on glass samples a moth eye-like structure made from a resin containing methacryloyloxypropyl polysilsesquioxane (**Figure 1.6av**). Following treatment with 1H,1H,2H,2H-heptadecafluorodecyl methacrylate, optimal surfaces with ommatidial features of 20 μm in diameter (WCA ≈ 151° and CAH ≈ 2°) displayed very low average reflectance (ca. 4.8%) and very fast transmittance recovery ($T_{average}$ = 100% in ≈ 10 s) after exposure to saturated steam. Without the need for hydrophobization post-treatments, moth eye-like nanostructures consisting in PMMA nanonipples covered with solid silica nanoparticles were also found to retain transparency under fogging conditions [268]. Despite an aspect ratio as low as 1, nanostructured surfaces reduced drastically glare and remained optically clear when exposed to moisture for 15 min due to their superhydrophilicity (WCA = 2°).

1.6.2.3 Template-assisted fabrication

Generally speaking, template-assisted fabrication involves two basic steps. An anti-fogging solution is deposited into a micro/nanoporous material (template), allowing the solvent to

evaporate. Afterwards, the template is selectively removed, yielding micro/nanostructured arrays or freestanding 3D structures. Following this protocol, Han and collaborators [269] recently developed a relatively complex yet elegant method to fabricate biologically-inspired anti-fogging films. Here, butterfly's wing scales were used as a template to produce a SiO_2 film with multiscale hierarchical pagoda structures. The hierarchical surface roughness resulting in the significantly high surface density of the hydrophilic OH groups, translated to extreme wetting behavior. Coated glass samples featured excellent anti-fogging activity, as supported by the observed optical transparency ($T_{average} \approx 95\%$) under aggressive fogging conditions. Using the colloidal templating method, Vogel et al. [270] demonstrated the feasibility of preparing a SiO_2-based periodic array of nanopores with tunable re-entrant geometry. Regardless of the pore size and the opening angle, which were changed by adjusting the TEOS/EtOH ratio in the starting sol-gel solution, all of the coated glasses exhibited extreme wetting behavior (WCA $\approx 0°$) following calcination at 500°C. SiO_2 layers prepared from colloidal particles of 200 nm in diameter imparted superior anti-fogging capacity to glass slides.

1.6.3 Surface functionalization and related techniques

In addition to "top-down" and "bottom-up" processing, another way to confer anti-fogging performance to a given material consist in modifying its surface chemistry. Surface treatments such as plasma treatment [271] and ionic implantation [67] have amply demonstrated their effectiveness in conferring resistance to fogging to poorly wettable polymers such as polyethylene, polypropylene, and polyethylene terephthalate. The main reason for this relies on the formation of hydrophilic groups on the surface, such as OH, COOH, COH, CN, NH_2, etc., well known for their favorable interaction with water drops (spreading mechanism) [272–274]. Worthy of mention are the studies conducted by Patel and collaborators [28,237], who prepared anti-fogging polyethylene terephthalate (PET) using low-pressure plasmas operating under a controlled O_2 gas atmosphere (20 sccm, sccm: standard cubic centimeters per minute). Following plasma treatment for 5 min, PET films did become superhydrophilic (WCA went from 95 to $\approx 0°$) in response to a concurrent rise in the

number of carbonyl-containing functionalities on the surface. Even though the plasma-treated PET retained transparency when placed over a cup of hot water, the hydrophilicity was found to degrade upon exposure to both dry and humid environments for 7 days. These authors have also demonstrated [237] the feasibility of conferring anti-fogging property to ITO glass, following application of 50 V for 20 min to an aqueous solution of H_2SO_4 were a ITO sample was immersed. These authors argued that the electrochemical oxidation of water yielded hydroxyl groups on the ITO surface, which explains why, WCA abruptly decreased from 80 to 0°. Although not prevented, hydrophilicity loss due to surface aging was slower than that observed in the plasma-treated PET films under the same fogging conditions. Alternatively, extremely wettable (WCA < 5°) films of polydiethylene glycol bis(allylcarbonate) with resistance to fogging were prepared by implantation of Ar^+ ions under very low O_2 pressure [67]. A pre-implantation treatment with He^+ ions was found to delay significantly the hydrophilicity loss, hence the occurrence of fogging.

While the above-mentioned surface treatments hold great promise for the manufacture of agricultural and food packaging films with anti-fogging characteristics, the problem of surface aging remains unresolved. This fact may explain why the incorporation of surfactants appears to be gaining in popularity in this regard [29,275,276]. Surfactants are molecules consisting of two well-differentiated parts, namely, a hydrophobic tail and a hydrophilic head. In general the hydrophilic domain contains hydroxyl [277–283] or amine groups [284]. When incorporated to polymer formulations, these molecules migrate from the bulk to the film surface, where they dissolve in the condensed water, decreasing its surface energy. As a result, water drops wet evenly the surface and scattering events are mitigated [280]. According to Irustra [284] and Salmeron [285] the use of additives comes with two major problems. First, as long as a sufficient amount of surfactant dissolves in the condensed water, the anti-fogging/anti-dripping film will perform adequately; however, given that it takes a while for these molecules to migrate and dissolve in water, these films usually fog up when exposed to sudden temperature or humidity changes. Second, considering that surfactants are gradually washed away by the dripping water, the anti-fogging/anti-dripping performance deteriorates over time. Thus, controlling the migration rate of these molecules is crucial to retaining the anti-fogging performance long term. In general, the migration of surfactants can

be slowed down if bonded to inorganic nanoparticles such as SSNPs [286–288] or if added to blends of hydrophilic grafted co-polymers with un-grafted ones [289]. To retain wetting features for longer periods of time, covalent grafting of "bulky" surfactants, also known as "graft co-polymerization", represents a feasible alternative to plasma and ionic implantation treatments, as well as the addition of surfactants *per se* [23,290]. The applicability of this surface treatment on low surface energy polymers is motivated by the fact that the steric hindrance prevents these molecules from hiding in the bulk, thus hampering surface aging. Voluminous surfactants such as monostearic acid monomaleic acid glycerol (MMGD), [291] glycerol monolauric acid monoitaconic acid diester (GLID) [292], trifluoroacetic acid allyl ester (TFAA) [293], maleic anhydride (MA) [294], or polyether pentaerythritol monomaleate (PPMM) [295] have been successfully grafted to the backbone of linear low-density polyethylene (LLDPE) without compromising its optical and mechanical properties.

1.7 Application trends of anti-fogging surfaces

In sectors of activity such as the medical, the photovoltaic, or the horticultural, the use of surfaces endowed with anti-fogging performance is on the rise and under perpetual development. In this section, some of the most relevant applications of these surfaces are briefly presented.

1.7.1 Food industry

In the horticultural sector, the presence of condensation inside greenhouses causes injury to produce (dripping water) [55,289] and favor the development of fungal diseases [29]. Further to this, the decline in sunlight passing through the greenhouse claddings due to the total internal reflection occurring at the water drop/air interface has also been reported to affect crop yield [22,49,296]. Far from being an irrelevant issue, the effects of condensation on light transmission have been studied extensively for more than 20 years. For instance, using different agricultural films, including polyethylene (PE), PE with IR-absorbing features, UV-stabilized PE, and double-layered PE films, Cemek and Demir [55] estimated an average loss

in light transmittance between 5 and 17% for a 2-month testing period. Similar results were reported by Pearson and colleagues [297] (transmission loss ≈ 13%) and Geoola's group [298] (transmission loss = 9–10%) with modified and unmodified PE films. In this context, the use of plastics containing anti-fogging/anti-dripping additives (**section 1.6.3**) is more than welcome, as better light transmission translates to enhanced plant growth rates and more abundant crops. Commercial additives such as Atmer^{TM}400 and Atmer^{TM}103 (Uniquema Polymer Additives, Switzerland), Loxiol A4 Spezial (Emery Oleochemicals, Malaysia), Dyneon^{TM} MM5935 EF (Dyneon LLC, USA), and AF0406PE (Tosaf, Israel) deliver proven anti-fogging/anti-dripping performance to the most commonly used cladding materials (e.g., PE, PP, PTFE, PVC, PS, and PC).

Regarding food packaging, plastic films used to pack freshly chopped meats or vegetables play two crucial roles: they help limit waste by displaying the content more attractively and provide protection, so that food remains safe to eat for a reasonable period of time. However, unless the package contains moisture absorbers (e.g., sorbitol, xylitol) or enables moisture to permeate, sudden changes in temperature results in a packed produce surrounded of condensation. Experience shows that consumers are less likely to purchase when the "see-through" property is severely compromised. As in the case of greenhouse cladding materials, the incorporation of anti-fogging additives into polymeric films (e.g., PP [299–302], PTFE [303], LLDPE [29,304,305], and PLA [306].) represents the most cost-effective solution adopted thus far by the manufacturing sector to minimize the effects of condensation.

1.7.2 Photovoltaic industry

Solar cells are electrical devices made of semiconductors that generate voltage when exposed to light [307]. It is widely known that silicon is the leading material in solar cell production; however, its use comes with a major problem: more than 30% of the incident light is reflected because of its high refractive index. In addition to this, dust accumulation has been reported to contribute up to another 10% to overall non-absorbed light [308]. Surprisingly, compared to existing literature on anti-reflective coatings for solar cells, few studies have addressed the

issue of condensation, even though the formation of surface fog adversely affects the energy conversion efficiency of these devices. Indeed, according to Lu et al. [25] the scattering phenomenon provoked by water drops decreases the amount of photons reaching the cell surface, hence the ratio between the number of collected carriers and the number of all the incident photons, namely, the quantum efficiency.

A reasonable approach to address this problem involves the use of coatings made of highly porous SiO_2. These surfaces reduce contaminant adsorption and enable water drops to wet the surface [25,26,165]. For example, after covering the photoanodes of a high-performance solid-state dye-sensitized solar cell with SSNPs, Park and collaborators [26] observed an improvement in the photovoltaic efficiency of 5.9% in the presence of condensation. These anti-fogging coatings endowed with anti-reflective characteristics would not only improve the optical properties of future transparent solar cells but also their photovoltaic conversion efficiency, by enhancing light harvesting. Dual anti-fogging/anti-reflective coatings with self-cleaning property, have also shown to further improve the performance of solar cells. In general, these coatings are made of TiO_2 and SiO_2/TiO_2 mixtures [309–311]. In addition to featuring resistance to fogging, the cell surface is cleaned at room temperature as a result of the photocatalytic activity (ROS species) and the "sweeping" effect of water (photoinduced superhydrophilicity).

1.7.3 Medicine

In light of the growing number of endoscopic procedures reported annually in developed countries (e.g., 15–20 millions in the US), it is an incontestable fact that camera-guided instruments have become indispensable surgeon's colleagues [312]. In these situations, where a sharply defined field of view is required for obvious reasons, surgeons must paradoxically struggle with the low-quality images provided by the endoscope camera. The root cause of the impaired surgeon's vision reflects the result of at least two factors acting together. The first one arises from the soiling of endoscope lens when in contact with physiological fluids and tissues during surgery. The second factor pertains to lens fogging

induced by temperature and relative humidity differences between operating rooms and human body [16]. To restore optimal view, surgeons are usually compelled to pull out the endoscope to clean the lens in water or saline. These recurring disruptions of the operative process put the patient's health at risk, slow down the surgery's progress, and contribute to surgeon frustration. In this regard, several studies [313,314] have evidenced that an increase in the number of times that the endoscope is withdrawn led to the increases in both the estimated blood loss and the operative time. Longer operative times make financial costs for both hospitals and patients skyrocket.

Within this framework, the implementation of anti-fogging technology is key to ensuring a safe and a successful surgical procedure. Available strategies aimed at maintaining a clear operating field can be divided into four broad categories: endoscope lens warming, use of temporary anti-fogging coatings and modified endoscopes, and other defogging approaches [16]. Regarding those changing the morphology of water drops, anti-fogging strategies based on temporary coatings involve applying commercial solutions such as Covidien FRED [14,18,315], Betadine [316], Hibiscrub [18], and baby shampoo [18] on the endoscope lenses. FRED^{TM} (Fog Reduction and Elimination Device) and Betadine^{TM} are aqueous solutions: the first one containing isopropyl alcohol (< 15 wt%) and surfactants (2 wt%); and the second one, well known for its antiseptic activity, containing povidone-iodine (10 wt%). Cheaper alternatives such as the use of patients' saliva [317] or saline solutions [318], as well as rubbing the lens on viscera [319] have also proven to be suitable to mitigate fogging effects. Also, worthy of mention are the endoscopes incorporating lenses covered with permanent anti-fogging coatings. For instance, using the layer-by-layer assembly, Aizenberg and colleagues [312] coated bronchoscope lens with solid silica nanoparticles embedded in a thermally cured polydimethylsiloxane resin. 100-nm-thick SSNPs/PDMS films endowed endoscope lens with anti-fogging and blood-repelling characteristics. Ohdaira et al. [15,320] prepared TiO_2-coated lenses using the spin-coating technique followed by silicone-sealing and post-treatment at 200°C for 10 min. After 12–15 h of exposure to UV light, the as-fabricated coatings displayed better anti-fogging performance than did heated or washed lenses [15], making it possible to perform surgery with no retraction of the laparoscope [320].

1.7.4 Optical applications

From swimmers to surgical technicians to mining workers, dealing with fogged eyeglasses can be a challenging task. Indeed, this frustrating phenomenon usually forces the person to focus on wiping eyeglasses dry or wait for them to defog, putting under certain circumstances her/his safety at risk [4–6,321–323]. Protective eyewear fogging experienced by construction workers when laboring outside illustrates one among many obvious paradigmatic examples of surface fog formation, as it encompasses all of the favorable conditions to induce water condensation, namely, transitions between warm and cool environments, worker exertion, and oftentimes tight eyewear. Even tough Mother Nature dictates that the fogging of eyewear must occur, human intervention can efficiently prevent it. For example, the fogging of surgical goggles can be reduced by applying a temporary anti-fogging solution called "Body Glove Fog Away" [324]. Permanent coatings of TiO_2 have been very successful in preventing condensation on mirrors [325–328]. In the same vein, coatings based on cellulosic ethers, have also shown to confer notable anti-fogging capability to a plethora of elements, including visors and transparent shields, sports goggles, safety glasses, face shields, and surgical masks, among others [329,330].

1.8 Concluding remarks and outlook

Anti-fogging mechanisms and their link with recent progress in fabrication techniques toward anti-fogging property are discussed in length in this review. Anti-fogging surfaces with additional features such as self-healing, self-cleaning, and anti-bacterial properties as well as the main sectors of human activity making use of them, including food and photovoltaic industries and medical practice, are also addressed. Nevertheless, despite years of tremendous efforts and achievements made in the field of anti-fogging surfaces, some relevant challenges remain.

Standards applied in North America (e.g., CSA Z611-M86 [331] and ASTM F659–10/–06 [332,333]) and Europe (e.g., CEN EN 168 [334]) for guaranteeing (protective) eyeglasses to

reliably perform under fogging conditions are quite limited and not necessarily adapted to daily activities. In F659-10 and EN 168 standards, the sample is immersed in distilled water at room temperature ($23 \pm 5°C$) for 1 h, and then placed over a water bath ($50.0 \pm 0.5°C$) after being dried at room temperature (50% RH) for $\geq$ 12 h. For a sample to be considered anti-fogging, the time required for the light transmittance to decrease to 80% of its initial value (non-fogged sample) must be less than or equal to 30 s. In Z611-M86 standard, the sample is cooled at $-25°C$ and exposed thereafter to ambient conditions (23°C, 50% RH). Here, rather than measuring light transmission, the time it takes for a transparent substrate to defog is reported. The application of these standards is highly questionable when assessing the fogging resistance of eyeglasses during day-to-day activities, for example, when taking a walk, when moving from a warm to a cold environment, when cooking in a steaming environment or even when breathing. In our opinion, developing a certification adapted to everyday activities would be welcomed.

According to Briscoe [22], Grosu [67], and Pieters [49] a WCA angle of less than 40–50° is required for a surface to be anti-fogging; that said, several studies [135,138,143,145,175,195,199] disagree with this rule, as it is possible to prevent fogging effects despite WCA exceeding this cut-off value. The main reason for this lies in the fact that this rule only holds true for nonporous anti-fogging coatings whose surface features do not display time-dependent behavior. In addition to the contact angle, several factors related to fogging effects, such as the number and the size of water drops [123,133], surface rearrangement phenomena [193], as well as the capability of the coating to transport water molecules [198,199], must also be considered to establish a more robust anti-fogging criterion.

On the other hand, designing of a "well-rounded" anti-fogging material is more than a simple adjustment in the morphology of water drops, as many other features, such as mechanical durability and optical properties, must also be considered. For example, the use of inorganic materials to elaborate anti-fogging coatings faces two major challenges, namely, the deposition on thermally sensitive materials and the problem of light reflection. Following

coating deposition, it is standard practice to implement thermal treatments (e.g., calcination, annealing); however, high temperatures make it challenging to coat polymeric substrates because of thermal degradation concerns. In this regard, developing coating techniques adapted to thermally sensitive substrates would undoubtedly be welcomed. Optical transparency is another critical parameter to consider when designing anti-fogging layers. The adjustment of the refractive indices of the coating and the substrate is of considerable relevance to minimize the reflection of light. This implies that the thickness of the coating must be equal to $\lambda/4n_c$, where λ is the wavelength of the incident light and n_c is the refractive index of the coating [335]; and that the refractive index of the coating must be $n_c = \sqrt{n_s n_{air}}$, where n_s is the refractive index of the substrate and n_{air} is the refractive index of the air ($n_s > n_c$) [336]. Fulfilling simultaneously these two design criteria is quite often more difficult than imagined.

Despite the plethora of materials and fabrications techniques employed thus far to design anti-fogging surfaces, bridging the gap between fundamental research and industry is a pending issue. Even though their large-scale fabrication is not particularly challenging, addressing the problem of mechanical durability is crucial to make it a reality. Experience shows that any surface is exposed to mechanical wear caused by rubbing during day-to-day use or by solvents under normal cleaning practices. In coated surfaces, temperature variations can lead to coating deformation or detachment because of the differences in thermal expansion coefficient between the coating and the substrate. Mechanical wear, temperature variations, and exposure to cleaning products may result in a deterioration of the anti-fogging performance over time. Thus, designing anti-fogging surfaces with abrasion resistance (e.g., durable self-healing properties) with optimal adherence to the substrate is key to ensuring a long service life once integrated in items, such as mirrors, eyeglasses, and home windows, that make our day-to-day living more comfortable.

According to recent studies, the future trend in this promising field points to unique anti-fogging surfaces exhibiting an optimal combination of features to cover a wide range of applications. For example, dual anti-fogging/anti-bacterial surfaces will likely be most

welcome in endoscopic surgery, while anti-fogging surfaces endowed with self-healing properties would find a niche of opportunity in swimming goggles, solar panels, or automobile windshields. Undoubtedly, anti-fogging surfaces would be welcomed in applications where a clear visualization of the liquid medium plays a crucial role. Such is the case, for example, with micro/nanofluidic devices and microreactors for chemical synthesis and cell culture. Another opportunity niche for anti-fogging surfaces can be found in fiber optics [337] as well as among amateur and professional photographers. We firmly believe that future development of anti-fogging technology will be based on two fundamental pillars—industrial research and the use of eco-friendly materials. For example, developing less time-consuming and cost-effective fabrication techniques compatible with industrial manufacturing is undoubtedly a pending issue. Similarly, improving mechanical durability of anti-fogging surfaces and using of anti-fogging materials coming from renewable sources to bring environmental savings continues to be the "Achilles Heel" of anti-fogging technology. In conclusion, research focusing on fundamental aspects of anti-fogging surfaces is still necessary to make industrial and professional applications of anti-fogging technology a reality.

1.9 Acknowledgements

2 Phenomenology: From discharge physics to coating deposition

2.1 Introduction

The ever-growing performance demands on sectors of activity such as the military, the biomedical, or the automotive, have promoted the fabrication of coatings with functional properties (e.g., thermochromism, anti-bacterial activity, fouling resistance, etc.), by plasma enhanced chemical vapor deposition (PECVD). This interest mainly arises from the advantages that this coating technology has compared to conventional deposition techniques (e.g., dip-coating, spin-coating, etc.), including a low environmental impact, more control over coating thickness, and a great versatility as regards coating composition and microstructure. That said, PECVD features constraints related to high capital costs and time-consuming operation requirements derived from vacuum processing. To overcome these drawbacks, atmospheric pressure processing has emerged as a promising approach for the one-step fabrication of functional coatings, because of its potential for integration into in-line processes without the economic constraints imposed by vacuum operation. In this context, the use of dielectric barrier discharges (DBDs) at atmospheric pressure, a well-known strategy to generate non-thermal plasmas, holds great promise for the preparation anti-fogging coatings.

On this basis, the aim of this chapter is to describe the theoretical notions of atmospheric pressure dielectric barrier discharges (AP-DBD) and their use in coating deposition. Some aspects relevant to PECVD are briefly described in **section 2.1**. Beginning with the definition of the plasma state followed by a description of some plasma parameters, **section 2.2** focuses on the basics of plasma physics. Types of plasmas and electrical breakdown in gases are presented in **sections 2.3** and **2.4**, respectively. Fundamentals of dielectric barrier discharges (DBD), including the requirements for plasma generation, self-sustaining mechanisms, and operation regimes are discussed in **section 2.5**. Interactions between the plasma species and the substrate occurring during coating deposition are detailed in **section 2.6**. **Section 2.7**

concludes with a concise overview of the deposition of siloxane coatings using AP-DBD, with the focus on 1,3,5,7-tetramethylcyclotetrasiloxane (TMCTS).

2.2   Fundamentals of plasmas: Getting the basics right

2.2.1 Definition of plasma

A plasma is an ionized gas, often referred to as the "fourth state of matter", consisting of neutral and charged particles exhibiting a collective behavior [338]. With an equal number of negative and positive charges, the plasma state is electrically neutral at the macroscale, that is [339]:

$$-e(n_i + n_e) + \sum_z en_z Z = 0 \qquad (2.1)$$

where n_e is the electron number density, n_i is the ion number density (ions with charge $-e$), and n_z is the ion number density (ions with charge $+Ze$). The unit of n is m^{-3}.

To illustrate the concept of collective behavior, let us briefly recall the kinetic theory of gases. According to this theory, gas particles interact only during collision events. Between two consecutive collisions, they move in straight lines because of the rapid decay of the interparticle forces with the distance—Van der Waals forces $\propto r^{-7}$. Accordingly, the motion of gas particles is governed by short-range interactions. In the plasma state, the random motion of plasma particles results in local concentrations of positive and negative charges. Given that the Coulomb force behind the electrostatic interactions decays more slowly ($\propto r^{-2}$) than van der Waals forces do, these charge concentrations affect the motion of the neighboring particles, even over relatively long distances. Owing to the long-range effects of the Coulomb force, plasma species feature a cooperative response when subjected to external stimuli (e.g., electric, electromagnetic fields), namely collective behavior. Debye shielding is a clear example of collective response of plasma particles (**section 2.2.2.3**).

One of the simplest ways to generate a plasma consists in applying an electric or an electromagnetic field to a gas [340]. Any gas at room temperature possesses a few free electrons per cm^3, most coming from cosmic rays. On application of a sufficiently high electric field, these electrons gain kinetic energy and travel a very short distance before they collide with the gas particles. Collisions leading to the formation of ions, radicals, and electronically excited species are called "inelastic collisions". In contrast, collisions that result in neither excitation nor ionization of the gas particles, but rather in a change in the direction of motion of electrons are called "elastic collisions". During an elastic collision, electrons do not transfer their kinetic energy to the gas particles because of the large mass difference. Man-made plasmas are sustained electrically by direct current DC (100 kHz), radio frequency RF (13.56 or 27.12 MHz), or microwave MW (433 and 915 MHz or 2.45 GHz) power applied to a gas at a pressure ranging from a few mTorr to 760 Torr (atmospheric pressure) [341].

The exposure of a gas to extremely high temperatures also makes it possible to generate a plasma. For that to occur, the thermal energy of the gas must be higher than the ionization energy of its constituent particles. In this case, there is some realistic probability that somewhere in the gas, the thermal agitation of the atoms or molecules results in inelastic collisions. This is the process occurring in star cores where temperatures can reach millions of degrees.

2.2.2 Basic plasma parameters

2.2.2.1 The degree of ionization

Strictly speaking, the term "plasma" should be applied to a gaseous phase containing only charged particles. In practice, however, the terms "plasma" and "ionized gas" are often used interchangeably. To differentiate one from the other, it is standard practice to refer to the degree of ionization of the medium α_i. This parameter relates the number of ionized atoms/molecules to the total number of heavy particles in the gas [339]:

$$\alpha_i = \frac{n_i}{n_i + n_0} \tag{2.2}$$

where n_i and n_0 are the number densities of ions and neutrals, respectively.

When $\alpha_i \leq 10^{-4}$, most collisions occurring in the gas involve short-range interactions—elastic electron-neutral collisions are predominant. These weakly ionized gases are usually referred to as "cold plasmas" due to a misuse of language. In contrast, when $\alpha_i > 10^{-4}$, coulombic long-range interactions prevail over short-range ones. These highly ionized gases are called "hot" or "thermal" plasmas.

2.2.2.2 Plasma temperature

In a plasma, as in any gas in thermodynamic equilibrium, the temperature is determined by the mean translational kinetic energy of its constituent particles. When an electric field is applied to a plasma, electrons are the first particles to respond because of their high mobility (and low mass) compared to that of heavy particles. On collision with the heavy particles, electrons transfer part of their kinetic energy causing, in some cases, ionization, dissociation, or excitation, among other elementary processes (see **section 2.6**). The probability of ionization, excitation, or dissociation of the gas particles depends, to a great extent, on how many electrons have enough energy to trigger these processes. A good indicator of the electron population available to provoke inelastic (and elastic) collisions is the electron energy distribution function (EEDF). If the collision frequency electron-neutrals is independent of the velocity of the electrons (constant) and the effects of the electric fields are negligible, the EEDF can be described, as in an ideal gas, by a Maxwellian distribution [340]:

$$f(E) = 2.07 \left(\frac{E}{\langle E \rangle^3} \right)^{1/2} exp\left(-\frac{1.5E}{\langle E \rangle} \right) \tag{2.3}$$

where $\langle E \rangle$ is the average energy of electrons.

Under these conditions, electrons are in equilibrium with the gas particles, and therefore one temperature suffices to define the plasma ($T_{electrons} = T_{gas}$). Accordingly, it can be inferred that the EEDF tends toward a Maxwellian shape as the degree of ionization increases, because of the increase in the number of electron-electron collisions [342]. The average energy of the electrons for a Maxwellian distribution is given by:

$$\langle E \rangle = \int_0^\infty E \cdot f(E)dE = \frac{3}{2}k_B T_e \tag{2.4}$$

Which is the definition of the electron temperature, T_e. **Equation 2.3** can also be applied to ions and neutral species. Indeed, the energy distribution function for the heavy particles is not far from the Maxwellian one, with $T_{ions} \approx T_{gas}$. The plasma temperature is usually expressed in energy units. For $k_B T = 1$ eV $= 1.6 \times 10^{-19}$ J corresponds to a temperature of approximately 11600 K.
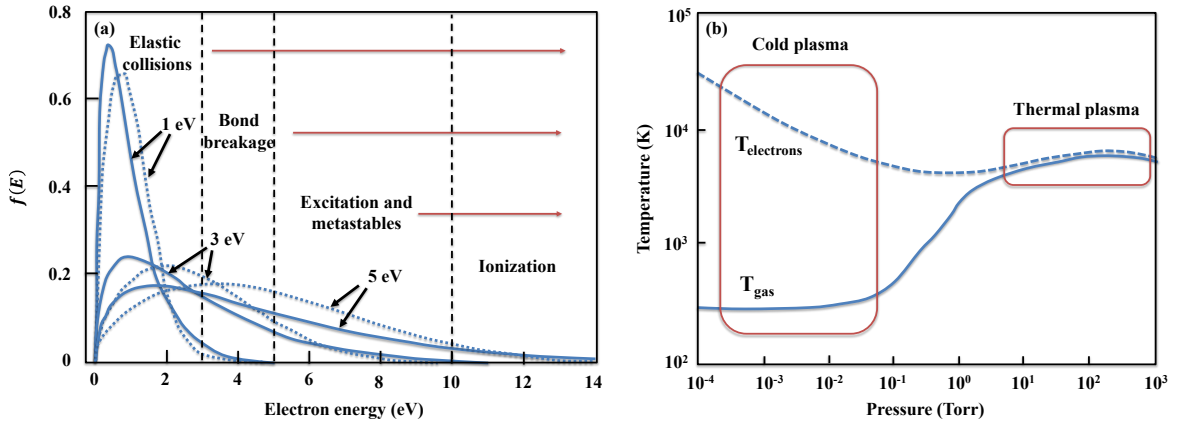
Figure 2.1: *(a) Maxwellian (solid blue line) and Druyvesteyn (dashed blue line) electron energy distributions with average electron energies of 1, 3, and 5 eV and corresponding elemental processes (Adapted from ref. [340]). (b) Pressure dependence of electron and gas temperatures in DC-driven plasma discharges (Adapted from ref. [343]).*

Electron-electron collisions tend to maintain the Maxwellian shape by driving the distribution toward low electron energies. However, when the degree of ionization is low, collisions between electrons and heavy particles become important. As a result, the EEDF

broadens and shifts toward high electron energies, thus becoming less Maxwellian. In this case, the Druyvesteyn distribution function usually provides more accurate results [344]:

$$f(E) = 1.04 \left(\frac{E}{\langle E \rangle^3}\right)^{1/2} exp\left(-\frac{0.55E^2}{\langle E \rangle^2}\right) \qquad (2.5)$$

where E is the energy and $\langle E \rangle$ is the average energy.

Under these conditions, the temperature of electrons is much greater than that of ions and neutrals, i.e., $T_e > T_i \approx T_g$. Although not explicitly shown in **Equation 2.5**, the exponent's argument contains the E/P ratio or "reduced electric field", where E is the applied electric field and P is the gas pressure. Therefore, the average electron energy $\langle E \rangle$ and the electron temperature T_e are also function of this parameter. As illustrated in **Figure 2.1a**, as the average energy decreases, the high-energy tail of the Druyvesteyn distribution decays faster than that of the Maxwellian distribution, which translates to fewer high-energy electrons producing ions, excited species, and excited species [345].

In general, laboratory plasmas can be defined by at least two different temperatures—one for the electrons and the other for the ions/neutral species. That said, if the interaction between these two species increases, for example, by increasing the pressure or the ionization degree, their associated temperatures tend to converge, thereby shifting the plasma from a "cold" state to a "hot" state (**Figure 2.1b**). As the pressure increases, the energy transfer from electrons to heavy particles becomes more effective, resulting in the thermalization of the plasma [343].

2.2.2.3 Debye length and plasma parameter

To illustrate the concepts of Debye length and plasma parameter, let us consider an extra positive charge + Q in an infinitely large homogeneous plasma, with $n_e \cong n_i$. Following the insertion of the charge, charge displacements that ensue (positive ions are repelled faster than

the electrons are attracted), lead to the formation of a negatively charged sheath in the vicinity of + Q that insulates it from the rest of the plasma (right side of **Figure 2.2**). The as-formed net space charge shields the plasma from the electric field generated by + Q [346].
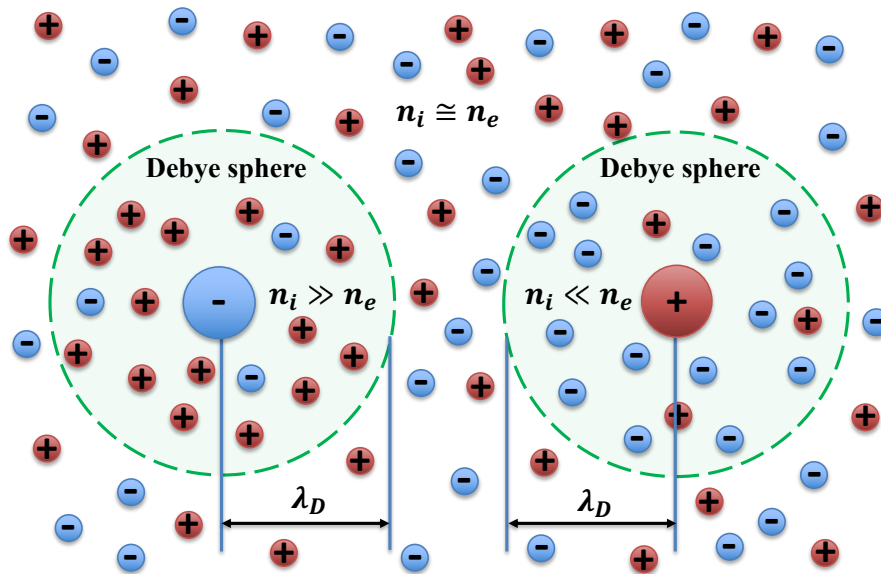
Figure 2.2: *Illustration of the "Debye shielding". If the charge density is perturbed, plasma reconfigures to reduce the resulting electric field. Image adapted from* *https://www.nextbigfuture.com/2016/09/electrostatic-glider-update.html.*

For a negatively charged particle, the shielding "cloud" contains an excess of positive ions (left side of **Figure 2.2**). A similar behavior is observed when an external electrical field is applied; charges redistribute to shield the plasma from it. This effect is known as "Debye shielding" and the space region over which the electric field due to a charged particle is collectively shielded is called "Debye sphere". The radius of this sphere or "Debye length" λ_D, is a characteristic dimension of the plasma (µm to mm in man-made plasmas) and can be expressed, as follows [338]:

$$\lambda_D = \sqrt{\frac{\varepsilon_0 k_B T_e}{n_e e^2}} \qquad (2.6)$$

69

where ε_0 is the permittivity of free space (8.8542×10^{-12} F m^{-1}), n_e is the electron number density, T_e is the electron temperature, k_B is the Boltzmann constant (1.3806×10^{-23} m^2 kg s^{-2} K^{-1}), and e is the charge of the electron (1.6022×10^{-19} C).

According to **Equation 2.6**, an increase in the number of electrons per unit volume makes shielding more effective—λ_D diminishes—because of the increment in the number of electrons available to populate the shielding sheath. The dependence on temperature of λ_D indicates that, the more energy the shielding particles have, the further away they are, on average, from the charge. Accordingly, the extent of the effects of the electric field generated by the charge are less localized. Outside the volume delimited by the Debye sphere, the criterion of neutrality is met because of the collective response of the plasma to external electric fields or internal charge perturbations. The number of electrons in a Debye sphere is given by [338]:

$$N_D = \frac{4\pi}{3} n_e \lambda_D^3 \qquad (2.7)$$

The dimensionless number N_D, often called "plasma parameter", must be greater than one to ensure effective shielding; in other words, the Debye sphere must contain a very large number of electrons. In conclusion, for an ionized gas to be a plasma—collective effects dominating over collisions—two criteria must be met simultaneously [338]. First, the physical dimensions of the system must be much larger than the Debye length ($L \gg \lambda_D$), and second, the number of particles (electrons or ions) inside the Debye sphere must largely exceed unity ($N_D \gg 1$).

2.3   Plasma types

Although plasmas are rarely found on earth, as most of them occur during unusual weather events such as lightning or aurorae borealis, they are common in the universe. Indeed, more than 99.9% of cosmic matter, e.g., stars, nebulae, comet tails, and interstellar medium, is

composed of ionized gas. Natural and man-made plasmas cover a wide range of electron temperatures and densities—T_e varies from 10^{-2} to approximately 10^5 eV while n_e can go from ~ 1 to more than 10^{20} electrons per cm^3 (**Figure 2.3**).
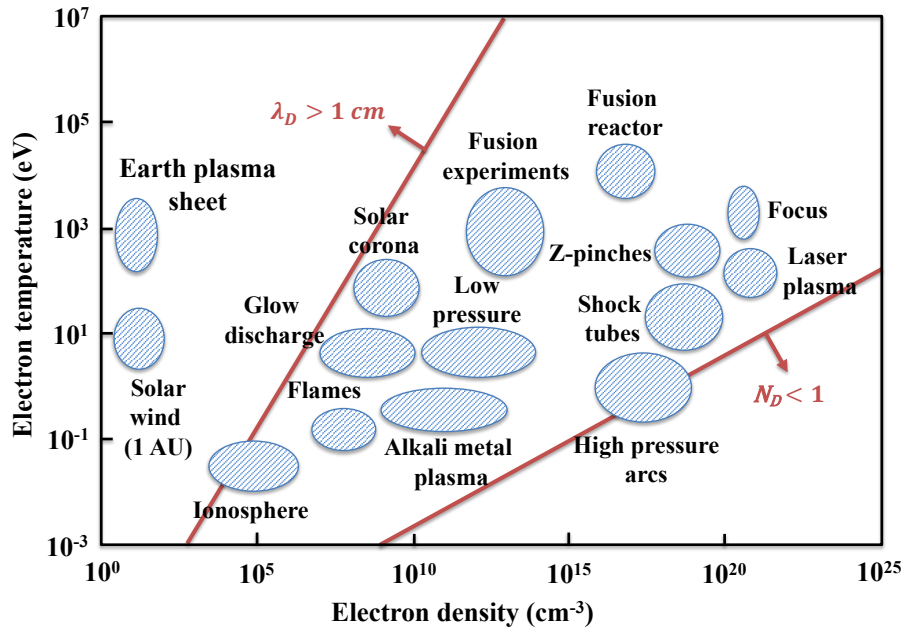
Figure 2.3: Classification of man-made and natural plasmas as a function of electron temperature and electron density (Adapted from http://pdml.tamu.edu/about.html.).

Regardless of the origin, plasmas can be divided into three categories:

2.3.1 Plasmas in complete thermodynamic equilibrium (CTE plasmas)

For a plasma to be in complete thermodynamic equilibrium (CTE), the principle of microscopic reversibility must be fulfilled, that is, each one of the radiative (photon emission) and non-radiative (e.g., excitation, ionization, dissociation) processes must be balanced by their inverse processes. Here, the effective energy transfer from electrons to heavy particles via collisions, derived from a very high ionization degree and high plasma densities, results in a uniform energy distribution among all plasma species; hence $T_{electrons} = T_{ions} = T_{gas}$.

The physical state of a CTE plasma can be described by a finite number of thermodynamic variables—the density of heavy particles and the temperature T—and is governed by the following four laws of equilibrium [346]:

- The velocity distribution of the plasma particles follows the **Maxwell-Boltzmann distribution**:

$$f(v) = \left(\frac{m_e}{2\pi k_B T}\right)^{3/2} exp\left(-\frac{m_e v^2}{2k_B T}\right) \tag{2.8}$$

where m_e is the mass of the electron (9.1094×10^{-31} kg), v is the velocity, k_B is the Boltzmann constant (1.3806×10^{-23} m^2 kg s^{-2} K^{-1}), and T is the plasma temperature.

The Maxwell-Boltzmann translational energy distribution (**Equation 2.3**) also pertains to all plasma species.

- The population of the excited states for all plasma species as a function of temperature obeys **Boltzmann's law**:

$$\frac{n_j}{n_0} = \left(\frac{g_j}{g_0}\right) exp\left[-\frac{(\varepsilon_j - \varepsilon_0)}{k_B T}\right] \tag{2.9}$$

where n_0 is the density of species in the energy state ε_0, n_j is the density of species in the excited energy state ε_j, T is the plasma temperature, and g_j and g_0 are the statistical weights (partition functions) associated with the energies ε_j and ε_0, that is, the degeneracy factors giving the number of states with energies ε_0 and ε_j, respectively.

- The ionization equilibrium is given by the **Saha equation**:

$$\frac{n_e n_i}{n_0} = \frac{2g_i}{g_0} \frac{(2\pi m_e k_B T)^{3/2}}{h^3} exp\left[-\frac{(\varepsilon_i - \varepsilon_0)}{k_B T}\right] \tag{2.10}$$

where n_e, n_i, and n_0 are the densities of electrons, ions, and neutrals, respectively; T is the plasma temperature, $\varepsilon_i - \varepsilon_0$ is the energy required to remove the outermost electron from an isolated atom in gaseous phase and form a cation, i.e., the first ionization energy; k_B is the Boltzmann constant $(1.3806 \times 10^{-23}\ \mathrm{m^2\ kg\ s^{-2}\ K^{-1}})$, h is the Planck constant $(6.63 \times 10^{-34}\ \mathrm{m^2\ kg\ s^{-1}})$, and g_i and g_0 are the statistical weights (partition functions) of ions and neutrals, respectively.

- The intensity of the radiation is governed by **Planck's law**, also called "black-body" radiation law:

$$I(v) = \frac{2hv^3}{c^2} \frac{1}{exp\left(\frac{hv}{k_B T}\right) - 1} \tag{2.11}$$

where c is the speed of light in vacuum $(2.9979 \times 10^8\ \mathrm{m\ s^{-1}})$ and v is the frequency of the radiation.

Plasmas in CTE have no practical relevance as they cannot be generated in a controlled manner under laboratory conditions; deviations from CTE are indeed very common [340]. Deviations from CTE are mainly due to irreversible energy losses by radiation, convection, and conduction, as well as to the presence of temperature gradients between the plasma and the reactor walls.

2.3.2 Plasmas in local thermodynamic equilibrium (LTE plasmas)

A more realistic description of plasmas is built upon the concept of the local thermodynamic equilibrium (LTE). In LTE plasmas, radiation is not required to be equilibrium with collisional processes; however, microscopic reversibility must be respected as in CTE plasmas. Collisional (no radiative) processes only allow for a sufficient energy transfer between electrons and heavy particles in plasma volumes on the order of the mean free path

length λ. The mean free path length is the average distance travelled by a particle between two collisions. In these small volumes, the equilibrium is similar to that of a CTE plasma with a single temperature T, which can vary slightly from point to point in the plasma. Except for the Planck's law, plasma obeys (locally) the above-mentioned equilibrium relations.

Plasma torches, flames, and high-pressure arcs are clear examples of LTE plasmas. With electron densities ranging from 10^{13} to 10^{18} cm^{-3}, these plasmas typically operate at atmospheric pressure and are often referred to as "thermal" or "hot" plasmas" [347]. Thermal plasma technology covers a wide spectrum of applications, including coating deposition (e.g., plasma spraying, wire arc spraying, etc.), synthesis and densification of powders, and waste treatment. However, LTE plasmas are not well suited for applications involving thermally sensitive materials, such as polymers or fabrics, because of their destructive nature.

2.3.3 Plasmas that are not in any local thermodynamic equilibrium (non-LTE plasmas)

Deviations from LTE are more the rule than the exception in low-pressure plasmas. The relatively low electron density, which typically ranges from 10^4 to 10^{15} cm^{-3}, does not allow for collisions to thermalize the plasma, and consequently one temperature no longer suffices to characterize it. In this case, electron temperature is much greater than that of the heavy particles, that is, ions and neutrals ($T_e \gg T_i \approx T_n$). The electron temperature can be as high as 10^4–10^5 K (1–10 eV), while that of the gas can be as low as room temperature, hence the terms "non-thermal" or "cold" when referring to non-LTE plasmas [348]. None of the above-mentioned equilibrium relations (**Equations 2.8–2.11**) can be applied to describe the physical state of a non-LTE plasma.

Unlike thermal plasmas, the non-destructive nature of cold plasmas makes them well suited for materials processing at room temperature. In this context, plasma enhanced chemical vapor deposition (PECVD) has generated growing interest, since the advent of the integrated circuit in the late 1960s, in the field of functional coatings. In a typical PECVD process,

reactant gases (e.g., SiH_4, $TiCl_4$, N_2O, NH_3) often diluted in a carrier gas (e.g., Ar, He, N_2) are introduced into a DC, RF, or MW low-pressure plasma where, they undergo dissociation, ionization, and excitation on interaction with plasma species. The resulting molecular fragments react with each other and adsorb on the substrate forming a coating.

This coating technology has made it possible to fabricate a multitude of high value-added products, including semiconductor devices, optical waveguides, energy efficient windows, displays, solar panels, cutting tools, antiseptic textiles, and medical equipment, among others. Compared to conventional deposition processes, such as CVD, PVD, or sol-gel coating deposition, PECVD has many advantages [349]:

- Control over coating composition (stoichiometry) and microstructure can be achieved by optimizing the plasma-surface interactions via deposition parameters.

- Wide variety of coating materials (e.g., SiO_x, SiN_x, SiO_xN_y, a-Si:H, SiC, diamond like carbon).

- Coatings combining electrical, thermal, optical, and other properties can be fabricated by stacking several thin layers (layer-by-layer deposition).

- High deposition rates ($\geq 1-10$ nm s^{-1}) and low operating temperatures ($\leq 350°C$) compared to those of vacuum-based techniques such as PVD.

- Uniform coatings on a variety of flat, spherical, hemispherical, and cylindrical substrates.

Although these features make PECVD very attractive to coating companies, the need for vacuum-processing required in low-pressure operation, imposes excessively high capital equipment and maintenance costs. Bearing this in mind, many research groups have demonstrated great interest, over the past two decades, in developing more cost-effective plasma-assisted coating processes. In this regard, atmospheric pressure plasma enhanced

CVD (AP-PECVD) is undoubtedly a very promising technology. Compared to low-pressure PECVD, the greater feasibility domain available for AP-PECVD is attributed to two factors. First, the reduction of the constraints imposed by vacuum compatibility of materials, and second, the lower capital cost of equipment associated with atmospheric pressure operation [347]. Despite these advantages, generating a cold plasma at atmospheric pressure is quite challenging. In general, the application of several tens of kilovolts above the breakdown voltage of the carrier gas causes the discharge to transit to an electric arc (thermal plasma). Temperatures of up to 20000 K typical of electric arcs make them unsuitable for the fabrication of anti-fogging coatings. Fortunately, the strategies listed below have proven to be effective in generating low temperature plasmas at atmospheric pressure by preventing the non-thermal-to-thermal plasma transition [350,351]:

- Decreasing the product "pressure $\times$ inter-electrode distance" to ensure operating conditions analogous to those of low pressure. This is the operating principle of micro-hollow cathodes (MHCD) [352,353].

- Using non-uniform electric or electromagnetic fields to localize the discharge, and thus prevent electrodes from short-circuiting by a discharge channel. This is the operating principle of corona discharges [354].

- Limiting the energy absorbed in the discharge by restricting the applied voltage or the current.

- Inserting a dielectric material between the electrodes. This approach, better known as "dielectric barrier discharges" (DBDs), was used in this doctoral project to fabricate anti-fogging glass.

To understand the working principle of DBDs, the following sections describe the electrical breakdown in gases, the main AP-DBDs configurations, and the operating conditions required to produce anti-fogging coatings.

2.4   Electrical breakdown in gases

Electrical breakdown is the process whereby a non-conductive material becomes conductive upon application of a sufficiently strong electric field [355]. Depending on the gas composition, pressure, and inter-electrode distance five different steady-state DC discharges can occur when a voltage is applied between two metal parallel electrodes (**Figure 2.4**).
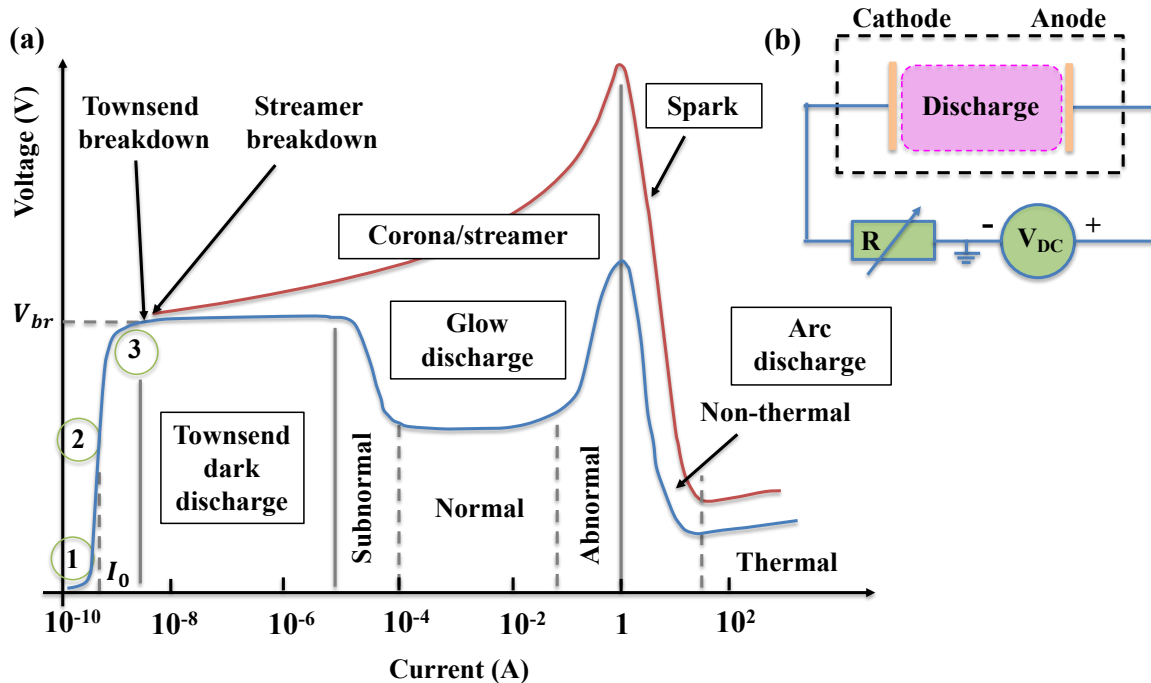
Figure 2.4: (a) Voltage-current characteristics of DC discharges (current values are illustrative) and (b) schematic diagram of a DC discharge between two metal parallel plate electrodes. Curve in red: atmospheric pressure discharges. Curve in blue: low-pressure discharges (typically < 10^3 Pa). V_{br}: breakdown voltage, I_0: saturation current. (Adapted from ref. [356]).

- The **Townsend dark discharge** is characterized by an inter-electrode voltage remaining nearly unchanged for very low current values. The degree of ionization is so small that no appreciable light is emitted, hence the term "dark".

- The **glow discharge** is characterized by current values higher than those of the Townsend dark discharge, despite requiring lower voltages to self-sustain. This weakly ionized

plasma emits light because of the radiative decay of the excited plasma species and is sustained by electrons coming from the cathode. Glow discharges are used in light sources, coating deposition, surface etching, surface cleaning, sterilization of materials, wastewater treatment, and analytical spectrochemistry, among other applications [357].

- **Corona discharges** are typically generated at atmospheric pressure in the presence of a non-uniform electric field near sharp tips, along thin wires, and between cylindrical electrodes. These luminous discharges are sustained by electrons produced at the cathode and in the gas phase by photo-ionization [354].

- **Streamer discharges** are also known as "filamentary" discharges. Streamers are transient filamentary plasmas, which makes them different from corona discharges, and are used in air purification, wound healing, and ozone production [358].

- **Arc discharge**s carry very high currents although they require low voltages to self-sustain. Arc discharges emit a very intense light. Unlike glow and corona discharges, electron emission is due to the heating of the cathode (thermionic emission) caused by ion bombardment. High-pressure arcs are plasmas in local thermodynamic equilibrium (**section 2.3.2**) and are applied in the synthesis of nanomaterials and metal powders, cutting technology, welding of metals, and treatment of industrial wastes [359,360].

Although dielectric barrier discharges are powered by oscillating voltages, continuous analogies and references to DC discharges are made in the literature [361]. In DC discharges, three types of electrical breakdown have been reported, namely, Townsend, streamer, and spark breakdown. The first two are observed in DBDs and result in two different operating regimes, namely homogenous/diffuse regime (Townsend and glow discharges) and filamentary regime.

2.4.1 Townsend breakdown mechanism

Electrical breakdown of gases for low $P \cdot d$ values (< 30 Torr cm), where P is the gas pressure and d is the inter-electrode distance, is called "Townsend breakdown" [362]. To illustrate the Townsend breakdown mechanism, let us consider two plane-parallel electrodes connected to a DC power supply and spaced distance d apart. The space between the electrodes is filled with a gas of given temperature and pressure. As mentioned above, any gas at room temperature has a few free electrons per unit volume ("seed" electrons), originating from external sources such as cosmic rays, natural radioactivity, or UV light.

When a relatively low voltage is applied between the electrodes, these "primary" electrons experience a force, $F = e \cdot E$ (where E is the electric field whose magnitude is V/d and e is the charge of the electron) that accelerate them toward the anode. As a result, a minute current in the circuit, which is proportional to the number of electrons arriving at the electrode, can be measured (**Figure 2.4**, point 1). Once these electrons have reached the anode, the current no longer depends on the voltage and saturates (**Figure 2.4**, point 2). The saturation value of the current is given by:

$$I_0 = e \cdot n_e^0 \tag{2.12}$$

where n_e^0 is the number of primary electrons and e is the charge of the electron (1.6022×10^{-19} C).

At this point, the dependence of current on external sources results in a non-self-sustaining discharge, which means that the discharge would extinguish upon removal of the electron source. If the voltage increases still further, electrons gain enough energy to ionize the gas atoms/molecules and thus trigger the so-called "electron avalanches" (**Figure 2.5a**). Accordingly, the current I_0 due to the external sources is amplified because of the generation of new electrons in the inter-electrode space.
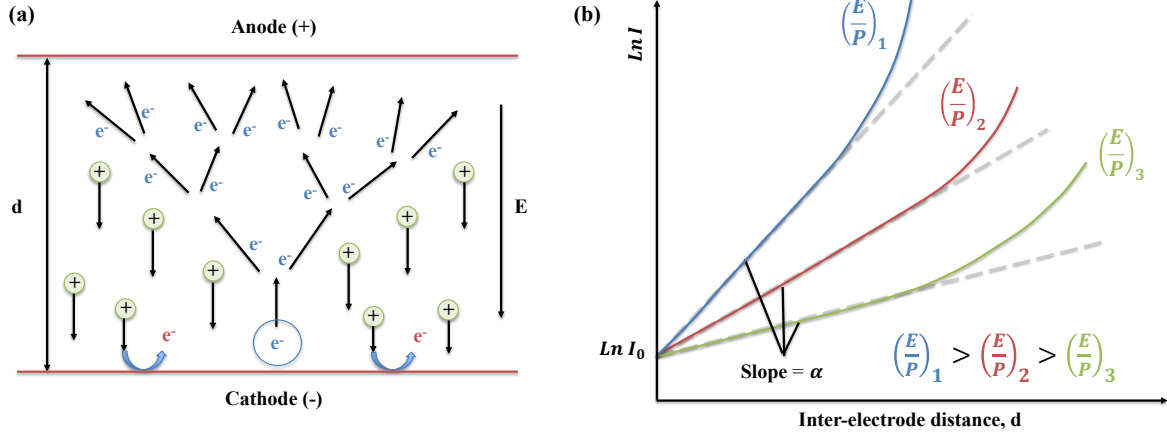
Figure 2.5: *(a) Electron avalanche in the presence of a uniform electric field $E = V/d$. In blue: seed electrons and electrons resulting from inelastic collisions. In red: secondary electrons emitted by the cathode. In green: positive ions resulting from the ionization of gas particles (Adapted from ref. [363]). (b) Variation of the Ln current as a function of the inter-electrode distance, with an E/P uniform (Adapted from ref. [364]).*

The increase in the number of electrons per unit length resulting from the avalanche process is given by:

$$\frac{dn_e}{dx} = \alpha \cdot n_e(x) \tag{2.13}$$

Integration over distance d between the cathode and the anode results in:

$$n_e = n_e^0 \cdot e^{\alpha d} \tag{2.14}$$

where n_e is the number of electrons arriving at the anode per second $(x = d)$, n_e^0 is the number of primary electrons generated per second at the cathode $(x = 0)$, and α is the Townsend's first ionization coefficient. The reciprocal of this coefficient is related to the average distance travelled by the electron between two ionizing collisions. **Equation 2.14** can be expressed in terms of current, as follows:

$$I = I_0 \cdot e^{\alpha d} \tag{2.15}$$

where I_0 is the saturation current as defined in **Equation 2.12** and $e^{\alpha d}$, also known as the "multiplication factor", represents the number of ionizing collisions, on average, produced by electron impact per unit length along the direction of the electric field; in other words, the number of electrons generated per unit length in the avalanche process [364].

In the case of electronegative gases such as SF_6, electron attachments can occur—more accurate results call for the use of an "effective ionization coefficient" defined as $\alpha_{eff} = \alpha - \eta$, where α and η are the Townsend's first ionization coefficient and the coefficient of attachment, respectively. The coefficient of attachment represents the number of attachments produced in the path of a single electron traveling a unit distance in the direction of the electric field. In this case, the expression for the current is:

$$I = I_0 \left[\frac{\alpha}{\alpha - \eta} \right] e^{(\alpha - \eta)d} - \frac{\eta}{\alpha - \eta} \tag{2.16}$$

In the absence of attachments ($\eta = 0$), **Equation 2.16** reduces to **Equation 2.15.**

For a given gas composition, the Townsend's first ionization coefficient features pressure and temperature dependence [365]. Assuming constant temperature, the exponent αd can be expressed as a function of the reduced electric field (E/P), as follows:

$$e^{\alpha d} = e^{\left[P \cdot d \left(\frac{\alpha}{P} \right) \right]} \tag{2.17}$$

With:

$$\frac{\alpha}{P} = A \cdot e^{\left(-\frac{B}{E/P} \right)} \tag{2.18}$$

where A and B are gas-dependent constants, P is the gas pressure, E the applied electric field, and α/P is the reduced Townsend's first ionization coefficient.

In view of **Equation 2.15**, graphical representation of $Ln\ I$ versus inter-electrode distance should give a straight line of slope α for a given value of (E/P). Experimental evidence shows, however, that this only applies to short inter-electrode distances, as long inter-electrode distances results in current growing faster than expected [364] (**Figure 2.5b**). Such deviation from linearity substantiates the presence of electrons involved in the avalanche process, other than those produced by gas ionization. According to Townsend, the emission of secondary electrons caused by ion bombardment of the cathode is the most likely source of this current enhancement [366]. That said, other sources of secondary electrons, such as those emitted by the cathode as a result of photon bombardment, and by the gas on collision with metastable species ("Penning ionization" [367]) or with photons (photo-ionization), can also contribute to increasing the current [368].

Considering the foregoing, Townsend introduced an additional ionization coefficient to characterize the emission of secondary electrons, namely Townsend's second ionization coefficient γ [369]. With values ranging from 10^{-4} to 10^{-1}, γ represents the probability of emission of secondary electrons from the cathode [370]. The value of this coefficient depends on the cathode material, the state of its surface (e.g., roughness, surface contamination, etc.), the type of gas, and the reduced electric field [371]. In general, the number of electrons emitted by the cathode, and therefore the secondary ionization coefficient, decreases with the work function of the cathode. Similarly, the higher the reduced electric field is, the higher the Townsend's second ionization coefficient becomes because of the increase in the population of positive ions capable of ejecting electrons from the cathode. The basic premise here is that each of the $e^{\alpha d}-1$ positive ions generated in the primary avalanche reach the cathode and cause the ejection of $\gamma(e^{\alpha d}-1)$ electrons.

Given that secondary electrons can initiate further avalanches, corresponding current must therefore be "added" to that of the primary electrons. In the steady state, the resulting current is given by:

$$I = I_0 \frac{e^{\alpha d}}{1 - \gamma[e^{\alpha d} - 1]}$$ (2.19)

where I_0 is the saturation current as defined in **Equation 2.12**, d is the inter-electrode distance, α and γ are Townsend's first and second ionization coefficients, respectively.

If $\gamma[e^{\alpha d} - 1] < 1$ the discharge is non-self-sustaining, that is, as soon as the external source of electrons, n_e^0 is removed, (e.g., a UV light source generating electrons from the cathode by photoelectric effect) the discharge will extinguish itself. With increasing voltages, a transition from the dark current I_0 to a self-sustaining discharge occurs at the so-called "breakdown voltage" V_{br}. At this point, current given by **Equation 2.19** becomes indeterminate because:

$$\gamma[e^{\alpha d} - 1] = 1$$ (2.20)

Equation 2.20 represents the "Townsend's breakdown criterion". Following gas breakdown, a slight increase in the applied voltage generates at least as many electrons by secondary emission and ionization as are lost at the anode or by recombination in the gas.

By combining **Equation 2.17** with **Equation 2.20** and taking into account that $E = V/d$, one can obtain the expression for the breakdown voltage or "Paschen's Law":

$$V_{br} = \frac{B(P \cdot d)}{Ln[A(P \cdot d)] - Ln\left[Ln\left(1 + \frac{1}{\gamma}\right)\right]}$$ (2.21)

Breakdown voltage depends on the gas (A and B are gas-dependent constants) and exhibits a minimum for a critical value of $P \cdot d$ product, as depicted in **Figure 2.6**.
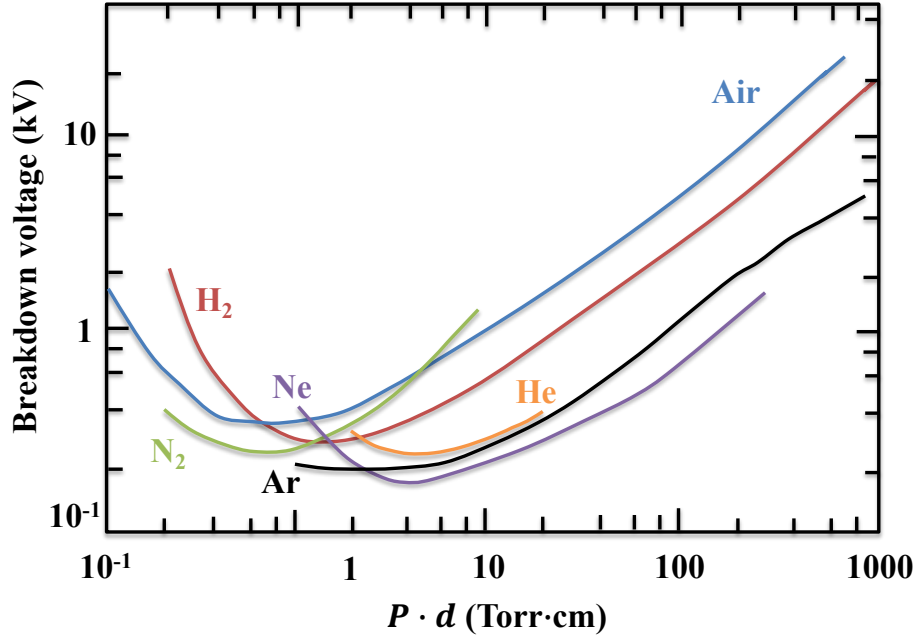
Figure 2.6: *Paschen's curves showing the breakdown voltage as a function of* **$P \cdot d$** *for different gases (Adapted from ref. [372]). The Paschen's curve is only applicable to parallel plane electrodes or uniform electric fields in the absence of a magnetic field.*

The minimum voltage required to break down the gas ("ignite" the plasma) can be calculated by differentiating **Equation 2.21**, $dV_{br}/d(P \cdot d)$, and by setting the result at zero. Accordingly, **Equation 2.22** is obtained:

$$V_{br(min)} = 2.718 \cdot \frac{A}{B} Ln\left(1 + \frac{1}{\gamma}\right) \tag{2.22}$$

In practice, for an applied voltage equal to V_{br}, the number of generated electrons is not enough to produce a self-sustaining discharge. To increase the number of electrons at the cathode and attain a self-sustaining regime, the applied voltage must be slightly higher than V_{br}. In other words, a slight overvoltage $\Delta V = V - V_{br} > 0$ must be applied to ensure a continuous renewal of electrons [356].

Slightly above the breakdown voltage along with a sufficiently large resistance in series with the discharge, the Townsend's breakdown criterion is met, $\gamma[e^{\alpha d} - 1] = 1$. The resistance has two purposes, namely, limiting the current to very low values and preventing the electric

field inside the inter-electrode space from being distorted by the positive space charge [351]. This type of discharge was briefly introduced above and is known as "Townsend dark discharge", and basically each electron emitted from the cathode, initiates an electron avalanche which generates exactly one secondary electron.

For most discharges with $P \cdot d < 30$ Torr cm (low-pressure discharges, typically in He, Ar, Ne, etc.), if current is "allowed" to increase above a certain value, the transition from the Townsend dark discharge to a glow discharge occurs ($\gamma[e^{\alpha d} - 1] > 1$) [373]. Here, the densities of charged particles, in particular that of ions, can reach such values that the ion space charge field is no longer negligible compared with the applied electric field. The electric field in the gas is then distorted by the presence of this volume space charge and becomes inhomogeneous. As the space charge becomes important, the voltage necessary to maintain the glow discharge diminishes (**Figure 2.4**). The distinguishing feature of a glow discharge is the presence of different "regions" across the inter-electrode space characterized by a particular light transmission intensity, electrical potential, electric field, and ion and electron densities (i.e., Aston dark space, cathode glow, cathode dark space, negative glow, Faraday dark space, positive column, anode glow, and anode dark space) [352]. Although, it is possible to generate a glow discharge at a pressure as high as 1 atm, it is not uncommon that above a few centimeters of mercury the current increases rapidly, because of heating of the cathode, and the glow discharge transitions into an arc discharge (thermal plasma).

During the breakdown process, each avalanche generally extends across the inter-electrode space and does not necessarily begin with a single electron, as many of them can be emitted at different points on the cathode. Electron avalanches fill the inter-electrode space making Townsend and glow discharges "homogeneous". This feature makes it possible to differentiate them from the filamentary discharges which are very localized, as will be seen in the following section.

2.4.2 Streamer breakdown mechanism

Electrical breakdown of gases for high $P \cdot d$ values (> 200 Torr cm) or sufficiently high overvoltages ($\Delta V = V - V_{br}$) is called "streamer breakdown" [356,362]. Two main features distinguish it from the Townsend breakdown mechanism. First, discharges develop much faster ($\sim$ ns vs. $\sim$ μs), because no secondary electron generation mechanisms with a long delay are involved (e.g., cathode processes [374]); and second, the breakdown voltage depends on the gas and not on the cathode material.

As in the Townsend breakdown, the presence of a primary avalanche is *a sine qua non* for the streamer breakdown to occur. Once initiated, should ionization of gas prevail over ion bombardment of the cathode, the streamer breakdown is most likely to take place. From a formal point of view, Townsend-to-streamer breakdown transition (avalanche-to-streamer transition) occurs when the number of ions generated by a single electron avalanche $e^{\alpha d}$ is approximately 10^8. Meek's criterion defines this cut-off value as follows [375]:

$$\alpha d \approx 18\text{–}20 \qquad\qquad (2.23)$$

During the primary avalanche, electrons move faster than ions do as they are much lighter. As a result, the positive ions remain virtually stationary where they are produced, i.e., at the tail of the avalanche, while the head of the avalanche becomes populated by electrons (**Figure 2.7b**). This configuration results in a dipole whose space charge field E' interacts with the external field E, so that the field in front of and behind the avalanche is enhanced while that "inside" the avalanche is lessened, with respect to the external field E (**Figure 2.7a**).

When the Meek's criterion is met (**Equation 2.23**), the electric field induced by the space charge becomes comparable to the applied field and the transition from the Townsend to streamer breakdown occurs with little or no participation of the cathode surface (**Figure 2.8a**). At this point, an intense ionization and excitation of the gas atoms/molecules in front of the avalanche head occurs. Excited atoms/molecules return to their ground states

86

and some electrons and ion recombines, emitting photons in both cases. Some of these photons generate secondary electrons by ionization of gas particles (photo-ionization) and initiate further avalanches ahead of the avalanche head [376].
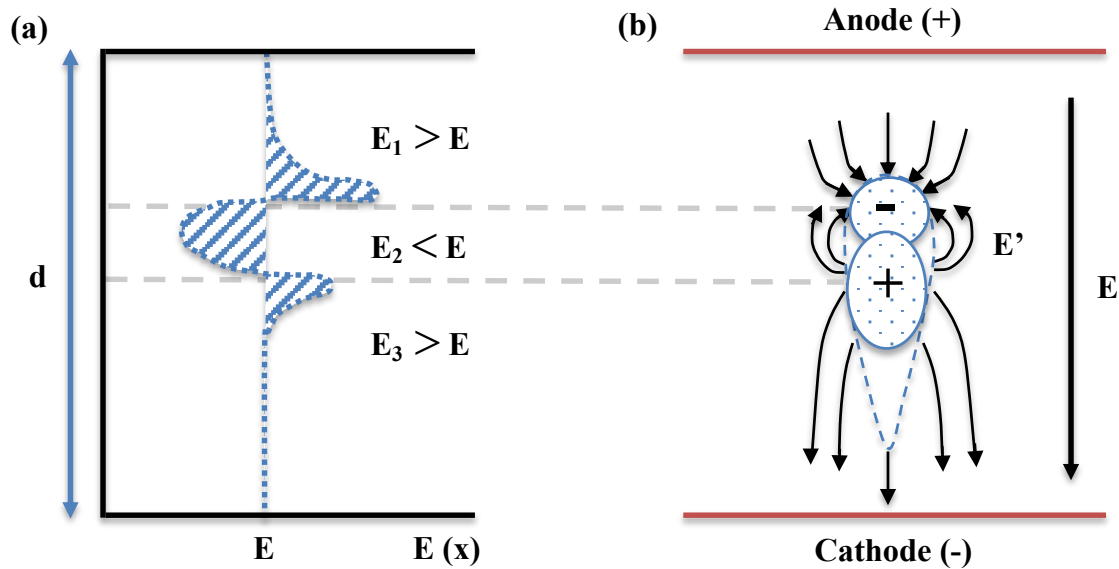
Figure 2.7: (a) Representation of field distortion in a gap caused by space charge of an electron avalanche (local electric field). (b) The space charge distribution in an electron avalanche. The head of the avalanche is rounded because the diffusion of electrons occurs in all directions and is assumed to be concentrated within a spherical volume with negative charge ahead of the positive charge. The form of the tail is wedge-shaped (Adapted from ref. [377]).

Given that photons travel at the speed of light, this process leads to the rapid development of a self-propagating streamer from the cathode to the anode. This type of streamer is called "negative streamer" (**Figure 2.8b**). The propagation of the streamer can be anode- or cathode-directed, depending on the inter-electrode distance and the applied voltage [355]. If the overvoltage ($\Delta V = V - V_{br}$) is high or the inter-electrode distance is large, the avalanche-to-streamer transition generally occurs before the avalanche head reaches the anode. In this case, the streamer initiates far from the anode and propagates against the direction of the electric field (anode-directed or negative streamer). For moderate inter-electrode distances or moderate overvoltages, the avalanche-to-streamer transition occurs when the primary avalanche has reached the anode, because the electric field induced by the space charge is not strong enough to ionize the gas particles previously. Positive ions remaining in the inter-

electrode space cause small avalanches in their vicinity, leading to the formation of a streamer propagating from the anode to the cathode or "positive streamer" (**Figure 2.8c**).

(a) Electron avalanche   **(b) Negative streamer**   **(c) Positive streamer**   **(d) Filament**
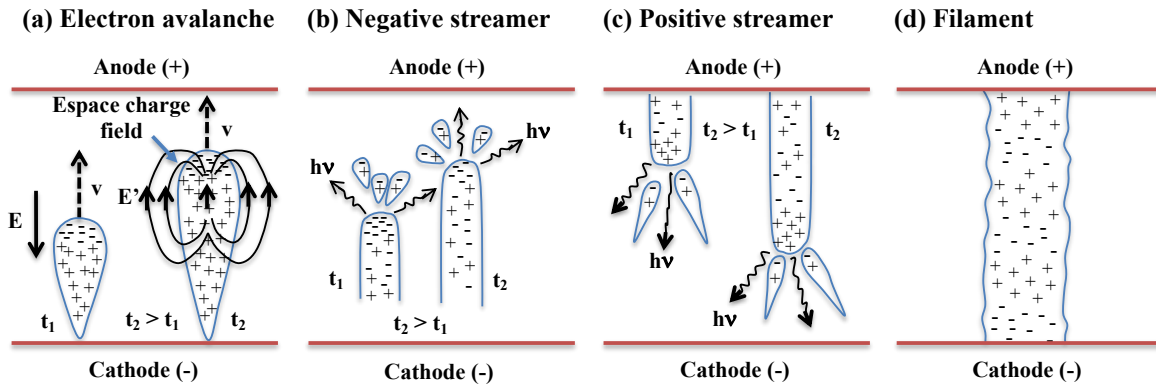
Figure 2.8: *Temporary and spatial evolution of a streamer. (a) Electronic avalanche propagation and avalanche-to-streamer transition, (b) negative or anode-directed streamer, (c) positive or cathode-directed streamer, and (d) formation of a conductive filament or micro-discharge (Adapted from ref. [376]).*

Streamers grow in length between the electrodes until they form a conductive filament (**Figure 2.8d**). At this point, an increase in current results in an arc discharge requiring relatively low voltages to self-sustain (**Figure 2.4**).

Considering the foregoing, when a sufficiently high voltage is applied between two metal electrodes ($V > V_{br}$), gas breaks down in a multitude of short-lived micro-channels of plasma. At atmospheric pressure, the small mean free path of the electrons causes these micro-discharges to transit easily to a thermal arc (LTE-plasma), in response to an increase in the number of collisions. Thermal plasmas are unsuited for the preparation of coatings on materials such as polymers or glass, because of their destructive nature—they can reach temperatures as high as 10000 K [351]. Nonetheless, the streamer-to-arc transition can be prevented by insulating at least one of the electrodes from the plasma by a dielectric barrier, as will be discussed in detail the following section.

2.5 Dielectric barrier discharges (DBDs)

Providing a non-LTE plasma at elevated pressure (e.g., atmospheric pressure) is certainly the distinguishing feature of dielectric barrier discharges (DBDs). That said, the wide variety of DBDs configurations and the ease of scaling-up of DBDs from laboratory conditions to full-scale industrial units are also worthy of mention. These remarkable features explain why the application of DBDs has attracted growing interest, particularly in recent years, in material processing and fundamental plasma research.

2.5.1 Fundamentals: DBD configurations and working principle

A dielectric barrier discharge (DBD) can be described as a system whereby a plasma forms between two electrodes, at least one of which is covered with an insulating material, on application of a voltage in the kilovolt range [361]. DBDs are typically operated at or near atmospheric pressure with inter-electrode distances ranging from 0.1 to 10 mm. Unlike discharges occurring between two metal electrodes, the capacitive character of DBDs imposes the use of alternating or pulsed voltages with frequencies between 0.05 and 100 kHz to displace the current between the dielectric(s) and the plasma phase [378].

Insulating materials with high breakdown strength and low dielectric loss are required for DBDs to operate with moderately high voltage amplitudes. Coinciding with the advent of DBDs for ozone generation in the mid-19th, glass has predominantly been used since then. Currently, apart from glass, DBD designs containing other ceramics (e.g., quartz, mica, enamel) and polymers (e.g., silicon rubber, Teflon) are not uncommon. Some examples of DBD configurations are shown in **Figure 2.9** [379].
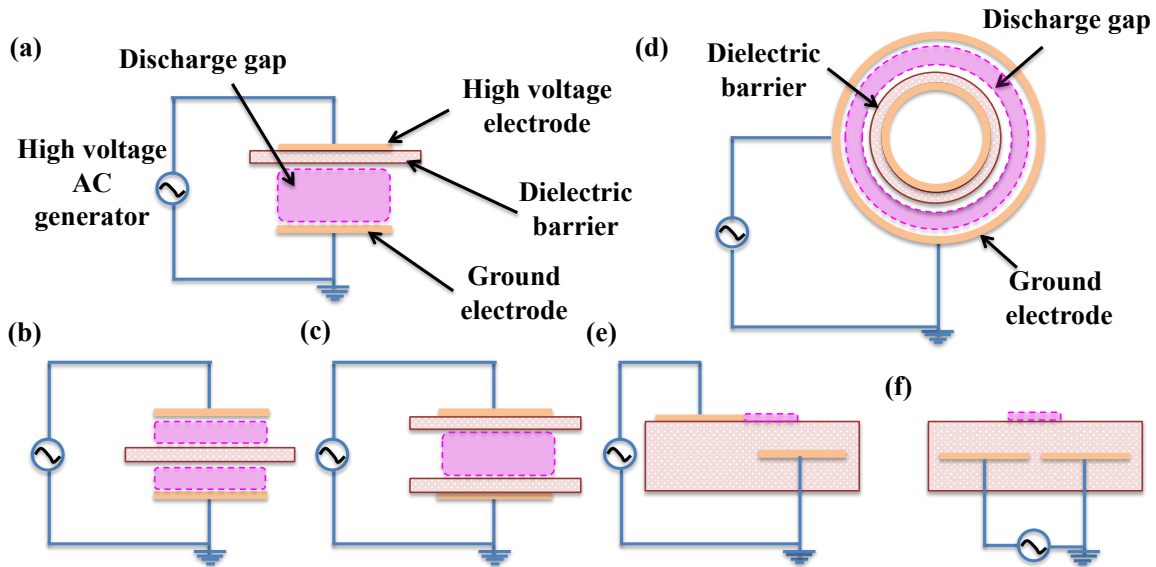
Figure 2.9: *Typical dielectric barrier discharge configurations: (a, b) single-barrier parallel-plate discharge, (c) double-barrier parallel-plate discharge, (d) single-barrier concentric discharge, (e) single-barrier surface discharge, and (f) double-barrier surface discharge (coplanar discharge). Adapted from ref. [361].*

Parallel-plate configurations are often employed in surface treatments such as the etching and functionalization of polymers [380]. The DBD design shown in **Figure 2.9b** allows for the generation of a discharge on both sides of the dielectric. When plasma treatment (e.g., surface functionalization, surface cleaning, coating deposition) is conducted on an insulating material behaving as a dielectric barrier, this DBD configuration is of choice. In this case, both sides of the material are treated simultaneously. The configuration illustrated in **Figure 2.9c**, which was used in this doctoral project for the fabrication of anti-fogging coatings, avoids the contact between the electrodes and the plasma. The cylindrical configuration shown in **Figure 2.9d** was designed by Werner von Siemens in 1857 for ozone production [378]. These configurations are "volume DBDs". Alternative DBD designs such as "surface DBDs" are also possible. A typical example is given in **Figure 2.9e**, in which electrodes are inside and on the top of the dielectric. A different layout is shown in **Figure 2.9f**. In this case, electrodes are inside the dielectric. DBD designs with electrodes buried in the dielectric can be found in plasma display panels for flat television screens.

Other no less important DBDs configurations include point-plane, multi-point-plane, knife-plane, knife-cylinder, wire-cylinder configurations, and packed bed dielectric barrier discharges (PBDBDs), among others. For example, PBDBs use beads made of a dielectric material for remediation of environmental pollutants (e.g., NO_x, SO_x, and volatile organic compounds, VOC) and conversion of greenhouse gases into useful chemicals [381].

By limiting the charge deposited on the electrodes, the dielectric barrier prevents the streamer-to-arc transition. Let us see how DBDs make this possible [351]. The physics behind the development of a micro-discharge is the same in the presence or absence of a dielectric barrier (**Figure 2.8**). The main difference is that the passage of current between the electrodes causes charges to accumulate on the dielectric surface, resulting in an increase in the voltage on the dielectric as the micro-discharges grow (**Figure 2.10a**). If this voltage increases fast compared to that applied between the electrodes, a voltage drop in the gas will ensue and the micro-discharges will extinguish, thus avoiding the formation of a thermal plasma (very high ionization degree).
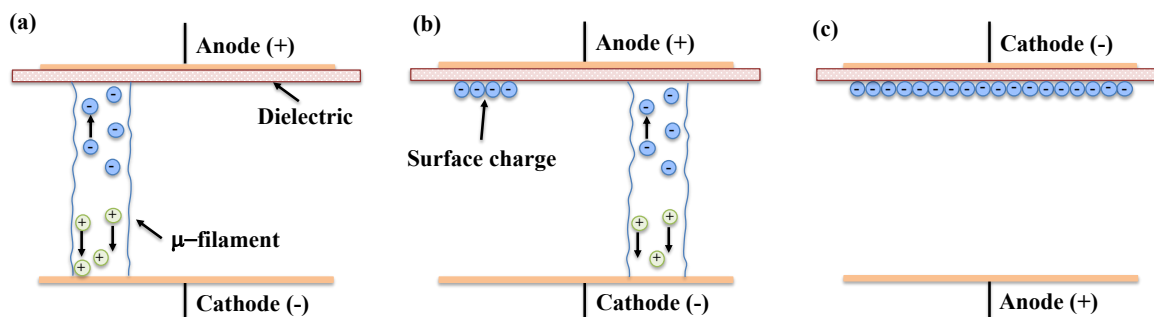
Figure 2.10: The working principle of a DBD. (a) Electrons in the micro-discharge spread across the dielectric surface when they reach the anode, while the positive ions in the tail head towards the cathode. (b) The micro-discharge extinguishes and a second one initiates elsewhere. (c) Transient reversal of the electrodes polarity induced by charge accumulation. The presence of a dielectric material leads to the formation of a transient discharge, which must be reactivate by the external circuit using an alternating or pulsed current power supply. (Adapted from ref. [351]).

If the applied voltage increases still further, micro-discharges will initiate at different locations, given that the charges accumulated on the dielectric surface decrease the electric field "felt" by the gas at the locations where micro-discharges previously formed

(**Figure 2.10b**). When the polarity is reserved in the following half-cycle (**Figure 2.10c**), the charges previously deposited on the dielectric enable the gas to break down under an electric field lower than that of the previous half-cycle. This makes it easier for a new micro-discharge to develop where micro-discharges initiated during the previous half-cycle ("memory effect") [382].

2.5.2 DBD regimes

DBDs have been reported to operate in at least two distinct regimes, namely homogeneous/diffuse regime (Townsend breakdown) and filamentary regime (streamer breakdown). Numerous factors including the gas purity, the inter-electrode distance, pressure, the electrode configuration, frequency, and the applied voltage determine which regime is present [383]. For example, it has been shown that the addition of oxygen to nitrogen plasmas tends to produce a filamentary regime [384]. Similarly, operating with relatively large inter-electrode distances and/or with voltages well above the breakdown voltage also result in a filamentary regime.

A filamentary DBD is composed of micro-discharges randomly distributed on the dielectric surface, which tend to self-organize under certain conditions [385,386]. With a diameter of ~ 100 μm, these discharges form and extinguish on the nanosecond time scale (10–100 ns) and correspond to many short current pulses in a "spiky" discharge current waveform (**Figure 2.11a**). In a homogeneous DBD, (e.g., Townsend and glow discharges), the plasma forms and extinguishes once per half-cycle of the applied voltage and exhibits a single current peak (**Figure 2.11b**). This current peak lasts a few microseconds in the case of a glow discharge (e.g., He, Ne, Ar, etc.) and a few tens of microseconds in the case of a Townsend discharge (e.g., N_2).
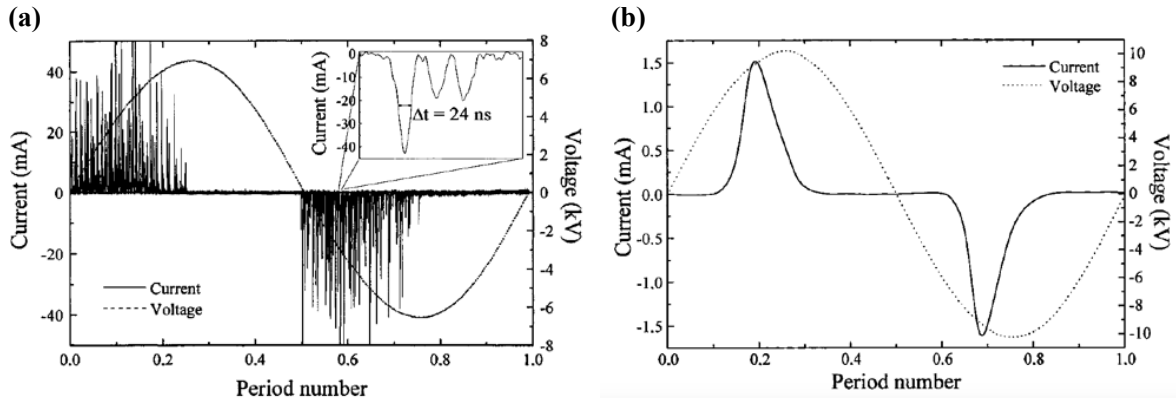
Figure 2.11: *V-I characteristics of (a) a filamentary discharge in nitrogen (gas gap = 1mm and applied voltage = 6.4kV) of (b) a homogeneous discharge in nitrogen —Townsend discharge (gas gap = 1mm and applied voltage = 10 kV) (Adapted from ref.* [387]*).*

At low pressure, DBDs typically operate in a homogenous regime (HDBD). At atmospheric pressure, obtaining a homogenous discharge is also possible—despite $P \cdot d$ values exceeding several tens of Torr cm—yet it is restricted to specific operating conditions (e.g., voltage, frequency, gas composition [388]). Experimental evidence shows that two conditions must be met simultaneously to obtain a homogenous DBD at atmospheric pressure (e.g., Townsend discharge in N_2 and glow discharge in rare gases, such as He, Ne, and Ar). First, the "γ emission" (i.e., emission of secondary electrons) must be enhanced with respect to the "α ionization" (i.e., ionizing collisions produced by electrons, see **Equation 2.15**) to ensure a Townsend breakdown. Second, the current amplitude must be limited to control the discharge development, for example, by adequately designing the electrode configuration and/or by selecting the power supply [389].

The idea behind these approaches is to prevent the streamer breakdown by ensuring many seed electrons between two consecutive discharges and thus, not meet the Meek's criterion. Indeed, many seed electrons are more likely to trigger many avalanches and not one, as in the streamer breakdown. In this regard, numerous studies have evidenced the key role of metastable atoms/molecules in providing these seed electrons either by Penning ionization (Glow discharges in rare gases) or by cathode ionization (Townsend discharges in nitrogen). Derived from to the presence of metastable species in the plasma, the so-called "memory

effect" observed between two consecutive discharges is *a sine qua non* for the Townsend breakdown to occur [390].

The Penning ionization involves the collision and energy transfer from a metastable atom or metastable molecule A^* to another atom or molecule B, leaving A^* unexcited and B ionized, that is [367]:

$$A^* + B \longrightarrow A + B^+ + e \qquad (2.24)$$

For Penning ionization to occur, the ionization potential of B must be lower than the excitation potential of A^* [391]. Penning mixtures in which glow discharges have been observed include He in the presence of minute concentrations of nitrogen—He (2^3S) metastable ionizes the nitrogen impurities—and Ar (4^3P state) in the presence of minute concentrations of acetone, methanol, hydrogen peroxide, or ammonia [388,392,393]. Penning ionization makes it possible to initiate the discharges at voltages below those predicted by the Paschen's law (i.e., breakdown voltage, **Equation 2.21**). Coupled with the emission of (secondary) electrons from the cathode by ion bombardment—ions are "trapped" in the positive column between two consecutive discharges and can diffuse toward the cathode—Penning ionization is responsible for the Townsend breakdown in rare gases.

As regards homogeneous discharges in nitrogen or "Townsend" discharges, several studies have revealed the key role of the N_2 ($A^3\Sigma_u^+$) metastable in the gas breakdown mechanism [362,387]. Because of the absence of positive column, the emission of (secondary) electrons from the cathode are due to N_2 ($A^3\Sigma_u^+$) metastable bombardment and not to ion bombardment, as is the case with glow discharges. In addition, the relatively low excitation potential of N_2 ($A^3\Sigma_u^+$) metastables precludes the ionization of gas particles via Penning collisions, and therefore, the generation of secondary electrons in this way.

2.5.2.1 The HDBD-to-FDBD transition in nitrogen

In nitrogen at atmospheric pressure, obtaining a homogenous DBD (HDBD) or Townsend discharge is restricted to specific conditions of gas composition, voltage, frequency, inter-electrode distance, and dielectric materials [387]. Outside the limits for each parameter, the discharge transitions easily to a filamentary regime (FDBD). For example, the voltage range in which a HDBD can be obtained is restricted from several kilovolts to a very few tens of kilovolts. For a given frequency, the lower limit is the voltage required to generate the discharge over the entire surface of the dielectric, while the upper limit corresponds to the maximum voltage at which "instabilities" begin to appear. Homogeneous DBDs have also shown to transition to a filamentary DBD when operated at very high frequencies (>> kHz) [387] or with relatively large inter-electrode distances. The choice of the dielectric is also of paramount importance. It has been shown that the range of operating conditions in which a HDBD can be generated is broader for a dielectric with a low permittivity [394].

As discussed in the previous section, the main species behind the self-sustaining of a Townsend discharge are the primary (seed) electrons and the N_2 ($A^3\Sigma_u^+$) metastables; hence any factor increasing the rate of destruction of these species will favor the HDBD-to-FDBD transition. Such is the case, for example, with the certain impurities such as O_2 ($\geq$ 500 ppm) [384,395,396], H_2 ($\geq$ 2500 ppm) [395], or C_2H_4 ($\geq$ 15 ppm) [397], which quench the N_2 ($A^3\Sigma_u^+$) population by Penning collisions (**Equation 2.24**).

In the case of polymeric dielectrics, atomic oxygen and atomic hydrogen, well-known N_2 ($A^3\Sigma_u^+$) scavengers, can be released into the discharge because of the damage to the dielectric surface during plasma treatment [387]. The presence of dust or airborne hydrocarbons on the dielectric surface and the formation of etching products during plasma treatment may also have a detrimental effect on the N_2 ($A^3\Sigma_u^+$) population. Fortunately, the laminar gas flow between the two electrodes limits the destruction of N_2 ($A^3\Sigma_u^+$) by maintaining the impurities at low concentration.

2.6 Plasma-surface interactions: Low-pressure vs. atmospheric pressure

The use of dielectric barriers represents a robust approach to generate non-thermal plasmas for plasma-assisted chemical vapor deposition (PECVD). This coating deposition technique, widely known in the microelectronic industry, allows for the preparation of functional coatings via reaction of gas-phase active species with a given substrate, at atmospheric or low pressure (**section 2.3.3**).

In a typical PECVD, the elementary processes occurring between the plasma species and the precursor molecules are very complex and not well understood (**Table 2.1**) [398]. Experimental evidence reveals that the species resulting from these interactions react with the surface in several ways leading to the insertion of functional groups (grafting), generation of radicals, chemical or physical ablation (etching), and deposition of thin films. Although, the prediction of likely reaction pathways is a challenging task, it is widely accepted that the elementary processes occurring in chemical vapor deposition (CVD) are similar to those occurring in PECVD [399] (**Figure 2.12**).
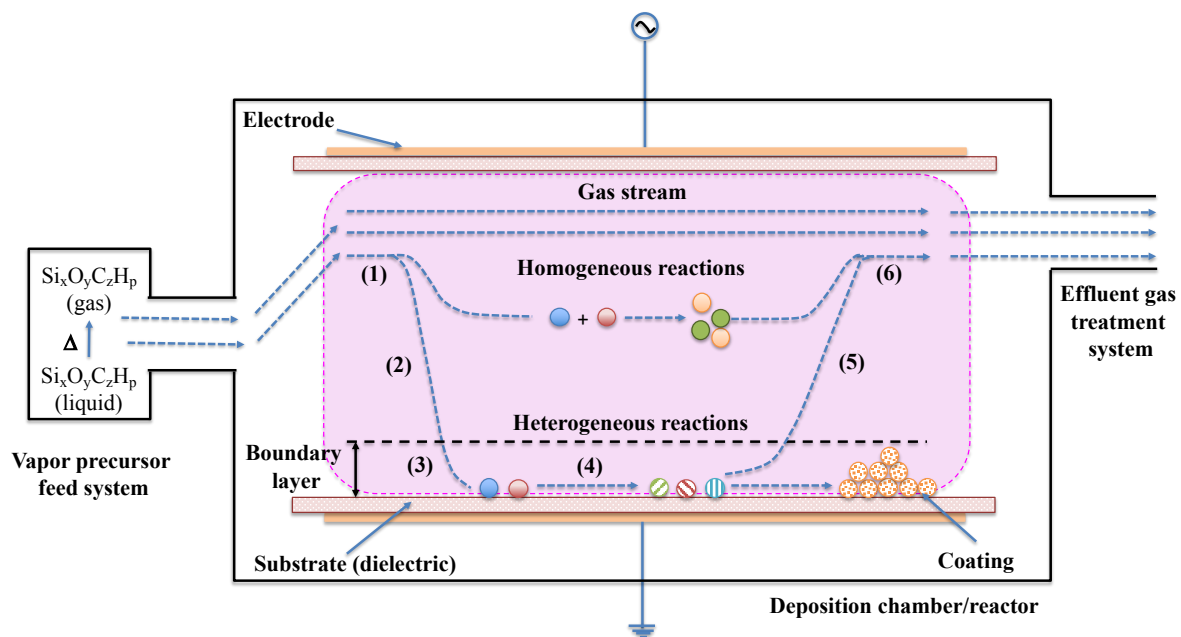
Figure 2.12: *Schematic of main processes involved in a CVD process. In bright purple: plasma generated by a DBD. (Adapted from ref. [399]).*

The CVD process comprises the following steps:

(1) The molecules of liquid precursor enter the reactor along with the carrier gas by forced convection, by diffusion, or under the action of electrostatic forces, once vaporized. On interaction with the plasma species (e.g., electrons, metastables), the precursor undergoes fragmentation producing molecular fragments, ions, radicals, and excited species. These species can react with each other either in the gas phase (homogeneous reactions) or on/with the surface (heterogeneous reactions). Gas-phase reactions can lead to the formation of large fragments, which can grow into powders.

(2) Diffusive and convective transport of reactants from the gas stream through the boundary layer to the substrate surface.

(3) Chemisorption (chemical or Langmuir adsorption) and physisorption (physical or van der Waals adsorption) of reactants on the substrate surface.

(4) Surface processes leading to the nucleation and growth of a coating, including diffusion to attachment sites (e.g., edges and kinks) and chemical decomposition of reactive species.

(5) Desorption of (volatile) by-products from the surface.

(6) Diffusive and convective transport of by-products away from the surface substrate through the boundary layer and back to the gas stream.

The use of a plasma source instead of heat (CVD) not only provides the energy required to generate the active species in the gas phase but also prevents thermal degradation of the substrate.

Table 2.1: *Elementary processes in active plasma environments. R: radical; S: surface; g: gas, f: fast, s: slow (Adapted from ref.* [349]).

Reaction	General equation	Example
Reactions with electrons		
Ionization	$e^- + A \rightarrow A^+ + 2e^-$	$e^- + N_2 \rightarrow N_2^+ + 2e^-$
Excitation	$e^- + A \rightarrow A^* + e^-$	$e^- + O_2 \rightarrow O_2^* + e^-$
Dissociation	$e^- + AB \rightarrow A + B + e^-$	$e^- + SiH_4 \rightarrow SiH_3 + H + e^-$
Dissociative ionization	$e^- + AB \rightarrow A^+ + B + 2e^-$	$e^- + TiCl_4 \rightarrow TiCl_3^+ + Cl + 2e^-$
Dissociative attachment	$e^- + AB \rightarrow A^- + B$	$e^- + SiCl_4 \rightarrow Cl^- + SiCl_3$
Three-body recombination	$e^- + A^+ + B \rightarrow A + B$	$e^- + H^+ + CH_4 \rightarrow H + CH_4$
Radiative recombination	$e^- + A^+ \rightarrow A + h\nu$	$e^- + Ar^+ \rightarrow Ar + h\nu$
Reactions between heavy species		
Charge exchange	$A^+ + B \rightarrow A + B^+$	$N_2^+(f) + N_2(s) \rightarrow N_2(f) + N_2^+(s)$
Penning ionization	$A^* + B \rightarrow A + B^+ + e^-$	$He^* + O_2 \rightarrow He + O_2^+ + e^-$
Ionization by interchange	$A^+ + BC \rightarrow AB^+ + C$	$N^+ + O_2 \rightarrow NO^+ + O$
Combination	$A + B \rightarrow AB$ $AB + CD \rightarrow AC + BD$	$2SiH_3 \rightarrow Si_2H_6$ $SiH_2 + O_2 \rightarrow SiO + H_2O$
Heterogeneous interactions (with surfaces)		
Adsorption	$R_g + S \rightarrow R_S$	$CH_2 + S \rightarrow (CH_2)_S$
Metastable deexcitation	$A^* + S \rightarrow A + S$	$N_2^* + S \rightarrow N_2 + S$
Sputtering	$A^+ + B_S \rightarrow A + B$	$Ar^+ + H_S \rightarrow Ar + H$
Secondary electron emission	$A^+ + S \rightarrow S + e^-$	$O^+ + S \rightarrow S + e^-$

As indicated in the **section 2.3.3**, due to the economic constraints imposed by low-pressure (LP) processing, considerable interest has been placed on the development of atmospheric pressure (AP) plasma sources for use in CVD. Even though AP-PECVD techniques have considerable advantages over LP-CVD ones, some features typical of atmospheric pressure processing must not be overlooked when designing coating equipment and selecting precursors [350,400]. These include:

- The inorganic or organometallic precursor is diluted in a carrier gas (e.g., N_2, He, Ne, Ar) at atmospheric pressure.

- Precursor (partial) pressures are higher at atmospheric pressure than at low pressure. This results in an increase in the rate of homogeneous reactions and, in many cases, in the formation of powders, which deposit on the substrate as the coating forms. Although higher precursor pressures are linked to higher coating growth rates, a rapid consumption of the precursor in the gas stream may translate to poor coating thickness uniformity.

- Because of the relatively high density of plasma species, three-body reactions, often neglected in low-pressure processes, become of great importance at atmospheric pressure.

- Collisional de-excitation of metastables atoms/molecules with the carrier gas atoms/molecules gains in importance. As a result, some radiative species, generally observed at low pressure, will not necessarily be observed at atmospheric pressure (e.g., H alpha).

- Ions do not possess kinetic energy when they reach the surface because of the low collisional mean free path ($\sim \mu$m) at atmospheric pressure. For this reason, physical etching (sputtering) is unlikely to occur.

- Mass transport limitations are comparatively more significant at atmospheric pressure. Diffusion is a relatively slow process compared to convection.

As mentioned above, atmospheric pressure DBDs in N_2 can be operated in two distinct regimes, namely homogeneous and filamentary. The suitability of HDBDs for the fabrication of coatings has been amply demonstrated; however, the use of FDBD for the same purpose is highly questionable because of the quality of the coatings. Indeed, coatings obtained using FDBDs are less dense and less homogeneous than those obtained using homogeneous DBDs (**Figure 2.13**).

Filamentary DBD   **Homogeneous DBD**

Highly localized energy
(short-lived micro-filaments, 10 ns and 100 μs)

Energy is homogeneously distributed
(discharge over the entire electrode surface, 100 ms)

High electron density (10^{14} cm^{-3})

Lower electron density ($< 10^{14}$ cm^{-3})

Rapid dissociation of the precursor

Slower dissociation of the precursor

High amount of radicals at the same time and at the same locations

Radicals are given more time to reach the surface

Production of powders

Production of dense coatings

Figure 2.13: *Influence of the discharge regime on the coating morphology. (+): anode, (-): cathode.*

2.7 Atmospheric pressure deposition of SiO$_x$C$_y$:H coatings from siloxane precursors: Focus on 1,3,5,7-tetramethylcyclotetrasiloxane

The application of plasma technology for coating deposition, almost always at low pressure, has witnessed the use of several siloxane precursors including the 1,3,5,7-tetramethylcyclotetrasiloxane (TMCTS). Coinciding with the development of the microelectronics industry in the 1990's, the TMCTS was used for the fabrication of high-quality SiO$_2$ layers and Al/SiO$_2$ interconnects for integrated circuits and waveguides. With the advent of device miniaturization in the 2000's, the TMCTS was used for fabrication of SiO$_2$ coatings with low dielectric constant or "low-K" coatings. Currently, the application of TMCTS for the manufacture of SiO$_2$-like coatings continues to be in the early stages of its development, most likely due to the reluctance of research groups to use siloxane precursors other than those employed thus far for that purpose, such as hexamethyldisiloxane (HMDSO), tetraethoxysilane (TEOS), and silane (SiH$_4$).

Surprisingly, the use of TMCTS for the fabrication of anti-fogging coatings by atmospheric pressure PECVP has not been explored, despite the interesting results reported by Ward et al. [401]. These authors deposited SiO$_x$C$_y$:H coatings from TMCTS and octamethylcyclotetrasiloxane (OMCTS) using a He plasma in the presence or absence of O$_2$ (oxidant) at atmospheric pressure. When O$_2$ was added, coatings were wettable (hydrophilic) because of silanol groups at the coating surface. The presence of hydrophilic groups at the surface is *a sine qua non* for most of the anti-fogging coatings prepared thus far to minimize the effects of fogging [402]. An overview of the experimental conditions used in the deposition of TMCTS coatings by low-pressure or atmospheric pressure plasmas is shown in **Table 2.2**. Interestingly, coatings deposited from TMCTS (or other precursors) at low pressure do not possess silanols (i.e., Si-OH). However, at atmospheric pressure, silanol groups appear only in TMCTS-based coatings, suggesting that the combination of TMCTS with atmospheric pressure plasma deposition is a necessary condition to prepare anti-fogging coatings.

Table 2.2: *Deposition conditions for TMCTS and other siloxane precursors at low and atmospheric pressure.*

Experimental conditions	Precursor/oxidant/ carrier gas	Coating	Substrate	Purpose	Si-OH (930 cm^{-1})	Ref.
ECR-CVD **10–50 mTorr** **2.45 GHz/13.56 MHz** **400–1000 W**	TEOS/TMCTS (1–20 sccm) O_2 (0–48 sccm)	HQ SiO_2	Al	Electronic interconnections	No	[403]
ECR-CVD **13-53 mTorr** **2.45 GHz/13.56 MHz**	TMCTS (6.5–21 sccm) O_2 (42–64 sccm)/Ar	HQ SiO_2	Al	Electronic interconnections	No	[404]
ECR-CVD **900–1800 mTorr** **13.56 MHz/100 W**	SiH_4/TMCTS (1/50) O_2 (20–54.4 sccm)/N_2	HQ SiO_2	Al	Electronic interconnections/ waveguides	No	[405]
ECR-CVD **mTorr?/13.56 MHz** **400–1000 W**	TMCTS/He + CH_n (porogen)	SiO_xC_y:H	Si (100)	Electronic interconnections (low-k coating)	No	[406]
ECR-CVD **5–15 mTorr/900 W** **2.45 GHz/13.56 MHz**	OMCTS/TMCTS/HMDSO (50/50/100 sccm) O_2 (100–400 sccm)	HQ SiO_2	Si (100)/ Stainless steel	Electronic interconnections	-	[407]
RF-PECVD **3–3.8 Torr** **250–700 W**	TMCTS (0.5–4 sccm) CO_2 (3000–5000 sccm)	SiO_xC_y:H	Si (100)	Electronic interconnections (low-k coating)	No	[408]
RF-PECVD **2–6 Torr/400°C** **0–800W (LFRF)** **200–60 W (HFRF)**	3MS/TMCTS (500 sccm) O_2 (0–500 sccm) CO_2 (1000–18000 sccm) He (0–4000 sccm)	SiO_xC_y:H	Si (100)	Electronic interconnections (low-k coating)	No	[409]
LFRF-PECVD **266–600 Pa** **400–800 W**	TMCTS CO_2 ($1.67.10^{-5}$–3.10^{-4} m^3/s) O_2 (0–$8.35.10^{-6}$ m^3/s)	SiO_xC_y:H	Si (100)	Electronic interconnections (low-k coating)	No	[410]

Table 2.3: *Continuation*

Experimental conditions	Precursor/oxidant/ carrier gas	Coating	Substrate	Purpose	Si-OH (930 cm^{-1})	Ref.
RF-PECVD 100 mTorr/20–150 W 373–573 K	TMCTS/DMDMOS/3MS N$_2$O, O$_2$ Precursor/oxidant = 0–30	SiO$_x$C$_y$:H	Si (100)/ KBr	Electronic interconnections (low-k coating)	Weak FTIR signal	[411]
RF-PECVD 500 mTorr 15 W/180°C	TMCTS + CPO/BMO (porogens)	SiO$_x$C$_y$:H	Si (100)	Low-k coating	No	[412]
RF-PECVD 500 mTorr/13.56 MHz 83 W/180°C	TMCTS (84 sccm) + Drug (Daunomycin, Rapamycin, NPC-15199)	SiO$_x$C$_y$:H	Stainless steel (316 L)	Drug-eluting coating	-	[413]
PECVD 760 Torr 350–450°C	TMCTS (1 sccm) O$_3$ (0.2–4%)/N$_2$ (1 sccm)	HQ SiO$_2$	Si (100)/ SiO$_2$	Electronic interconnections	-	[414]
APGD-PECVD 1020 mbar/15 kHz 350–450°C	OMCTS/TMCTS O$_2$ (1%)/He (1900 sccm)	SiO$_x$C$_y$:H	PE	Gas barrier coating (O$_2$ blocking)	No/(OMCTS) Yes/(TMCTS)	[401]
APGD-PECVD 1 atm/27.12 MHz 100 W/25°C	HMDSN/HMDSO/ TMDSO/TMCTS/TEOS O$_2$ (2%)/He	SiO$_x$C$_y$:H	Si (100)	-	Yes (TMCTS)	[415]
APGD-PECVD 1 atm/27.12 MHz 250 W/120°C	TMCTS+TEOFS/ O$_2$ (2%)/He	SiF$_x$O$_y$C$_z$:H	Si (100)	Fiber optics/waveguides	Non	[416]
APGD-PECVD 1 atm/13.56 MHz 60–80W/120°C	TEOS/TMCTS/BTESE O$_2$ (0.35–0.5 L/min) He (30 L/min)	HQ SiO$_2$	Si, PC, and PMMA	Hard coating (scratch-resistant)	Non	[417]

BTESE: Bis(triethoxysilyl)ethane, BMO: Butadiene monoxide, CPO: Cyclopenteneoxide, DMDMOS: Dimethyldimethoxysilane, ECR-CVD: Electron Cyclotron Resonance Chemical Vapor Deposition. LFRF-HFRF: Low-frequency & high-frequency radiofrequency, HQ: High-quality, HMDSN: Hexamethyldisilazane, TEOFS: Tetraethoxyfluorosilane, 3MS: Trimethylsilane.

3 Characterization techniques of anti-fogging coatings

In this chapter, the techniques used for the characterization of anti-fogging coatings are briefly described to provide the reader with an essential background. The experimental details are discussed in the following chapters.

3.1 Chemical characterization

3.1.1 Attenuated total reflectance Fourier transform infrared spectroscopy (ATR-FTIR)

Fourier transform infrared (FTIR) spectroscopy is an analysis technique that uses infrared (IR) light to identify molecular structures, chemical bonding, and functional groups in solid, liquid, and gaseous samples [418–421]. Infrared light, also known as "infrared radiation", covers the region of the electromagnetic spectrum between the visible (~ 760 nm, red light) and the microwave (~ 1 mm). The infrared range is often subdivided, in relation to the visible range, into three spectral regions, namely near-IR (14000–4000 cm^{-1}), mid-IR (4000–400 cm^{-1}), and far-IR (400–30 cm^{-1}). When a sample is illuminated with IR light, a part of the radiation is transmitted while the other is absorbed by the "vibrating bonds" of the sample. Given that each bond vibrates at specific frequencies, the use of IR light allows for the qualitative and quantitative analysis of any material, including coatings and biological samples. From a formal point of view, two conditions must be met simultaneously for a vibration to occur in the IR spectrum [422]. First, the electric dipole moment must change during the vibration, that is:

$$\frac{d\boldsymbol{\mu}}{dq} \neq 0 \tag{3.1}$$

where $d\mu$ is the change in dipole moment and dq is the change in bond length or bond angle.

Vibrations satisfying **Equation 3.1** are said to be IR active. In the mid-IR region, chemical bonds can vibrate in several modes (**Figure 3.1**). Vibrational modes can lead to changes either in bond lengths or in bond angles, i.e., stretching and bending vibrations, respectively. Stretching vibrations can be symmetric (ν_s) and asymmetric (ν_a). For bending vibrations, there are four modes: scissoring (δ_s), rocking (ρ), wagging (ω), and twisting (τ). The first two bending vibrations are "in-plane" modes and the other two are "out-of-plane" modes.

STRETCHING VIBRATIONS

Symmetric, ν_s Asymmetric, ν_{as}

BENDING VIBRATIONS

In-plane

Scissoring, δ_s Rocking, ρ

Out-of-plane

Wagging, ω Twisting, τ
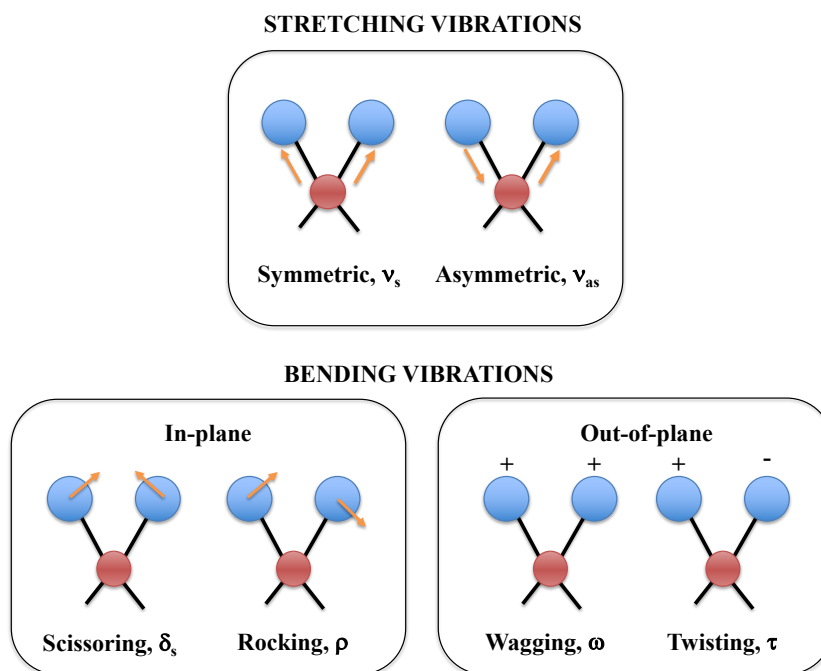
Figure 3.1: *Vibrational modes in IR spectroscopy.*

Second, the energy of the incident IR light (photon) must be equal to the difference between two vibrational energy levels. The frequencies at which a molecule absorbs are governed by the same equation as for a classical harmonic oscillator:

$$\tilde{\nu} = \frac{1}{2\pi c}\sqrt{\frac{k(m_1 + m_2)}{m_1 \cdot m_2}} \qquad (3.2)$$

where $\tilde{v}$ is the frequency at which a specific vibration occurs, c is the speed of light (2.99792×10^8 m s^{-1}), k is the force constant (N m^{-1}) of the vibrating bond, and m_1 and m_2 are the masses (kg) of the two atoms involved in the vibration.

The portion of the IR light passing through the sample under study is examined by a spectrometer, a device that decodes the chemical information contained in it to produce a spectrum. The IR spectrometer used in the study of anti-fogging coatings houses two key components, namely a Michelson interferometer and an attenuated total reflectance (ATR) accessory. The ATR accessory is placed in the sample compartment (**Figure 3.2a**).
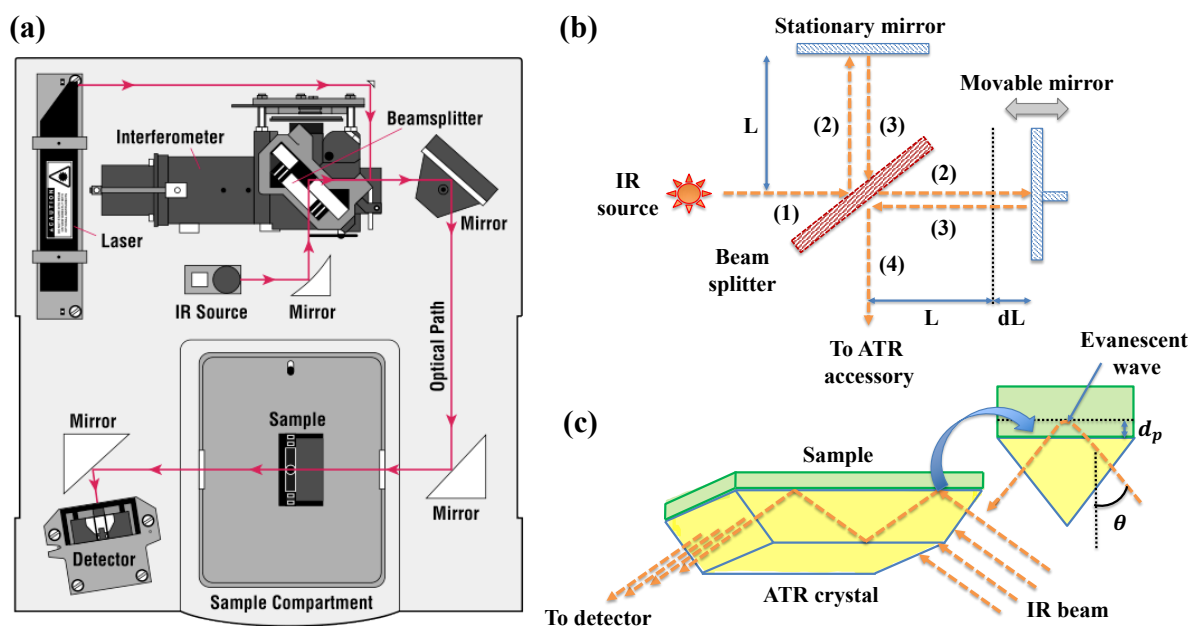
Figure 3.2: *(a) FTIR spectrometer layout*, (b) working principle of an interferometer, and (c) ATR crystal. (*http://mmrc.caltech.edu/FTIR/Literature/General/FTIRintro.pdf).*

An interferometer consists of a beam splitter and two perpendicular plane mirrors, one of which moves back and forth a distance dL and the other is stationary (**Figure 3.2b**). The distance dL is measured with high accuracy using a He-Ne laser [423]. The beam splitter is an optical element that allows for 50% of the incident IR light to travel toward the fixed mirror while reflecting the rest to the movable mirror (points 1 and 2). Beams leaving the beam splitter are reflected back from the stationary and movable mirrors, after travelling a

distance of 2L and 2(L + dL), respectively (point 3), so that they reach the beam splitter with an optical path difference OPD (or optical retardation) of 2dL. Depending on the wavelength and the optical path difference, waves composing the beams combine by constructive and destructive interference and then pass through an ATR accessory (point 4). The IR beam is focused at a certain angle θ, on the edge of an internal reflection element or ATR crystal, which is in close contact with the sample (**Figure 3.2c**). Because of the low refractive index of the sample compared to that of the crystal, the infrared beam is totally reflected when it reaches the crystal/sample interface. This physical phenomenon, called "total internal reflection", occurs if the angle of incidence θ exceeds a certain limiting angle or "critical angle" θ_c, which be calculated as follows [424]:

$$\theta_c = sin^{-1}\left(\frac{n_2}{n_1}\right) \tag{3.3}$$

where n_1 and n_2 are the refractive indices of the crystal and the sample, respectively.

Under conditions of total internal reflection, a part of the IR beam penetrates the sample as an evanescent wave ("Goos-Hänchen effect" [425]), thus being partially absorbed by the IR active vibrations (upper part of **Figure 3.2c**). The evanescence wave is said to be attenuated, hence the appellation "attenuated total reflectance" for this IR technique. The evanescent wave extends into the sample a distance known as "depth of penetration" d_p, which is defined as the distance from the sample/crystal interface in which the intensity of the evanescent wave decreases to approximately 63%. The depth of penetration is given by the Harrick equation [426]:

$$d_p = \frac{\lambda}{2\pi n_1 \sqrt{sin^2\theta - (n_2/n_1)^2}} \tag{3.4}$$

where λ is the wavelength of the incident light (nm), n_1 and n_2 are the refractive indices of the crystal and the sample, respectively; and θ is the angle of incidence of the IR beam with respect to the normal of the crystal surface.

It can be inferred from **Equation 3.4** that the evanescent wave penetrates the sample to a greater or lesser extent depending on the values of the tetrad λ, θ, n_1, and n_2. This feature makes the ATR technique suitable for the analysis of thick or strongly absorbing samples [427,428]. For the most common ATR crystals (e.g., Ge, Si, CdTe, ZnSe, ZnS, ZrO_2, Al_2O_3, diamond), the depth of penetration ranges from 0.5 to 5 µm [429–431]. After one or more internal reflections, the IR beam leaving the ATR crystal is focused onto the detector. The detector collects and digitizes the intensity of the infrared light as a function of the time (OPD) for all frequencies, thereby constructing an interferogram. The mathematical function known as "discrete Fourier transform" (DFT) makes it possible to extract the component "frequency" from the interferogram to produce an interpretable IR spectrum, such as those shown in the **chapters 4**, **5**, and **6**.

3.1.2 X-ray photoelectron spectroscopy (XPS)

X-ray photoelectron spectroscopy (XPS), also known as "Electron Spectroscopy for Chemical Analysis" (ESCA), is a high-sensitive surface analysis technique used since the late 1970s for the chemical characterization of a wide variety of surfaces, thin films, and interfaces. The physical principle behind the XPS technique is the photoelectric effect, phenomenon by which electrons are emitted from a surface on exposure to light. Although somewhat sophisticated and expensive, XPS instrumentation is relatively simple to use. Briefly, a solid sample is introduced into a chamber, which is then pumped down to ultra-high vacuum (UHV, $< 10^{-8}$ mbar). Afterwards, the sample is irradiated with low-energy, monochromatic X-rays coming from a metal anode. Typically, commercial XPS systems are equipped with aluminium (K_α 1486.6 eV) and magnesium anodes (K_α 1253.6 eV) as X-ray sources (**Figure 3.3a**). Soft X-rays cause the emission of photoelectrons and Auger electrons

from the core and valence levels of the atoms composing the sample (**Figures 3.3b** and **3.3c**) [432].
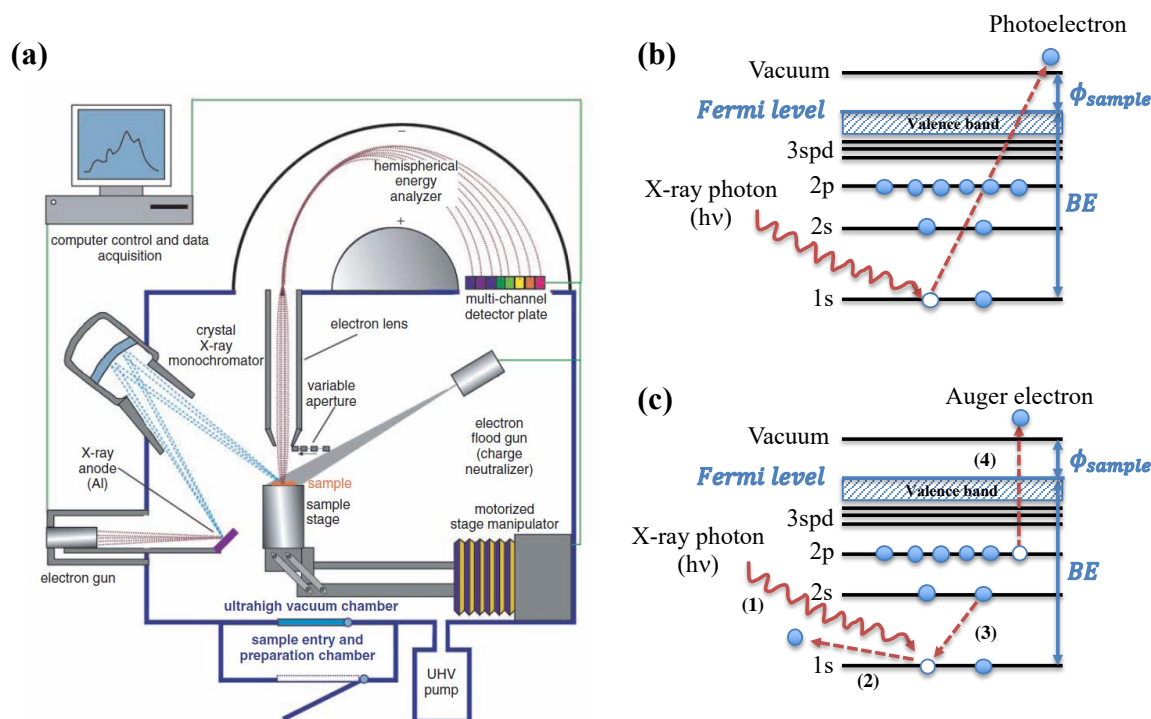
Figure 3.3: *(a) XPS instrumentation* [433]. *(b) Emission of photoelectrons and (c) Auger electrons. Auger process involves four sequential steps: (1) absorption of a X-ray photon by a core electron (e.g., 1s or K electron), (2) emission of a core electron leaving a hole in the shell, (3) a second electron from an outer shell (e.g., 2s or L_1 level) fills in the hole (4) with simultaneous emission of an outer electron (e.g., 2p electron). The result is a three-electron process that results in a doubly ionized atom. Spectroscopic notation of this Auger electron is $KL_1L_{2,3}$ or KLL.*

According to Berglund and Spicer [434], the emission of photoelectrons can be explained as follows. A core electron is excited from its ground state to a higher energy state on absorption of X-ray photon. The excited electron travels through the material without undergoing inelastic scattering, until it reaches the surface, from which is ejected into the vacuum. For photoelectron emission to occur, it basically requires that the energy gained by the electron after absorption of an X-ray photon be higher than the work function of the sample, ϕ_{sample}. Given that the total energy is conserved in the process, the binding energy BE, that is, the energy required to eject a core electron from the atom can be expressed, as follows:

$$BE = h\nu - KE - \phi_{spec} \qquad (3.5)$$

where $h\nu$ (eV) is the energy of the incident X-ray photon, KE (eV) is the kinetic energy of the photoemitted electron which is measured by the energy analyzer, and ϕ_{spec} is the work function of the spectrometer (eV). Note that binding energies are referred to the Fermi level of the sample (**Figures 3.3b and 3.3c**).

According to **Equation 3.5**, it is possible to determine the binding energy of a specific core level by measuring the kinetic energy of its corresponding photoemitted electron ($h\nu$ and ϕ_{spec} are known beforehand). The term ϕ_{spec} is the work required to bring an electron from the sample (vacuum level) to the entrance of the energy analyzer and can be determined by calibrating the spectrometer with a standard reference material, such as gold ($4f_{7/2}$ peak at 84.0 eV) or copper ($2p_{3/2}$ peak at 932.5 eV) [435]. Further details on the instrument calibration procedure can be found in the ASTM E2108 standard [436].
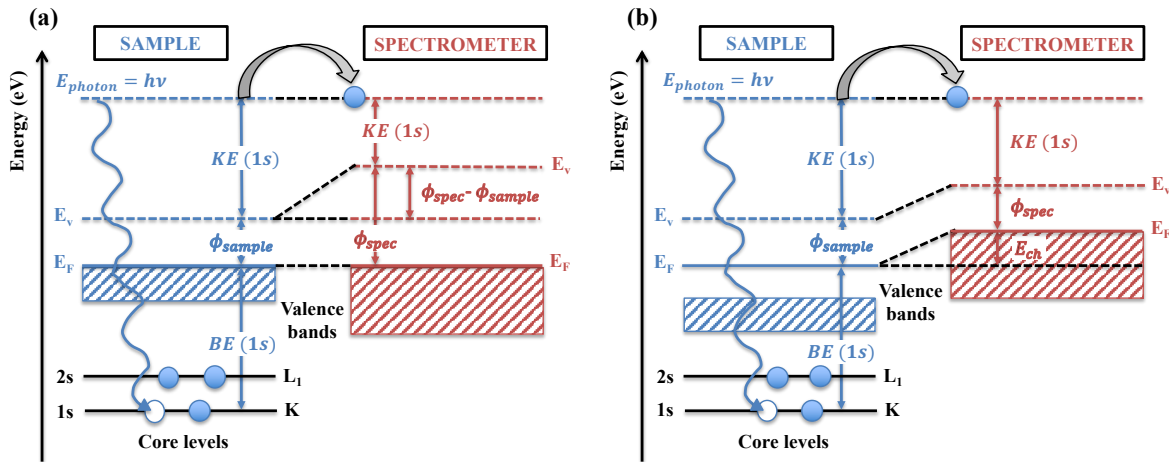
Figure 3.4: *Sample/spectrometer energy level diagram for (a) conductive and (b) insulating samples. In conductive samples, the Fermi level (E_F) of the sample and that of the spectrometer are aligned because of the ohmic contact between them. A potential "E_{ch}" appearing in insulating samples in response to a surface charging phenomenon causes the Fermi level of the spectrometer to raise with respect to that of the sample. (E_V = Energy level of vacuum, E_F = Fermi level, ϕ_{sample} = Work function of the sample, $\phi_{spectrometer}$ = Work function of the spectrometer).*

Given that each ejected core electron has a unique binding energy (BE), XPS allows for the identification of all elements (excluding H and He) with detection limits between 0.005 and 1.0 at.%. Further to this, binding energies are very sensitive to the chemical environment of the element being analyzed. Indeed, when the same atom is attached to different chemical species, shifts in binding energies of up to 10 eV can be observed [437]. This effect is referred to in the literature as the "chemical shift". Thus, in addition to the wide elemental coverage, XPS provides information on the surface chemistry as essential as valence states and bonding environments. In general, binding energies shift to high energies as the oxidation state of the element increases. For example, the C1s binding energy increases with the number of oxygen atoms bonded to the carbon atom, namely, $BE_{C-C} < BE_{C-O} < BE_{C=O} < BE_{O-C=O} < BE_{O-(C=O)-O}$.

In the case of insulating samples, the emission of photoelectrons leaves the surface positively charged. As a result, the surface acquires a positive potential E_{ch} that cause misalignment of Fermi levels of the sample and spectrometer (**Figure 3.4b**). If not counteracted, surface charging results in distorted XPS peaks appearing at binding energies higher than those predicted by **Equation 3.5**. Using an internal reference such as the adventitious carbon contamination on the sample (C-H/C-C component of the C 1s spectrum is set at 285.0 eV), coating the sample with a thin layer of gold, neutralizing surface charge by an electron beam, or isolating electrically the sample from the specimen holder are among the well-proven methods to minimize charging effects [438].

In XPS, operating under ultra-high vacuum (UHV) is key to performing a successful surface analysis, for two main reasons. First, remnant gases such as CO_2 or water vapor are less likely to cover the sample, and therefore contribute to the XPS spectrum. That said, most samples are covered with a few monolayers of adventitious carbon, coming from the vacuum system (vacuum pump oils) or from airborne hydrocarbons. Second, UHV operation enables electrons to reach the energy analyzer without being inelastically scattered, that is, with unaltered kinetic energy. Electrons coming from a sampling depth between 3 and 10 nm, retain their original kinetic energy and therefore are responsible for recognizable XPS peaks. In contrast, inelastically scattered electrons contribute to the background. This explain why XPS is a surface sensitive technique.

A typical XPS spectrum covers a range of several hundreds of eV (wide scan or survey spectrum) and consists of a series of photoelectron peaks. XPS spectra are usually given by intensity (counts or counts per second, cps) as a function of the binding energy (eV), although kinetic energy can be plotted instead. Following calibration for charging compensation and background subtraction, survey scan spectrum enables us to conduct a semi-quantitative analysis of the sample. To this end, the intensity of the photoelectron peaks is assumed to be proportional to the number of atoms of a given element in the surface. The atomic concentration of an element in the surface can be estimated, as follows [439]:

$$ C_i = \frac{I_i/\phi_i}{\sum_k I_k/\phi_k} \tag{3.6} $$

where C_i is the atomic concentration of the i-th element (at.%), I_i is the signal intensity due to any elemental constituent of the sample, and ϕ_i is the sensitivity factor for the element i.

In addition to photoelectron peaks, other not less important spectral features, such as Auger peaks, satellites (shake-up and shake-off peaks), plasmon loss peaks, and valence band peaks can also appear in an XPS survey spectrum. As in the case of photoelectron peaks, these features provide information on the elemental composition, even though their interpretation is more complex. Further details on each element can be obtained from the narrow scan or high resolution XPS spectrum (HRXPS) of photoelectron peaks found in the survey spectrum. The shape of each peak and the binding energy at which they occur can vary depending on chemical state of the emitting atom; hence HRXPS analysis makes it possible to distinguish atoms with different oxidation states and/or bonding environments.

3.2 Surface characterization

3.2.1 Atomic force microscopy (AFM)

The atomic force microscopy (AFM) is a surface characterization technique belonging to the family of the so-called "scanning probe microscopies" (SPM) [440]. The AFM employs a

flexible cantilever to measure the interaction forces between the tip and the sample and thus generate a 3D profile of the surface on the nanoscale.

A standard AFM instrument consists of a flexible cantilever (100–500 μm in length) with a sharp tip (probe), a laser, a 4-quadrant photodiode detector (2-quadrant photodiode detectors are also possible), a piezoelectric scanner, and the feedback and measurement electronics (**Figure 3.5**). Probes are generally made of silicon or silicon nitride, although other materials such as diamond or quartz can also be used. Probes are 3–15 μm in length with tip radii < 15 nm [441,442].
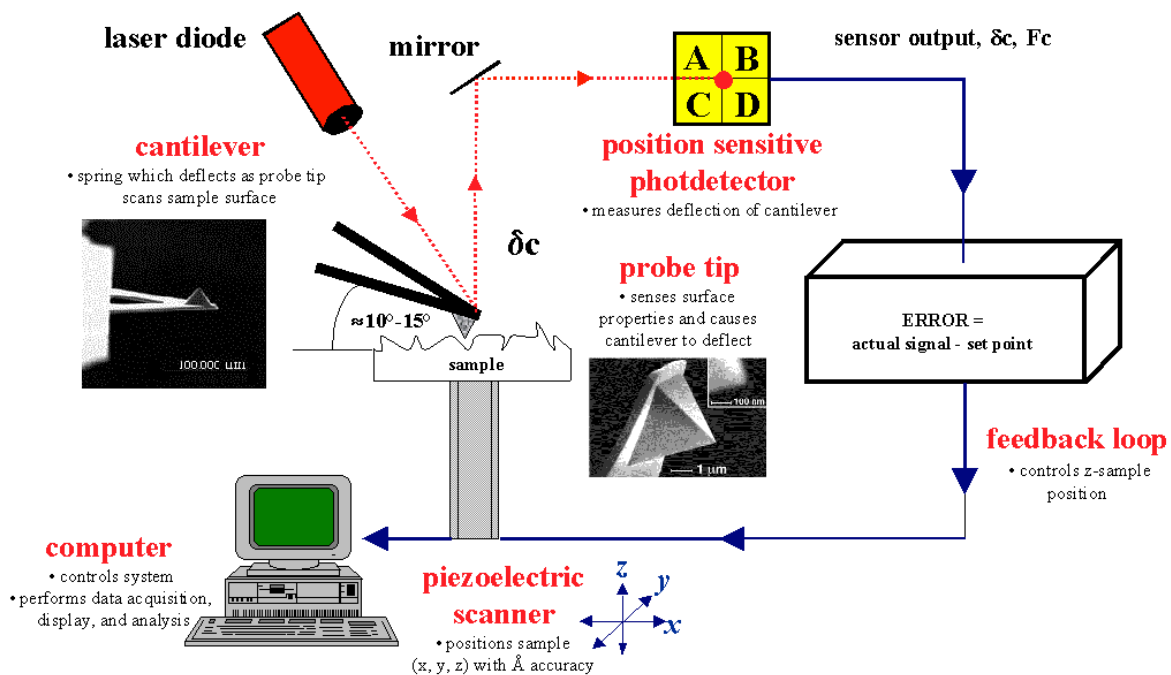
Figure 3.5: *AFM instrumentation. (Image from http://web.mit.edu/cortiz/www/afm.gif).*

Generally, the sample under study is placed on a scanner containing a piezoelectric material, which controls the movement of the sample along with a feedback loop. A piezoelectric material changes its physical dimensions in response to an applied voltage (inverse piezoelectric effect). When constructed in a hollow cylindrical shape, the piezoelectric moves the sample laterally in the x-y plane with a resolution ranging from 0.1 to 1.0 nm and in the z-axis with atomic resolution.

Sample scanning causes the cantilever to bend as a result of the forces exerted on the tip. Deflections of the cantilever are detected by measuring the position of a reflected laser beam on the different segments of the photodiode (**Figure 3.5**). A 4-quadrant photodiode detector measures lateral and vertical forces, while a 2-quadrant photodiode detector only measures vertical forces. The as-measured cantilever deflections are used to generate an image of the surface topography without causing any (significant) damage to the sample [443].

During sample scanning, the force between the tip and the sample varies depending on the spring constant of the cantilever and the surface-probe distance. According to Hooke's Law, this force can be calculated as follows:

$$F_c = -k \cdot \delta_c \tag{3.7}$$

where F_c is the force tip/sample (N), k is the spring constant (N m^{-1}), and δ_c is the cantilever deflection (m).

Forces acting between the tip and the sample surface include van der Waals forces, coulombic, capillary, and adhesive forces, among others. Among these, van der Waals interactions (short-range interactions) contribute most to the movement of the cantilever. Depending on the magnitude of the van der Waals forces, AFM can operate in three different modes, namely, contact mode, tapping mode, and non-contact mode [444].

Contact Mode: Repulsive van der Waals forces are measured in this operation mode. Here, the tip comes into contact with the sample and moves with a specific height (the deflection of the cantilever varies) or under a constant force (cantilever deflection is kept constant). The first mode is used to scan flat samples while the second is used to image samples with protruding surface features. The small distances between the probe and the surface (< 0.5 nm) allow for the analysis of frictional behavior of the sample. However, due attention must be given to soft samples, as frictional forces can cause surface damage.

Tapping Mode: In this operating mode, the cantilever oscillates up and down at or slightly below its resonance frequency. This mode is less destructive than the contact mode, as the tip contacts the surface intermittently (this eliminates the frictional forces). Surface imaging is performed by maintaining constant the oscillation amplitude, i.e., the tip-sample interaction remains unchanged. This operational mode was used in this study.

Non-Contact Mode: The spacing between the tip and the sample is on the order of tens to hundreds of angstroms. A very stiff cantilever oscillates above the sample surface with small amplitudes at a frequency greater than its resonance frequency. Using a feedback loop to monitor the changes in the amplitude due to attractive van der Waals forces, a high-resolution 3D image of surface topography can be obtained. Quite often, this AFM mode requires ultra-high vacuum to achieve best imaging [443].

Further to surface imaging, atomic force microscopy allows for the quantitative assessment of surface roughness. In this regard, it is standard practice to measure the so-called "roughness parameters" to provide a more complete description of the surface under study. In this work, two roughness parameters, namely the arithmetic average height (R_a) and the root mean square roughness (R_{rms} o R_q) were measured (**Figure 3.6**). These amplitude parameters refer to variations of the surface features in the z-axis (variations in height) with respect to a reference line (or reference plane).

The arithmetic average height (R_a), also known as "center-line average" (CLA), is defined as the average absolute deviation of the roughness irregularities from the mean line along the sampling length l. In mathematical form [445,446]:

$$R_a = \frac{1}{l} \int_0^l |Z(x)| dx \qquad (3.8)$$

The root mean square roughness (R_{rms}) is the square root of the mean of the square of the vertical deviations from the mean line; in other words, is the standard deviation of the

distribution of surface heights. This parameter is more sensitive than R_a to large deviations from the mean line. In mathematical form [446,447]:

$$R_{rms} = \sqrt{\frac{1}{l}\int_0^l Z^2(x)dx} \qquad (3.9)$$
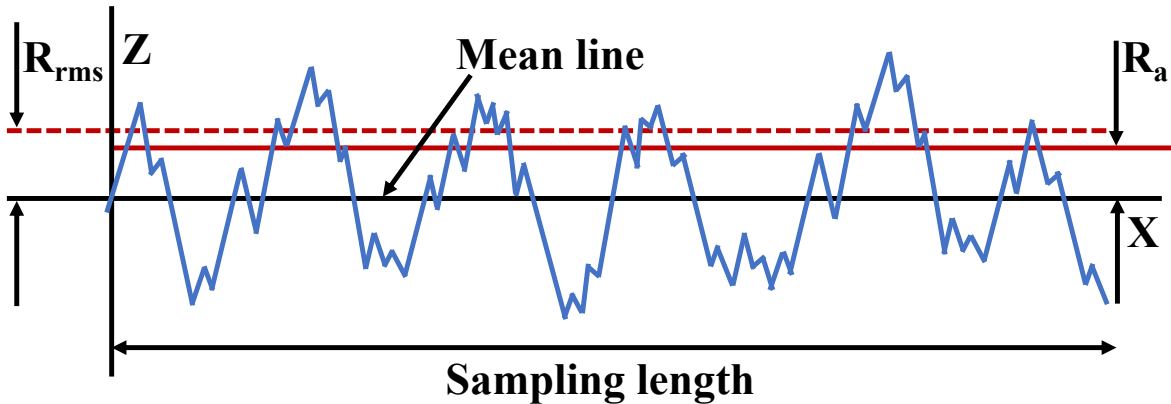
Figure 3.6: *Schematic of a surface profile Z(x). Note that $R_{rms} > R_a$.*

3.3   Assessment of the deposition rate

3.3.1 Stylus profilometry

A stylus profilometer allows for the measurement of surface roughness on a micrometric scale. The principle of operation is relatively simple. Briefly, a sharp tip in contact with the surface under study (stylus load = 0.05–100 mg) is displaced across the surface, moving at a constant speed between 1 μm s^{-1} and 25 mm s^{-1} (**Figure 3.7**). The scanned lengths can be as long as 200 mm while the scanned areas can be as large as 5 × 5 mm^2 [445]. Vertical motions of the stylus (i.e., variations in z coordinate) are converted into electrical signals using a linear variable differential transformer (LVDT) or an optical or a capacitance sensor. Afterwards, the electrical signals are amplified and digitally converted for analysis by imaging software. Three-dimensional images of the surface topography can be obtained, with a vertical resolution as low as 0.1 nm for smooth surfaces and as low as 1 nm for rough

surfaces [448]. That said, the vertical range typically can go from 2 to 250 µm, making it possible to determine the deposition rate of coatings of several tens of microns thick.
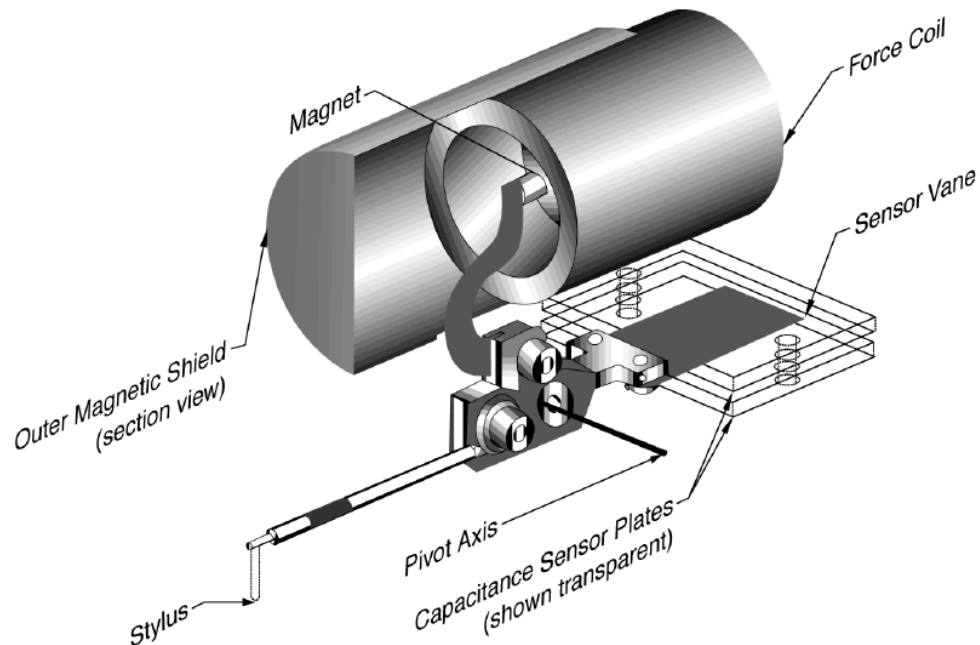
Figure 3.7: *Schematics of a stylus profilometer head with loading system and scan mechanism used in Veeco/Sloan Dektak profilers [445].*

The stylus tip is usually made of diamond, even though other materials such as Al_2O_3 (ruby and sapphire) and Si_3N_4 (silicon nitride) can also be employed. Most tips are cone-shaped with included angles between 60 and 90° and radii of curvature of 2, 5, or 10 µm (ISO 3274-1975). The lateral resolution of this technique is of the order of the square root of the tip radius [445].

3.4 Assessment of wetting behavior

Wettability is the property illustrating the degree of affinity between a liquid and a solid surface, while the contact angle is the parameter that makes it possible to quantify this concept. In general, it can be said that surface chemistry determines surface tension γ, and therefore the wettability in a strict sense, while surface roughness allows for its modification, to a certain extent. As discussed in length in **section 1.4**, several theories have been proposed

to explain the wettability of solid surfaces, considering both parameters in a straightforward way. Indeed, to control the wettability and thus the anti-fogging property, surface roughness and surface chemistry must both be properly adjusted [402].

Methods as diverse as the drop sessile method, the captive bubble method, the tensiometric (Wilhelmy balance) method, the tilting plate method, or the capillary bridge method, have been thus far developed to measure contact angles [449]. Among these, the drop sessile method is likely one of the most frequently used, as it allows for the measurement of contact angles in a straightforward way. Here, the contact angle that appears between the surface and the tangent to the point where solid, liquid, and gas phases meet is measured using a setup such as the one depicted in **Figure 3.8a**.
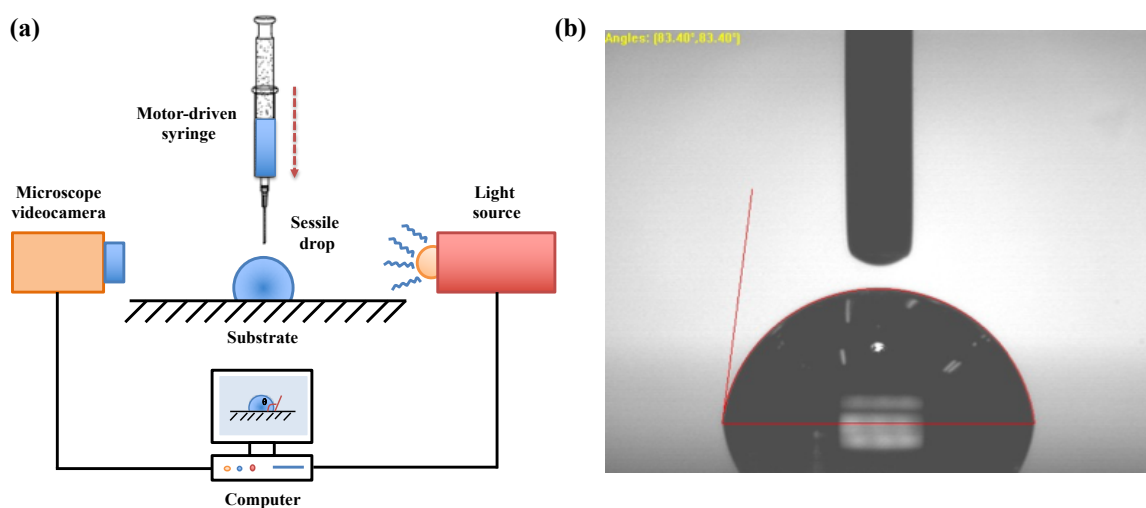
Figure 3.8: *(a) Schematic setup used in this doctoral project to measure contact angles. (b) Photograph of a sessile drop lying on clean glass showing the tangent line at the three-phase point, the base line, and the outer contour of the drop.*

The equipment used to measure contact angles consists of a horizontal platform where the coated glass under study is placed, a motor-driven syringe, a light source, and a video camera. The video camera enables us to photograph the water drops and the motor-driven syringe enables us to control rate at which water drops are dropped on the coating. Following the pinning of the three-phase contact line, the image of the droplet is captured and analyzed by a computer software. To determine the water contact angles, grey scale values are adjusted

to trace the so-called "base line", i.e., contact line between droplet and the surface, and the outer contour of the drop (**Figure 3.8b**). The tangent at the triple-phase point and the base line delimit two contact angles, one on the right side of the droplet and the other on the left side. The value mean of these two angles is used to characterize each drop.

When selecting a method to determine contact angles, two aspects must be kept in mind, namely, advantages and disadvantages of the method and the factors influencing the experimental determination of contact angles (**Table 3.1**).

Table 3.1: *Advantages and disadvantages of the sessile drop method.*

Advantages	Disadvantages	References
Simple, easy handling, and visual clarity	Two contact angle values per drop	[449–452]
It is possible to measure samples with small surface areas	Measurements at multiple locations when collecting information from a large area is time-consuming	[450]
Small amount of water required (~ µL)	Droplet evaporation may distort contact angles	[449–451]
Suitable for heterogenous surfaces	The needle may distort the droplet shape (especially in surfaces with high hysteresis)	[449,451]
Measurements under extreme temperature and pressure conditions	The placement of base line in non-reflective and extreme wettable surfaces is challenging	[449,452]
Image analysis software reduces subjectivity when determining contact angles	Susceptible to operator error if a strict protocol is not followed	[449,450]

Factors such as the roughness and chemical heterogeneity of the surface, the presence of impurities on the surface, drop volume, time after drop deposition, temperature, mechanical vibration, and liquid reactivity have been reported to affect contact angles. Undoubtedly, controlling these parameters simultaneously is a challenging task. Despite this, the sessile drop method is considered the method of choice if high accuracy in contact angle

measurements is not required—standard deviations ranging from < 0.5 to $5°$ are usually reported in literature [453,454].

3.5   Assessment of the anti-fogging performance

A slightly modified setup compared to the ASTM F 659-06 setup [332,333] or its equivalent European version BS EN 168 [334] (**Figure 3.9a**) was used to assess the resistance to fogging of coated glasses (**Figure 3.9b**). Briefly, 590-nm light coming from a LED (point 1) is directed through an iris diaphragm (point 2). Light reaches the sample after being reflected from a 45-degree mirror and passed through a 50:50 beam splitter (points 3 and 4). The sample is placed on a 1×1 cm^2 aperture made in a polymer plate covering a bath containing water at $50.0 \pm 0.5°C$ (point 5). Perpendicular incident light is reflected back to the sample from a mirror placed inside the bath and then directed from the 50:50 beam splitter to a converging lens (point 6). A silicon photodiode placed in front of the converging lens (point 7) converts light into an electrical current, which is then converted into transmittance values. A sliding mirror door isolates the sample from the water bath, thus making it possible to measure the light transmitted through the sample before exposure to water vapor.

The protocol described in the ASTM F 659-06 standard requires us to prepare the samples. Before testing, coated glasses were immersed in distilled water at $23 \pm 5°C$ for 1 h and dried thereafter at room temperature for ≥ 12 h. For a coated glass to be considered anti-fogging, the time required for the light transmittance to decrease to 80% of its initial value (non-fogged sample) must be less than or equal to 30 s.
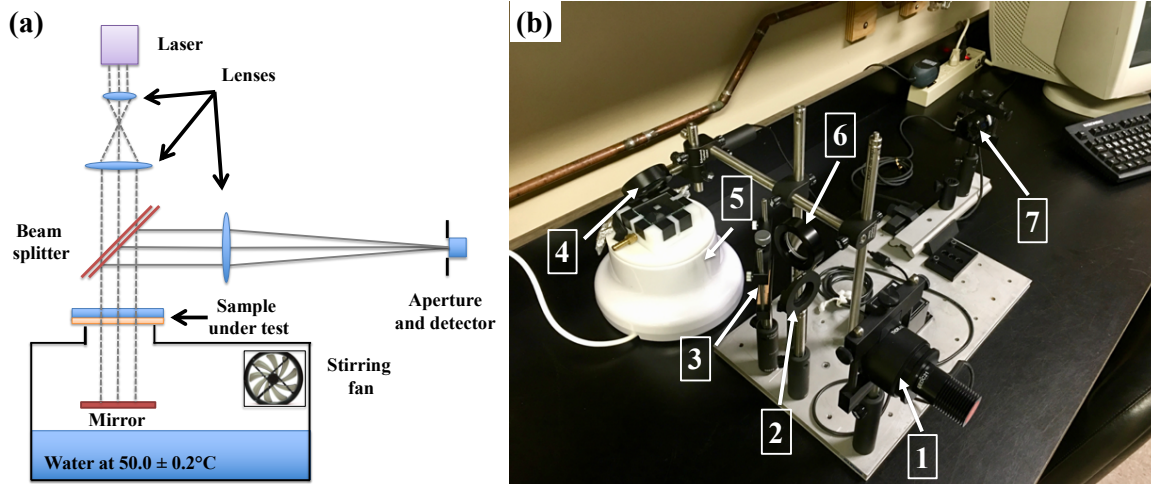
Figure 3.9: *(a) ASTM F 659-06 setup (equivalent BS EN 168) for the assessment of fogging resistance. (b) Setup for the assessment of the anti-fogging performance. The setup is composed of (1) a 590 nm LED (light emitting diode), (2) a diaphragm, (3) a beam splitter, (4) a mirror, (5) a mirror inside the water bath as shown in (a), (6) a converging lens, and (7) a photodetector.*

The resistance to fogging of coated glasses was also evaluated by "hot fog" test. In this test, the anti-fogging performance was evaluated by visual inspection and by taking photographs of the samples after being placed on an Erlenmeyer flask containing water at 80°C for 15 s.

4 Atmospheric pressure Townsend discharges as a promising tool for the one-step deposition of anti-fogging coatings from N₂O/TMCTS mixtures

Iván Rodríguez Durán[ab], Antoine Durocher-Jean[c], Jacopo Profili[c], Luc Stafford[c], and Gaétan Laroche[ab†]

[a]Laboratoire d'Ingénierie de Surface, Centre de Recherche sur les Matériaux Avancés, Département de Génie des Mines, de la Métallurgie et des Matériaux, Université Laval, 1065 Avenue de la médecine, Québec G1V 0A6, Canada.
[b]Centre de Recherche du Centre Hospitalier Universitaire de Québec, Hôpital St-François d'Assise, 10 rue de l'Espinay, Québec G1L 3L5, Canada.
[c]Département de physique, Université de Montréal, Montréal, Québec, Canada, H3C 3J7.

4.1 Résumé

Garantir la propriété de « voir à travers » des matériaux transparents dans des conditions très humides a favorisé la mise au point de stratégies antibuée visant à prévenir les effets de la condensation, notamment les modifications de certains paramètres environnementaux, le dépôt de revêtements présentant des affinités avec l'eau et la modification directe des caractéristiques de surface du substrat. Parmi ceux-ci, le dépôt de revêtements (super) hydrophiles représente une option plus attrayante en raison de sa nature plus malléable et de son effet antibuée plus durable. Cela dit, la plupart des techniques de dépôt utilisées jusqu'à présent pour la fabrication de revêtements antibuée présentent des contraintes liées à des processus fastidieux ou à une implémentation restreinte. Pour remédier à ces inconvénients, nous rapportons l'application de décharges à barrière diélectrique à la pression atmosphérique (AP-DBD) comme alternative prometteuse au dépôt en une étape de revêtements antibuée sur des échantillons de verre en utilisant de faibles quantités de 1,3,5,7, de tétraméthylcyclotétrasiloxane (TMCTS) et d'oxyde nitreux (N_2O). L'effet des paramètres de dépôt, à savoir le rapport $[N_2O]/[TMCTS]$ et la somme $[N_2O] + [TMCTS]$, sur la chimie et la structure des revêtements a été étudié par spectroscopie infrarouge à transformée de Fourier (FTIR) et par spectroscopie photoélectronique par rayons X (XPS). L'épaisseur des revêtements et la topographie de la surface ont été étudiées par profilométrie et par microscopie à force atomique (AFM), respectivement. Le comportement au mouillage des revêtements a été évalué par des mesures d'angle de contact avec l'eau (WCA) et leurs propriétés antibuée ont été déterminées visuellement et quantitativement selon le protocole décrit dans le standard ASTM F659-06. Quelles que soient les conditions de dépôt, les revêtements étaient lisses (R_{rms} = 2–4 nm) et ils ne présentaient pas de défauts de surface majeurs. Cependant, les revêtements préparés à $[N_2O]/[TMCTS]$ = 30 étaient supe hydrophiles en raison de la présence de groupes silanol et présentaient des performances antibuée supérieures à celles du verre nu lorsqu'exposé à de l'eau chaude à 50°C. En revanche, les revêtements préparés sous $[N_2O]/[TMCTS]$ = 10 n'étaient pas antibuée en raison de leur moins hydrophilicité. La somme $[N_2O] + [TMCTS]$ n'a pas eu d'impact significatif sur les performances antibuée.

4.2 Abstract

Ensuring the "see-through" property of transparent materials under very humid conditions has promoted the development of anti-fogging strategies focusing on preventing the effects of condensation, including changes in certain environmental parameters, the deposition of coatings with water-attracting features, and the direct modification of the substrate's surface features. Among these, the deposition of (super)hydrophilic coatings represents a more attractive option because of the more manageable nature and longer-lasting anti-fogging effect. That said, most of the deposition techniques used thus far for the fabrication anti-fogging coatings feature constraints related either to time-consuming processes or to limited scalability. To overcome these drawbacks, we report on the application of atmospheric pressure dielectric barrier discharges (AP-DBDs) as a promising alternative for the one-step deposition of anti-fogging coatings on glass samples using minute amounts of 1,3,5,7-tetramethylcyclotetrasiloxane (TMCTS) and nitrous oxide (N_2O). The effect of the deposition parameters, namely the $[N_2O]/[TMCTS]$ ratio and the $[N_2O] + [TMCTS]$ sum, on the chemistry and structure of the coatings was investigated by Fourier Transform Infrared Spectroscopy (FTIR) and X-ray Photoelectron (XPS) Spectroscopies. Coating thickness and surface topography were investigated by profilometry and atomic force microscopy (AFM), respectively. The wetting behavior of the coatings was assessed by water contact angle (WCA) measurements and their anti-fogging properties were determined visually and quantitatively according to the ASTM F659-06 standard protocol. Regardless of the deposition conditions, coatings were smooth (R_{rms} =2–4 nm) and exhibited no major surface defects. However, coatings prepared at $[N_2O]/[TMCTS] = 30$ were superhydrophilic (WCA ≈ 5–10°) because of the presence of silanol groups, i.e., Si-OH, and featured superior anti-fogging performance compared to bare glass when exposed to hot water at 50°C. In sharp contrast, coatings prepared under $[N_2O]/[TMCTS] = 10$ did not display anti-fogging performance because of their less hydrophilicity (WCA ≈ 60°). The $[N_2O] + [TMCTS]$ sum did not have a significant impact on the anti-fogging performance.

4.3 Introduction

Fogging is the natural phenomenon whereby water vapor condenses into the form of tiny droplets on a solid substrate whose temperature falls below the dew point [48]. The condensed drops scatter the incident light in all directions creating a whitish layer on the surface, known as "breath figures" [133]. The effects of breath figures (or fogging) have been reported to depend primarily on the morphology and the size of water drops. In general, the higher the contact angle and the smaller size, the more pronounced the effects of fogging [134].

The fogging of surfaces can cause serious problems in such spheres of human activity as the medicine, the architecture, and the horticultural sector, and photovoltaic industry. For example, the fogging of camera-guided instruments such as those employed in endoscopic surgeries (e.g., laparoscopes) distorts the field of vision, thus putting the patient's life at risk [14,15]. The formation of surface fog has been reported to lower the energy conversion efficiency of solar cells [25,26] and reduce the light transmission through the greenhouse claddings [295]. Less sunlight entering the greenhouse translates to a delayed crop maturity derived from a decrease in the rate of photosynthesis [295]. These examples aside, dealing with fogged eyeglasses, windows, or bathroom mirrors can be both dangerous and incredibly frustrating [5,7,455].

Several anti-fogging strategies have thus far been explored to prevent these situations from occurring. Most of them have focused either on changing certain parameters, such as the temperature [13,456–458] or the air flow velocity [459–462], or on changing the morphology of water drops by the deposition of (super)hydrophilic coatings [137,160,190,216]. Even though the first category of anti-fogging strategies has proven successful in avoiding or removing condensation, the deposition of (super)hydrophilic coatings appears to be the preferred option, in view of the growing number of papers that have been published in this regard.

Due to the favorable interaction with water molecules, a (super)hydrophilic coating causes fog drops to spread across the surface. Drop spreading leads to the formation of a thin layer of water allowing for the incident light to pass through without being scattered, thus preventing the effects of fogging [27]. According to recent literature, these coatings can be prepared in three different ways. The first way is based on the deposition of inorganic materials that are hydrophilic, such as SiO_2, or become superhydrophilic when exposed to UV light, such as TiO_2, ZnO, SnO_2, WO_3, and V_2O_5 [97,230,463]. The second way involves depositing thin films from polymers containing hydrophilic groups, such as hydroxyl [195,196,280], amino [241], carboxyl/ester [24,143], or sulfonic [152,199] groups. Finally, the third way employs "building blocks", such as solid or mesoporous SiO_2 nanoparticles, blended with hydrophilic polymers to produce nanostructured coatings [179,464].

Even though these procedures make it possible to obtain coatings with the anti-fogging performance, their integration into mass production face two major hurdles. First, the fabrication of anti-fogging coatings usually involves multistep processes, and second, the synthesis of the starting materials often requires chemicals that are either toxic or detrimental to the environment [195,196]. To circumvent these technological barriers, atmospheric pressure dielectric barrier discharges (AP-DBDs) have emerged as a promising tool to produce SiO_xC_y:H coatings in one step from siloxane precursors, such as hexamethyldisiloxane (HMDSO) or tetraethoxysilane (TEOS), with rapid deposition rates and tunable wetting properties [383,465,466]. In adition, the use of atmospheric pressure DBDs represents an eco-friendly and cost-effective alternative to conventional deposition techniques, such as dip-coating or layer-by-layer deposition, as it requires no solvents nor considerable amounts of precursor to produce thin films.

On this basis, the aim of this paper is to report on the feasibility of preparing anti-fogging coatings on glass samples using 1,3,5,7-tetramethylcyclotetrasiloxane (TMCTS) and nitrous oxide (N_2O) by a DBD operated in N_2 at atmospheric pressure (i.e., Townsend discharge). The composition and structure of the coatings was studied by Fourier Transform Infrared (FTIR) and X-ray photoelectron (XPS) spectroscopies. Surface roughness and coating thickness were measured by atomic force microscopy (AFM) and profilometry, respectively.

The wetting behavior was assessed by water contact angle (WCA) measurements. Anti-fogging performance of coated glasses was evaluated by visual inspection following exposure to hot water at 80°C, and by the protocol described in the ASTM F 659-06 standard.

4.4   Materials and methods

4.4.1   Materials and sample preparation

The siloxane precursor used in this study was 1,3,5,7-tetramethylcyclotetrasiloxane ($O_4Si_4(CH_3)_4H_4$), also known as "TMCTS" (**Figure 4.1**). Liquid TMCTS (NMR grade and purity $\geq 99.5\%$) was purchased from Sigma-Aldrich. Nitrogen (N_2, grade 4.8) and nitrous oxide (N_2O, 99.998%) were provided by Linde (Québec, QC, Canada). Acetone and methanol were purchased from Laboratories MAT (Québec, QC, Canada) and commercial alcohols (Ontario, ON, Canada), respectively. Rectangular-shaped glass samples (13 cm × 5 cm × 2 mm) were kindly provided by Multiver Ltd (Québec, QC, Canada). Prior to coating deposition, glass samples were ultrasonically cleaned with acetone for 10 min and rinsed with methanol and deionized water to remove any organic remnant. Afterwards, glass samples were ultrasonically washed with deionized water for 10 min and wiped dry with a cotton cloth (Amplitude Kappa™, Contect, Inc., Spartanburg, SC, USA).
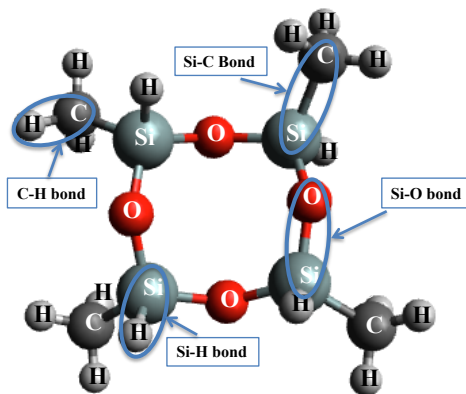
Figure 4.1: *Molecular structure of TMCTS.*

4.4.2 Deposition process

A DBD design, such as that in **Figure 4.2**, was used to prepare TMCTS-based coatings. The DBD reactor is composed of two parallel plate electrodes; the upper one is a 0.64-mm-thick alumina sheet coated with a conductive paint (3.5 cm × 3.0 cm), while the bottom one is a stainless-steel plate (13 cm × 9 cm). The plasma was generated within the inter-electrode space on application of a sinusoidal voltage with a peak-to-peak amplitude of 14 kV and a frequency of 3 kHz. These operating conditions correspond to a power dissipated in the discharge of 0.25 W cm^{-2}.
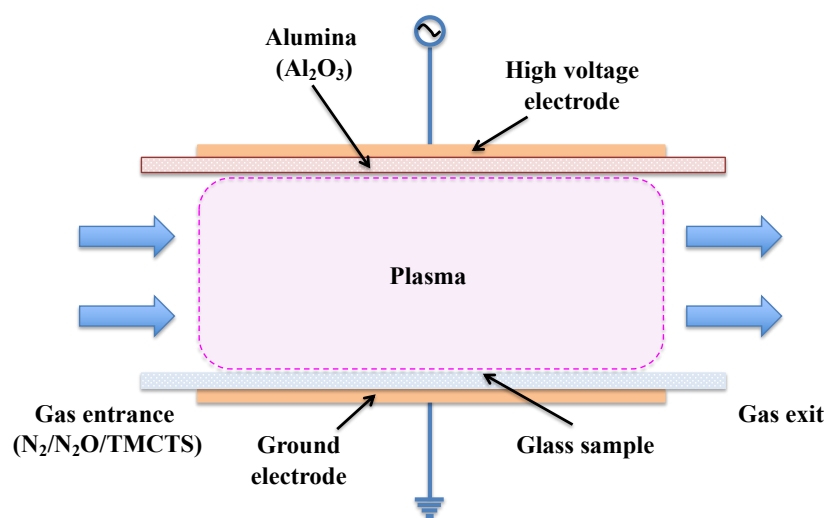
Figure 4.2: *DBD setup used for the deposition of TMCTS-based coatings.*

The gas inlet consisted of two independent lines, one for N_2 (carrier gas, 6 L min^{-1}) and other for N_2O (oxidant, variable flow rate). Gases were carried to the inter-electrode space through a diffuser, thereby ensuring a laminar flow and a continuous renewal of the gaseous atmosphere during the deposition process. The flow rates of N_2 and N_2O were measured using mass flow controllers (Bronkhorst^{TM}, Ruurlo, Holland). A TMCTS aerosol in N_2 was injected into the inter-electrode space at 1 L min^{-1} using a syringe pump (Fisherbrand^{TM}, Thermo Fisher Scientific, Runcorn, Cheshire, UK) coupled to a nebulizer (Mira Mist CE^{TM}, Burgener Research Inc., Mississauga, ON, Canada).

Prior to the deposition process, glass samples were placed on the bottom electrode keeping the inter-electrode distance at 1 mm. Afterwards, the reactor chamber was pumped down to 10^{-2} torr and filled with nitrogen until pressure reaches 760 Torr (1 atm). Coating deposition was carried out in static mode (i.e., no relative movement between the glass sample and the electrodes) for 20 min. **Table 4.1** summarizes the deposition parameters that were varied in this study.

Table 4.1: Deposition parameters. [X] indicates concentration in parts per million (ppm). R = [N₂O]/[TMCTS] and S = [N₂O] + [TMCTS].

Coating	[TMCTS]	[N₂O]	R	S
A	9.0	91.0	10	100
B	3.2	96.8	30	100
C	6.5	193.5	30	200
D	18.0	182.0	10	200

[N₂O]/[TMCTS] ratios were set at 10 (sub-stoichiometric ratio) and 30 (over-stoichiometric ratio) considering the following reaction between the TMCTS and the N₂O in the plasma:

$$[H(CH_3)SiO]_4 + 20 \; N_2O \rightarrow 40 \; N_2 + 4 \; CO_2 + 8 \; H_2O + 4 \; SiO_2 \qquad (4.1)$$

4.4.3 Coating characterization

4.4.3.1 Stylus profilometry

Coating thickness was determined by stylus profilometry. Following coating deposition, coatings were slightly scratched off with a tweezers tip each 2 mm from the entrance to the exit of the discharge. The average height of the resulting steps was measured in triplicate from the entrance and parallel to gas flow using a DektakXT^{TM} profilometer (Bruker Nano Surface Division, Tucson, AZ, USA) with a stylus force of 1 mg (radius = 5.0 mm). The

uncertainty in the average thickness was calculated as the standard deviation of these measurements. Measurements lasting 60 s were performed on a distance of 500 μm. Deposition rate of the coatings was calculated by dividing the as-measured thickness by the deposition time.

4.4.3.2 Attenuated total reflectance Fourier transformed infrared spectroscopy (ATR-FTIR)

The chemical bonds and structure of the coatings were analyzed using a FTIR spectrometer (Cary 660 FTIR, Agilent Technologies, Victoria, Australia) equipped with a DLaTGS detector and a Split-Pea attachment (Harrick Scientific Products, Pleasantville, NY, USA). Spectra were averaged over 128 scans and recorded from 400 to 4000 cm^{-1} at a resolution of 4 cm^{-1}. Following baseline correction, Origin software (Origin Lab Corp. v 8.5) enabled us to fitting curves to overlapping peaks for semi-quantitative analysis. For the sake of comparison, all spectra were normalized with respect to the 1000–1200 cm^{-1} peak from Si-O-Si asymmetric stretching, ν_a Si-O-Si. For each sample, spectra were recorded in triplicate perpendicular to the gas flow and at a distance of 0.5 cm from the entrance to the discharge. For each experiment presented here, all IR spectra exhibited identical features.

4.4.3.3 X-ray photoelectron spectroscopy (XPS)

The surface composition of the coatings was investigated by X-ray Photoelectron Spectroscopy (XPS) using a PHI 5600-ci spectrometer (Physical Electronics, Chanhassen, MN, U.S.A). A standard aluminium X-ray source (Al K$_\alpha$ 1486.6 eV) was used to acquire the survey spectra of Si, C, O, and N in the range 0–1400 eV, while a standard magnesium X-ray source (Mg K$_\alpha$ 1253.6 eV) was used to acquire the high-resolution spectra of C and Si. Photoelectrons coming from an area of 5×10^{-3} cm^2 were detected at an angle of 45° with respect to the surface normal. Analyses were conducted at 10^{-8} torr with no need for surface charge neutralization. The spectrometer work function was adjusted by setting the binding

energy of the C-C/C-H feature at 285 eV. By least squares minimization, curve fitting of the C1s and Si2p envelopes was carried out using Gaussian-Lorentzian functions and a Shirley-type background. All photoemission peak areas were calculated by PHI MultiPak^{TM} software v 9.3. Nine analyses per sample were performed to assess the chemical homogeneity of the coatings (from the entrance to the exit of the discharge) and provide a mean value with its corresponding standard deviation.

4.4.3.4 Atomic force microscopy (AFM)

The surface topography of the coatings was examined at the nanometer scale on 2×2 μm^2 and 20×20 μm^2 areas using an atomic force microscope (Dimension 3100, Veeco Digital Instruments by Bruker, Santa Barbara, CA, USA) equipped with an etched silicon tip with a radius of curvature < 10 nm (OTESPA probe, Bruker Nano Surface Division, Santa Barbara, CA, USA). AFM images were acquired in the tapping mode at a scan rate of 0.5 Hz and a line resolution of 256×256. Two roughness parameters, namely the root mean square roughness (R_{rms}) and the mean roughness (R_a) were measured following image flattening (NanoScope Analysis software v 1.5 by Bruker).

4.4.4 Wetting behavior assessment

The wetting behavior of the coatings was assessed using the sessile drop method. Briefly, 3-μL water drops were dropped from a height of 1 cm and contact angles were measured following the pinning of the three-phase contact line using a Video Contact Angle System (VCA-2500 XE^{TM}, AST products Inc., Billerica, MA, USA). For each sample, nine droplets were deposited on different locations from the entrance to the exit of the discharge area. The water contact angles (WCA) reported here are the average of the values measured on the right and left sides of sessile drops.

4.4.5 Fogging resistance assessment

The fogging resistance of coated glasses was assessed by means of a Fog Quantification Box (FQB), which was fabricated taking into account the anti-fogging requirements defined in the ASTM F659-06 standard [195]. Briefly, coated glasses were placed over a bath containing water at 50°C to measure the "two-pass" transmittance of a 590-nm light as a function of time. According to the ASTM F659-06 standard [333], if the percentage of light transmitted through the sample is greater than or equal to 80% following 30 s of exposure to water vapor, the anti-fogging requirement is met.

4.5 Results and discussion

4.5.1 Deposition rate of the coatings

Figure 4.3 shows the deposition rate of the coatings as a function of the position along the length of the discharge. Regardless of the deposition conditions, it was found that deposition rates were at their highest at approximately 2 mm from the entrance to the discharge. Nonetheless, the deposition profiles appeared to be governed by the $[N_2O]/[TMCTS]$ ratio. In this respect, two groups of coatings can readily be distinguished, namely, those fabricated under sub-stoichiometric $[N_2O]/[TMCTS]$ ratios (R = 10) and those fabricated under over-stoichiometric $[N_2O]/[TMCTS]$ ratios (R = 30).

In the case of sub-stoichiometric conditions ($[N_2O]/[TMCTS] = 10$), deposition profiles result in a thickness gradient characterized by a deposition rate at the entrance of the discharge of few nm min^{-1}, followed by a marked increase to 348 nm min^{-1} for the coating D, and 336 nm min^{-1} for the coating A. Afterwards, deposition rates decreased steadily along the length of the discharge to approximately 10 nm min^{-1} at the exit. In the case of over-stoichiometric conditions ($[N_2O]/[TMCTS] = 30$), deposition profiles exhibited similar features even though deposition rates were significantly lower. Here, deposition rates increased less abruptly to approximately 67.6 nm min^{-1} for the coating B and 98.3 nm min^{-1}

for the coating C, and then decreased more gently to 11 nm min^{-1} at the exit of the discharge. Such deposition profiles suggest a slow consumption of the precursor along the length of the discharge, compared to that of the samples A and D. Interestingly, for the same value of the [N$_2$O]/[TMCTS] ratio, deposition profiles were almost superimposable.
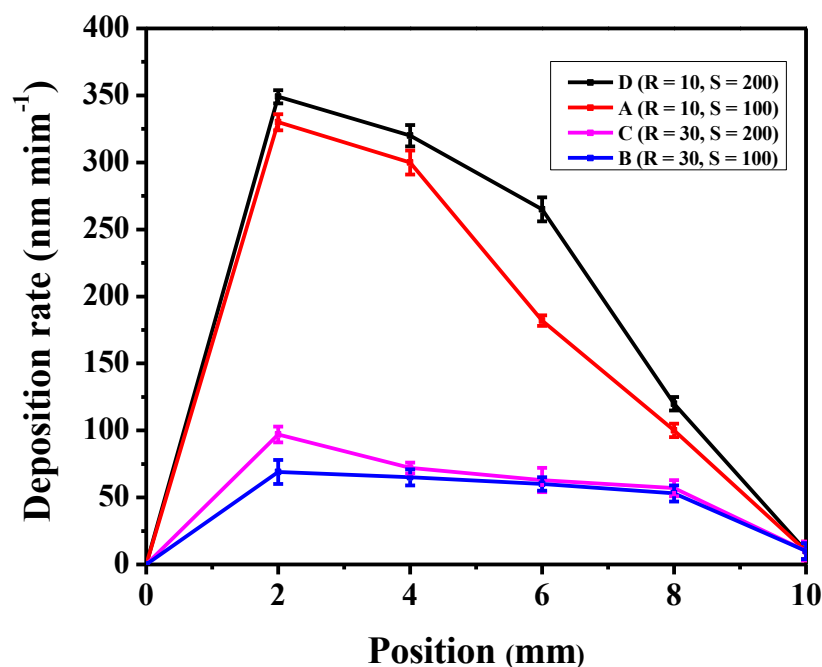
Figure 4.3: *Deposition rate as a function of the position for coatings deposited under different [N$_2$O]/[TMCTS] ratios and [N$_2$O] + [TMCTS] sums.*

Despite these particularities, the trend observed in the deposition rates are not surprising given that the amount of precursor must decrease along the length of the discharge as a result of the interaction with the plasma species (e.g., electrons, radicals, N$_2$ metastables, etc.). In investigating SiO$_2$-like cotings deposited from N$_2$/N$_2$O/HMDSO mixtures using an AP-DBD, Enache et al. [467] revealed similar deposition profiles. As did Premkumar and collaborators [468], who prepared coatings from Ar/N$_2$/O$_2$/HMDSO mixtures by PECVD, these authors formulated a simple mechanistic model to account for the observed deposition profiles [467].

The proposed mechanism was built on two basic assumptions, namely, that HMDSO molecules do not react with the substrate, and that the Si-O-Si containing radicals resulting from the interaction of HMDSO with the N$_2$ (A$^3\Sigma_u^+$) metastable species have sticking

coefficients equal to one (i.e., they are incorporated into the coating/substrate with probability unity). On the other hand, it can be argued that the residence time of the fragments resulting from these interactions is greater than that required for them to diffuse toward the glass surface, as no coating was observed outside the discharge (≥ 3.0 cm).

4.5.2 Structural analysis of the coatings

Understanding the chemistry and the structure of the plasma-deposited coatings is key to explaining their resistance to fogging (**section 4.5.5**). For this reason, IR features have been compared to those of the TMCTS and discussed further in **section 4.5.2.5,** in terms of band broadening and frequency shifts.

4.5.2.1 IR spectrum of liquid TMCTS

Figure 4.4 shows a detailed assignment of the infrared bands of TMCTS. Vibrational modes of methyl groups resulted in two small bands, one at 2968 cm^{-1} due to the C-H asymmetric stretching (ν_a), and other at 2922 cm^{-1} due to the C-H symmetric stretching (ν_s). Asymmetric (δ_a) and symmetric (δ_s) bending vibrations of C-H in CH$_3$ groups were found at 1406 and 1259 cm^{-1}, respectively [412,469–472]. As in the case of hydrocarbon compounds, these features are expected to occur at 1450 and 1380 cm^{-1}, respectively; however, the silicon atom bonded to the methyl group cause them to shift to lower frequencies [412,470–472]. The absorption originating from the CH$_3$ symmetric bending (δ_s CH$_3$) is likely the most characteristic one of the methylsilyl-containing siloxanes. The frequency at which this feature appears depends on the number of methyl groups bonded to the silicon atom in the (CH$_3$)$_n$-SiO$_{4-n}$ units (where n = 1, 2, and 3). In general, this band occurs at ~ 1275 cm^{-1} when n = 1 ("T-units"), at ~ 1265 cm when n = 2 ("D-units"), and at ~ 1255 cm^{-1} when n = 3 ("M-units") [473–475]. This absorption is always accompanied by the Si-C stretching and CH$_3$ rocking vibrations. In M-units, both the CH$_3$ rocking and the Si-C asymmetric stretching appear at 845 cm^{-1}, along with the Si-C symmetric stretching at 760 cm^{-1} [471,476]. In D-units, the CH$_3$ rocking appears at 855 cm^{-1}, while the asymmetric and symmetric stretching

vibrations of Si-C appear at 800 cm^{-1} and 690 cm^{-1}, respectively [471,474,476]. In T-units, only one peak in the 750–780 cm^{-1} range is observed, as in the case of TMCTS (ν Si-C/ρ CH$_3$ at 771 cm^{-1}) [412,471].
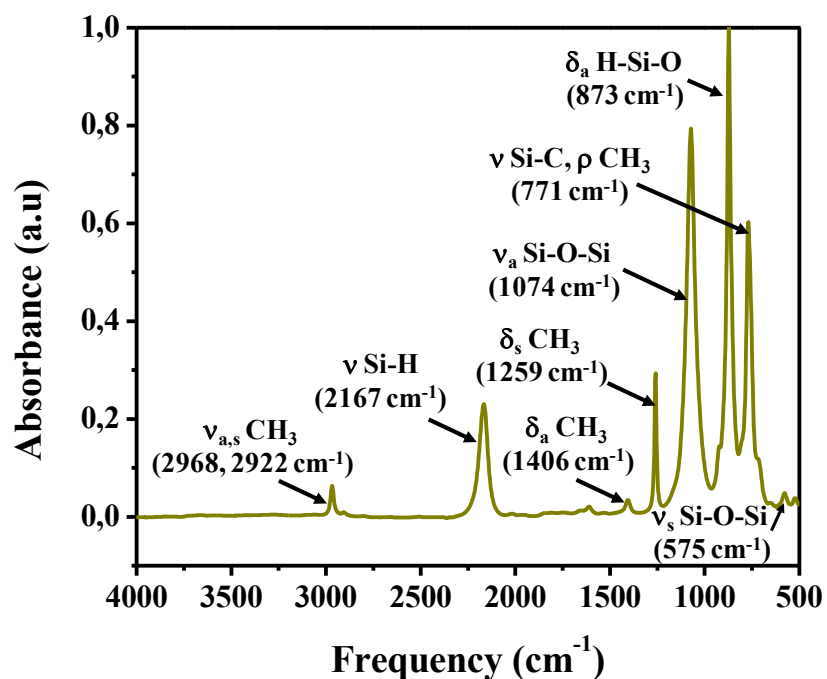
Figure 4.4: *IR spectrum of liquid TMCTS (ν = stretching, δ = bending, ρ = rocking, a = asymmetric, and s = symmetric).*

Numerous studies on siloxane compounds have evidenced that the frequency at which the Si-O-Si asymmetric stretching (ν_a Si-O-Si) occurs can vary from 1010 to 1125 cm^{-1} depending on the molecular structure. In linear siloxanes, this band broadens as the chain length increases and splits into two features at approximately 1080 and 1020 cm^{-1}, when the number of siloxane groups (Si-O-Si) is greater than or equal to three [477–480]. In cyclic siloxanes, this band shifts from 1020 to 1090 cm^{-1} as the cycle increases in size. As in linear siloxanes, this band broadens and splits into two features at approximately 1050 and 1090 cm^{-1}, but in this case, when the number of siloxane groups is greater than or equal to six (6-membered rings) [477–480]. The Si-O-Si asymmetric stretching results in only one spectral feature at 1074 cm^{-1}, given that the TMCTS is a cyclotetrasiloxane [412,472].The weak band at 575 cm^{-1} can be attributed to the symmetric stretching of Si-O-Si groups, i.e., ν_s Si-O-Si [469,472,476].

Absorptions characteristic of the Si-H group are strong and isolated, making it easier to identify them. The band at 2167 cm^{-1} can be assigned to the Si-H stretching (ν Si-H) [412,472]. The position of this feature, which usually ranges from 2100 to 2250 cm^{-1}, is extremely sensitive to the chemical environment of the Si-H group [428,481,482]. The ring strain in cyclic siloxanes and the number of O-Si-O units in the vicinity of the Si-H group also influence the position of this vibrational mode. In cyclic siloxanes [(CH$_3$)HSiO]$_n$ (n = 3–7), the Si-H stretching shifts to high frequencies as the cycle decreases in size. The electron attraction from adjacent O-Si-O units also causes ν Si-H to shift to high frequencies as a result of the Si-H bond strengthening [428,481]. This band is accompanied by another more intense at 873 cm^{-1}, which can be attributed to the asymmetric bending of H-Si-O groups (δ_a H-Si-O) [412].

4.5.2.2 IR spectra of the coatings

Coatings deposited on glass samples using an atmospheric pressure DBD exhibited many infrared features similar to those of the liquid TMCTS and several new ones. However, some differences in terms of peak areas, peak positions, and peak widths are worth mentioning. **Figure 4.5** shows the infrared spectra of selected sections of coatings deposited under a sub-stoichiometric ratio (coating A, [N$_2$O]/[TMCTS] = 10) and under an over-stoichiometric ratio (coating B, [N$_2$O]/[TMCTS] = 30). These samples were selected because of their different anti-fogging performance.
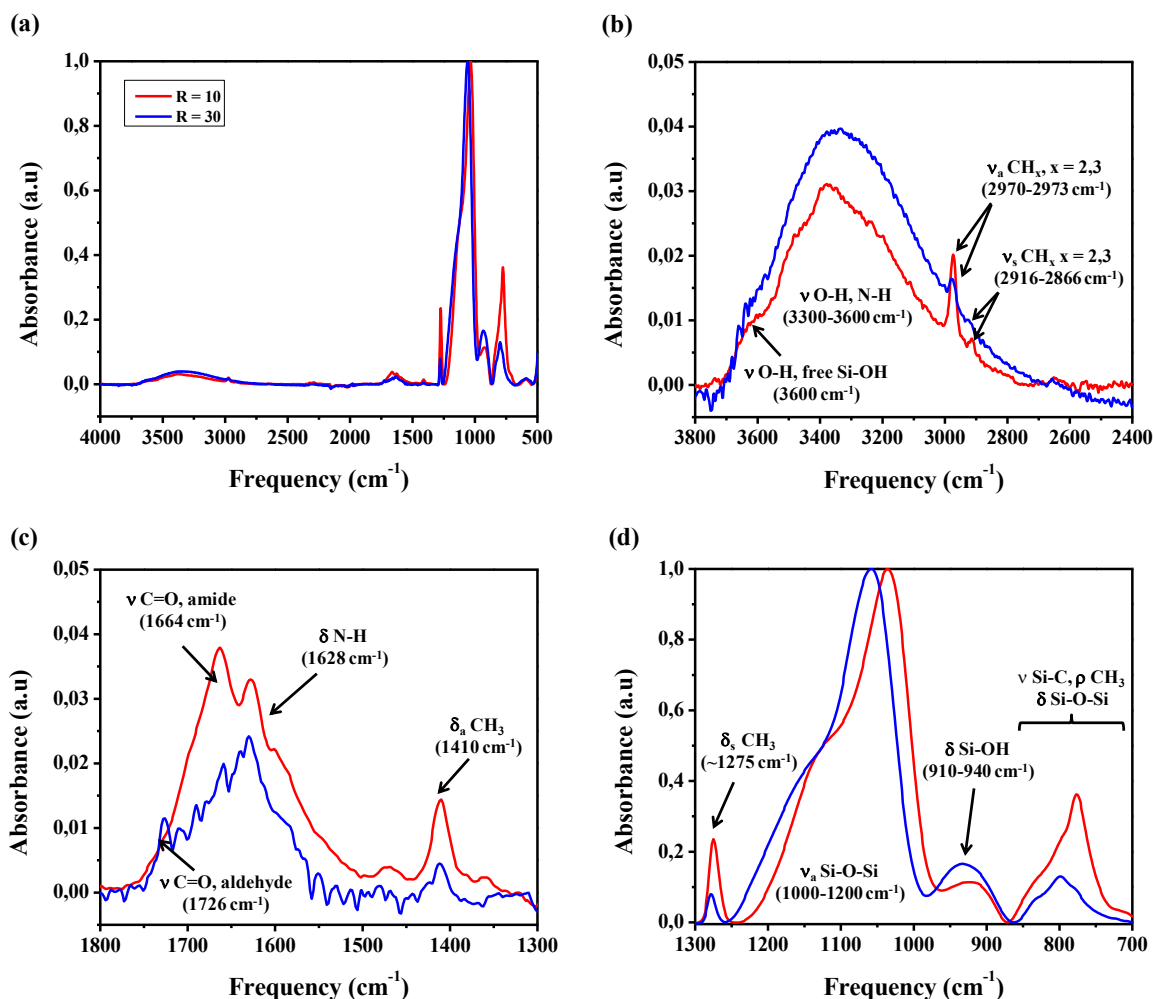
Figure 4.5: *IR spectra of (a) 4000−500 cm^{-1}, (b) 3800−2400 cm^{-1}, (c) 1800−1300 cm^{-1}, and (d) 1300−700 cm^{-1} regions of coatings deposited at R = 10 (in red) and R = 30 (in blue).*

4.5.2.2.1 Coatings deposited at [N$_2$O]/[TMCTS] = 10

Spectral features related to methyl groups such as $\nu_{a,s}$ CH$_3$ in the 2866−2970 cm^{-1} range (**Figure 4.5b**), δ_a CH$_3$ at 1410 cm^{-1} (**Figure 4.5c**), δ_s CH$_3$ at 1274 cm^{-1}, and ν Si-C/ρ CH$_3$ in the 750−850 cm^{-1} range (**Figure 4.5d**) were observed despite the addition of N$_2$O (oxidant) in the discharge. The presence of these bands suggests that under a [N$_2$O]/[TMCTS] ratio of 10 is not possible to completely remove the methyl groups from the TMCTS during the deposition process. The disappearance of bands due to Si-H vibrations, namely ν Si-H and δ_a H-Si-O (**Figure 4.5a**), provides evidence to support the greater reactivity of the Si-H bond

compared with that of Si-C or C-H bonds [417]. Accompanied by a shoulder at $\sim$ 1150 cm^{-1}, the Si-O-Si asymmetric stretching (ν_a Si-O-S) broadened and appeared at a frequency lower than that of the TMCTS (1029 vs. 1074 cm^{-1}). The unresolved band between 3000 and 3650 cm^{-1} due to O-H stretching vibrations [471,475,483] (**Figure 4.5b**) substantiates the presence of silanol groups in the coatings, a revealed by the feature at $\sim$ 920 cm^{-1}, i.e., Si-O bending in Si-OH groups (**Figure 4.5d**) [427,471,475,484]. Another less intense and complex band between 1500 and 1750 cm^{-1} can be attributed to presence of C=O (ν C=O in aldehydes and amides) and N-H bonds (δ N-H$_2$) [483] in the coatings (**Figure 4.5c**).

4.5.2.2.2 Coatings deposited at [N$_2$O]/[TMCTS] = 30

Because of the increase in the N$_2$O concentration in the discharge, CH$_3$-related absorptions, such as ν Si-C/ρ CH$_3$ in the 750–850 cm^{-1} range, δ_a CH$_3$ at 1410 cm^{-1}, and δ_s CH$_3$ at $\sim$ 1275 cm^{-1} were less intense when compared with those of the coatings deposited at [N$_2$O]/[TMCTS] = 10. Some contribution to the band between 750 and 850 cm^{-1} may also come from the bending of Si-O-Si groups (δ Si-O-Si), which typically occurs at 800 cm^{-1} (**Figure 4.5d**) [427,485]. The oxidative removal of CH$_3$ groups was accompanied by an increase in the intensity of the δ Si-OH band ($\sim$ 920 cm^{-1}) and the disappearance of the Si-H functionality. As in the case of coatings prepared under a [N$_2$O]/[TMCTS] = 10, the Si-O-Si asymmetric stretching, which also exhibited a shoulder at $\sim$ 1170 cm^{-1}, broadened and appeared at a frequency lower than that observed in the precursor (**Figure 4.4**). Bearing in mind the intensity enhancement of both the δ Si-OH band (**Figure 4.5d**) and the broad band ranging from 3000 to 3650 cm^{-1}, it can be argued that the amount of silanol groups is greater than that found in coatings prepared at [N$_2$O]/[TMCTS] = 10 (**Figure 4.5b**). Bands related to carbonyl- and nitrogen-containing groups (i.e., C=O, NH) also occurred in the 1500–1750 cm^{-1} range, but in this case, they were less intense than those observed in coatings prepared at R = 10 (**Figure 4.5c**).

4.5.2.2.3 Curve fitting of IR spectra

Along with the CH_3 symmetric bending (δ_s CH_3), the analysis of the band between 1000 and 1200 cm^{-1} (ν_a Si-O-Si) makes it possible to obtain structural information of the coatings. It has been reported that this spectral feature can be curve fitted with two [427], three [412,486], or four [473] components. In the case of SiO_2 coatings, the Si-O-Si asymmetric stretching results in two spectral features, one at ~ 1070 cm^{-1} due to the in-phase vibrations, known as "AS1"; and other at ~ 1200 cm^{-1} due to the out-of-phase vibrations, known as "AS2" [427,487,488]. The ratio of the area below the AS2 band to the area below the AS1 band allows for the qualitative assessment of the structural disorder in the coating. Indeed, the higher the AS2/AS1 ratio is, the more disordered the silica network is [489]. According to Rouchon et al. [490] the structural disorder is due to the presence of voids, stress, suboxides, or roughness at the interface coating/substrate, among other defects.

In the case of carbon-containing SiO_x coatings (i.e., SiO_xC_y:H), at least a third component must be taken into account when curve fitting the ν_a Si-O-Si band. In this regard, worthy of mention is the elegant curve fitting conducted by Grill and Neumayer [412] in SiO_xC_y:H coatings prepared by plasma enhanced chemical vapor deposition (PECVD) from mixtures of TMCTS and an organic precursor. These authors attributed the first component at 1020–1035 cm^{-1} to the presence in the coatings of cyclic siloxanes with D_{3h} symmetry and silicon sub-oxidized states (e.g., O-Si-Si and O-Si-C). The second component at 1065–1070 cm^{-1} was attributed to a Si-O-Si network with a Si-O-Si angle ~ 144° and some preserved TMCTS rings. Finally, the third component at 1135–1150 cm^{-1} was attributed to the presence of cage-like entities with Si-O-Si angles greater than 144°. It was also suggested that some contribution to the Si-O-Si envelope comes from the asymmetric stretching of Si-O-C and C-O-C groups; however, no curve fitting was performed in this regard.

Curve fitting of the most representative vibrational modes of Si-O-X (X = Si, C, and H), Si-$(CH_3)_n$ (where n = 1, 2, and 3), and CH_3 groups was conducted considering the foregoing. To illustrate this point, an example is given in **Figure 4.6**.
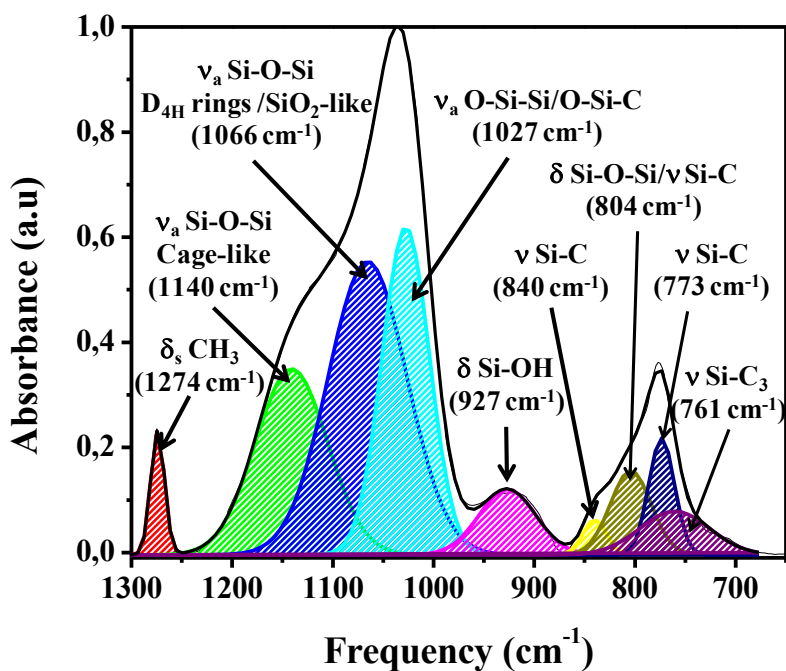
Figure 4.6: *Example of curve fitting of the 650–1300 cm^{-1} region for a coatings deposited at S = 100 and R = 10. The spectral features resulting from v_s O-Si-C [491,492], δ Si-O-Si, and v Si-C/ρ CH$_3$ vibrations were also considered to provide further detail on the chemistry and structure of the coatings.*

Table 4.2 summarizes the integrated band areas and full width at half maximum of bands for plasma-deposited coatings. From the results shown in **Table 4.2**, it can be inferred that an increase in the amount of TMCTS and N$_2$O in the discharge (i.e., [N$_2$O] + [TMCTS] sum) appears to not modify significantly, either the chemistry or the structure of the coatings, if the [N$_2$O]/[TMCTS] ratio remains unchanged. This indicates that the [N$_2$O]/[TMCTS] ratio is a key factor in determining the chemistry of the coatings, and therefore, their anti-fogging performance. For this reason, coatings obtained at S = 100 has been used as a reference in this study (**Figure 4.6**).

Table 4.2: *Full width at half maximum (FWHM) of bands and integrated band areas (A) for plasma-deposited coatings in the 650–1300 cm⁻¹ range.*

Coating	A R = 10 S = 100	B R = 30 S = 100	C R = 30 S = 200	D R = 10 S = 200
$A_{cage-like}$ (1135–1150 cm⁻¹)	50.4±0.5	56.5±0.2	55.2±0.5	52.6±0.6
$A_{D4H\ ring/SiO2-like}$ (1065–1070 cm⁻¹)	35.4±0.8	44.1±0.8	40.1±0.6	38.9±0.3
$A_{O-Si-Si/O-Si-C}$ (1020–1035 cm⁻¹)	40.5±0.2	22.4±0.5	25.8±0.4	39.2±0.4
$FWHM_{cage-like}$, (cm⁻¹)	86.7±0.6	97.6±0.3	93.9±0.7	84.1±0.7
$FWHM_{D4H\ ring/SiO2-like}$, (cm⁻¹)	61.1±0.5	54.2±0.6	56.9±0.4	58.5±0.6
$FWHM_{O-Si-Si/O-Si-C}$, (cm⁻¹)	49.1±0.4	45.7±0.7	40.7±0.4	54.2±0.5
$A_{\delta Si-OH}$ (920–930 cm⁻¹)	13.7±0.9	17.0±2.0	15.2±0.7	16.7±0.3
$FWHM_{\delta Si-OH}$ (cm⁻¹)	62.4±0.7	60.1±0.4	58.4±0.6	67.2±0.7
$A_{\delta CH3\ in\ Si-(CH3)n}$, (1270–1275 cm⁻¹)	3.1±0.5	1.4±0.7	1.7±0.5	2.6±0.4
$FWHM_{\delta CH3\ in\ Si-(CH3)x}$ (cm⁻¹)	12.6±0.4	10.3±0.3	10.6±0.2	12.1±0.2

Further analysis of the spectral features of the coatings A (R = 10) and B (R = 30) provides interesting structural information. As regards the v_a Si-O-Si feature, the observed band asymmetry/broadening and shift to low frequencies when compared to that of the TMCTS can be ascribed to a variation in the Si-O-Si bond angle, as indicated by Raballand and Keudell [493]. Changes in the Si-O-Si bonding environment are not surprising as only 0.1 eV is required to decrease by 13° the Si-O-Si angle [494], which substantiates the presence in the coatings of various Si-O-Si arrangements, such as cyclic entities, chains, and cage-like structures. As supported by the band in the 1135–1150 cm⁻¹ range, the presence of cage-like structures in the coatings suggests that the $(Si-O)_4$ rings of TMCTS were partially preserved. Furthermore, this feature broadened and shifted to higher frequencies as the amount of N_2O injected in the discharge increased. This may be due to the formation of cage-like structures with various symmetries, such as closed cages (e.g., "T6", and "T8") and open cages (e.g., "T7"), similar to those found in silsesquioxanes (i.e., $[RSiO_{3/2}]_n$ where R = H, alkyl, alkoxy, alkylene, aryl, etc.) [417]. In addition, the ratio of the area below the "cage-like" band to that

of the ν_a Si-O-Si band was greater in coatings prepared at R = 30 (46% vs. 40%), suggesting a higher proportion of these entities in the coatings.

Bands related to "open" structures were also found to vary with the [N$_2$O]/[TMCTS] ratio. In both coatings, the FWHM of the "DH4 ring/SiO$_2$-like" band was less than that reported in the SiO$_2$ ($\sim$ 75 cm^{-1}), which suggests that the distribution of the Si-O-Si bond angles is less widely spread and relatively close to 144° [493,495]. The observed decrease in "O-Si-Si/O-Si-C/"D4H ring/SiO$_2$-like" area ratio when [N$_2$O]/[TMCTS] ratio went from 10 to 30, may account for the shift in the ν_a Si-O-Si maximum from 1029 (R = 10) to 1050 cm^{-1} (R = 30), because of the oxidative removal of carbon from the O-Si-C entities. This finding is consistent with the loss of the CH$_3$ groups, as revealed by the decrease in the band due to the CH$_3$ symmetric bending (δ_s CH$_3$). The frequency at which the δ_s CH$_3$ feature occurred ($\sim$ 1275 cm^{-1}) in both coatings indicates that most of the CH$_3$ groups were integrated in "T" units (i.e., O$_3$Si-(CH$_3$)$_1$); that said, its asymmetry provides strong evidence of the presence of "D" (i.e., O$_2$Si-(CH$_3$)$_2$) and "M" (i.e., O$_1$Si-(CH$_3$)$_3$) units in the coatings.

At low N$_2$O/TMCTS ratios (R = 10), the Si-CH$_3$ bond is mainly preserved, in light of the features at 1275 cm^{-1} (δ_s CH$_3$ in Si-(CH$_3$)$_n$) and 774 cm^{-1} (ν Si-C/ρ CH$_3$) (**Figure 4.5d**). However, under these conditions, the emergence of the δ Si-OH absorption at $\sim$ 920 cm^{-1} was accompanied by the loss of the Si-H functionalities, as neither ν Si-H nor δ H-Si-O vibrations were observed (**Figure 4.5a**). Accordingly, it may be argued that, the formation of Si-OH groups at low oxidant/precursor ratios, occurs primarily through the breaking of Si-H bonds, most likely on interaction with the N$_2$ (A$^3\Sigma_u^+$) species [496], or/and with the oxygen atoms coming from the dissociation of the N$_2$O in the plasma [497]. That said, the hydroxylation of a small number of Si-CH$_3$ groups, that is, the conversion of Si-CH$_3$ groups into Si-OH ones cannot entirely be excluded. At high N$_2$O/TMCTS ratios (R = 30), it is reasonable to assume that most of the Si-CH$_3$ groups underwent hydroxylation, in view of the sharp decrease in the δ_s CH$_3$ band accompanied by a further increase in the δ Si-OH feature [498].

4.5.3 Surface composition of the coatings

Table 4.3 shows the surface composition of plasma-deposited coatings at R = 10 and R = 30 in terms of atomic percent (at. %) of carbon, oxygen, and silicon, as well as O/Si and C/Si ratios.

Table 4.3: *Surface composition of plasma-deposited coatings as a function of the position. (Middle: at 0.5 cm from the entrance to the discharge).*

Coating	Position	C1s	O1s	Si2p	N1s	O/Si	C/Si
A (R = 10)	Entrance	20.6±0.5	52.4±0.4	24.4±0.3	2.6±0.3	2.14±0.04	0.84±0.03
	Middle	19.4±0.3	53.4±0.6	24.5±0.2	2.7±0.1	2.17±0.04	0.79±0.02
	Exit	19.2±0.5	54.3±0.3	23.9±0.4	2.6±0.2	2.27±0.05	0.80±0.03
B (R = 30)	Entrance	9.5±0.3	65.2± 0.4	24.7±0.5	0.6±0.1	2.64±0.07	0.38±0.02
	Middle	8.1±0.6	66.8± 0.4	24.5±0.7	0.6±0.2	2.73±0.09	0.33±0.03
	Exit	7.9±0.4	66.3±0.6	25.3±0.4	0.5±0.1	2.72±0.07	0.31±0.02
TMCTS	-	33.3	33.3	33.3	-	1	1

XPS survey analyses reveal that surface composition of both coatings does not change significantly from the entrance to the exit of the discharge. This may indicate that the fragmentation of TMCTS occurring along the length of the discharge was not strongly affected by the $[N_2O]/[TMCTS]$ ratio.

When compared with the atomic composition of TMCTS, plasma deposition conducted under over-stoichiometric or sub-stoichiometric $[N_2O]/[TMCTS]$ ratios resulted in coatings with much less carbon (<< 33%) and more oxygen (>> 33%). In coatings deposited at R = 30, the average content of carbon and oxygen at the surface were approximately 9 and 66%, respectively. These values were approximately 20 and 53%, respectively, in coatings deposited at R = 10. Not surprisingly, coating deposition conducted in the presence of a higher amount of N_2O in the discharge (R = 30) resulted in coatings with less carbon, thus supporting the removal of methyl groups observed in the FTIR analyses. Interestingly, the

average silicon content appears unaffected by the addition of the oxidant, as it remains almost unchanged at approximately 24–25%. This particular feature coupled with a relatively low carbon percentage compared to that of the TMCTS, explains the C/Si ratios found in the coatings.

Interestingly, O/Si ratios were greater than that of the stoichiometric silica (O/Si = 2). The non-stoichiometricity of the SiO_xC_y:H coatings evidences the incorporation of oxygen from the discharge and substantiates the presence silanol groups (FTIR results). The low O/Si values observed in coatings prepared at R = 10 compared with those of the coatings prepared at R = 30, highlights how important is the amount of N_2O to remove carbon from the precursor molecules. With a more important concentration at R = 10, a slight amount of nitrogen, most likely coming from the N_2 in the discharge [499], was found in both coatings. The incorporation of nitrogen has also been reported in SiO_xC_y:H coatings made from $HMDSO/N_2O$ and SiH_4/N_2O mixtures using a DBD operated in N_2 at atmospheric pressure [485]. Interestingly, a low content of N_2O in the discharge correlated with an enhanced nitrogen incorporation efficiently.

Although XPS analyses were consistent with the results obtained by FTIR, it has been deemed appropriate to provide further detail on the carbon and silicon bonding environments. As illustrated in **Figures 4.7a** and **4.7b**, C1s envelopes were resolved into two or three bands. In both coatings, the feature at 285.0 eV revealed that most of the carbon comes from C-H and C-C containing species [500,501]. The components at approximately 286.3 eV and 288 eV can be attributed to the presence of single-bonded C-O/C-N [500,501] and double-bonded C=O/N-C=O [500,501] containing species, respectively. The C-O/C-N band was slightly more intense in coatings deposited under soft oxidizing conditions (**Figure 4.7a**). This result was in agreement with FTIR spectra, where it was found that vibrations of C=O and N-H groups resulted in more intense IR features at R = 10 than at R = 30 (**Figure 4.5c**). With the XPS survey scan and the HRXPS analyses in mind, it can be said that coatings fabricated at R = 10 contain more carbon, and that this carbon is less oxidized than that of the coatings fabricated at R = 30, because of the additional feature at 288 eV.
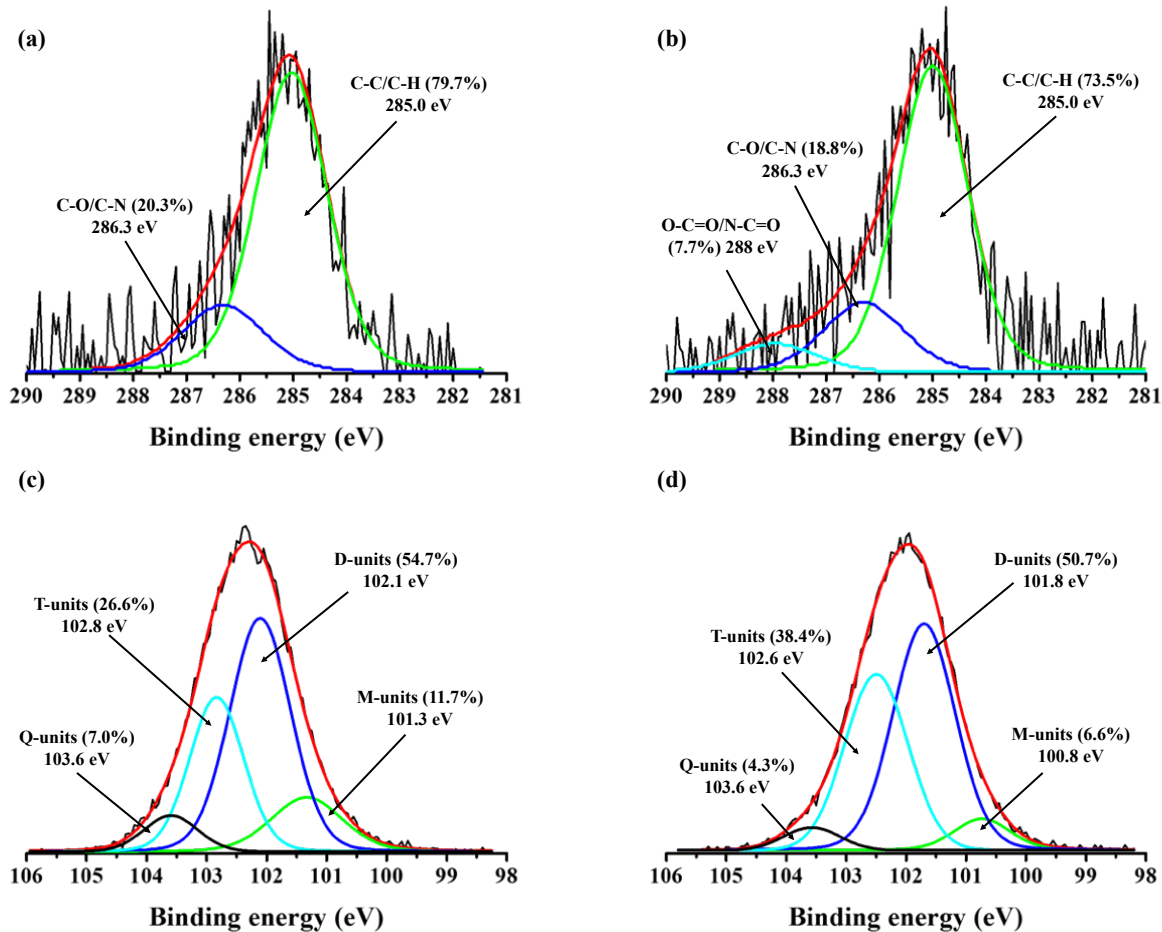
Figure 4.7: *HRXPS C1s and Si2p spectra for the coating A (R = 10) (a,c) and the coating B (R = 30) (b,d), respectively, on areas located at 0.5 cm from the entrance to the discharge.*

Even though the Si percentage does not vary significantly with the [N_2O]/[TMCTS] ratio, the Si bonding environment does slightly. According to O'Hare's [502] and Alexander's groups [503], Si2p envelopes can be composed of up to four peaks depending on the number of oxygen and carbon atoms bonded to the silicon, i.e., $(CH_3)_nSiO_{(4-n)/2}$ (where n = 0–3). The first peak at 101.5 eV is generally attributed to M-units (n = 1), the second peak at 102.1 eV to D-units (n = 2), the third peak at 102.8 eV to T-units (n = 3), and the last one at 103.4–103.6 eV to the presence of SiO_4 entities or Q-units in the coatings (n = 4). As shown in **Figure 4.7c** and **4.7d**, the Si2p core level can be described by the abovementioned components. It is worth mentioning that the layer deposited at over-stoichiometric ratio (**Figure 4.7d**) is more oxidized given that the Q-units+T-units/D-units+M-units ratio is greater than that found in the sub-stoichiometric case (0.75 vs. 0.5; **Figure 4.7c**). It can

therefore be concluded that the coatings deposited at R = 30 possessed a higher inorganic character, and therefore, are somewhat closer to the SiO_2-like structure. This is in line with the results shown in **Table 4.3**. Indeed, the coatings obtained under an over-stoichiometric ratio (R = 30) possesses a greater amount of oxygen and less amount of carbon than those prepared at R = 10.

4.5.4 Surface topography of the coatings

Coatings were quite homogeneous and exhibited no surface defects at the microscale (**Figure 4.8**). Interestingly, an increase in the N_2O in the discharge (compare **Figures 4.8a** and **4.8b**, and **Figures 4.8c** and **4.8d**) appears to not affect significantly the morphology of the surface features nor the surface roughness. Indeed, coatings were smooth, in view of the small R_{rms} values (2–4 nm) for both 2×2 and 20×20 μm^2 areas. A similar trend was noticed in the mean roughness measured on both 2×2 and 20×20 μm^2 areas, with R_a values of 2 and 1.8 nm, respectively. In either case, plasma-deposited coatings were rougher than the glass substrate, which exhibited surface features in the range of 0.5–1.5 nm range (not shown).
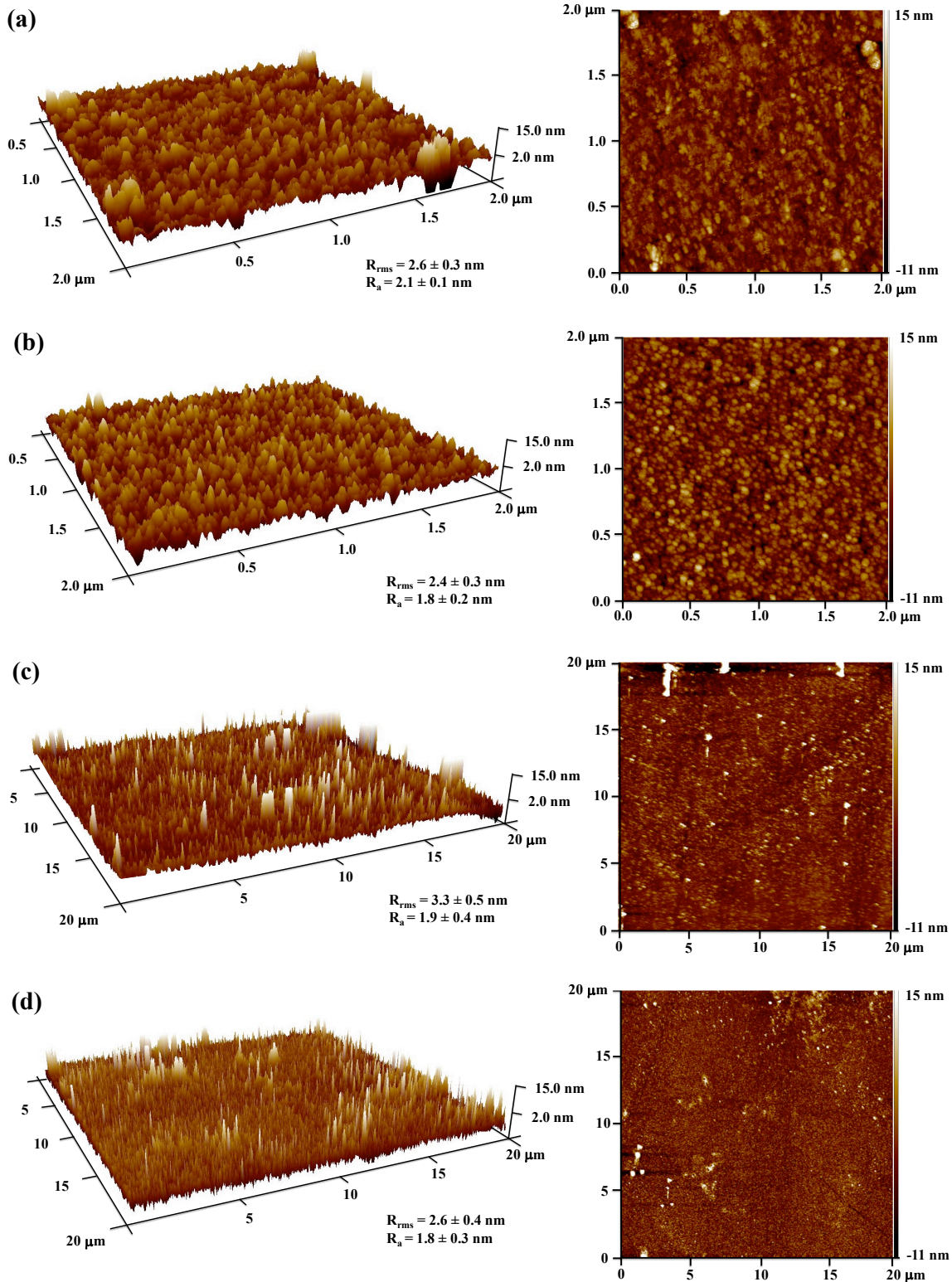
Figure 4.8: *Atomic force micrographs of the plasma-deposited coatings on glass using a homogeneous N$_2$/N$_2$O Townsend discharge. (a) R = 10, (b) R = 30 on a 2 × 2 μm^2 scanning area, and (c) R = 10 and (d) R = 30 on a 20 × 20 μm^2 scanning area (AFM analyses were performed on areas located at 0.5 cm from the discharge).*

147

4.5.5 Anti-fogging performance and wetting behavior of the coatings

To assess the anti-fogging performance of coated glasses, light of wavelength 590 nm transmitted through the coated glasses in the presence of water vapor at 50°C was measured as a function of time (ASTM F659-06 protocol). For comparative purposes, an uncoated glass sample was also tested (**Figure 4.9a**).
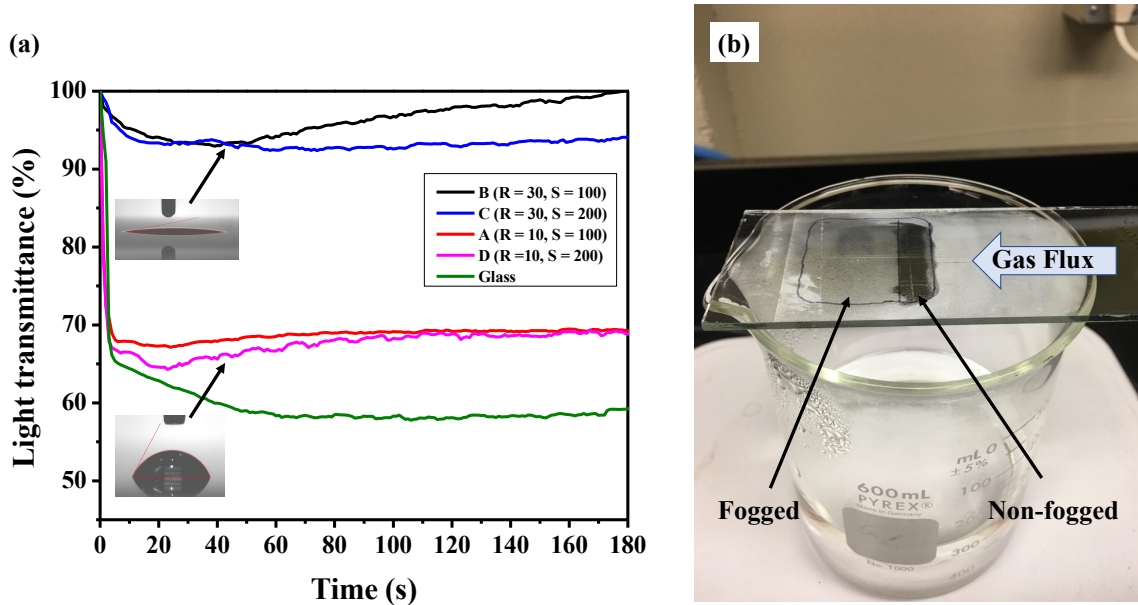
Figure 4.9: *(a) Percentage of light transmitted as a function of time through plasma-coated glasses fabricated under different [N₂O]/[TMCTS] ratios and [N₂O] + [TMCTS] sums. (b) Side view of a coated glass obtained at [N₂O]/[TMCTS] = 30 and [N₂O] + [TMCTS] = 100, when exposed to water vapor at 80°C (Fog testing was performed on areas located at 0.5 cm from the discharge).*

Regardless of the deposition conditions, transmittance curves exhibited a marked decrease within the first seconds followed by a very slow recovery. According to Chevallier and colleagues [195], the drop in light transmission observed within the first ~ 10 s is due to the scattering of incident light provoked by water drops and can be correlated with the anti-fogging performance by the following exponential relationship:

$$T = 100 \cdot e^{-kt} \qquad\qquad 0 < t < t_{T_{min}} \qquad (4.2)$$

where T is the light transmission (%), t is the elapsed time (s), and $t_{T_{min}}$ is the time required for light transmission to decrease to a minimum value.

Although simple, **Equation 4.2** proves successful in predicting whether a coated glass will be fogging-resistant or not, as small values of k are linked to a better anti-fogging performance. Indeed, the smaller the exponent k, the slower the drop in light transmission, and therefore, the more likely the coated glass to meet the anti-fogging requirements defined in the ASTM F659-06 standard, that is, transmittances above 80% after 30 s of exposure to water at 50°C (**Table 4.4**).

Table 4.4: *Typical data measured from the light transmission curves presented in* **Figure 4.9**. **The uncertainty in the A $_{\delta CH3}$/A $_{\delta Si-OH}$ ratios was calculated by error propagation using data from* **Table 4.2**.

Coating	k (s^{-1})	Transmittance at 30 s (%)	WCA (deg.)	A $_{\delta CH3}$/A $_{\delta Si-OH}$
B (R = 30, S=100)	0.12 ± 0.01	93.4	5–10	0.08 ± 0.05
C (R = 30, S=200)	0.20 ± 0.01	93.2	5–10	0.11 ± 0.02
A (R = 10, S= 100)	0.38 ± 0.03	67.8	62 ± 4	0.23 ± 0.05
D (R = 10, S=200)	0.44 ± 0.02	66.2	55 ± 5	0.17 ± 0.03
Uncoated glass	0.85 ± 0.03	61.4	72 ± 2	-

Fog testing revealed that uncoated glass fogged up promptly when exposed to the water vapor 50°C, while those coated with a TMCTS-based film maintained, in the worst case, ~ 66% of the light transmitted after 30 s of exposure (coating D). Further to this, the analysis of light transmittance at 30 s makes it possible to distinguish two families of coatings in terms of the anti-fogging response: those that meet the anti-fogging requirements (coatings deposited under over-stoichiometric [N$_2$O]/[TMCTS] ratio (R = 30)) and those that did not (coatings deposited under sub-stoichiometric [N$_2$O]/[TMCTS] ratio, R = 30). Coatings deposited under higher oxidizing conditions exhibited superior anti-fogging performance (Transmittances > 80% at 30 s) and featured a drop in light transmission (i.e., smaller values of k) faster than that observed in coatings prepared at low oxidant/precursor ratio (i.e.,

smaller values of k). Interestingly, the anti-fogging performance and the wetting behavior of the coatings can be correlated by the ratio $A_{(\delta s\ CH3\ in\ Si-(CH3)n)}/A_{(\delta\ Si-OH)}$, that is, the area below the IR band due to the symmetric bending of CH_3 groups to the area below the IR band due to silanol groups. It was found that the smaller the ratio, the lower the contact angle, and thus, the better anti-fogging performance.

Numerous studies on wetting phenomena have demonstrated that the wetting behavior of any surface is not only determined by its chemistry but also by its roughness. According to the Wenzel model [79], when a water droplet meets a rough surface, the resulting contact angle can be described as follows:

$$\cos \theta_{rough} = R_f \cos \theta_{smooth} \qquad (4.3)$$

where θ_{rough} is the contact angle measured on a rough surface (i.e., apparent contact angles), R_f is the roughness factor, which is defined as the ratio between the actual surface area in contact with the liquid drop and its projection onto a planar surface (equivalent to a smooth surface), and θ_{smooth} is the contact angle for an ideal smooth surface.

From **Equation 4.3**, it can be inferred that an increase in the roughness factor enhances the hydrophilicity of the coating (i.e., decrease in the water contact angle) if its water contact angle is below 90°. Nonetheless, the decrease in the WCA observed in the plasma-deposited coatings as the ratio increased from 10 to 30 cannot be due to an enhancement of surface roughness, because R_{rms} and R_a values remained virtually unchanged. Accordingly, the anti-fogging performance of the coatings prepared at R = 30 can primarily be explained in terms of a surface chemistry governed by the Si-OH groups (see FTIR and XPS results). These hydrophilic functionalities cause water drops to spread to form a continuous water film on the surface (WCA = 5–10°), resulting in a non-fogged surface such as that shown in **Figure 4.9b**.

4.6   Conclusions

A coating made from 1,3,5,7-tetramethylcyclotetrasiloxane (TMCTS), a cyclic siloxane precursor, with remarkable anti-fogging properties has been prepared for the first time. The chemistry, the surface topography, and the anti-fogging performance of coatings deposited under different operating conditions were investigated in detail. Light transmission measurements (ASTM F 659-06) revealed that the anti-fogging performance was governed by the $[N_2O]/[TMCTS]$ ratio and not by the $[N_2O] + [TMCTS]$ sum. The better anti-fogging performance observed in glass substrates coated under generous oxidant conditions ($[N_2O]/[TMCTS] = 30$)—compared with that of the coatings prepared under less oxidant conditions ($[N_2O]/[TMCTS] = 10$)—was due to their capacity to spread fog drops to form sheet-like water layers (WCA = 5–10° vs. 55–62°). Considering that coatings deposited at $[N_2O]/[TMCTS] = 30$ were very smooth ($R_{rms} = 2.4$–2.6 nm), their superhydrophilicity, and therefore, their resistance to fogging was attributed to a surface chemistry characterized with small $Si\text{-}CH_3/Si\text{-}OH$ ratios (i.e., concentration of surface $Si\text{-}OH$ groups greater than that of the $Si\text{-}CH_3$ ones), as revealed by FTIR and XPS. The independence of the anti-fogging performance on the $[N_2O] + [TMCTS]$ sum can be beneficial if the atmospheric pressure Townsend discharges are implemented on an industrial scale to fabricate anti-fogging coatings. In this regard, minimizing the total amount of gases injected into the discharge, while keeping a suitable $[N_2O]/[TMCTS]$ ratio, would undoubtedly reduce the manufacturing cost, thus bringing economic savings.

4.7   Acknowledgments

5 Anti-fogging coatings deposited by atmospheric pressure dielectric barrier discharges: A comprehensive structural and chemical analysis

Iván Rodríguez Durán[ab], Jacopo Profili[c], Luc Stafford[c], and Gaétan Laroche[ab]

[a]Laboratoire d'Ingénierie de Surface, Centre de Recherche sur les Matériaux Avancés, Département de Génie des Mines, de la Métallurgie et des Matériaux, Université Laval, 1065 Avenue de la médecine, Québec G1V 0A6, Canada.

[b]Centre de Recherche du Centre Hospitalier Universitaire de Québec, Hôpital St-François d'Assise, 10 rue de l'Espinay, Québec G1L 3L5, Canada.

[c]Département de physique, Université de Montréal, Montréal, Québec, Canada, H3C 3J7.

5.1 Résumé

Au cours des dernières années, un nombre croissant d'études ont été consacrées à la conception de revêtements destinés à être utilisés dans des applications traitant la formation de buée, tels que les endoscopes, les rétroviseurs des automobiles ou les lunettes de protection. Malheureusement, la mise en œuvre à l'échelle industrielle de la plupart des techniques de dépôt des couches utilisées à cette fin est une tâche ardue en raison des contraintes liées à une faible reproductibilité ou à des délais de fabrication trop longs. Il est donc nécessaire de développer des stratégies rentables et rapides compatibles avec la production en série pour la fabrication de revêtements antibuée. Dans cette optique, nous rapportons l'utilisation de décharges à barrière diélectrique à pression atmosphérique (AP-DBD) fonctionnant en présence de petites quantités d'oxyde nitreux (N_2O) et de 1,3,5,7-tétraméthylcyclotétrasiloxane (TMCTS), comme étant une approche prometteuse pour la fabrication en étape unique de verre antibuée. Il a été constaté qu'une augmentation du rapport [N_2O]/[TMCTS] ou de la puissance dissipée dans la décharge avait pour résultat des revêtements ayant une structure similaire à celle de la SiO_2 avec des groupes hydrophiles abondants, tels que Si-OH, C-O ou O=C-O, en surface. En raison de leur hydrophilicité (WCA< 40°), les revêtements fabriqués sous des ratios [N_2O]/[TMCTS] $\geq$ 30 et de puissance dissipée $\geq 0,25$ W cm^{-2} confèrent aux échantillons de verre une remarquable performance antibuée en présence de vapeur d'eau à 80°C. De plus, le protocole ASTM F 659-06 a révélé que les verres traités montraient une transmission de la lumière plus élevée ($T_{average} > 90\%$) que du verre non traité qui s'est embué dans les mêmes conditions ($T_{average} \approx 55\%$), après 30 s d'exposition à la vapeur d'eau à une température de 50°C.

5.2 Abstract

Over the past few years, a growing number of studies have focused on designing coatings for use in applications dealing with fogging such as endoscopes, automobile side view mirrors, or protective googles. Unfortunately, the implementation on an industrial scale of most of the coating techniques used for that purpose is a challenging task, because of constraints related either to low reproducibility or to long manufacturing times. Developing cost- and time-effective strategies compatible with mass production to fabricate anti-fogging coatings is thus necessary. With this goal in mind, we report on the use of atmospheric pressure dielectric barrier discharges (AP-DBDs) operated in the presence of small amounts of nitrous oxide (N_2O) and 1,3,5,7-tetramethylcyclotetrasiloxane (TMCTS), as a promising approach for the one-step fabrication of fog-resistant glass. It was found that an increase in either the [N_2O]/[TMCTS] ratio or the dissipated power resulted in coatings with a structure similar to that of SiO_2 with abundant hydrophilic groups, such as Si-OH, C-O, or O=C-O, on the surface. Because of their water-attracting features (WCA < 40°), coatings deposited under [N_2O]/[TMCTS] ratios ≥ 30 and dissipated power ≥ 0.25 W cm^{-2} conferred a remarkable anti-fogging performance to glass samples when placed over water at 80°C. Moreover, the ASTM F 659-06 protocol evidenced that coated glasses maintained a higher light transmittance ($T_{average} > 90\%$) after 30 s of exposure to water vapor at 50°C and exhibited a slow light transmission drop compared to that of uncoated glass, which promptly fogged up ($T_{average} \approx 55\%$).

5.3 Introduction

Experience shows that the loss of the "see-through" property and the blurred view typical of fogged surfaces can be incredibly frustrating. Eyeglasses steaming up during physical activity, condensation forming on the inside of windows during cold winters, or bathroom mirrors becoming blurred during a steamy shower are some obvious examples [402]. In addition to being upsetting, the fogging of surfaces has been shown to cause adverse effects on sectors of activity as diverse as the medical (e.g., endoscopic surgery [16]), the food industry (e.g., food packaging [239], refrigerated display cabinets [35], and greenhouses [295]), and the automotive (e.g., automobile windshields [11] and side view mirrors [328]) and photovoltaic sectors (e.g., solar cells [162]). Although it may appear surprising, these examples have at least two features in common. First, the solid surface on which water condenses is able to reduce the temperature of nearby water vapor below the dew point; and second, condensation takes the form of tiny droplets ("dropwise" condensation) [504,505]. Each droplet scatters the incident light in all directions leading to the formation of a whitish layer on the surface, commonly referred to as "breath figures" [506].

Numerous studies have evidenced that changing the morphology of water drops, for example, through the interaction with a (super)hydrophilic coating, is key to endowing surfaces with the anti-fogging feature [22]. The working principle of an anti-fogging coating with water-attracting features consists in spreading water drops across the surface to form sheet-like layers, and thus minimize light scattering [507]. Generally speaking, these coatings can be grouped according to their chemical nature, into two main categories, namely organic and inorganic coatings. Organic coatings are typically made from synthetic polymers bearing hydrophilic groups, such as hydroxyl, carboxyl, ester, amino, or amide groups. These include polyvinyl polymers (e.g., poly(vinyl alcohol) [195] and poly(vinylpyrrolidone) [175]); (metha)acrylic polymers (e.g., poly(acrylic acid) [194] and poly(methacrylic acid) [180]); and polyethers (e.g., poly(ethylene glycol) [178] and poly(ethylene glycol) dimethacrylate [177]), to name only a few. Nevertheless, the preparation of anti-fogging coatings from natural polymers, such as carboxymethyl cellulose [192], alginate [190], or chitosan [199] appears to have gained in popularity over the last five years. The distinctive features of these

macromolecules, including low cost, high availability, and non-toxic nature, may explain this interest. As regards inorganic coatings, intrinsically hydrophilic materials (e.g., SiO_2 [218], zeolites [169], graphene oxide [43], Cu_3SnS_4 [189], and In_2O_3-SnO_2 [229]) or materials that become superhydrophilic on exposure to UV light (e.g., TiO_2 [508] and ZnO [509]) are commonly used in coating formulations.

Despite the wide variety of available materials, the multistep nature of most of the deposition techniques explored thus far makes it difficult to produce anti-fogging coatings on an industrial scale. For this reason, less complex and less time-consuming alternatives compatible with mass production are necessary to fabricate fogging-resistant coatings in a more cost-effective manner. In this context, the implementation of plasma-assisted deposition techniques at atmospheric pressure may represent a promising coating approach, because of the advantages over conventional deposition techniques, including the environmentally friendly nature (solventless deposition) and the potential for industrial scale integration (one-step processing) [349].

Within the plasma deposition processes, the application of atmospheric pressure dielectric barrier discharges (AP-DBDs) is on the rise and under perpetual development [383]. In an AP-DBD, an ionized gas at atmospheric pressure (i.e., plasma) forms between two electrodes spaced a few millimeters apart upon application of voltage amplitudes typically in the kilovolt range. At least one of the electrodes is insulated from the plasma with a dielectric material to allow for the deposition process to occur at room temperature [378].

In recent years, the growing use of AP-DBDs for the fabrication of functional SiO_xC_y:H coatings from siloxane precursors, such hexamethyldisiloxane (HMDSO), tetramethyldisiloxane (TMDSO), or tetraethoxysilane (TEOS), has been most likely motivated by two reasons. First, the coatings' surface features (roughness and chemistry), can be tuned by adjusting the deposition parameters, including the dissipated power, the precursor flow rate, the inter-electrode distance, and the deposition time [383]. Second, deposition rates can be controlled by using the appropriate siloxane precursor (structure and

156

functional groups) [415]. Surprisingly, despite this versatility and the numerous studies on plasma-deposited siloxane coatings endowed with interesting features, such as gas barrier properties [510], abrasion [511] and corrosion [512] resistance, no papers on AP-DBDs for the fabrication of anti-fogging coatings are evidenced thus far.

The aim of this study is to use an atmospheric pressure dielectric barrier discharge (AP-DBD) to deposit anti-fogging coatings on glass substrate using nitrous oxide (N_2O) and 1,3,5,7-tetramethylcyclotetrasiloxane (TMCTS), as siloxane precursor. To comprehend how deposition parameters, namely the $[N_2O]/[TMCTS]$ ratio and the dissipated power, influence the anti-fogging performance, both the structure and the chemistry of the plasma-deposited coatings were thoroughly analyzed. Surface chemistry of coatings was studied by X-ray photoelectron (XPS) and Fourier transform infrared (FTIR) spectroscopies. Surface topography was investigated by atomic force microscopy (AFM). Wetting behavior of coatings was studied by contact angle measurements and coating thickness was measured by profilometry. The resistance to fogging was assessed by measuring the light transmission of the coated glasses as a function of time (ASTM F 659-06 standard) and by photographing the samples following exposure to water at 80°C.

5.4 Materials and methods

5.4.1 Materials and sample preparation

The siloxane precursor used in this study was 1,3,5,7-tetramethylcyclotetrasiloxane $[(CH_3)HSiO]_4$ ($\geq$ 99.5%, Sigma-Aldrich), also known as "TMCTS" (**Figure 5.1**).
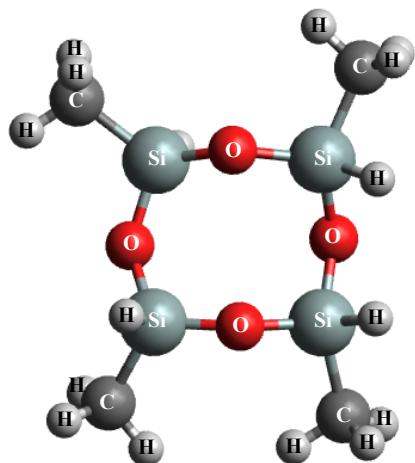
Figure 5.1: *Structure of 1,3,5,7-tetramethylcyclotetrasiloxane (TMCTS).*

Rectangular-shaped glass samples (13 cm × 5 cm × 2 mm) were kindly provided by Multiver Ltd (Québec, QC, Canada). Prior to the deposition process, glass samples were ultrasonically cleaned twice; the first time with acetone for 10 min to remove persistent pollutants followed by rinsing with methanol; and the second time with soapy water for 10 min to remove any organic remnant. Afterwards, glass samples were rinsed with de-ionized water for 10 min and wiped dry with a cotton cloth (Amplitude Kappa™, Contect, Inc., Spartanburg, SC, USA). Methanol and acetone were purchased from commercial alcohols (Ontario, ON, Canada) and Laboratories MAT (Québec, QC, Canada), respectively. Alumina sheets used in the manufacture of the DBD reactor were acquired from Goodfellow (Huntingdon, UK, England). Nitrogen (N_2, grade 4.8, plasmogenous gas) and nitrous oxide (N_2O, 99.998%, oxidant gas) were provided by Linde (Québec, QC, Canada).

5.4.2 DBD setup and deposition conditions

A schematic of the atmospheric pressure DBD deposition system is shown in **Figure 5.2a**. The DBD setup is integrated by two parallel-plate electrodes spaced 1 mm apart. The AC-driven upper electrode is a 640-µm-thick alumina sheet covered with a silver-based conductive paint and the bottom electrode is a grounded stainless-steel plate. Glass samples were placed on this electrode prior to coating deposition. The atmospheric pressure DBD was operated in the Townsend regime with applied peak-to-peak voltage amplitudes between 13

158

and 17 kV and voltage frequencies between 3 and 6 kHz (**Figure 5.2b**). A minimum voltage of ~ 12.5 kV was required to generate the plasma between the two electrodes (i.e., breakdown voltage). Using LabVIEW^{TM} software, the average power per unit area (W cm^{-2}), hereinafter referred to as "dissipated power" (DP), was calculated as the product of the applied voltage and the discharge current integrated over one discharge period. All waveforms were recorded on a numerical oscilloscope (DPO2000, Tektronix Inc., Beaverton, OR, USA).
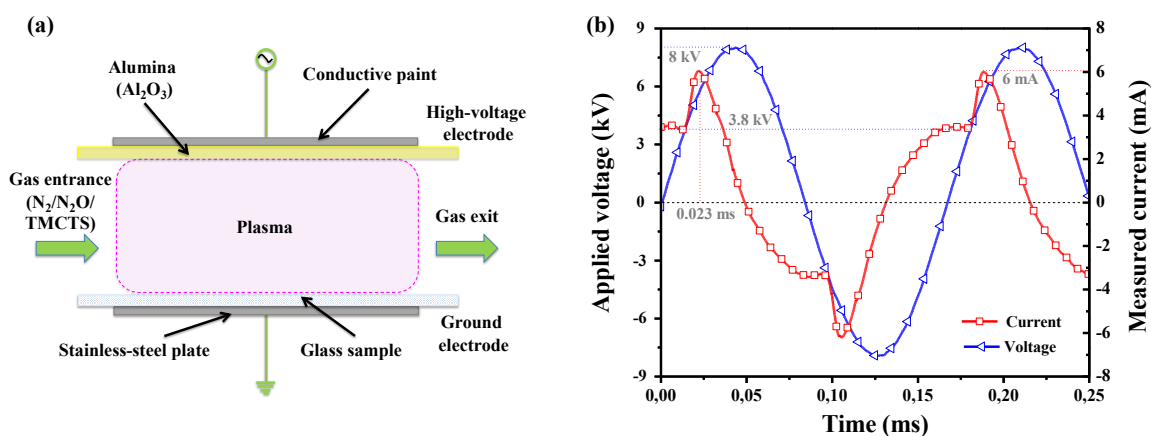
Figure 5.2: (a) DBD setup showing gas flow, electrodes, and glass sample. (b) A current-voltage characteristic of an atmospheric pressure TMCTS/N$_2$O/N$_2$ discharge operating in the homogeneous regime or "Townsend" regime (f = 6 kHz, V$_{applied}$ = 16 kV$_{peak-to-peak}$).

A gas inlet composed of two independent lines made it possible to carry N$_2$ at 4 L min^{-1} and N$_2$O at variable flow rate to the inter-electrode space, while ensuring a pressure of 760 mm Hg over the course of the deposition process. Flow rate of both gases was measured by mass flow controllers (Bronkhorst^{TM}, Ruurlo, Holland). A third line enabled to inject a TMCTS aerosol in N$_2$ into the inter-electrode space at 1 L min^{-1} via a nebulizer (Mira Mist CE^{TM}, Burgener Research Inc., Mississauga, ON, Canada) coupled to a syringe pump (Fisherbrand^{TM}, Thermo Fisher Scientific, Runcorn, Cheshire, UK). This line was heated at 40°C to prevent nebulized TMCTS from condensing inside. The deposition time was set at 20 min and coating characterization was performed at a distance of 0.5 cm from the entrance to the discharge. **Table 5.1** summarizes the deposition parameters that were varied in this study.

Table 5.1: *Deposition parameters. [X] indicates concentration in parts per million (ppm)*

Experiment	Sample code	[TMCTS] (ppm)	[N₂O] (ppm)	[N₂O]/[TMCTS]	Dissipated power (W cm⁻²)
	A1		0	0	
	A2		100	10	
A	A3	10	200	20	0.25
	A4		300	30	
	A5		400	40	
	B1				0.10
B	B2	10	300	30	0.40
	B3				0.55
	B4				0.70

[N₂O]/[precursor] ratios were set at 0, 10, 20, 30, and 40, taking into account the following reaction between TMCTS and the oxidant in the discharge:

$$[H(CH_3)SiO]_4 + 20\ N_2O \rightarrow 40\ N_2 + 4\ CO_2 + 8\ H_2O + 4\ SiO_2 \tag{5.1}$$

5.4.3 Characterization of surface chemistry

5.4.3.1 Attenuated total reflectance Fourier transformed infrared spectroscopy (ATR-FTIR)

Functional groups present in the coatings were investigated by means of a FTIR spectrophotometer (Cary 660 FTIR, Agilent Technologies, Victoria, Australia) equipped with a DLaTGS detector (deuterated L-alanine-doped triglycine sulfate), a Ge-coated KBr beam splitter (Harrick Scientific Products, Pleasantville, NY, USA), and a Split-Pea accessory (Harrick Scientific Products, Pleasantville, NY, USA). Spectra over the 400–4000 cm⁻¹ range were recorded by the co-addition of 128 scans with a resolution of 4 cm⁻¹ and normalized with respect to the intensity of the band due to the Si-O-Si asymmetric stretching, ν_a Si-O-Si (1000–1200 cm⁻¹). Under the same deposition conditions, spectra

reported here (in triplicate) displayed similar spectral features. Origin software (Origin Lab Corp. v 8.5) was used to curve fit overlapping peaks following baseline correction.

5.4.3.2 X-ray photoelectron spectroscopy (XPS)

Surface composition of plasma-deposited coatings was studied by X-ray photoelectron spectroscopy (XPS) using a PHI 5600-ci spectrometer (Physical Electronics, Chanhassen, MN, U.S.A). For survey spectra (0–1400 eV), samples were analyzed using a standard Al Kα X-ray source (1486.6 eV) at 300 W, while a standard Mg Kα X-ray source (1253.6 eV), also operated at 300 W, was used to acquire high-resolution spectra. In either case, no charge neutralization was required. Photoelectrons coming from an analyzed area of ~ 0.5 mm^2 were detected at a take-off angle of 45º from the sample normal. Charge referencing was carried out by setting the binding energy of the adventitious carbon C1s feature at 285.0 eV. The analysis chamber was kept at a pressure below 10^{-6} Pa during each acquisition. The curve fitting of the C1s envelopes was performed using Gaussian-Lorentzian functions following Shirley-type background subtraction. All photoemission peak areas were calculated by PHI MultiPak^{TM} software v 9.3. Three analyses per sample were performed to provide an average atomic percentage of surface elements along with their corresponding standard deviations.

5.4.4 Characterization of surface topography

5.4.4.1 Atomic force microscopy (AFM)

Surface topography of coated glasses was investigated at the nanoscale by means of an atomic force microscope (Dimension 3100, Veeco Digital Instruments by Bruker, Santa Barbara, CA, USA) operated in the tapping mode. A standard etched-silicon cantilever system (OTESPA probe, Bruker Nano Surface Division, Santa Barbara, CA, USA) was used for the acquisition of topographical images at a scan angle of 90°. The radius of curvature and the aspect ratio of the silicon tip were < 10 nm and ~ 1.6/1, respectively. AFM images were recorded at a scan rate of 0.5 Hz with a line resolution of 256 × 256 and analyzed by

NanoScope Analysis software v 1.5 (Bruker). Surface roughness was evaluated on $10 \times 10\ \mu m^2$ (tip velocity = 50 $\mu m\ s^{-1}$) and $1 \times 1\ \mu m^2$ (tip velocity = 5 $\mu m\ s^{-1}$) areas and characterized by the mean roughness (R_a) and the root mean square roughness (R_{rms}).

5.4.5 Coating thickness and deposition rate measurements

Coating thickness were measured using a DektakXT^{TM} profilometer (Bruker Nano Surface Division, Tucson, AZ, USA) with a stylus force of 1 mg (radius = 5.0 mm). Coatings were first scratched off with a pointed tip tweezers in direction of gas flow. Afterwards, the height of the as-formed steps was measured in triplicate at 0.5 cm from the entrance of the discharge and perpendicular to gas flow. Lasting for 10 s, each acquisition was performed on a distance of 300 μm. Deposition rate of the coatings was calculated by dividing the as-measured thickness by the deposition time.

5.4.6 Wetting behavior of the coatings

The wetting behavior of uncoated and coated glass samples was investigated by contact angle measurements using the sessile drop method. To this end, 3 μL of ultrapure water were dropped from a height of 10 mm to ensure consistency in contact angle measurements. Static contact angles were measured following the pinning of the three-phase contact line using a Video Contact Angle System (VCA-2500 XETM, AST products Inc., Billerica, MA, USA). Ten contact angles per sample were measured to provide an average value with its corresponding standard deviation.

5.4.7 Anti-fogging performance assessment

Assessment of the anti-fogging performance was carried out according to the protocol described in the ASTM F 659-06 standard [332,333] (European version: BS EN 166-168). Briefly, coated glasses were placed over a bath containing water at 50°C to measure light of

wavelength 590 nm passing through the sample as a function of time. For a coated glass to be considered anti-fogging, the time required for the light transmittance to decrease to 80% of its initial value (non-fogged) must be lower than or equal to 30 s. The anti-fogging performance was also tested by visual inspection. In this case, coated glasses were photographed after being placed on an Erlenmeyer flask containing 200 ml of water at 80°C for 15 s (hot-fog test).

5.5 Results and discussion

5.5.1 Structural analysis of the coatings

Thoroughly describing the chemistry and the structure of the plasma-deposited coatings is key to substantiating their anti-fogging performance (**section 5.5.4**). For this reason, IR features have been compared with those of the TMCTS and discussed, in terms of band broadening and frequency shifts, in this section. **Figure 5.3** shows the assignment of major bands in the IR spectrum of TMCTS.
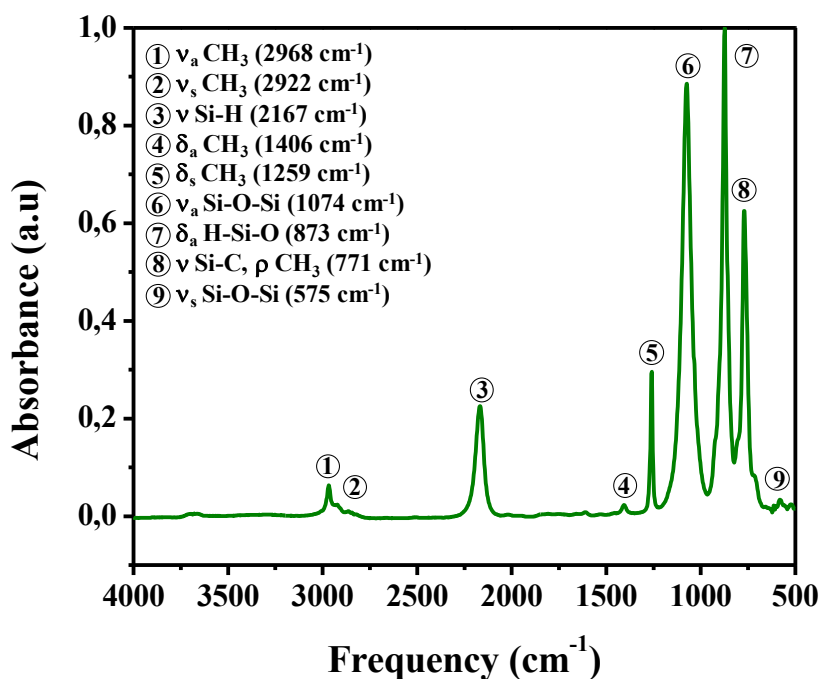
Figure 5.3: *IR spectrum of liquid TMCTS (ν= stretching, δ = bending, ρ = rocking, a = asymmetric, and s = symmetric).*

Vibrational modes of Si-O-Si groups resulted in two spectral features, one at 1074 cm^{-1} due to the asymmetric stretching (ν_a), and other at 575 cm^{-1} due to the symmetric stretching (ν_s) [412]. These vibrational modes arise from the 4-membered tetrahedral ring in the TMCTS molecule, which is characterized by a Si-O-Si angle of 160.5° and a D$_{4h}$ point symmetry [513]. Asymmetric and symmetric stretching of C-H in CH$_3$ groups were observed at 2968 and 2922 cm^{-1}, respectively [472,514]. Frequencies at which these vibrations occurred were similar to those reported in hydrocarbon compounds. Bending modes of methyl groups were, however, found at lower frequencies: the asymmetric (δ_a) and symmetric (δ_s) bending of methyl groups were observed at 1406 and 1259 cm^{-1}, respectively [401,472]. These absorptions were accompanied by a band at 771 cm^{-1}, which can be attributed to CH$_3$ rocking (ρ) and Si-C stretching ($\nu_{a,s}$) vibrations in the (CH$_3$)HSiO$_2$ moieties. Two intense bands at 2167 and 873 cm^{-1} evidenced the presence of Si-H bonds in the precursor; the first one can be assigned to the stretching of Si-H groups (ν Si-H) while the second one can be assigned the asymmetric bending of H-Si-O groups (ν_a H-Si-O) [472].

Coatings deposited on glass substrates using an atmospheric pressure N$_2$/N$_2$O Townsend discharge displayed many IR spectral features similar to those observed in the liquid precursor and several new ones. **Figure 5.4** shows infrared spectra of selected sections of coatings deposited under different [N$_2$O]/[TMCTS] ratios and 0.25 W cm^{-2}. Absorptions characteristic of CH$_3$ groups, such as the symmetric (δ_s) and asymmetric (δ_a) bending in Si-CH$_3$ at 1273–1280 cm^{-1} and 1410 cm^{-1}, respectively, became less intense as the amount of the oxidant in the discharge increased. Similarly, symmetric (ν_s) and asymmetric (ν_a) stretching of C-H at 2909 and 2972 cm^{-1}, respectively, as well as the Si-C ($\nu_{a,s}$) stretching and CH$_3$ rocking (ρ) vibrations in the 750–790 cm^{-1} range also became attenuated, substantiating the oxidative removal of methyl groups (**Figure 5.4a**). The sharp decrease in the intensity of bands pertaining to Si-H groups provides evidence to support the high reactivity of the Si-H bond, compared with that of Si-C or C-H bonds (**Figures 5.4b** and **5.4d**) [417]. Moreover, the presence of two very weak bands at 2170 and 2190 cm^{-1} reveals that the complete removal of the Si-H groups is not possible in the absence of N$_2$O in the discharge. This doublet may be due to stretching vibrations of unreacted Si-H bonds in

H$_2$SiO$_2$ and HSiO$_3$ moieties, respectively [515]. The Si-O-Si asymmetric stretching (ν_a Si-O-Si) appeared at frequencies lower than that of the liquid precursor (1074 cm^{-1}). Coupled with the emergence of a shoulder at ~ 1150 cm^{-1}, this feature broadened and shifted from 1026 to 1072 cm^{-1}, as the [N$_2$O]/[TMCTS] ratio increased from 0 to 40 (**Figure 5.4d**).
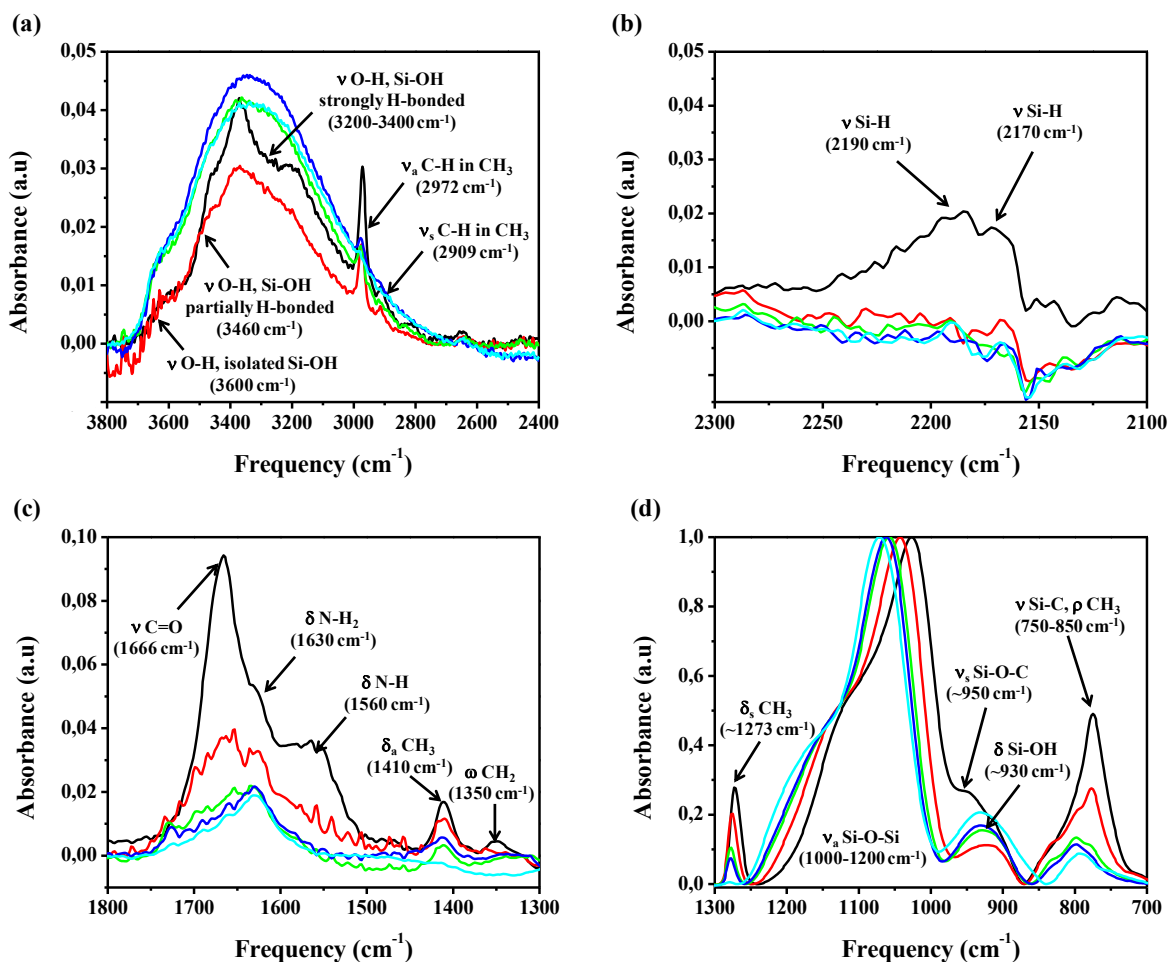
Figure 5.4: *IR spectra of (a) 2400−3800 cm^{-1}, (b) 2100−2300 cm^{-1}, (c) 1300−1800 cm^{-1}, and (d) 700−1300 cm^{-1} regions of plasma-deposited coatings under different [N$_2$O]/[TMCTS] ratios, namely, 0 (in black), 10 (in red), 20 (in green), 30 (in navy blue), and 40 (in light blue).*

Coatings exhibited several features that were not observed in the liquid precursor. These include a very weak band at 1350 cm^{-1} due to CH$_2$ wagging (ω) in Si-CH$_2$-Si entities (R = 0), a strong band at 920−950 cm^{-1} due to the Si-O bending in silanols (i.e., Si-OH groups), and a broad band in the 3000−3700 cm^{-1} range due to O-H stretching vibrations. In view of the

features at 1630 and 1560 cm^{-1} (**Figure 5.4c**), some contribution to the last band may also come from the N-H stretching in NH$_2$ or -NH- groups. The CH$_2$ wagging mode has been reported to provide hints on how the siloxane precursor polymerizes in the plasma phase [516], which intimates that the Si-CH$_2$-Si "bridges" were formed in a manner similar to that reported in coatings deposited from HMDSO/Ar and HMDSO/He plasmas [471]. The weak band at 1666 cm^{-1} can be attributed to the stretching of carbonyl group (C=O) in carboxyl (COOH) or amide functionalities (CONH) [517].

In general terms, effects similar to those described above were observed in coatings deposited under different levels of dissipated power (DP) and [N$_2$O]/[TMCTS] = 30 (**Figure 5.5**). Absorptions related to CH$_3$ groups, such as ν Si-C/ρ CH$_3$ (700–850 cm^{-1}), symmetric and asymmetric bending of CH$_3$ in Si-(CH$_3$)$_n$ (1275–1279 cm^{-1} and 1410 cm^{-1}, respectively), and stretching vibrations of C-H in CH$_3$ (2900–3000 cm^{-1}) decreased with the dissipated power. (**Figures 5.5a** and **5.5c**). The diminishment of these features was accompanied by the complete loss of the Si-H functionality (**Figure 5.5b**). The Si-O-Si asymmetric stretching, which also exhibited a shoulder at ~ 1170 cm^{-1}, broadened and shifted from 1040 to 1069 cm^{-1} as the dissipated power increased (**Figure 5.5d**).

As in the case of coatings prepared under different [N$_2$O]/[TMCTS] ratios, the broad band between 3000 and 3700 cm^{-1} substantiates the presence of silanol groups (band at 920 cm^{-1}) and amine groups (band at 1630 cm^{-1}) in the coatings. Here, the absence of the CH$_2$ wagging supports the idea that the formation of Si-CH$_2$-Si entities is not possible when N$_2$O is added in the discharge. In addition, coatings prepared either in the absence of oxidant (R = 0) or under very low dissipated power (0.1 W cm^{-2}) exhibited two features that deserve to be mentioned. The first one at ~ 950 cm^{-1} (**Figure 5.4d**) may be attributed to the Si-O-C symmetric stretching [518] (**Figure 5.4d**), while the second one at 910 cm^{-1} may be attributed to the O-Si-O bending in dangling bonds "Si-O$^-$"(**Figure 5.5d**) [519].

(a)

Absorbance (a.u)

ν O-H, Si-OH strongly H-bonded (3200-3400 cm^{-1})

ν$_a$ C-H in CH$_3$ (2976-2980 cm^{-1})

ν$_s$ C-H in CH$_3$ (2914-2916 cm^{-1})

ν O-H, Si-OH partially H-bonded (3460 cm^{-1})

ν O-H, isolated Si-OH (3600 cm^{-1})

Frequency (cm^{-1})

(b)

Absorbance (a.u)

Frequency (cm^{-1})

(c)

Absorbance (a.u)

δ N-H$_2$ (1630 cm^{-1})

δ$_a$ CH$_3$ (1410 cm^{-1})

Frequency (cm^{-1})

(d)

Absorbance (a.u)

δ$_s$ CH$_3$ (~1275 cm^{-1})

ν$_a$ Si-O-Si (1000-1200 cm^{-1})

δ Si-OH (910-940 cm^{-1})

δ Si-O-Si (800 cm^{-1})

ν Si-C, ρ CH$_3$ (750-850 cm^{-1})

Frequency (cm^{-1})

Figure 5.5: IR spectra of (a) 2400–3800 cm^{-1}, (b) 2100–2300 cm^{-1}, (c) 1300–1800 cm^{-1}, and (d) 700–1300 cm^{-1} regions of plasma-deposited coatings under different power dissipated in the discharge, namely 0.10 (in black), 0.25 (in red), 0.40 (in green), 0.55 (in navy blue), and 0.70 W cm^{-2} (in light blue).

Further analysis of some of the most relevant IR bands provides valuable structural information on the coatings. Focusing on the unresolved feature between 700 and 850 cm^{-1} makes it possible to evaluate how many CH$_3$ groups are bonded to one silicon atom. In coatings prepared in the absence of oxidant (R = 0) or under very low DP (0.1 W cm^{-2}), the frequency at which this feature appears (775–777 cm^{-1}), suggests that most of the CH$_3$ groups were included in "T" units (i.e., O$_3$Si-(CH$_3$)$_1$). That said, the asymmetry of this band provides strong evidence of the presence of "D" (i.e., O$_2$Si-(CH$_3$)$_2$) and "M" (i.e., O$_1$Si-(CH$_3$)$_3$) units in the coatings. Indeed, in M-units, CH$_3$ rocking occurs at ∼ 845 cm^{-1}, while the ν$_{a,s}$ Si-C stretching vibrations occur at 760 and 845 cm^{-1} [471,476]. Similarly, in D-units, CH$_3$ rocking

at 855 cm^{-1} is always accompanied by the asymmetric and symmetric stretching vibrations of Si-C at 800 and 690 cm^{-1}, respectively [471,474,476]. Surprisingly, an increase in the dissipated power or the [N$_2$O]/[TMCTS] ratio translated to a loss of T-units, thus supporting the removal of methyl groups mentioned above. However, the various overlapping features observed even at very high levels of DP or high [N$_2$O]/[TMCTS] ratios, makes it difficult to determine the precise contribution of the remaining D- and M-units.

These findings were consistent with the changes observed in the symmetric deformation mode of CH$_3$ groups. This spectral feature has been shown to shift to high frequencies as the number of CH$_3$ groups bonded to the silicon atom in (CH$_3$)$_n$-SiO$_{4-n}$ units (where n = 1, 2, and 3) diminishes. In general, this band appears at ~ 1275 cm^{-1} in T-units, at ~ 1265 cm in D-units, and at ~ 1255 cm^{-1} in M-units [520–523]. Coupled with the asymmetry of this absorption, the observed narrowing and shift of up to 5 cm^{-1} to high frequencies as both the dissipated power and the [N$_2$O]/[TMCTS] ratio increased, substantiates the prevailing presence of T-units over that of D- and M-units (not shown).

The presence of Si-C and C-H bonds noticed in coatings deposited at high DP or high N$_2$O concentration suggests that the energy provided per TMCTS molecule did not suffice to yield highly crosslinked coatings [524]. With this in mind, it can be argued that the lack of energy per siloxane molecule is somehow responsible for the formation of Si-OH groups, as supported by the bands at 920–940 cm^{-1} and 3000–3800 cm^{-1}. Interestingly, the amount of these hydrophilic functionalities was found to increase with the N$_2$O concentration in the plasma phase (**Figures 5.4a** and **5.4d**). In addition, the overlapping features in the 3000–3800 cm^{-1} region reveal that various Si-OH populations [525,526], including isolated, partially H-bonded, and strongly H-bonded Si-OH groups, were present in the coatings. Interestingly, these populations were shown to vary with the [N$_2$O]/[TMCTS] ratio. Thus, the main contributions to this band came from isolated and partially H-bonded Si-OH groups when [N$_2$O]/[TMCTS] ≤ 10, while strongly H-bonded Si-OH groups were observed for greater [N$_2$O]/[TMCTS] ratios.

Surprisingly, this does not appear to apply to coatings deposited under different levels of dissipated power. As a matter of fact, both the O-H bending and stretching vibrations were nearly unaffected by changes in the DP, as neither significant intensity variations nor band broadenings were observed (**Figures 5.5a** and **5.5d**). As in the case of coatings deposited at $R \geq 20$, the broad and asymmetric band at 3430 cm^{-1} evidenced the presence of strong and moderately strong H-bonded silanols.

Regarding the Si-O-Si features, three points deserve to be mentioned. First, the band resulting from the Si-O-Si asymmetric stretching can be resolved into three [412,527,528] or four components [529–531] (**Figure 5.6a**). According to Grill et al. [412] the first component at 1135–1150 cm^{-1} arises from Si-O-Si entities with angles > 144°, such as those found in cage-like structures. The second component at 1065–1070 cm^{-1} includes absorptions originating from a siloxane network with a Si-O-Si angle of ~ 144°, such as that of a fully relaxed SiO$_2$, and preserved TMCTS cycles. The third component at 1023–1035 cm^{-1} arises from strained siloxane rings with D$_{3h}$ point symmetry and various silicon sub-oxidized states, such as O-Si-Si and O-Si-C, with Si-O-Si angles < 144°. Second, plasma deposition conducted either under very high oxidizing conditions ($R = 40$) or under very high dissipated power (0.7 W cm^{-2}), yielded coatings with a Si-O-Si bending and a Si-O-Si stretching vibrations resembling those of the stoichiometric SiO$_2$ (800 cm^{-1} and 1080 cm^{-1}, respectively) [532]. Not surprisingly, this is consistent with the loss of Si-X end groups (X = H, CH$_3$, O-CH$_3$), which obviously hinder the formation of a SiO$_2$ structure [524]. Third, the shift to high frequencies observed in the ν_a Si-O-Si can primarily be ascribed to a variation in the average Si-O-Si bond angle [533]. This issue was addressed in the late 1980s by Sen and Galeener [534,535], who proposed a model based on the nearest neighbor atoms interactions, by which the frequency at which the ν_a Si-O-Si occurs can be calculated, as follows:

$$\nu_a = \frac{1}{2\pi c}\left[\left(\frac{k}{m_O}\right)(1 - \cos\theta) + \left(\frac{4k}{3m_{Si}}\right)\right]^{1/2} \qquad (5.2)$$

169

where k is the force constant of the Si-O bond (N m^{-1}), m_O and m_{Si} are the mass of oxygen and silicon atoms (kg), respectively; and θ is the average Si-O-Si bond angle (deg.).

Should the force constant k remain unchanged, that is, the Si-O bond length is assumed not to vary with the carbon content in the coating, the above equation thus becomes [536]:

$$v_a = v_0 \sin(\theta/2) \tag{5.3}$$

where $v_0 = 1135.6$ cm^{-1} for an average Si-O-Si bond angle of 144° (thermally grown SiO$_2$ coatings, v_a Si-O-Si at 1080 cm^{-1}).

It was found that the Si-O-Si bond angle as calculated from **Equation 5.3**, increases linearly with the [N$_2$O]/[TMCTS] ratio and the dissipated power (**Figure 5.6b**).
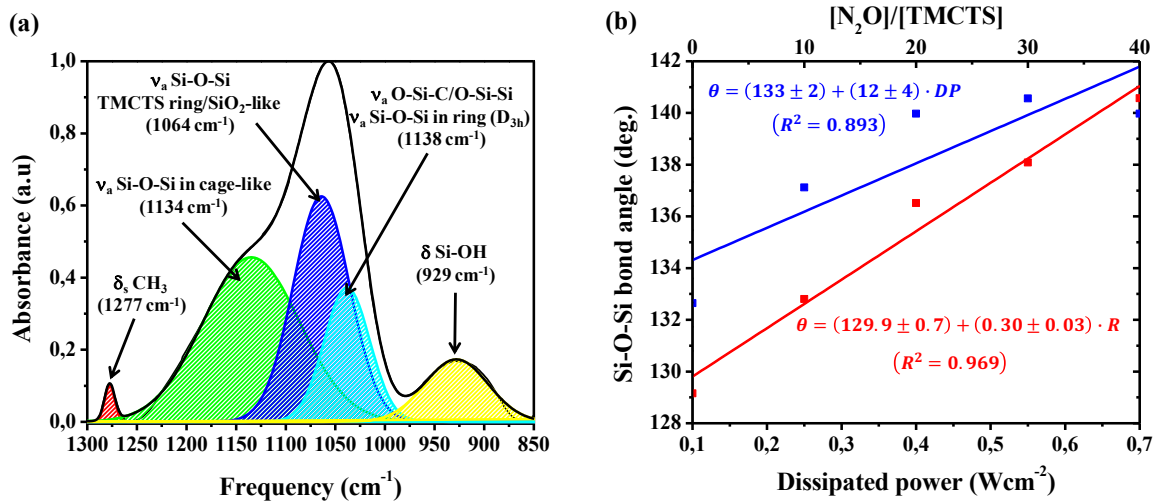
Figure 5.6: Curve fitting of the 850–1300 cm^{-1} region (deposition conditions: [N$_2$O]/[TMCTS] = 30, DP = 0.25 W cm^{-2}). (b) Variation of the Si-O-Si bond angle as a function of the [N$_2$O]/[TMCTS] ratio and the dissipated power.

In the case of coatings fabricated under different oxidant/precursor ratios, the shift in v_a Si-O-Si from 1026 to 1072 cm^{-1} can be attributed to an increase in the Si-O-Si bond angle from 129 to 141°, with a rate of change of ~ 0.3°/[N$_2$O]/[TMCTS] (red straight line Figure 6b).

Similarly, the shift in ν_a Si-O-Si from 1040 to 1067 cm^{-1}, with a rate of change of ~ 12°/W cm^{-2}, observed in coatings produced under different DP, can be attributed to an increase in the average Si-O-Si bond angle from 132 to 140° (blue straight line in **Figure 5.6b**).

In investigating SiO$_x$C$_y$:H coatings deposited from bistrimethylsilylmethane, Kim and colleagues [536] reported a similar trend between ν_a Si-O-Si and the carbon content. In their study, it was shown that the fewer the number of Si-CH$_3$ groups in the coatings, the higher the frequency at which ν_a Si-O-Si occurred. These authors argued that the shift in the ν_a Si-O-Si frequency was due to the conversion of Si-C groups into Si-O ones. To illustrate this point, let us consider a T-unit (i.e., O$_3$Si-(CH$_3$)$_1$). When the Si-C bond is converted into a new Si-O one, the bond electron density is further away from the silicon atom than it was in the Si-C bond, because of the greater electronegativity of oxygen (χ_O (3.44) > χ_C (2.55)). As a result, the electrostatic repulsion between the as-formed Si-O bond and the other three Si-O bonds is lessened and consequently, the Si-O-Si bond angle in the resulting Q-unit (i.e., SiO$_4$) increases concomitantly.

5.5.2 Surface composition of the coatings

XPS survey spectra revealed that the surface of coatings was composed of silicon, oxygen, carbon, and nitrogen, with atomic percentages (at. %) and elemental ratios (O/Si and C/Si) depending on the dissipated power and the oxidant/precursor ratio (**Table 5.2**).

When compared with the percentage composition of TMCTS, plasma deposition conducted under different [N$_2$O]/[TMCTS] ratios or dissipated power yielded coatings with more oxygen and much less carbon. The average carbon percentage decreased monotonically from ~ 25 to 4% as the oxidant/precursor ratio went from 0 to 40. This reduction, which was accompanied by an increase in the oxygen content from ~ 42 to 70%, substantiates the loss of CH$_3$ groups observed in IR spectra. Interestingly, increasing the DP at intervals of

0.15 W cm^{-2} from 0.10 to 0.70 W cm^{-2}, did not lead to a gradual variation in the percentages of carbon and oxygen. The average carbon content was approximately 5% in all of the analyzed coatings, except for those prepared at 0.10 W cm^{-2}, in which carbon percentage was as high as 21%. The levelling off of the carbon content suggests that the fragmentation of TMCTS molecules in the plasma reaches saturation at 0.25 W cm^{-1}.

Similarly, plasma deposition carried out at 0.10 W cm^{-2}, yielded coatings with an oxygen content less than that found in the coatings fabricated at $\geq$ 0.25 W cm^{-2}, which was shown to level off at $\sim$ 68%. The oxidative removal of carbon coupled with a silicon percentage that remained nearly unchanged explains the C/Si ratios ranging from 0.14 to $\sim$ 1. It is interesting to note that coatings prepared in the absence of the oxidant ([N$_2$O]/[TMCTS] = 0) or under low dissipated power (0.10 W cm^{-2}) exhibited a C/Si ratio close to that of the TMCTS (C/Si $\approx$ 1).

Table 5.2: *Surface composition of the coatings (at. %). * Percentage composition of TMCTS.*

	Sample	Si2p	O1s	C1s	N1s	O/Si	C/Si
A1	R = 0	26 ± 2	42 ± 5	25 ± 6	7 ± 3	1.6 ± 0.4	1.0 ± 0.1
A2	R = 10	27 ± 1	54 ± 4	19 ± 4	0.5 ± 0.3	2.0 ± 0.2	0.7 ± 0.2
A3	R = 20	26.0 ± 0.9	59 ± 3	14 ± 3	0.4 ± 0.1	2.3 ± 0.1	0.6 ± 0.2
A4	R = 30	28 ± 1	67.2 ± 0.8	4.6 ± 0.3	0.08 ± 0.08	2.4 ± 0.1	0.16 ± 0.02
A5	R = 40	26.8 ± 0.6	69.5 ± 0.4	3.6 ± 0.4	0.1 ± 0.1	2.6 ± 0.1	0.14 ± 0.01
B1	0.10 W cm^2	26. 1 ± 0.5	52 ± 3	21 ± 3	0.9 ± 0.9	1.9 ± 0.1	0.8 ± 0.1
B2	0.40 W cm^2	27.7 ± 0.4	67 ± 1	5 ± 1	0.1 ± 0.1	2.43 ± 0.05	0.18 ± 0.04
B3	0.55 W cm^2	28.0 ± 0.6	68 ± 2	4 ± 2	0.1 ± 0.2	2.42 ± 0.09	0.16 ± 0.06
B4	0.70 W cm^2	27.4 ± 0.7	67.2 ± 0.8	5 ± 1	0.1 ± 0.1	2.45 ± 0.08	0.20 ± 0.03
	TMCTS*	33.3	33.3	33.3	-	1	1

The incorporation of oxygen from the discharge may account for the O/Si ratios exceeding unity (O/Si ratio in TMCTS). Several studies on atmospheric pressure N$_2$/N$_2$O plasmas

[537,538] have evidenced the dissociation of N_2O following impact with N_2 $(A^3\Sigma_u^+)$ metastables, as a potential source of such element in the plasma phase. Electron-impact dissociation of N_2O to produce oxygen is also possible [539,540], yet less likely to occur, given that electron number density is approximately 10^5 times less than that of N_2 $(A^3\Sigma_u^+)$ metastables [496]. In addition, most of the O/Si ratios were between 2 (O/Si ratio in SiO_2) and 2.6. These values substantiate the presence of Si-OH groups in the coatings (FTIR results), and lead us to believe that, on average, the building units (i.e., M, D, T, and Q) at the coating surface bear at least one OH group.

It is worth highlighting that coatings prepared either in the absence of oxidant (R = 0) or under very low DP (0.1 W cm^{-2}) exhibited O/Si ratios below 2, yet surprisingly possessed Si-OH groups. That said, such ratios are compatible with the presence on the surface of OH-containing surface entities, such as $O_2Si(OH)(CH_3)$ units (O/Si = 2), combined, for example, with M-units (O/Si = 1). Using different siloxane precursors (i.e., tetramethylcyclotetrasiloxane, dimethyldimethoxysilane, and trimethylsilane), Fisher's group [411] also found that OH-containing SiO_xC_y:H coatings can be obtained in the absence of an oxidant in the discharge.

Considering the foregoing, it can be said that, depending on the $[N_2O]/[TMCTS]$ ratio and the dissipated power, coatings are either organic SiO_xC_y:H or inorganic SiO_2-like, both with a non-negligible amount of surface silanols. In addition to the oxygen, the slight amount of nitrogen incorporated into the coatings concurs with previous findings reported by Gherardi et al. [499] with coatings prepared from hexamethyldisiloxane (HMDSO) using a N_2/N_2O Townsend discharge. Interestingly, soft deposition conditions (e.g., $[N_2O]/[TMCTS] = 0$, DP = 0.1W cm^{-2}) correlated with enhanced nitrogen incorporation efficiency, which reaches up to 7%.

Although XPS analyses were consistent with the results obtained by FTIR, it has been deemed appropriate to provide further insight into the carbon bonding environment at the coating surface. The main reason for this lies in the fact that carbon-containing groups can

also be involved in the anti-fogging performance [507]. For each study, curve fitting of C1s envelopes was performed on (three) coatings obtained under different deposition conditions (**Figure 5.7**). C1s envelopes can be fitted with two or three components. The first component at 285 eV can be attributed to C-C/C-H bonds, the second at $\sim$ 286 eV to C-O bonds (e.g., hydroxyl groups), and the third at $\sim$ 288 eV to C=O bonds (e.g., carboxyl and ester groups) [500].

In general terms, an increment in the N_2O concentration resulted in a surface chemistry characterized by carbon-containing functionalities with more than one oxidation state. Surprisingly, coatings deposited in the absence of N_2O, exhibited a minor feature related to C-O bonds (286.3 eV), which explains in part, the band in the 3000–3700 cm^{-1} range (FTIR results) (**Figure 5.7a**). In pure nitrogen, it can be assumed that the oxygen atoms involved in the formation C-O bonds come from the opening of the TMCTS ring. When N_2O was added in the discharge, films displayed an additional feature at higher binding energies (288 eV), pertaining to carbonyl-containing species (**Figures 5.7b,c**). The observed variation in the (C-O + C=O)/C-C ratio from 0.24 to 0.83 as the $[N_2O]/[TMCTS]$ ratio went from 0 to 40, may be due to an increase in the number of COOH and OH functionalities (at the expense of C-C/C-H bonds), coupled with the formation of nitrogen-containing groups at the coating surface.

Mutel et al. [541] and Strobel et al. [542] showed that a N_2 plasma containing either oxygen impurities or N_2O yielded polypropylene films covered with not only oxygen-containing functionalities, such as OH and COOH, but also with nitrogen-containing functionalities, such as NH_2, -C=NH, and -CO-NH_2. Accordingly, one can infer that N_2O in the discharge can also promote the formation of these functionalities, and therefore the curve fitting of C1s envelopes must include features pertaining to nitrogen-containing species, such as C-NH_2 (286.4 eV), -C=NH (287.3 eV), -CO-NH_2 (289.2 eV) entities [541]. Indeed, the presence of nitrogen in the coatings (**Table 5.2**) supports the likely contribution of these species to the features at 286 and 288 eV.
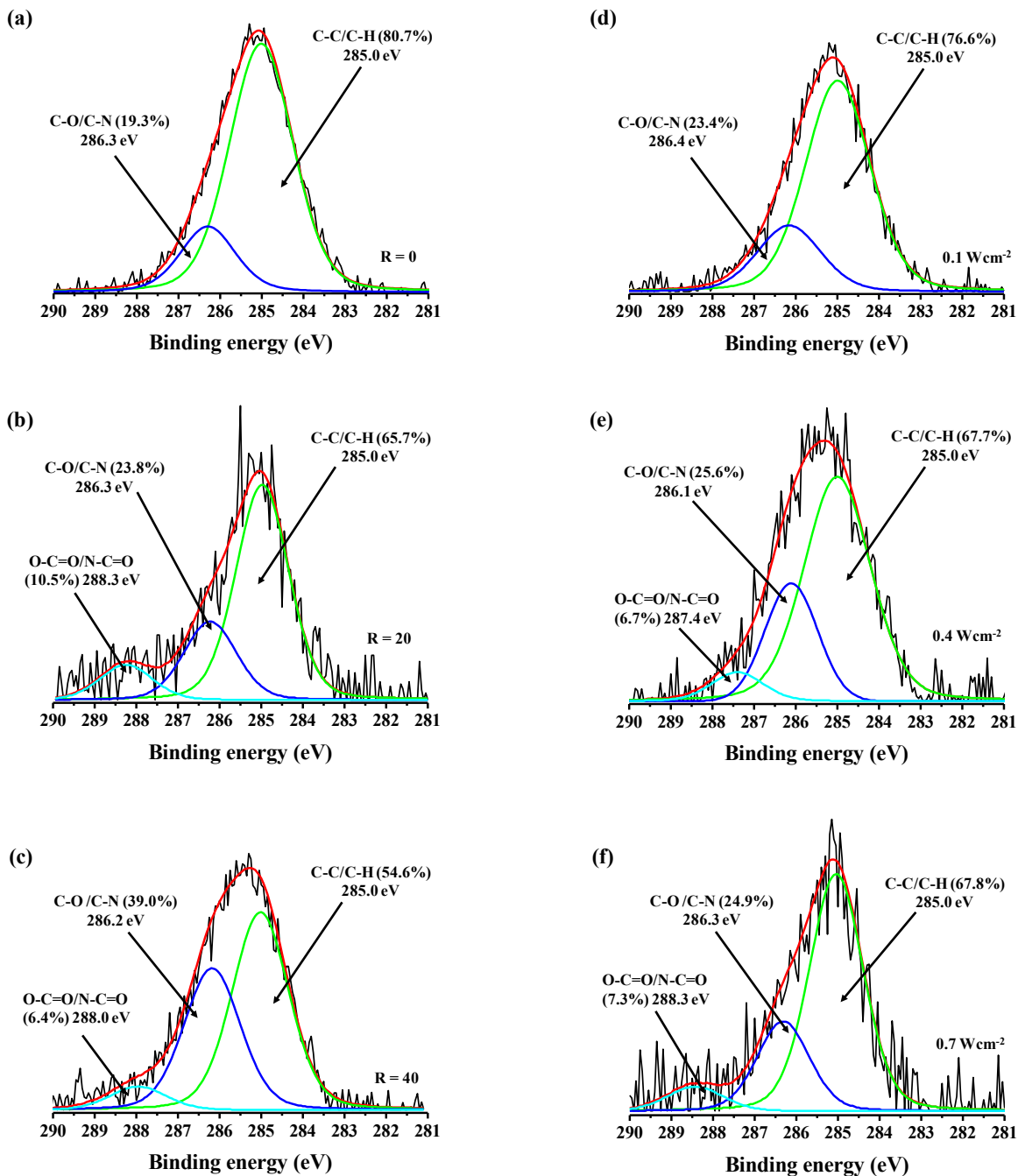
Figure 5.7: *Curve fitting of C 1s core level spectra for (a-c) coatings obtained under [N₂O]/[TMCTS] = 0, 20, and 40 (0.25 W cm⁻²), and (d-f) coatings obtained at 0.1, 0.4, and 0.7 W cm⁻² ([N₂O]/[TMCTS] = 30).*

Coatings deposited at 0.10 Wcm⁻² exhibited a major feature at 285 eV and a minor feature at 286.5 eV (**Figure 6.7d**), while those deposited at higher DP exhibited an additional feature at higher binding energies (~ 288 eV) (**Figures 5.7e** and **5.7f**). Interestingly, an increase in

the DP from 0.1 to 0.7, did not prove to be as successful as increasing the [N_2O]/[TMCTS] ratio in generating hydrophilic functionalities (i.e., C-O, C-N, C=O, C=N, etc.). As a matter of fact, the (C-O + C=O)/C-C ratio levelled off at approximately 0.48 when the dissipated power ≥ 0.4 W cm^2, unlike that of the coatings deposited under different [N_2O]/[TMCTS] ratios which increased from 0.24 to 0.83 as the ratio went from 0 to 40.

As regards **Figures 5.7b** and **5.7e**, two aspects are worth mentioning. First, at least a DP = 0.25W cm^{-2} and a [N_2O]/[TMCTS] = 20 were required to form carbonyl-containing groups at the coating surface. Second, a simultaneous increase in both deposition parameters did not translate to a greater number of C=O and C-O containing groups. In fact, the (C-O + C=O)/C-C ratio for coatings prepared under a [N_2O]/[TMCTS] = 20 and 0.25 W cm^{-2} was slightly greater than that of the coatings prepared under [N_2O]/[TMCTS] = 30 and 0.40 W cm^{-2} (0.52 and 0.48, respectively). This may reflect a synergistic effect between the different plasma species in favoring the removal of CH$_3$ groups over the generation of C=O- and C-O-containing groups.

5.5.3 Surface topography and deposition rate of the coatings

Plasma-deposited coatings were smooth at the microscale, in light of the small values of R_{rms} (2.6−6 nm) and R_a (2−5 nm) for both 1×1 and 10×10 µm^2 areas (**Table 5.3**).

It was found that an increase in the dissipated power from 0.1 to 0.70 W cm^{-2} resulted in coatings with surface roughness following no definite trend and varying by 1.5 nm at most. In contrast, except for coatings obtained at R = 30, an increase in the [N_2O]/[TMCTS] ratios from 0 to 40 correlated with a rise in surface roughness of up to 3.1 nm. One possible explanation for this trend is that an increase in the N_2O concentration in the plasma phase may promote the nucleation of small particles in the plasma and the modification of the plasma-surface interactions during the deposition process [543]. Under this scenario, more particles in the plasma phase may translate to coatings with rougher surfaces.

Table 5.3: *Root mean square roughness (R_rms), mean roughness (R_a), and deposition rates of plasma-deposited coatings on 1 × 1 and 10 × 10 μm² areas.*

Sample		R_{rms} (nm)	R_a (nm)	R_{rms} (nm)	R_a (nm)	DR (nm min^{-1})
		1×1 μm²		10×10 μm²		
A1	R = 0	2.9 ± 0.1	2.23 ± 0.09	2.63 ± 0.06	2.00 ± 0.08	2 ± 1
A2	R = 10	5.0 ± 0.5	3.9 ± 0.2	4.69 ± 0.07	3.65 ± 0.09	3 ± 1
A3	R = 20	5.5 ± 0.6	4.4 ± 0.4	5.0 ± 0.2	3.93 ± 0.03	2 ± 1
A4	R = 30	4.3 ± 0.1	3.4 ± 0.1	4.5 ± 0.2	3.2 ± 0.3	2 ± 1
A5	R = 40	6.0 ± 0.5	4.9 ± 0.5	5.05 ± 0.07	3.95 ± 0.05	3 ± 1
B1	0.10 Wcm²	5.1 ± 0.9	4.5 ± 0.9	4.8 ± 0.4	3.9 ± 0.2	3 ± 1
B2	0.40 Wcm²	5 ± 3	3 ± 1	4.5 ± 0.7	3.8 ± 0.3	1 ± 1
B3	0.55 Wcm²	3.4 ± 0.5	2.6 ± 0.4	3.5 ± 0.9	2.5 ± 0.9	2 ± 1
B4	0.70 W cm²	4.1 ± 0.9	3.0 ± 0.8	4.6 ± 0.5	3.2 ± 0.7	2 ± 1
Clean glass				1.0 ± 0.2	0.8 ± 0.1	

In addition, no significant differences in the morphology of surface features were observed. To illustrate this point, atomic force micrographs of an anti-fogging coating deposited at 0.7 W cm^{-2} and [N$_2$O]/[TMCTS] = 30 are shown in **Figure 5.8**. Except for some isolated island-like features, coatings exhibited no remarkable surface defects, such as pinholes, scratches, or cracks and were quite homogeneous at the microscale, as supported by the R$_{rms}$ and R$_a$ values. Furthermore, the smoothness of these coatings, which can be ascribed to the homogeneous nature of the Townsend discharges employed in this research, may be due to an efficient packing at molecular level [470].

In this regard, Shirtcliffe et al. [544] state that smooth coatings are produced when plasma generated species have a high sticking probability, and therefore bond when they come into contact with the substrate. The interpretation of the height and phase images is similar and suggests that plasma-deposited coatings exhibited no spatial variations of the surface chemical composition. Based on this assumption, the phase contrast images shown in **Figure 5.8** are most likely due to a variation of friction across the coating surface, derived from the nanometric differences in roughness [545,546].
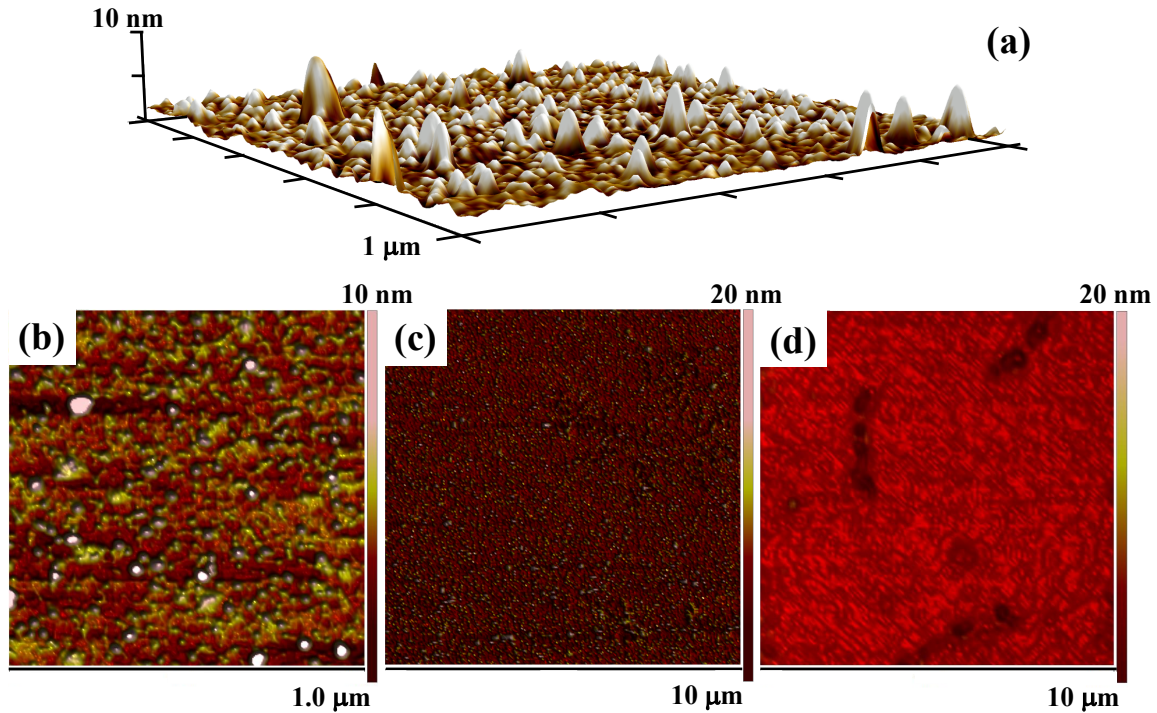
Figure 5.8: *(a) 3D and (b, c) 2D phase contrast images of a plasma-deposited TMCTS on glass using a homogeneous N_2/N_2O Townsend discharge. (d) 2D phase contrast image of an untreated glass substrate. Deposition conditions = 0.7 W cm^{-2} and $[N_2O]/[TMCTS]$ = 30 (In the 3D image, the phase contrast colors are used to enhance the standard topographic information obtained from the height).*

The presence of island-like features was also observed by Trunec and colleagues [547]. They evidenced that SiO_xC_y:H coatings prepared from hexamethyldisilazane and hexamethyldisiloxane using a homogeneous (Townsend) discharge in N_2 were quite smooth ($R_{rms} \approx 8$ nm), in contrast to those prepared using a filamentary discharge in N_2 that exhibited surface features of approximately 150 nm. These findings lead us to believe that a transient transition from a homogeneous discharge (Townsend discharge) to a filamentary discharge is behind the island-like features observed on the coatings. It is a well-documented fact that obtaining a DBD operating in the Townsend regime is limited to restricted conditions of gas composition, electrical parameters (e.g., voltage, frequency), inter-electrode distance, and dielectric materials [383,387]. Outside the limits for each parameter, the discharge transitions easily to the filamentary regime. Among these, a local variation in the gas composition caused by adventitious impurities coming from the electrodes is the most likely cause of this transition, given that the other deposition parameters did not vary during the deposition

process. Indeed, certain impurities have been reported to favor the homogeneous-to-filamentary transition because of the quenching of the N_2 ($A^3\Sigma_u^+$) metastables by Penning collisions (N_2 metastables are the main responsible species for the self-sustaining of Townsend discharges) [395,548].

Regarding deposition rates, they were found not to depend on the deposition conditions as no definite trend was observed. Their low variability (they remained in the 1–3 nm min^{-1} range) may be due to the fact that the amount of TMCTS injected in the plasma was set at 10 ppm in all experiments.

5.5.4 Anti-fogging performance and wetting behavior of the coatings

Quite a number of studies have evidenced that, under fogging conditions, the primary factor in determining whether the condensed water vapor will fog a given surface or not is the morphology of water drops [402]. It is a well-documented fact that surface chemistry and topography must both be properly adjusted to change water drops shape, and in this way, design coatings meeting suitable anti-fogging requirements [402]. For this reason, structural properties and chemistry of plasma-deposited coatings have been correlated with the anti-fogging performance by means of water contact angle measurements (**Figure 5.9**).

Depending on the deposition conditions, coatings were superhydrophobic with a WCA of ~ 102° (R = 0), hydrophilic with a WCA in the 10–70° range ($10 < $ [N_2O]/[TMCTS] $ < 30$, 0.1 W cm$^{-2} < $ DP $ < 0.55$ W cm^{-2}), or superhydrophilic with a WCA < 10° ([N_2O]/[TMCTS] $ = 40$, DP $ = 0.70$ W cm^{-1}). While an increase in the [N_2O]/[TMCTS] ratio or the dissipated power resulted in coatings with enhanced hydrophilicity, the way water contact angles varied with the deposition parameters was significantly different (compare **Figures 5.9a** and **5.9c**). Water contact angles decreased in a linear manner with the [N_2O]/[TMCTS] ratio, in contrast to those of the coatings prepared at different dissipated power, which featured a marked decrease between 0.1 and 0.25 Wcm^{-2} followed by a levelling off at 0.4 W cm^{-2}.
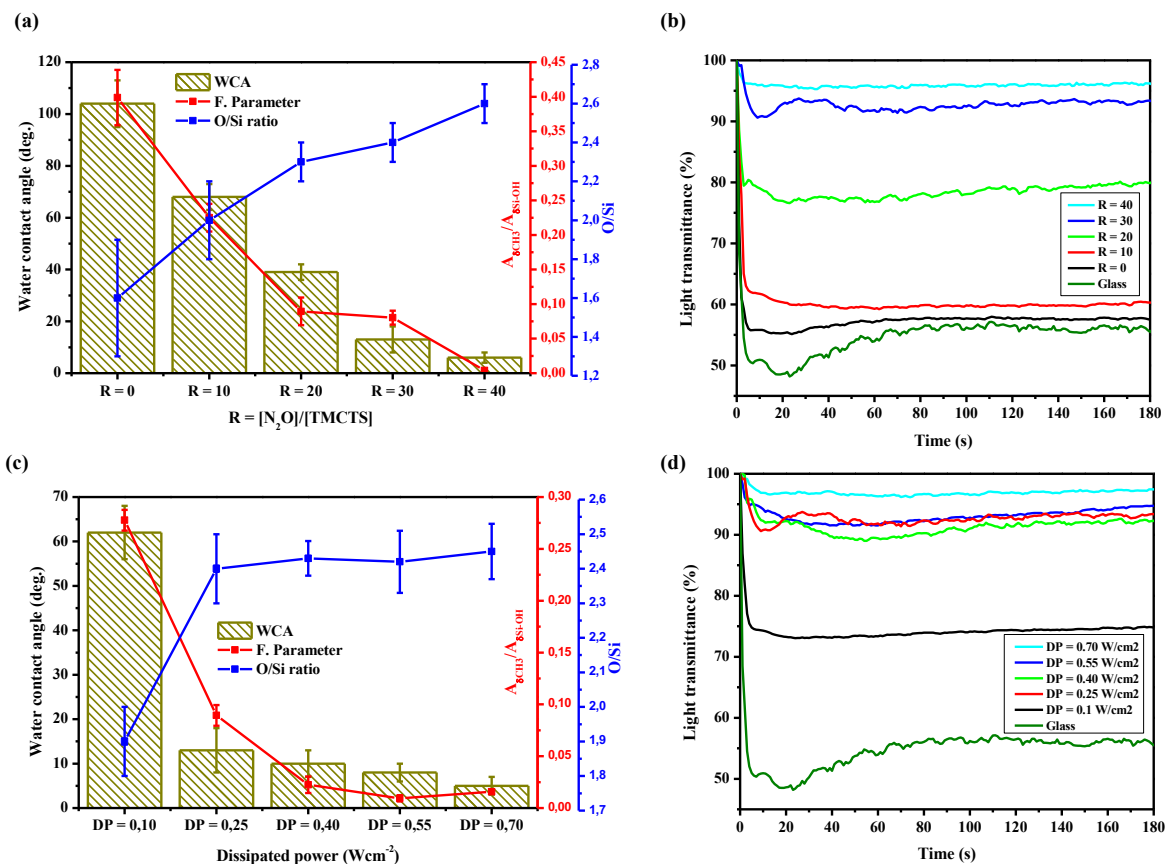
Figure 5.9: *Water contact angles, "fogging parameter", and O/Si ratios for coatings deposited under different (a) [N₂O]/[TMCTS] ratios (0.25 W cm⁻²) and (c) dissipated power ([N₂O]/[TMCTS] = 30). Percentage of light transmitted as a function of time through plasma-coated glasses obtained under different (b) [N₂O]/[TMCTS] ratio and (d) dissipated power.*

This enhancement of the water-attracting features cannot be ascribed to a rise in surface roughness, in light of the R_{rms} and R_a values [81,82], but rather to the presence of hydrophilic groups such as Si-OH formed as the expense of other more hydrophobic or reactive groups, such as Si-CH₃ or Si-H, respectively, as revealed by FTIR and XPS analyses. In this respect, the above-illustrated trends of contact angles correlated with the chemistry of the coatings through an arbitrary parameter, here referred to as "fogging parameter". The fogging parameter was defined as the ratio of the area below the band at 1260–1270 cm⁻¹ (δ_s CH₃ in Si-CH₃) to the area below the band at 920–940 cm⁻¹ (δ Si-OH). It was found that, the greater the [N₂O]/[TMCTS] ratio or the dissipated power, the lower the fogging parameter. Low values of the fogging parameter translate to coatings with low or very low contact angles because of the relatively high concentration of (hydrophilic) Si-OH groups at the surface

compared to that of (hydrophobic) Si-CH$_3$ groups. As mentioned in the introduction, hydrophilic groups are able to interact with water drops to form a thin film of water on the coating surface, and thus alleviate light scattering typical of fogged surfaces.

To assess the fogging resistance of plasma-coated glasses, light of wavelength 590 nm transmitted through the samples was measured in the presence of water vapor at 50°C as a function of time (ASTM F 659-06 standard). For comparative purposes, a clean glass sample was used as a reference (**Figures 5.9b** and **5.9d**). Regardless of the deposition conditions, transmittance curves revealed similar features, namely, a drop within the first 5–10 s followed by a recovery levelling off very slowly to a plateau. Interestingly, the drop in light transmission was shown to be much slower in coatings deposited under [N$_2$O]/[TMCTS] ratios $\geq$ 30 or dissipated power $\geq$ 0.25 W cm^{-2}. With light transmittances well above 80% at 30 s, these coatings conferred superior anti-fogging properties to glass samples because of their (super)hydrophilicity (WCA $\leq$ 20°). In addition, their associated fogging ratio values between 0 and 0.10 evidences that the absence of hydrophobic Si-CH$_3$ groups at the surface is not a *sine qua non* for these coatings to proffer anti-fogging effect to glass samples. That said, O/Si ratios above approximately 2.3 appear to be linked to the anti-fogging feature (**Figures 5.9a** and **5.9c**).

Because of water drops with WCA $\geq$ 60°, coatings fabricated at lower [N$_2$O]/[TMCTS] ratios or dissipated power experienced a more rapid decrease in transmittance during the same period of time. Here, water drops scattering light in all directions resulted in a light transmission recovery not exceeding 80% at 30 s, and therefore not compliant with the anti-fogging requirements contained in the ASTM F 659-06 standard. Note that with a dramatic drop in light transmission to T$_{average}$ $\approx$ 55%, uncoated glasses were severely fogged (WCA $\approx$ 55°). These findings support those of Briscoe et al. [22] and Pieters et al. [49] who analyzed the transmittance of normally incident light on glass and plastic films (polyethylene, polystyrene, and polymethylmethacrylate) under fogging conditions. It was found that light transmission was higher in fogged surfaces with water drops with contact angles below 40°, in contrast to those covered with water drops with contact angles between 40 and 90°, in

which light transmission was significantly lower. In investigating the anti-fogging feature of glasses coated with thermally crosslinked poly(ethylene glycol)-functionalized (poly(vinylalcohol)/ poly(acrylic acid))$_{30}$ coatings, Lee et al. [199] also demonstrated that a better anti-fogging performance was linked to transmittance curves exhibiting a slow drop within the first 5–10 s.

This particular feature of transmittance curves can be explained in terms of growth and coalescence of water drops. In this respect, of note are the studies conducted by Beysens [48] and Knobler [549] on the growth of "breath figures" on different substrates such as silicon and hydrophobized glass. The kinetics of surface fog formation can be described by three different growth regimes, each of them characterized by several physical parameters, including the average radius $\langle R \rangle$ of the droplets and the surface coverage ε (the latter defined as the ratio of the surface area covered by water drops to the substrate area). The first regime, which takes place once drops are nucleated on the surface, is characterized by a low surface coverage and a drop growth without significant interactions. The distances between droplets are relatively large compared to their sizes, so that coalescence events are rare. Here, the average radius of the droplets varies with time according to the following power law:

$$\langle R \rangle \approx t^{\mu_0} \tag{5.4}$$

where t is the elapsed time and μ_0 is equal to $1/3$ when the temperature of the surface is kept constant.

During the second regime, also known as "self-similar regime", surface coverage ε increases because of the growth and coalescence of drops. When $\varepsilon \geq 0.3$, the rate of coalescence begins to speed up significantly, so that the exponent in **Equation 5.4** is better defined by $\mu_0 = 1$. Interestingly, in this regime no visible drops appear in the space between the already existing drops and surface coverage reaches a saturation value of 0.55, regardless of the wetting behavior of the substrate. In the third regime, a second generation of droplets grow in the space between the already formed drops. The second generation of water drops exhibits all

of the features, including growth laws and surface coverage, of the first generation. In the long term, many generations of droplets will coexist on the surface. Even tough each generation exhibits a $\varepsilon = 0.55$, the fraction of the surface covered by the droplets approaches unity in the steady state.

Unfortunately, the above-mentioned regimes do not adequately reflect the complexity of the growth of breath figures, as they apply strictly to solid surfaces that are smooth, chemically homogeneous, as well as to those that do not dissolve as a result of interactions with water. Undoubtedly, there is no such ideal surface in real life and other factors such as the hysteresis of the contact angle, the nucleation rate of water drops, and the wetting behavior of the surface must be taken into account. Hysteresis of the contact angle resulting from the pinning triple phase contact line has been reported to reduce the duration of the self-similar regime and cause water drops to spread anisotropically as they coalesce. The nucleation rate of water drops, that is, the number of water drops nucleated per unit volume with radii exceeding a critical value r^*, depends on the wetting behavior. In this regard, the classical theory of nucleation reveals that the more water-attracting the surface is, the higher the nucleation rate.

Considering the foregoing, it can be argued that the hysteresis of the contact angle coupled with the relatively high nucleation rate of water drops in (super)hydrophilic surfaces is behind the slower decrease in light transmission observed in coatings deposited under $[N_2O]/[TMCTS]$ ratios ≥ 30 or dissipated power ≥ 0.25 W cm^{-2}. In this case, relatively flat water drops with high contact angle hysteresis nucleating, growing, and coalescing fast on the surface may account for the lower decrease in light transmission observed within the first seconds of fogging testing. The light the transmission recovery that follows in all coated glasses can be attributed to the formation of a sheet-like water layer. Accordingly, it can be inferred from transmittance curves shown in **Figures 5.9b** and **5.9d**, that the morphology of water drops (WCA), which relies on the wettability of the solid surface, is the parameter that makes it possible to determine whether the coated glasses will remain optically clear or not under very humid conditions.

To illustrate this point, the resistance to fogging of a plasma-coated glass ([N$_2$O]/[TMCTS] = 30, DP = 0.7 W cm^{-2}) was tested under more aggressive fogging conditions (**Figure 5.10a**). The portion of the glass sample coated with the anti-fogging coating remained optically clear when placed over hot water at 80°C. Moreover, the "see-through" property was maintained when the coated glasses were brought back to ambient conditions, thereby enabling an easy legibility of the letters behind them (**Figures 5.10b**). However, both the uncoated part of the glass and the coated part closer to the gas exit fogged up under the same testing conditions making it more difficult to see through them. For comparative purposes, a plasma-coated glass ([N$_2$O]/[TMCTS] = 20, DP = 0.25 W cm^{-2}) with a transmittance close to the threshold value set in the ASTM F 659-06 standard (76% at 30 s) was also tested (**Figure 5.10c**). Even though this configuration resulted in a fogged surface, the "see-through" property was not severely compromised (**Figure 5.10d**).
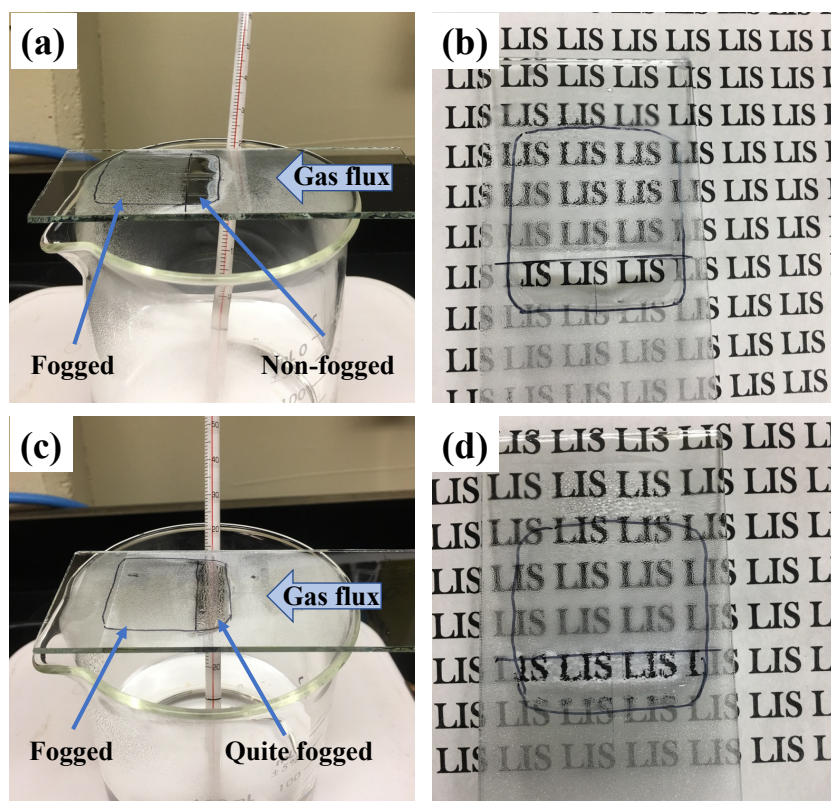
Figure 5.10: *Side view of coated glasses obtained (a) at [N$_2$O]/[TMCTS] = 30, DP = 0.7 W cm^{-2} and (c) at [N$_2$O]/[TMCTS] = 20, DP = 0.25 W cm^{-2}, respectively, when exposed to water vapor at 80°C. (b,d) The coated glasses on a paper with letters written in it following hot-fog testing.*

5.6 Conclusions

In this study, anti-fogging coatings were deposited on glass samples using 1,3,5,7-tetramethylcyclotetrasiloxane as precursor by means of a DBD in N_2/N_2O operated at atmospheric pressure. It was observed that an increase in either the $[N_2O]/[TMCTS]$ ratio or the DP led to similar changes in the structure and chemistry of the coatings and made it possible to produce coatings with enhanced water-attracting features, hence more likely to be fogging-resistant. Interestingly, AFM results showed that, regardless of the deposition conditions, coatings were quite homogeneous and exhibited surface features of the order of 4–5 nm. After 30 seconds of exposure to a moist environment at 50°C, quantitative assessment of the anti-fogging performance revealed that coatings obtained under $[N_2O]/[TMCTS]$ ratios ≥ 30 or dissipated power ≥ 0.25 W cm^{-2} conferred superior visual characteristics to the glass samples. Indeed, the average light transmission values, which were found to be relatively similar, were considerably better than those of an uncoated glass sample (i.e., > 90% and 55%, respectively). The anti-fogging characteristics were correlated with the surface chemistry of the coatings through an arbitrary parameter, called "fogging parameter" and the O/Si ratios. O/Si ratios ≥ 2.3 coupled with fogging ratio values in the 0–0.10 range were found to be necessary to procure an excellent fogging property under very humid conditions. As revealed by the XPS and FTIR analyses, the presence of hydrophilic functionalities, such as silanol (Si-OH), hydroxyl (C-OH) carboxyl (COOH), ester (COOR), at the coating surface accounted for these values. These results lead us to believe that the high reactivity of Si-H bonds is behind the formation of these hydrophilic functionalities and the incorporation of nitrogen from the plasma phase. In conclusion, the possibility of tuning the structure and composition of the coatings by means of atmospheric pressure dielectric barrier discharges operated under a controlled $TMCTS/N_2/N_2O$ atmosphere undoubtedly represents a unique opportunity niche to produce anti-fogging coatings in one step with potential integration on an industrial scale.

5.7 Acknowledgments

6 Unveiling the origin of the anti-fogging performance of plasma-coated glass: Role of the structure and chemistry of siloxane precursors

Iván Rodríguez Durán[ab], Jacopo Profili[c], Luc Stafford[c], and Gaétan Laroche[ab]

[a]Laboratoire d'Ingénierie de Surface, Centre de Recherche sur les Matériaux Avancés, Département de Génie des Mines, de la Métallurgie et des Matériaux, Université Laval, 1065 Avenue de la médecine, Québec G1V 0A6, Canada.
[b]Centre de Recherche du Centre Hospitalier Universitaire de Québec, Hôpital St-François d'Assise, 10 rue de l'Espinay, Québec G1L 3L5, Canada.
[c]Département de physique, Université de Montréal, Montréal, Québec, Canada, H3C 3J7.

6.1 Résumé

Au cours des dernières années, les revêtements super hydrophiles ont suscité un intérêt considérable en raison de leur applicabilité potentielle dans les secteurs d'activité affectés par la formation de buée, tels que l'industrie alimentaire, le secteur de l'architecture et la médecine. Malheureusement, la plupart des techniques de dépôt en couches utilisées jusqu'à présent ne sont pas adaptées à la production de revêtements à grande échelle en raison de leur nature à plusieurs étapes. Dans ce cadre, l'utilisation de décharges à barrière diélectrique à pression atmosphérique (AP-DBD) fonctionnant sous une atmosphère gazeuse contrôlée de N_2/N_2O offre une alternative prometteuse aux techniques de dépôt classiques, pour la fabrication de revêtements antibuée en une étape. En utilisant cette approche, quatre précurseurs de siloxane ayant des structures différentes et un nombre différent de groupes Si-H et Si-CH$_3$; à savoir, le 1,3,5,7-tétraméthylcyclotétrasiloxane (TMCTS), l'octaméthylcyclotétrasiloxane (OMCTS), le 1,1,3,3-tétraméthyldisiloxane (TMDSO) et l'hexaméthyldisiloxane (HMDSO) ont été déposés sur des échantillons de verre. La résistance à la buée des verres revêtus a été évaluée quantitativement par le protocole décrit dans la norme ASTM F659-06 et qualitativement par inspection visuelle. L'effet de la structure et de la chimie de ces précurseurs sur les performances antibuée a été étudié par spectroscopie infrarouge à transformée de Fourier (FTIR) et spectroscopie photoélectronique par rayons X (XPS). La rugosité de surface et l'épaisseur des revêtements ont été déterminées par microscopie à force atomique (AFM) et profilométrie, respectivement. Les performances antibuée, la chimie de surface et la topographie de surface de verres revêtus par plasma étaient corrélées aux mesures d'angles de contact avec l'eau (WCA). Les verres à revêtement TMCTS présentaient une remarquable performance antibuée résultant d'une hydrophilicité supérieure (WCA < 5°) par rapport à celle des verres à revêtement OMCTS, TMDSO et HMDSO, qui présentaient des angles de contact avec l'eau de 80°. La rugosité rehaussée observée dans les revêtements TMCTS, couplé à la présence des fonctionnalités hydrophiles telles que C-O, O=C-O et Si-OH à la surface, explique les caractéristiques visuelles supérieures des verres revêtus lorsqu'ils sont exposés à la vapeur d'eau chaude. Ces résultats nous amènent à conclure que la structure cyclique du TMCTS, en conjonction avec la réactivité élevée des liaisons Si-H, est responsable de la performance antibuée.

6.2 Abstract

In recent years, superhydrophilic coatings have attracted enormous attention because of their potential applicability in sectors of activity concerned by fogging, such as the food industry, the architectural sector, and medicine. Unfortunately, most of the thin film deposition techniques used thus far, are not suitable for large-scale coating production due to their multistep nature. In this regard, the use of atmospheric pressure dielectric barrier discharges (AP-DBD) operated under a N_2/N_2O gas atmosphere offers a promising alternative to conventional deposition techniques, for the fabrication of anti-fogging coatings. Using this approach, four siloxane precursors with different structures and different number of Si-H and Si-CH$_3$ groups; namely, 1,3,5,7-tetramethylcyclotetrasiloxane (TMCTS), octamethylcyclotetrasiloxane (OMCTS), 1,1,3,3-tetramethyldisiloxane (TMDSO), and hexamethyldisiloxane (HMDSO), were deposited on glass samples. The fogging resistance of coated glasses was assessed quantitatively by the protocol described in the ASTM F659-06 standard, and qualitatively by visual inspection. The effect of the structure and chemistry of these precursors on the anti-fogging performance was investigated by Fourier Transform Infrared Spectroscopy (FTIR) and X-ray Photoelectron Spectroscopy (XPS). Surface roughness and coating thickness were determined by atomic force microscopy (AFM) and profilometry, respectively. The anti-fogging performance, surface chemistry, and surface topography of plasma-coated glasses were correlated with water contact angles (WCA) measurements. TMCTS-coated glasses featured a remarkable anti-fogging performance arising from a hydrophilicity higher than that of the OMCTS-, TMDSO-, and HMDSO-coated glasses (WCA < 5° vs. 80°), which were not fogging-resistant. Coupled with surface hydrophilic functionalities, such as C-O, O=C-O, and Si-OH, the relatively high roughness of TMCTS-based coatings, compared to that of OMCTS-, TMDSO-, and HMDSO-based cotings, accounted for the superior visual characteristics of TMCTS-coated glasses when exposed to hot water vapor (80°C). These results lead us to conclude that the cyclic structure of TMCTS in conjunction with the high reactivity of the Si-H bonds is responsible for the anti-fogging performance.

6.3 Introduction

When one breaths on a transparent material, the exhaled water vapor condenses into a myriad of tiny droplets, resulting in deterioration of the "see-through" property. This typical feature of condensation, often referred to in the literature as "breath figures", is primarily due to the interaction between the water drops and the incident light [550]. In essence, the effects of fogging arise from the total internal reflection of light at the water drop/air interface and the change in the direction of propagation of the transmitted light [551,552].

Although fogging is not harmful, its occurrence has been reported to cause serious problems in sectors of activity, such as the solar industry, the transport sector, the medical field, or the food industry, in which transparent or optical materials are required [402]. For example, the presence of condensation on photovoltaic cells decreases the percentage of solar energy that is converted into usable electricity, because of a reduction in the number of photons reaching the surface of these devices [25]. The fogging of endoscope lenses during a minimally invasive surgery (e.g., laparoscopic surgery) contributes to medical errors derived from a suboptimal visualization of the operating field [16]. In the same vein, severe condensation on aircraft [12] or automobile [11] windshields can give rise to safety concerns. As regards the food industry, it has been found that moisture condensed on the inner surface of the packages reduces the consumers' ability to see the product (e.g., freshly chopped vegetables or meats), when exhibited in a chiller cabinet in supermarkets. Further to this, when produce are not esthetically displayed, the condensation may result in food spoilage [56]. Vegetable growers acknowledge that the formation of water drops on greenhouse claddings translates to a decrease in crop yield and contributes to the development of fungal diseases [553].

To prevent these situations, the application of hydrophilic or superhydrophilic coatings has strongly emerged, particularly in recent years, as a promising anti-fogging approach. A coating with water-attracting features prevents the effects of condensation by spreading the water drops across the surface [49]. Generally speaking, these coatings are made of natural polymers such as pullulan and chitin [27,191]; synthetic polymers such as vinyl derivatives [195–197,201] and fluorocarbon surfactants [138,139]; and inorganic materials such as SiO_2

and TiO_2 [112,114,169,170,218]. Other inorganic materials such as ZrO_2 [554], In_2O_3-SnO_2 [229], MgO-Al_2O_3 [555], Cu_3SnS_4 [189], and graphene [42] have also shown to be promising candidates for the fabrication of anti-fogging coatings.

Even though these materials have amply demonstrated their effectiveness in minimizing the effects of fogging, their large-scale application is a challenging task for cost-effectiveness and practical reasons. Indeed, most of the coating techniques explored thus far involve multiple steps and, in some cases, are incompatible with thermally sensitive substrates because of the application of thermal post-treatments [174]. Developing less time-consuming coating techniques adapted for mass production is therefore crucial to overcome these drawbacks, and thus broaden the range of application of anti-fogging coatings beyond laboratory research.

In this context, the use of plasma enhanced chemical vapor deposition (PECVD) at atmospheric pressure may represent a promising alternative to conventional coating deposition techniques. Compared to vacuum-based plasma processing or sol-gel techniques, atmospheric-pressure plasma deposition has many advantages, including its potential for integration into mass production (vacuum equipment is not necessary), its environmentally friendly nature (solvent-free processing), and its suitability for treating thermally sensitive materials such as polymers with low glass transition temperatures [417].

Within the family of plasmas operated at or near atmospheric pressure, the so-called "dielectric barrier discharges" (DBDs) hold great promise for the one-step fabrication of anti-fogging coatings on a wide range of substrates. A dielectric barrier discharge can be described as a system in which an ionized gas, commonly referred to as "plasma", is generated between two electrodes, when an alternating voltage of the order of kilovolts, is applied [378]. To ensure coating deposition at room temperature, at least one layer of an insulating material is placed between the electrodes. DBDs have typically been used to prepare siloxane-based coatings with electrical [416,514,556] or protective features [417,557,558], so as to meet the ever-growing demand for functional materials in the optical industry, the food industry, and

the microelectronic industry. Surprisingly, no papers on the use of DBDs for the deposition of siloxane-based anti-fogging coatings on glass are evidenced thus far.

On this basis, the aim of this study is thus to fabricate anti-fogging glass by coating deposition using an atmospheric pressure DBD. To this end, two cyclic siloxane precursors, 1,3,5,7-tetramethylcyclotetrasiloxane (TMCTS), and octamethylcyclotetrasiloxane (OMCTS); and two acyclic ones, 1,1,3,3-tetramethyldisiloxane (TMDSO), and hexamethyldisiloxane (HMDSO), were used in this study. The anti-fogging performance of plasma-deposited coatings was discussed in terms of surface roughness and chemistry and correlated with the structure and chemistry of siloxane precursors. The structure and chemical composition of plasma-deposited coatings were investigated by Fourier Transform Infrared Spectroscopy (FTIR) and X-ray photoelectron spectroscopy (XPS). Surface roughness and coating thickness were measured by atomic force microscopy (AFM) and profilometry, respectively. The wetting behavior of the coatings was assessed by water contact angle (WCA) measurements. The resistance to fogging of coated glasses was assessed quantitatively by the protocol included in the ASTM F659-06 standard, and qualitatively by visual inspection by photographing the samples after being exposed to hot water. Glasses endowed with the anti-fogging feature were subjected to different thermal treatments to enhance the mechanical robustness of the coatings and impart a better adhesive to the coating/substrate. The fogging resistance of thermally treated glasses was measured following vigorous washing in order to evaluate the reliability of the anti-fogging treatment.

6.4 Experimental section

6.4.1 Materials and sample preparation

Four siloxane precursors, namely, 1,3,5,7-tetramethylcyclotetrasiloxane $[H(CH_3)SiO]_4$ (TMCTS), octamethylcyclotetrasiloxane $[(CH_3)_2SiO]_4$ (OMCTS), 1,1,3,3-tetramethyldisiloxane $H_2(CH_3)_2Si_2O$ (TMDSO), and hexamethyldisiloxane $(CH_3)_3Si_2O$ (HMDSO) were purchased from Sigma-Aldrich (NMR grade, purity $\geq$ 99.5 vol.%) and used as received without further purification (**Figure 6.1**).
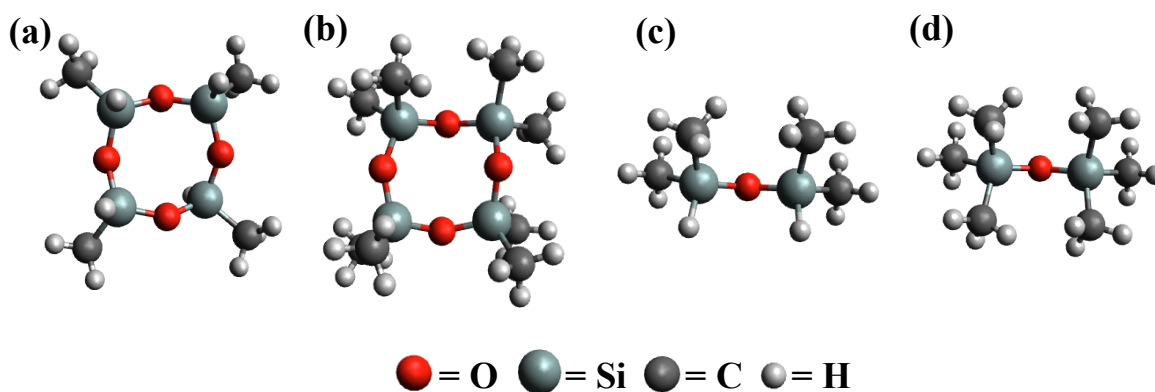
Figure 6.1: *Siloxane precursors used for the preparation of coatings by AP-DBD. (a) TMCTS, (b) OMCTS, (c) TMDSO, and (d) HMDSO.*

Methanol and acetone were purchased from commercial alcohols (Ontario, ON, Canada) and Laboratories MAT (Québec, QC, Canada), respectively. Nitrogen (N_2, grade 4.8) and nitrous oxide (N_2O, 99.998%) were provided by Linde (Québec, QC, Canada). Glass samples measuring $13 \, cm \times 5 \, cm \times 2 \, mm$ were kindly provided by Multiver Ltd (Québec, QC, Canada). Prior to the deposition process, glass samples were ultrasonically cleaned with acetone for 10 min followed by rinsing with methanol and deionized water to remove any organic remnant. The as-treated glasses were ultrasonically washed for 10 min with deionized water and then wiped dry with a cotton cloth (Amplitude Kappa™, Contect Inc., Spartanburg, SC, USA). Afterwards, glass samples were immersed in a piranha solution (H_2SO_4:H_2O_2, 3:1 v/v%,) for 10 min to generate reactive Si-OH groups on the surface (surface activation), rinsed with abundant deionized water, and dried with a dry air jet.

6.4.2 Experimental setup and operating conditions

A parallel-plate DBD reactor, such as the one in **Figure 6.2**, was used in this study. It consists of two electrodes spaced 1 mm apart, one of which is a 0.64-mm-thick alumina sheet (Goodfellow, Coraopolis, PA, USA) covered with a silver-based conductive paint ($3.5 \, cm \times 3 \, cm$), and the other is a stainless-steel mobile plate ($13 \, cm \times 9 \, cm$) where glass samples were positioned prior to the deposition process.
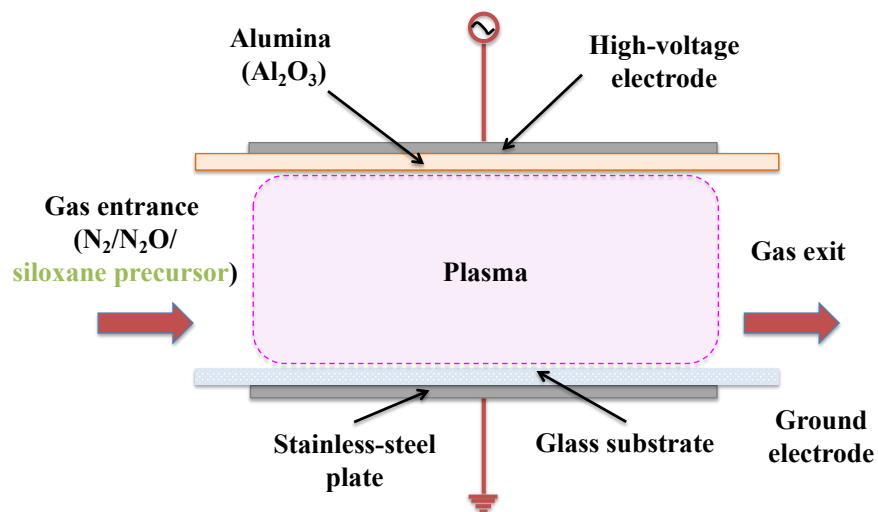
Figure 6.2: *DBD design used for the deposition of siloxane-based coatings.*

The DBD reactor was by an oscillating voltage with a peak-to-peak amplitude of ~ 16.5 kV and a frequency of 6 kHz. The breakdown voltage was found to be approximately 12.5 kV. These operating conditions, which resulted in an average power per unit area of 0.70 W cm^{-2}, made it possible to maintain the discharge in a homogeneous regime (i.e., Townsend regime) throughout the deposition process. The average power per unit area was calculated using LabVIEW^{TM} software, as follows:

$$P = \frac{1}{T \cdot S} \int_{0}^{T} V_{app}(t) \cdot I_{meas}(t) dt \qquad (6.1)$$

where T is the period (s), S is the surface of the glass sample in contact with the plasma (cm^2), V_{app} is the applied voltage (V), I_{meas} is the measured current (A). Note that the integral extends over one cycle.

The voltage applied across the electrodes V_{app} was measured by a high-voltage probe (Tektronix P6015A), while the current passing through the electric circuit I_{meas} was determined by a passive oscilloscope probe (Tektronix P2200). The voltage drop across a 50 Ω resistor connected in series with the ground electrode enabled us to measure the current. All waveforms were recorded using a numerical oscilloscope (DPO2000, Tektronix Inc.,

Beaverton, OR, USA). The gas inlet was composed of two independent lines, one of which carried N_2 (plasmogenous gas) at 3 L min^{-1} and the other carried N_2O (oxidant gas) at variable flow rate to the discharge site. This configuration allowed for a continuous renewal of the gaseous atmosphere during the coating process. The flow rate of gases was measured by mass flow controllers (Bronkhorst^{TM}, Ruurlo, Holland). Using a syringe pump (Fisherbrand^{TM}, Thermo Fisher Scientific, Runcorn, Cheshire, UK) coupled to a nebulizer (Mira Mist CE^{TM}, Burgener Research Inc., Mississauga, ON, Canada), a third line made it possible to inject N_2 at 1 L min^{-1} along with 10 ppm of the corresponding precursor (aerosol) into the inter-electrode space. Gases passed through a diffuser to ensure a laminar flow over the deposition area. In all experiments, the concentration of N_2O in the discharge was 50% greater than that required if one assumes stoichiometric conditions between the precursor and the oxidant, that is:

$$\textbf{TMCTS}: [H(CH_3)SiO]_4 + 20\ N_2O \rightarrow 40\ N_2 + 4\ CO_2 + 8\ H_2O + 4\ SiO_2 \qquad (6.2)$$

$$\textbf{OMCTS}: [(CH_3)_2SiO]_4 + 32\ N_2O \rightarrow 32\ N_2 + 8\ CO_2 + 12\ H_2O + 4\ SiO_2 \qquad (6.3)$$

$$\textbf{TMDSO}: H_2(CH_3)_2Si_2O + 18\ N_2O \rightarrow 18\ N_2 + 4\ CO_2 + 7\ H_2O + 2\ SiO_2 \qquad (6.4)$$

$$\textbf{HMDSO}: (CH_3)_3Si_2O + 24\ N_2O \rightarrow 24\ N_2 + 6\ CO_2 + 9\ H_2O + 2\ SiO_2 \qquad (6.5)$$
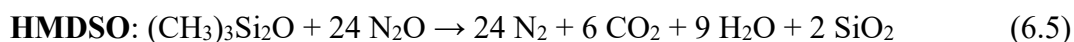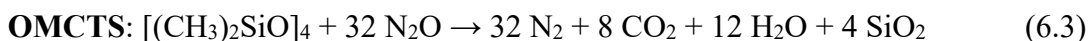
Accordingly, 270, 300, 360, and 480 ppm of TMDSO, TMCTS, HMDSO, and OMCTS, respectively, were injected into the discharge. The aerosol delivery line was heated and kept at ~ 40°C to prevent precursors from condensing on the inside before they reach the discharge site. Prior to the deposition process, a cleaned glass sample was positioned on the bottom electrode at room temperature. Afterwards, the plasma chamber was pumped down to 0.01 Torr and filled with N_2 until pressure reaches 760 Torr (1 atm). Pressure was allowed to stabilize before feeding the aerosol. The deposition time was set at 10 min, except for the coatings that were analyzed by FTIR, for which the deposition time was set at 60 min. The speed at which glass samples were moved was kept constant at 35 cm min^{-1}, i.e., the bottom electrode moving back and forth 50 times.

6.4.3 Thermal and washing treatments

Coated glasses exhibiting anti-fogging performance were thermally treated to enhance mechanical robustness and impart a better adhesive to the coating/substrate. The effect of temperature (100 and 500°C), treatment time (1 and 5 h), and gas atmosphere (Ar and O_2/Ar, 2% v/v) on the anti-fogging performance was studied. The resistance to fogging of thermally treated samples was also investigated after an industrial washing treatment. The washing process involved the following steps: (1) inserting the samples into a washing reactor at 8 m min^{-1} using a small mobile cart, (2) pre-washing with a water jet at 50–55°C; (3) washing by water jet projection (50–55°C) followed by a vigorous brushing (two rotating brushes were placed on the coated side and the other two on the uncoated side); (4) rinsing with a water jet at 50–55°C followed by washing with two rotating brushes; and (5) fan drying at room temperature. Brushes rotating at 1700 rpm (rpm = revolutions per minute) were made of nylon fibers of either 0.15 or 0.3 mm in diameter, depending on whether they were in contact or not with the coated side, respectively.

6.4.4 Chemical characterization of the coatings

6.4.4.1 Attenuated total reflectance Fourier transformed infrared spectroscopy (ATR-FTIR)

The chemical structure of the coatings was investigated by FTIR spectroscopy using a FTIR spectrophotometer (Cary 660 FTIR, Agilent Technologies, Victoria, Australia) equipped with a DLaTGS detector, a Ge-coated KBr beamsplitter, and a Split-Pea attachment (Harrick Scientific Products, Pleasantville, NY, USA). Infrared spectra were recorded at room temperature with a resolution of 4 cm^{-1} and 128 scans using a 45-degree incident ATR accessory (1.5 mm^2 active sample area, Si crystal with a depth of penetration at 1000 cm^{-1} of 0.81 µm for $n_{sample} = 1.5$) in the 400–4000 cm^{-1} range (mid-IR). For each coating, 9 equally spaced points were analyzed from the gas entrance side to the gas exit side (**Figure 6.2**). Using Origin software (Origin Lab Corp. v 8.5), spectral features were normalized with

respect to the band due to the Si-O-Si asymmetric stretching, ν_a Si-O-Si (1000–1200 cm^{-1}) following baseline correction.

6.4.4.2 X-ray photoelectron spectroscopy (XPS)

Chemical surface composition of coated glasses was determined by X-ray photoelectron spectroscopy (XPS) on a PHI 5600-ci spectrometer (Physical Electronics, Chanhassen, MN, USA) operated under high vacuum ($< 10^{-6}$ Pa). A standard Al X-ray source (Kα, hν = 1486.6 eV) at 300 W was used to record survey spectra (0–1400 eV), while a standard Mg X-ray source (Kα, hν = 1253.6 eV) at 300 W was used to record high-resolution spectra (HRXPS). Photoelectron detection was carried out at a take-off angle of 45° and surface charging effects were compensated by setting the C-C/C-H aliphatic carbon binding energy peak at 285.0 eV. The analyzed area was approximately 0.005 cm^2 for all samples. By means of the least squares fitting, curve fitting of C1s and Si2p features was performed using Gaussian-Lorentzian functions, following Shirley-type background subtraction (PHI MultiPak^{TM} software v 9.3). Nine analyses per sample were carried out to evaluate the chemical homogeneity of coated glasses and provide a mean value with its corresponding standard deviation.

6.4.5 Morphological characterization of the coatings

6.4.5.1 Atomic force microscopy (AFM)

The nanoscale topography of coated glasses was investigated by means of an atomic force microscope (Dimension 3100, Veeco Digital Instruments by Bruker, Santa Barbara, CA, USA) operated in the tapping mode. A silicon tip (OTESPA probe, Bruker Nano Surface Division, Santa Barbara, CA, USA) with a radius of curvature < 10 nm and an aspect ratio of approximately 1.6/1 was used to scan the surface (scan angle 90°). AFM images were recorded at a scan rate of 0.5 Hz with a line resolution of 256 × 256 and flattened using a first order line fit (NanoScope Analysis software v 1.5 by Bruker). Surface roughness was

examined on 5 × 5 (tip velocity = 5 μm s^{-1}) and 50 × 50 μm^2 (tip velocity = 50 μm s^{-1}) areas, and characterized by two roughness parameters, namely the root mean square roughness (R_{rms}) and the mean roughness (R_a).

6.4.6 Coating thickness and deposition rate measurements

Coating thickness and deposition rates were determined by stylus profilometry. Briefly, a pointed tip tweezers was used to scratch off the coatings from the entrance to the exit of the discharge (in direction of gas flow). The height of the resulting steps was measured each 1 mm perpendicular to gas flow using a DektakXT^{TM} profilometer (Bruker Nano Surface Division, Tucson, AZ, USA) with an applied force of 1 mg. A cone shaped stylus (45 deg.) with a tip radius of 5.0 μm was used for that purpose. Each acquisition lasted for 10 s and was performed on a distance of 300 μm. The thickness measured on 6 equally spaced points enabled us to calculate an average value and its corresponding standard deviation. The deposition rate of the coatings was determined by dividing the as-measured thickness by the deposition time. The uncertainty in the deposition rates was calculated by error propagation.

6.4.7 Wetting behavior of the coatings

The wetting behavior of coated glasses was assessed by the sessile drop method using a Video Contact Angle System (VCA-2500 XETM, AST products Inc., Billerica, MA, USA) equipped with a built-in high-resolution CCD camera. 3-μL drops of ultrapure water were dropped from a height of 10 mm and contact angles were measured following the pinning of the three-phase contact line. Each water contact angle value (WCA) was averaged from measurements on eight drops and was accompanied by its corresponding standard deviation.

6.4.8 Fogging resistance assessment

A slightly modified version of the standard test method ASTM F 659-06 was used to assess the resistance to fogging of coated glasses [195]. Briefly, coated glasses were immersed in distilled water at 23°C for 1 h and then air dried at room temperature for at least 12 h. Afterwards, they were placed over a bath containing water at 50°C and exposed to light of wavelength 590 nm. For a surface to be anti-fogging, the F 659-06 standard states that the percentage of light transmitted through the sample must be equal or greater than 80% following 30 s of exposure to water vapor at 50°C. The anti-fogging performance was also tested under more aggressive fogging conditions by placing the coated glasses on an Erlenmeyer flask containing water at 80°C for 15 s. In this case, the resistance to fogging was evaluated by visual inspection by photographing the samples immediately after they were brought back to ambient lab conditions (i.e., 17–20°C, 50% RH).

6.5   Results and discussion

6.5.1   Electrical characterization of the discharge

Figure 6.3a shows the voltage-current characteristics of a N_2O/N_2 discharge obtained in the presence of TMCTS. The current pulse appearing at every half cycle of the applied voltage, on the capacitive current reveals a discharge operating in a homogeneous regime (Townsend regime).
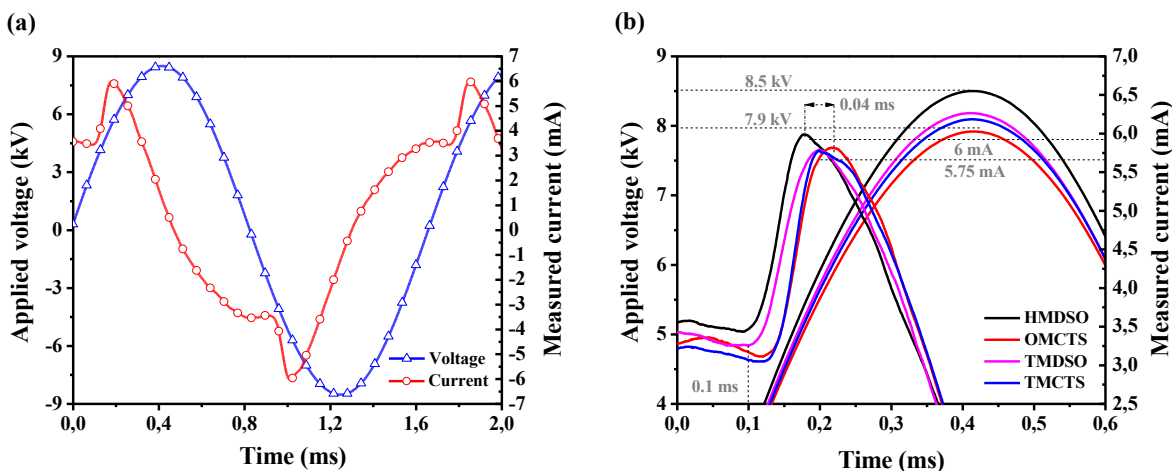
Figure 6.3: *(a) The I-V characteristic of a $N_2O/N_2/TMCTS$ discharge, and (b) a detail of the I-V characteristics of a N_2/N_2O discharge in the presence of TMCTS, OMCTS, TMDSO, and HMDSO.*

Similar I-V characteristics were observed in OMCTS-, HMDSO-, and TMDSO-containing N_2/N_2O plasmas (**Figure 6.3b**), suggesting that the presence or absence of the "anti-fogging feature" in the coated glasses cannot be attributed to a change in the discharge physics. Nonetheless, the voltages applied to sustain the discharge depended slightly on the siloxane precursor. For example, in a HMDSO-containing N_2/N_2O plasma, the peak-to-peak voltage amplitude was found to be 7.1% greater than that observed in an OMCTS/N_2/N_2O, for the same dissipated power (0.7 W cm^{-2}). Moreover, this amplitude variation appears to be linked to a slightly faster N_2 breakdown, i.e., 0.04 ms faster than in an OMCTS-containing N_2 plasma.

6.5.2 Structural analysis of the plasma-deposited coatings

Figure 6.4 shows the infrared spectra of the siloxane precursors and their associated plasma-deposited coatings. Main IR absorption assignments for TMCTS, OMCTS, TMDSO, and HMDSO are summarized in **Table 6.1**.
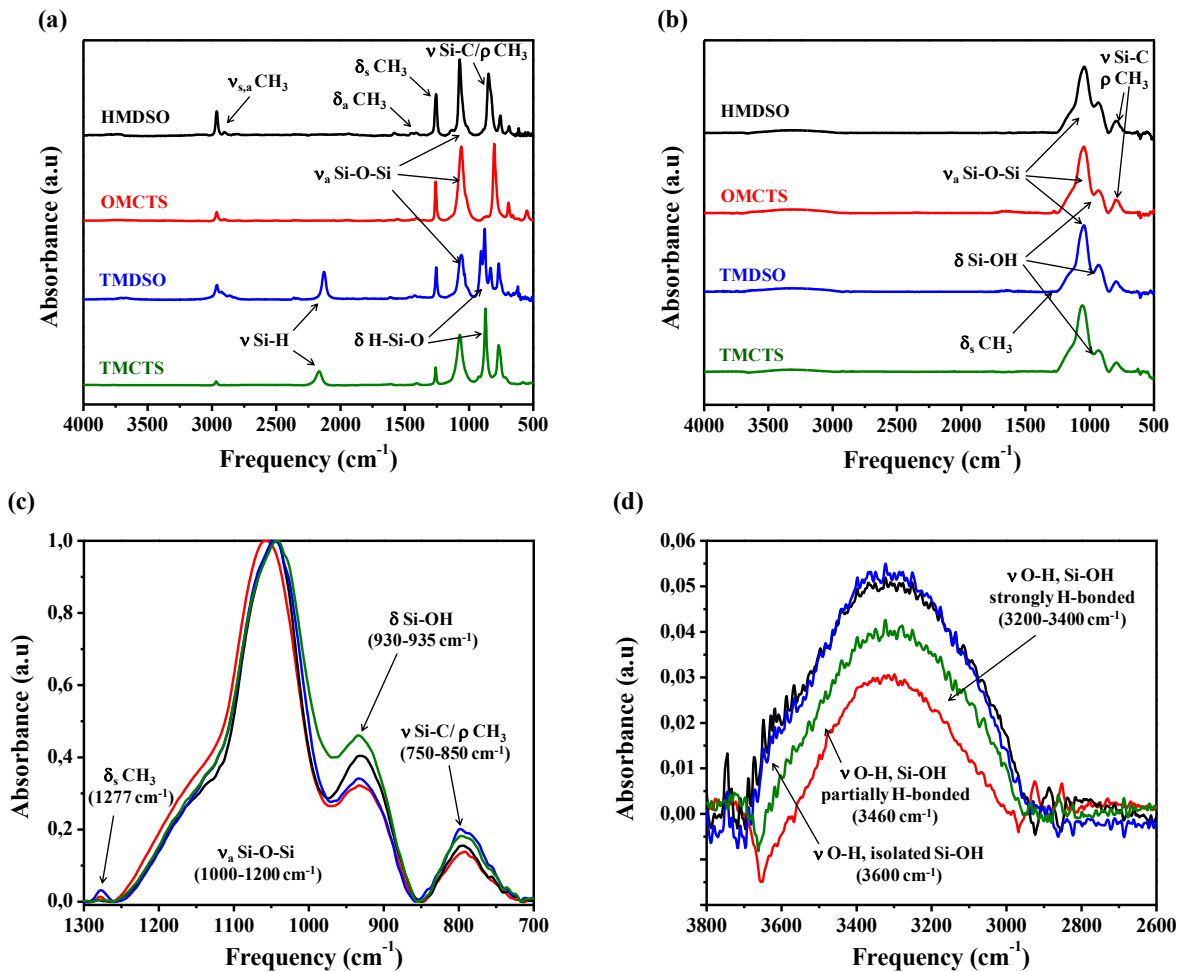
Figure 6.4: *(a) IR spectra of TMCTS, OMCTS, TMDSO, and HMDSO. (b) IR spectra of plasma-deposited coatings in the 500–4000 cm⁻¹ range. Detail of the (c) 700–1300 and (d) 2600–3800 cm⁻¹ regions showing the main IR spectral features (ν = stretching, δ = bending, ρ = rocking, a = asymmetric, and s = symmetric).*

Coatings deposited on glass substrates using a N_2/N_2O atmospheric Townsend discharge exhibited some IR absorptions similar to those observed in the liquid precursors (**Figure 6.4a**). These include the CH_3 rocking and Si-C stretching between 750 and 850 cm⁻¹, the CH_3 symmetric bending in $Si-(CH_3)_x$ groups (x = 1, 2, and 3) at ~ 1277 cm⁻¹, and the Si-O-Si asymmetric stretching between 1000 and 1200 cm⁻¹ (**Figure 6.4b**).

On the other hand, changes in peak half-widths, intensities, and positions reveal clear structural differences. When compared with the IR spectra of the siloxane precursors, the asymmetric stretching of Si-O-Si groups, i.e., ν_a Si-O-Si, broadened and shifted slightly to

low frequencies, accompanied by the emergence of a shoulder at ~ 1150 cm^{-1} (**Figure 6.4c**). The bonding environment of Si-O-Si groups in carbon-containing SiO$_x$ coatings (i.e., SiO$_x$C$_y$:H), can be described in terms of linear chains as well as cyclic and polycyclic entities, such as cage-like and ladder-like structures. In this regard, the broad band ranging from 1000 to 1200 cm^{-1} can be fitted with three [412,527,528] or four components [529–531] (**Figure 6.5**).
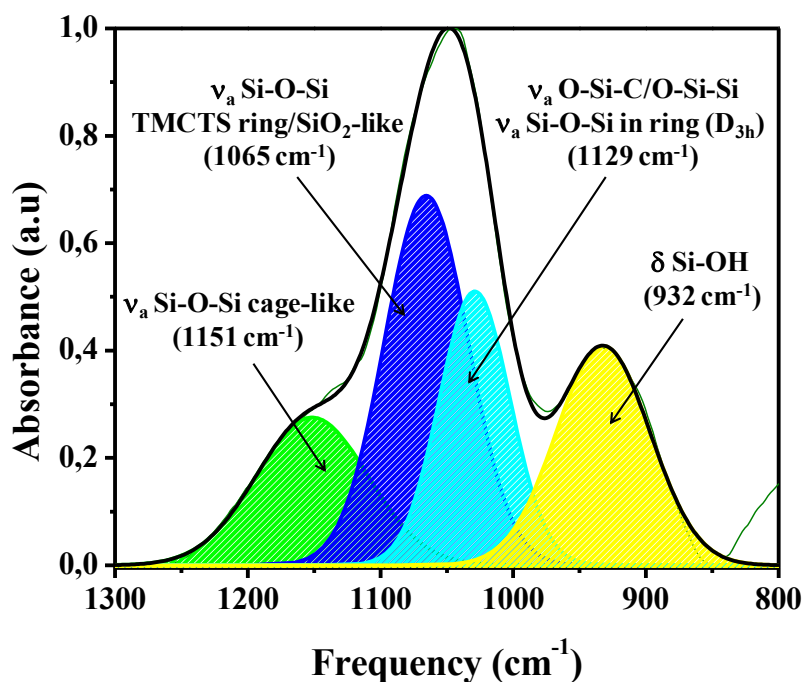
Figure 6.5: *Curve fitting of the 800−1300 cm^{-1} region (TMCTS-based coating).*

According to Grill and Neumayer [412], the first component at 1023−1035 cm^{-1} can be assigned to silicon sub-oxidized states (e.g., O-Si-C and O-Si-Si groups), long chains with Si-O-Si angles of less than 144°, and siloxane rings with a D$_{3h}$ point symmetry. The second contribution at 1065−1070 cm^{-1} can be attributed to a siloxane network with Si-O-Si angles of ~144° and some 4-membered tetrahedral rings, such as those integrating the TMCTS and OMCTS cycles. In the 1135−1150 cm^{-1} range, the third contribution to the Si-O-Si stretching originates from cage-like entities in the coatings, such as those found in silsesquioxane polymers (Si-O-Si angles > 144°).

Table 6.1: *Principal IR bands of the siloxane precursors used in this study. ν = stretching, δ = bending, ρ = rocking, a = asymmetric, and s = symmetric.*

HMDSO	OMCTS	TMDSO	TMCTS	Vibrational mode	Comment	References
2962	2962	2962	2968	ν_a C-H	in CH_3	[412,472,514,559,560]
2902	2904	2903	2906	ν_s C-H	in CH_3	[412,472,514,559]
		2127	2165	ν Si-H	in H-SiOSi	[412,472,559,560]
1410	1412	1419	1406	δ_a C-H	in $Si(CH_3)_x$	[412,472,514,560]
1256	1259	1255	1259	δ_s C-H	in $Si(CH_3)_x$	[412,472,514,560]
1072	1061	1061	1063	ν_a Si-O-Si	-	[412,560]
		906		ν Si-C, ρ CH_3	in $Si(CH_3)_2$	[412,472,559,560]
		877	865	δ H-Si-O	in H-SiOSi	[412,559,560]
849				ν Si-C, ρ CH_3	in $Si(CH_3)_3$	[412,472,514,560]
		831		ν Si-C, ρ CH_3	in $Si(CH_3)_2$	[412,472,514,560]
756	804	769	754	ν Si-C, ρ CH_3	in $Si(CH_3)_{1,3}$	[412,472,514,560]
689	692 660 549	619	710	ν_s Si-O-Si	-	[412,472,559]

Because of the presence of N_2O in the discharge, the IR features pertaining to CH_3 groups (i.e., δ_s C-H, δ_a C-H, ν Si-C, ρ CH_3, etc.) either diminished or disappeared. In OMCTS- and TMDSO-based coatings, the weak absorption at ~ 1277 cm^{-1} (δ_s CH_3 in Si-$(CH_3)_x$) suggests that most of the remaining CH_3 groups were bonded to one silicon atom in the form of O_3-Si(CH_3)_1 entities ("T-units"). Nonetheless, the presence of both O_2-Si(CH_3)_2 (D-units) and O_1-Si(CH_3)_3 (M-units) in the coatings cannot be excluded, in view of the several overlapping features in the 750–850 cm^{-1} region (**Figure 6.4c**). In addition, in the case of TMCTS and TMDSO-based coatings, the CH_3 loss was accompanied by the disappearance of the Si-H bond, as no absorption in the range of 2130–2170 cm^{-1} was observed (**Figure 6.4b**).

Further evidence of the loss of CH_3 functionalities is available upon examination of the region ranging from 2600 to 3800 cm^{-1} (**Figure 6.6d**). The absence of the C-H asymmetric (ν_s) and symmetric (ν_a) stretching of CH_3 groups in the 2900–2970 cm^{-1} range, supports the loss of the organic component of the coatings. Even though plasma-deposited films did not display a marked organic character, both the position (1043–1057 cm^{-1}) and the full width at

half maximum (FWHM $\approx$ 250 cm^{-1}) of the ν_a Si-O-Si absorption reveal a coating structure different from that of the stoichiometric SiO$_2$ (ν_a Si-O-Si at 1075–1080 cm^{-1} and FWHM $\approx$ 70 cm^{-1} [561]).

Coatings exhibited several features that were not observed in the IR spectra of the siloxane precursors. These include two bands pertaining to Si-OH (silanol) groups, one at 930–935 cm^{-1} due to the Si-O bending, and other in the 3000–3700 cm^{-1} range due the O-H stretching [525]. From the shape of the latter feature, it can be inferred that various populations of silanol groups were present in the coatings [525,526]. Specifically, three populations of these functionalities were identified, namely isolated Si-OH groups at 3600–3700 cm^{-1}, partially hydrogen-bonded Si-OH groups at 3460 cm^{-1}, and strongly hydrogen-bonded Si-OH groups at 3200–3400 cm^{-1}. Quite a number of studies have revealed two interesting aspects regarding silanol groups [411,485,497,499]: first, the addition of an oxidant in the discharge, such as N$_2$O or O$_2$, appears to be linked to the formation of these functionalities, and second, the content of Si-OH groups in the coatings can be varied by modifying the oxidant/precursor ratio. Of interest is the study reported by Fanelli et al. [497] who deposited SiO$_x$C$_y$:H coatings from siloxane precursors with a different number of Si-CH$_3$ and Si-H groups (i.e., hexamethyldisiloxane, pentamethyldisiloxane, and 1,1,3,3-tetramethyldisiloxane) using an atmospheric pressure DBD fed with Ar/O$_2$. Regardless of the precursor, a minimum O$_2$/precursor ratio of 25 was found to be the threshold value to provide coatings with a high Si-OH content. Similarly, Massines and collaborators [485] evidenced that SiO$_2$-like coatings, with a non-negligible amount of silanol groups can be obtained using N$_2$/N$_2$O Townsend discharges with N$_2$O/HMDSO ratios > 6.

Minor absorptions in the range of 1550–1750 cm^{-1}, most likely due to the C=O stretching, intimates the presence of carbonyl-containing functionalities in the coatings, such as carboxyl (COOH), ester (COOR), or amide groups (CONH) [517]. That said, CN-related absorptions cannot be excluded, given that the C=N stretching also falls within the same frequency range [517].

6.5.3 Surface chemical composition

Table 6.2 shows the chemical composition of plasma-deposited coatings in terms of atomic percent (at. %) of Si, C, O, N, as well as O/Si and C/Si atomic ratios, as determined by XPS survey analyses.

***Table 6.2:** Surface composition of plasma-deposited coatings. * Percentage composition of siloxane precursors.*

Sample	Si2p	O1s	C1s	N1s	O/Si	C/Si
TMCTS*	33.3	33.3	33.3	-	1	1
TMCTS	27.9 ± 0.8	67.0 ± 0.6	5 ± 1	0.1 ± 0.2	2.40 ± 0.07	0.18 ± 0.04
OMCTS*	25	25	50	-	1	2
OMCTS	28.7 ± 0.6	64.9 ± 0.7	6.5 ± 0.8	-	2.26 ± 0.06	0.23 ± 0.03
TMDSO*	28.6	14.3	57.1	-	0.5	2
TMDSO	28.4 ± 0.6	63.9 ± 0.7	7.6 ± 0.7	0.08 ± 0.08	2.25 ± 0.06	0.27 ± 0.03
HMDSO*	22.2	11.1	66.7	-	0.5	3
HMDSO	27.8 ± 0.3	66 ± 1	6 ± 1	-	2.38 ± 0.05	0.20 ± 0.05

Plasma deposition conducted under conditions of over-stoichiometric $[N_2O]/[\text{precursor}]$ ratios resulted in coatings with much less carbon and more oxygen, when compared with the theoretical composition of siloxane precursors. The average carbon content was found between 6 and 7% in all coatings, except for those prepared from TMCTS, in which carbon percentage was a slightly lower (~ 5%). Such carbon content coupled with a relatively high silicon percentage compared to that of the TMCTS, accounts for the lowest C/Si ratio found in the coatings.

With regard to O/Si ratios, two points deserve to be highlighted. First, O/Si ratios greatly exceeding that of the precursors (O/Si = 1 for TMCTS and OMCTS, and O/Si = 0.5 for TMDSO and HMDSO) substantiate the incorporation of oxygen, most likely resulting from the dissociation of N_2O on collision with the N_2 $(A^3\Sigma_u^+)$ species [485,499,562]. Second, O/Si ratios are greater than 2 (O/Si ratio in stoichiometric silica), substantiating the presence of Si-OH functionalities in the coatings (FTIR analyses). Strictly speaking, O/Si ratios > 2 are also compatible with the presence of Si-O-C groups at the surface; however, their

identification by FTIR is challenging, because the asymmetric stretching of Si-O-C and Si-O-Si groups falls within the same frequency range [563].

The coatings deposited from TMCTS- and TMDSO-containing plasmas incorporated a slight amount of nitrogen. This result significantly differs from that reported by Gherardi et al. [499] who found a greater amount of nitrogen (0.5–0.7%) in the coatings deposited in static conditions (stationary bottom electrode) using a N_2/N_2O/HMDSO Townsend discharge. This discrepancy may be explained in terms of gas dynamics. Because of the movement of the bottom electrode during the deposition process, the flow of gases through the inter-electrode space is likely more turbulent. A turbulent flow may hinder the incorporation of nitrogen-containing species from the plasma phase into the coatings, thus explaining the lower nitrogen content. Interestingly, the presence of Si-H in the precursor appears to correlate with an enhanced nitrogen incorporation efficiency.

Although XPS analyses were consistent with the results obtained by FTIR, it has been deemed appropriate to provide further insight into the carbon bonding environment at the surface. The main reason for this lies in the fact that carbon-containing surface groups can also be involved in the anti-fogging performance [507]. To this end, curve fitting of the C1s envelopes obtained from high-resolution XPS spectra was performed for each coating (**Figure 6.6**). In general terms, the C1s core level spectrum can be decomposed into two or three components, namely, C-C/C-H at 285 eV, C-O (epoxy and hydroxyl groups) at 287 eV, and O-C=O (carboxyl and ester groups) at 289 eV [500]. Unlike coatings obtained from OMCTS, TMDSO, and HMDSO, TMCTS-based coatings exhibited a third component at higher binding energies, pertaining to carbonyl-containing species (compare **Figures 6.6a** and **6.6b-d**). The additional feature at 288.8 eV intimates that the cyclic structure coupled with the presence of Si-H bonds in the TMCTS is behind the formation of carboxyl (COOH) and ester (COOR) groups. As a matter of fact, this feature was not observed either in TMDSO-based coatings, despite the Si-H bonds in the TMDSO, or in OMCTS-based coatings, despite the cyclic structure of OMCTS.
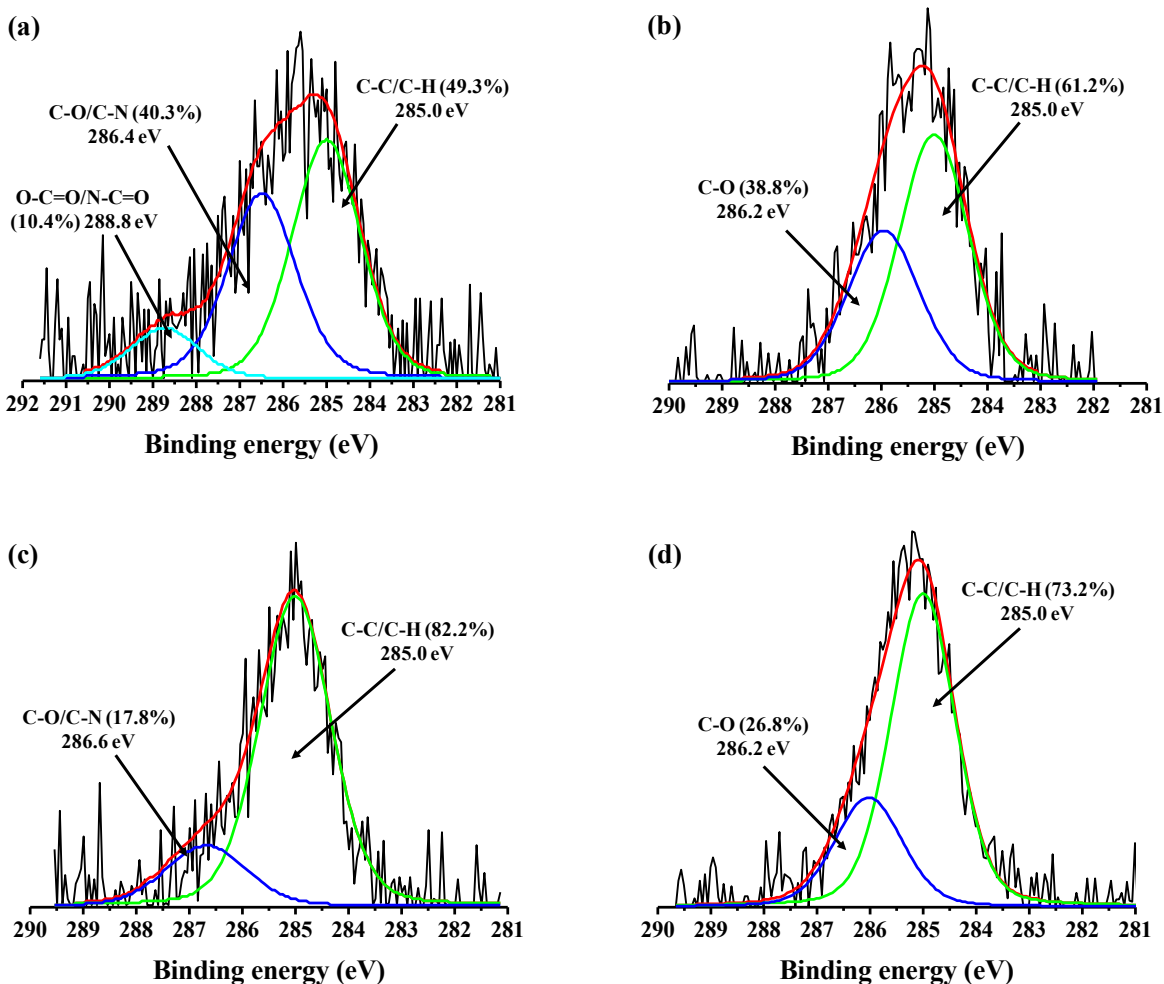
Figure 6.6: *Curve fitting of the C1s core level spectrum of (a) TMCTS-based, (b) OMCTS-based, (c) TMDSO-based, and (d) HMDSO-based coatings.*

Bearing in mind the incorporation of nitrogen in TMCTS- and TMDSO-based coatings (**Table 6.2**), the XPS peaks due to the presence of (hydrophilic) nitrogen-containing functionalities, such as such as C-NH$_2$ (286.4 eV), C=NH (287.3 eV), and CO-NH$_2$ (289.2 eV), should also be included in the C1s analysis (**Figures 6.6a** and **6.6c**) [541,542].

Curve fitting of the Si2p feature provides structural information of the coatings on extreme surface (**Figure 6.7**). Depending on the number of oxygen and carbon atoms bonded to the silicon, i.e., (CH$_3$)$_x$SiO$_{(4-x)/2}$ (where x = 0–3), the Si2p envelopes can be composed of up to four peaks. In general, the first peak at 101.5 eV is attributed to M-units (x = 3), the second

at 102.1 eV to D-units (x = 2), the third at 102.8 eV to T-units (x = 1), and the last one at 103.4–103.6 eV (x = 0) to Q-units, such as those found in stoichiometric SiO_2 [502,503].
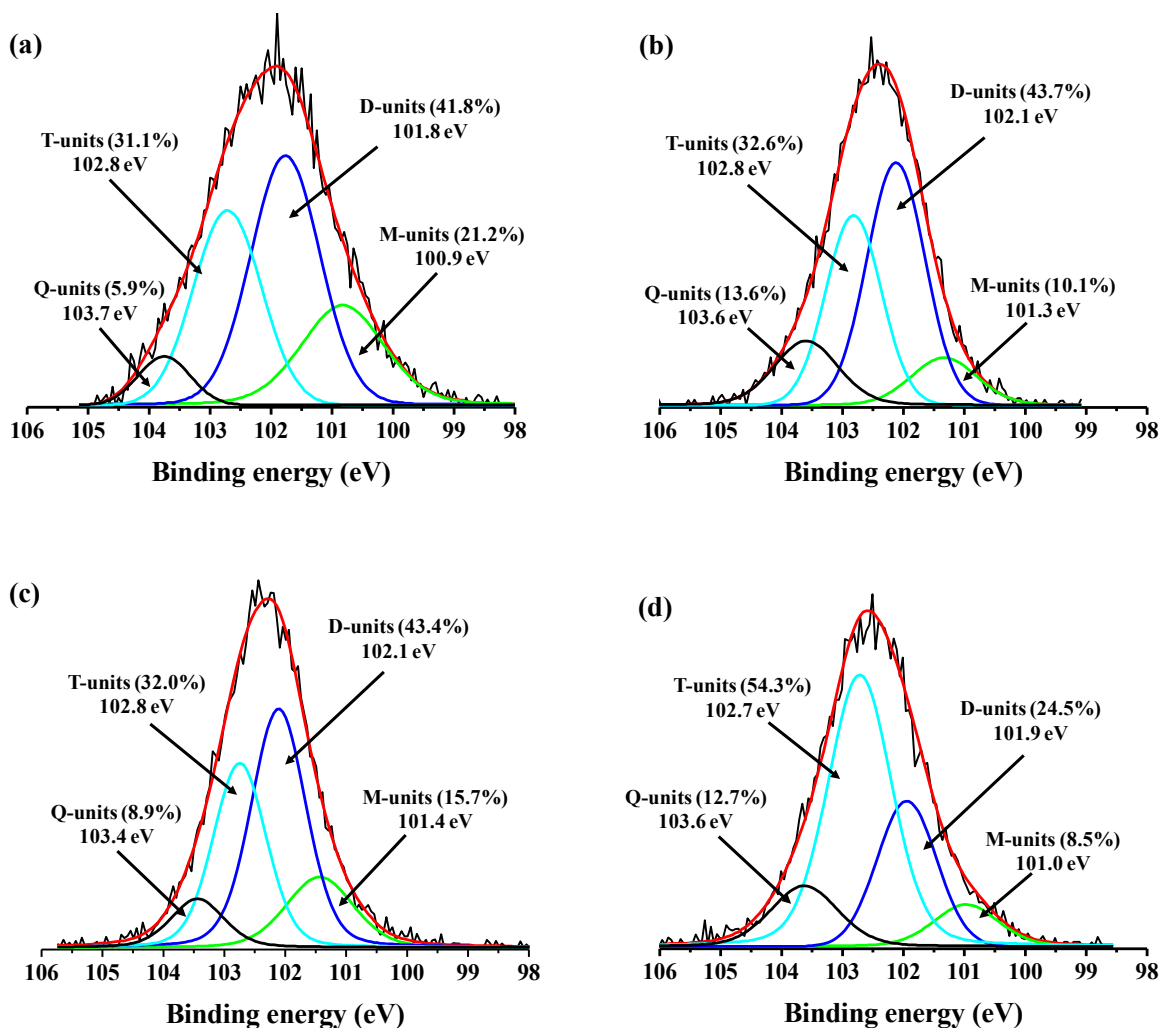
Figure 6.7: *Curve fitting of Si2p core level spectra of (a) TMCTS-based, (b) OMCTS-based, (c) TMDSO-based, and (d) HMDSO-based coatings.*

Approximately 75% of the silicon can be described by the same "building units" that integrate the precursors, that is, D- and T-units. Indeed, TMCTS (or "D4H"), OMCTS (or "D4"), and TMDSO (or "D2H") are composed of D-units while HMDSO (or "T2") is composed of T-units. The remaining 25% was found in the form of Q- and M-units (**Figure 6.7**). Interestingly, the percentage of Q-units in TMCTS- and TMDSO-based coatings (5.9 and 8.0%, respectively) was lower than that found in OMCTS- and HMDSO-based coatings (13.6 and 12.7%, respectively). In view of these results, it could be argued

that the bonding environment of the silicon slightly depends on the starting siloxane, and that the precursors containing Si-H bonds (i.e., TMCTS and TMDSO) make it more difficult to obtain SiO_2-like coatings.

6.5.4 Surface morphology and deposition rate of the coatings

Figure 6.8 shows the atomic force micrographs of the coatings deposited using a N_2/N_2O plasma at atmospheric pressure in the presence of TMCTS, OMCTS, TMDSO, and HMDSO. In general terms, the coatings were homogeneous and devoid of surface defects, such as pinholes or cracks. This result is consistent with the application of a N_2 discharge operating in the Townsend regime **(Figure 6.3)**, such as that employed by Gherardi's [564] and Starostin's [468] groups to prepare high-quality SiO_2-like coatings. That said, some differences in surface roughness as well as in the morphology of surface features are worthy of mention. While OMCTS-, TMDSO-, and HMDSO-based coatings were very smooth, in light of the small R_{rms} values (1.3–7 nm) for both 5×5 and 50×50 μm^2 areas, the island-like features with a higher aspect ratio observed on TMCTS-based coatings caused R_{rms} to increase to 19 nm. Not surprisingly, the mean roughness values R_a measured on both 5×5 and 50×50 μm^2 areas (**Table 6.3**) were relatively close to those of R_{rms}. With a R_a of ≈ 14 nm, TMCTS-coated glasses were rougher than OMCTS-, TMDSO-, or HMDSO-coated glasses, in which R_a values were between 1 and 5.3 nm, and than the glass substrate, which exhibited surface features in the 0.5–1.5 nm range (not shown).
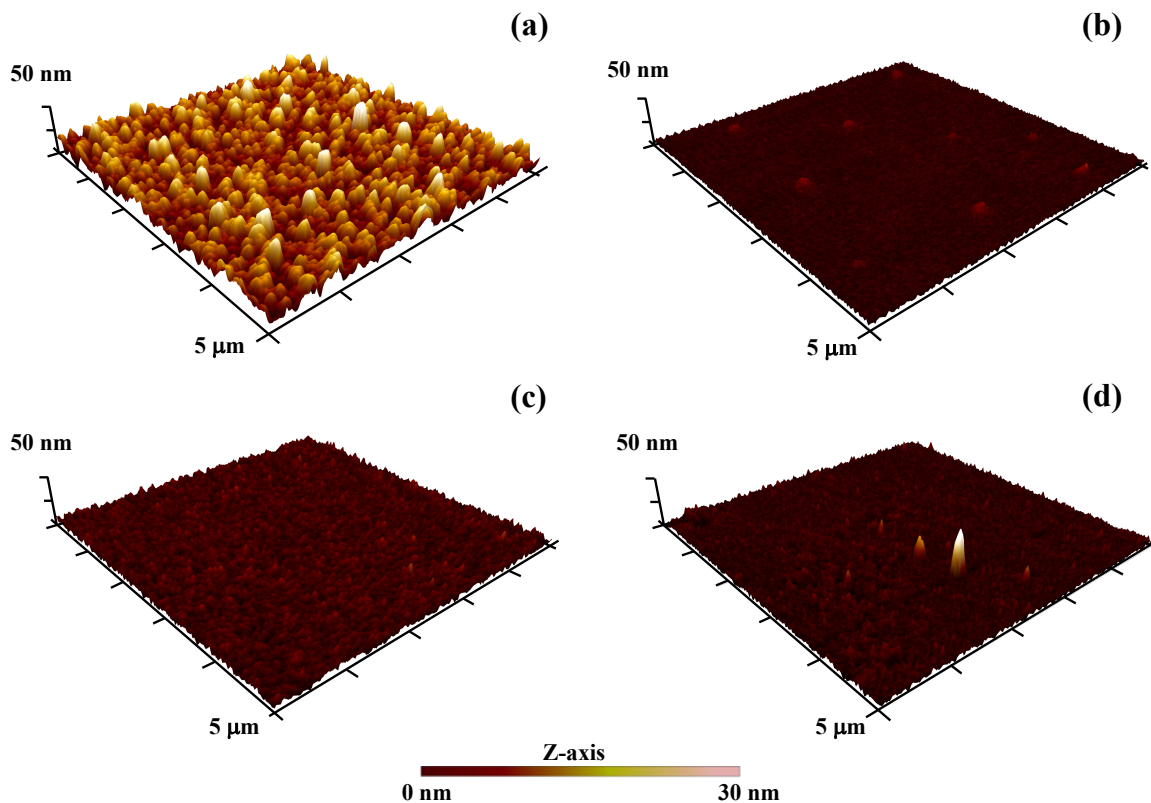
Figure 6.8: *Atomic force micrographs of the plasma-deposited coatings on glass using a homogeneous N_2/N_2O Townsend discharge. (a) TMCTS-, (b) OMCTS-, (c) TMDSO-, (d) HMDSO-based coatings.*

Interestingly, the values of surface roughness R_a and R_{rms} followed a trend similar to that of the deposition rates. In addition, the relatively high surface roughness of TMCTS-based coatings compared to that of OMCTS-, TMDSO-, and HMDSO-based coatings may result from the high deposition rate of TMCTS, i.e., TMCTS (23 nm min^{-1}) >> TMDSO (6.8 nm min^{-1}) > HMDSO (4 nm min^{-1}) > OMCTS (1.6 nm min^{-1}). Bearing in mind the deposition rates and the surface features shown in **Figures 6.8b-d**, it could be argued that the coatings deposited from OMCTS, TMDSO, and HMDSO are denser than those deposited from TMCTS. Moreover, the smoothness of these coatings may indicate an efficient packing on the molecular level [470]. According to Shirtcliffe and collaborators [544], very smooth coatings are obtained when the species generated in the plasma have a high sticking probability, and therefore bond at the first contact point.

Table 6.3: *Root mean square roughness (R_{rms}), mean roughness (R_a), and deposition rates (DR) of plasma-deposited coatings on 5 × 5 and 50 × 50 µm² areas (VP: vapor pressure).*

Sample	R_{rms} (nm)	R_a (nm)	R_{rms} (nm)	R_a (nm)	DR (nm min^{-1})	VP (torr) /20–25°C
	5 × 5 µm²		50 × 50 µm²			
TMCTS	17.9 ± 0.7	14.1 ± 0.5	19 ± 1	14 ± 1	23 ± 2	7
TMDSO	6.76 ± 0.07	5.33 ± 0.05	4.9 ± 0.2	3.9 ± 0.2	6.8 ± 0.5	110
HMDSO	2.0 ± 0.1	1.42 ± 0.02	4 ± 2	3 ± 2	4.0 ± 0.2	42
OMCTS	1.32 ± 0.07	1.02 ± 0.05	7 ± 1	1.9 ± 0.9	1.6 ± 0.6	1
Glass	0.7 ± 0.2	0.5 ± 0.1	1.6 ± 0.5	1.1 ± 0.5	-	-

Considering that the amount of TMCTS, OMCTS, TMDSO, and HMDSO was set at 10 ppm for all experiments, the differences in the deposition rates cannot be due to changes in the concentration of the precursors in the discharge. In addition to this, the siloxane precursors containing Si-H bonds (e.g., TMCTS and TMDSO) allowed for the preparation of coatings with high deposition rates—a feature that has also been reported by several research groups. In investigating SiO_x coatings for gas barrier applications, Badyal and colleagues [401] revealed that TMCTS deposited faster than OMCTS did under identical conditions (He/1% O_2 discharge at atmospheric pressure and 0.12 mL h^{-1} of each precursor). These authors emphasized that the labile nature of the Si-H bond ($\Delta H_{dissociation}$ Si-H < Si-C < Si-O) makes TMCTS more reactive than OMCTS, thus providing suitable justification for the high deposition rates. These results also support those of Cui et al. [417], who deposited SiO_2-like coatings on poly(methyl methacrylate) and polycarbonate from TMCTS, tetraethoxysilane (TEOS), and 2-bis(triethoxysilyl)ethane (BTESE), by a RF-driven atmospheric plasma. In addition to the high reactivity of the Si-H bond, they referred to the four-membered siloxane ring in the TMCTS molecule as a contributing factor to the deposition rate. As indicated by Badyal and colleagues, [401] Si-H bonds would preferentially break on collision with the reactive oxygen species in the plasma, leading to the formation of "activated" siloxane rings. These rings would then react with each other to produce multiringed structures possessing high sticking coefficients. Considering the surface topography of the coatings (**Figure 6.8**), these arguments lead us to believe that these multiringed structures do not pack efficiently at the molecular level, unlike the species generated in the presence of OMCTS, TMDSO, and

HMDSO in the plasma. In another study conducted by Pai et al. [404], TMCTS was used to prepare high-quality SiO_2 coatings on Si wafers by electron cyclotron resonance CVD under an Ar/O_2 atmosphere. By comparing the deposition rates with those reported in TEOS-based coatings (TEOS = tetraethylorthosilicate), these authors suggested that both the greater volatility (i.e., vapor pressure) and the greater number of silicon atoms in the TMCTS are behind the higher deposition rates. In this case, no mention to the Si-H bond nor the cyclic structure of the TMCTS was made.

As shown in **Table 3**, for the same number of silicon atoms, the precursors with a greater vapor pressure make it possible to obtain coatings with higher deposition rates, as pointed out by Badyal and colleagues [401]. Similarly, Fujino et al. [414] found that the greater the number of silicon atoms in the starting siloxane, the higher the deposition rate (TMCTS and TEOS were used in their study). That said, this result appears to not apply here, as the OMCTS (4 silicon atoms per molecule) did not deposit faster than did TMDSO or HMDSO (2 silicon atoms per molecule).

6.5.5 Anti-fogging performance and wetting behavior of the coated glasses

Figures 6.9a-f shows the resistance to fogging of the coated glasses when placed over hot water at 80°C (hot-fog test). Glass samples covered with a TMCTS-based coating remained optically clear (**Figure 6.9a**) and maintained the "see-through" property when they were brought back to ambient conditions (**Figures 6.9b,c**). Under the same testing conditions, OMCTS-, TMDSO-, and HMDSO-coated glasses promptly fogged making it difficult to see through them. Moreover, fogged glasses did not become clear when they were brought back to ambient lab conditions (**Figures 6.9f,i,l**).
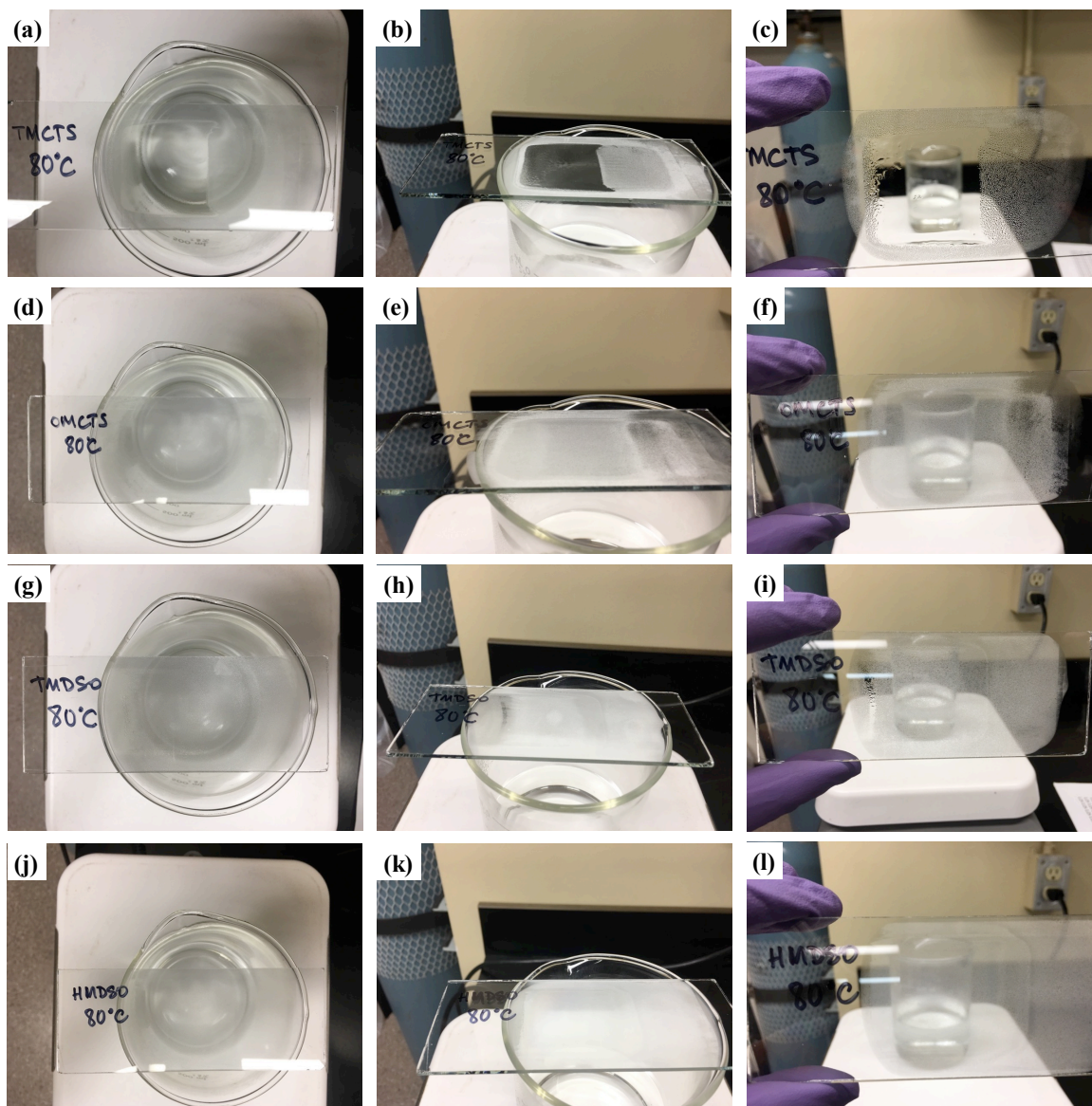
Figure 6.9: *(a,d,g,j) Top and (b,e,h,k) side views of coated glasses placed over an Erlenmeyer flask containing water at 80°C for 15 s. (c,f,i,l) Coated glasses at a distance of ~ 1 m from the Erlenmeyer following hot-fog testing.*

By means of contact angles measurements, the surface features of the coatings, such as the chemistry and roughness, have been correlated with the observed anti-fogging performance. **Figure 6.10** shows the water contact angles measured on plasma-deposited coatings. The small standard deviations (~ 3°) of the measured water contact angles is in line with the surface homogeneity of the coatings at the microscale (see AFM results). Glasses covered with TMCTS-based coatings were superhydrophilic (WCA < 5°), thus substantiating the presence of silanol groups (Si-OH) and other hydrophilic functionalities, such as hydroxyl

(C-OH), carboxyl (COOH), ester (COOR), and amino (NH$_2$) groups at the surface (**Figure 6.10a**). Coupled with surface hydrophilic groups, the high surface roughness of TMCTS-based coatings (**Figure 6.8a**) makes it possible to procure an excellent anti-fogging property by increasing the specific surface area available for the wetting phenomenon. Here, any light ray at normal incidence (perpendicular) to the coating surface passes through without being scattered, and consequently the coated glass remains optically clear under very humid conditions (**Figures 6.9a** and **6.9b**).

(a) WCA $< 5°$
(b) WCA $= 83 \pm 3°$
(c) WCA $= 80 \pm 2°$
(d) WCA $= 79 \pm 3°$
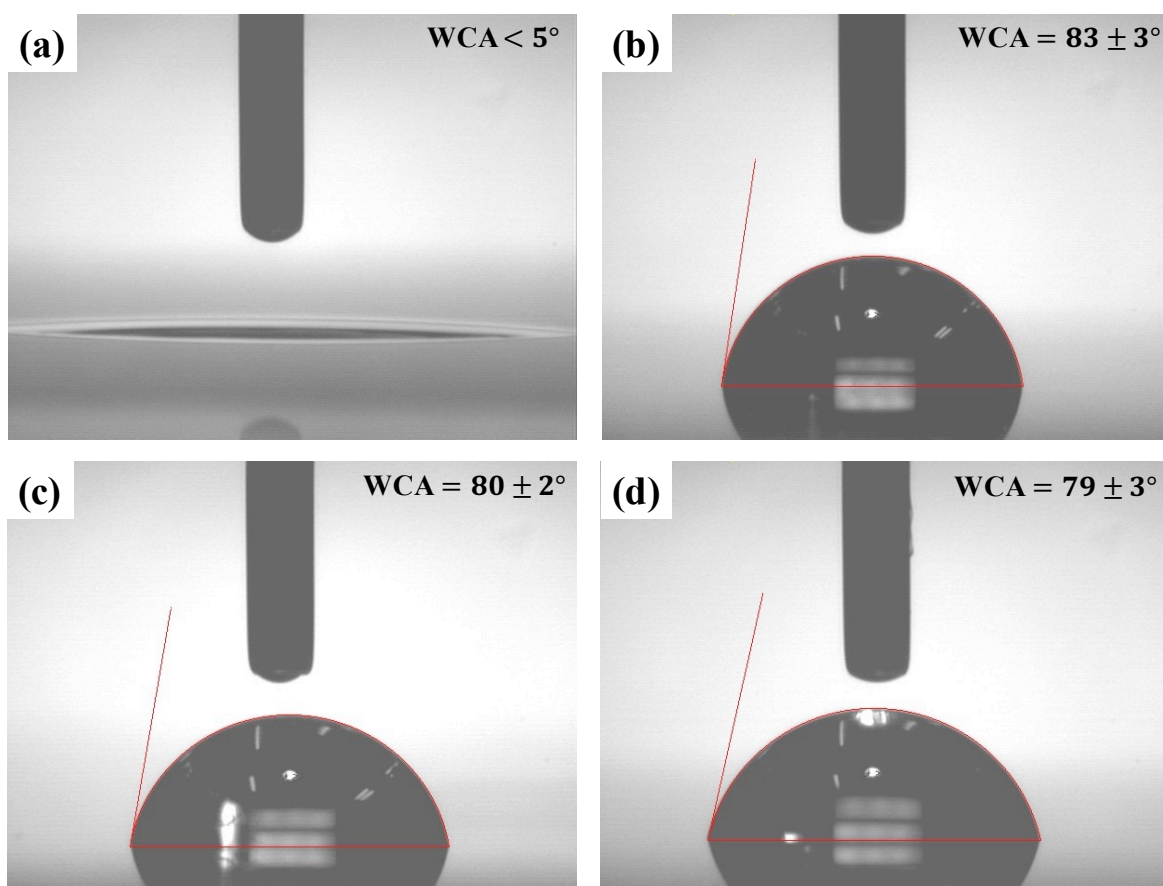
Figure 6.10: *WCA measured on (a) TMCTS-, (b) OMCTS-, (c) TMDSO-, and (d) HMDSO-based coatings.*

In sharp contrast, the glasses coated with OMCTS-, TMDSO-, or HMDSO-based coatings were far less wettable, despite the hydrophilic groups, such as Si-OH and C-OH, at the surface. Surprisingly, the wetting behavior of these coatings was found to not depend on the starting siloxane—the measured contact angles were very similar (WCA $\approx 80°$,

Figures 6.10b-d). The relatively low surface roughness compared to that of the TMCTS-coated glasses, explains why OMCTS-, TMDSO-, and HMDSO-coated glasses were less hydrophilic, and therefore fogged up on exposure to water vapor at 80°C. In this case, water drops on the surface remain in a nearly hemispherical shape, so that a significant portion of the incident light is not transmitted because of the total internal reflection occurring at the water drop/air interface. For this reason, the "see-trough" property is dramatically compromised as shown in **Figures 6.9d-l**.

Numerous studies have shown that both the surface chemistry and surface roughness must be properly adjusted to change the morphology of water drops (i.e., wetting behavior), and in this way, design coatings meeting the desired anti-fogging requirements [402]. The wetting behavior of the coatings (**Figure 6.10**) can be explained by two classical models, namely the Wenzel model [79,80] and the Cassie-Baxter model [81,82]. According to these wetting models, given a smooth and hydrophilic surface ($10° <$ WCA $< 90°$), an increment in its surface roughness results in a more wettable surface ($WCA_{rough} < WCA_{smooth}$), and consequently more likely to be fogging-resistant. The results shown in **Figures 6.9** and **6.10** support this assertation. Even though the surface chemistry of plasma-deposited coatings was relatively similar, the higher roughness of the TMCTS-based coatings accounts for their extreme wetting behavior, and thus the anti-fogging performance conferred to the glass samples.

To quantify the "see-through" property of the TMCTS-coated glasses (**Figures 6.9a-c**), light transmission (590 nm) was recorded as a function of time according to the procedure described in the ASTM F 659-06 standard. **Figure 6.11** shows the transmittance percentage of the TMCTS-coated glasses before and after being thermally treated under a controlled Ar atmosphere at different temperatures. For comparative purposes, an uncoated glass, a thermally treated TMCTS-coated glass previously exposed to room conditions for two weeks (natural aging of the coating), and a thermally treated TMCTS-coated glass subjected to a vigorous washing were also tested.
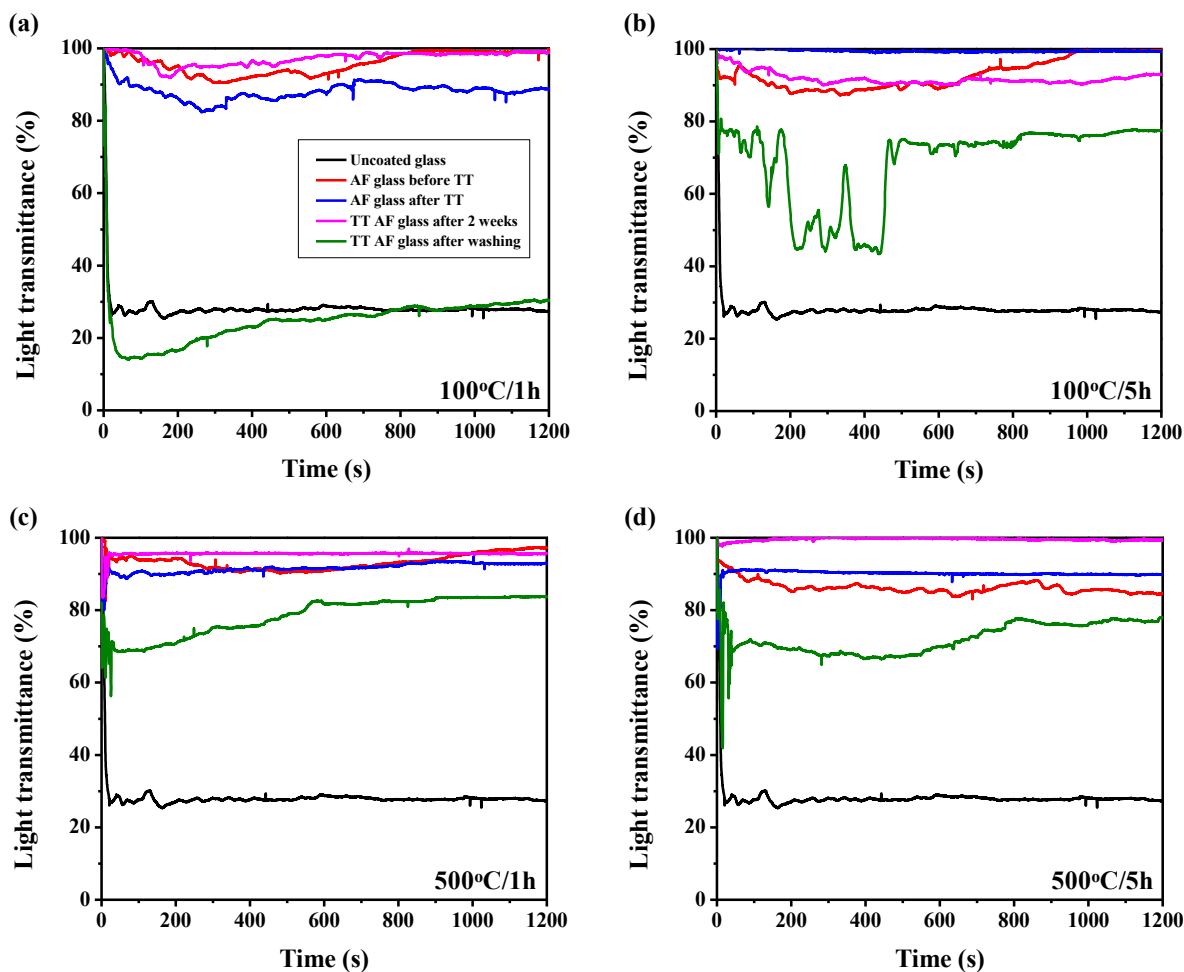
Figure 6.11: *Percentage of light transmitted as a function of time through the TMCTS-coated glasses treated at (a) 100 °C for 1 h, (b) 100 °C for 5 h, (c) 500 °C for 1 h, and (d) 500 °C for 5 h, under an Ar atmosphere.*

With transmittance values well above 80% at 30 s, TMCTS-coated glasses demonstrated excellent capacity to prevent fogging effects (red line). Similarly, coated glasses displayed outstanding anti-fogging performance after two weeks of exposure to (non-controlled) room conditions and following thermal treatment (pink and blue lines, respectively). Based on these findings, it can therefore be concluded that the duration and temperature of the thermal treatment barely alter the anti-fogging performance of TMCTS-coated glasses. Interestingly, the increase in both parameters (temperature and duration of thermal treatment) either separately or in combination has a positive impact on the anti-fogging performance of thermally treated glasses after being subjected to a vigorous washing (compare green lines in **Figures 6.11a** and **6.11b**, **6.11a** and **6.11c**, and 6.**11a** and **6.11d**). Except for the coated

glasses shown in **Figure 6.11a** (green line), in which transmittance values were between 15 and 30% after 30 s of exposure to water vapor at 50°C, the washing treatment was found to not deteriorate considerably the anti-fogging performance (60% < Transmittance < 80%).

To produce coatings with a longer lasting anti-fogging performance once subjected to a vigorous washing, thermal treatments were conducted under a controlled Ar atmosphere in the presence of a small amount of O_2 (2% v/v).
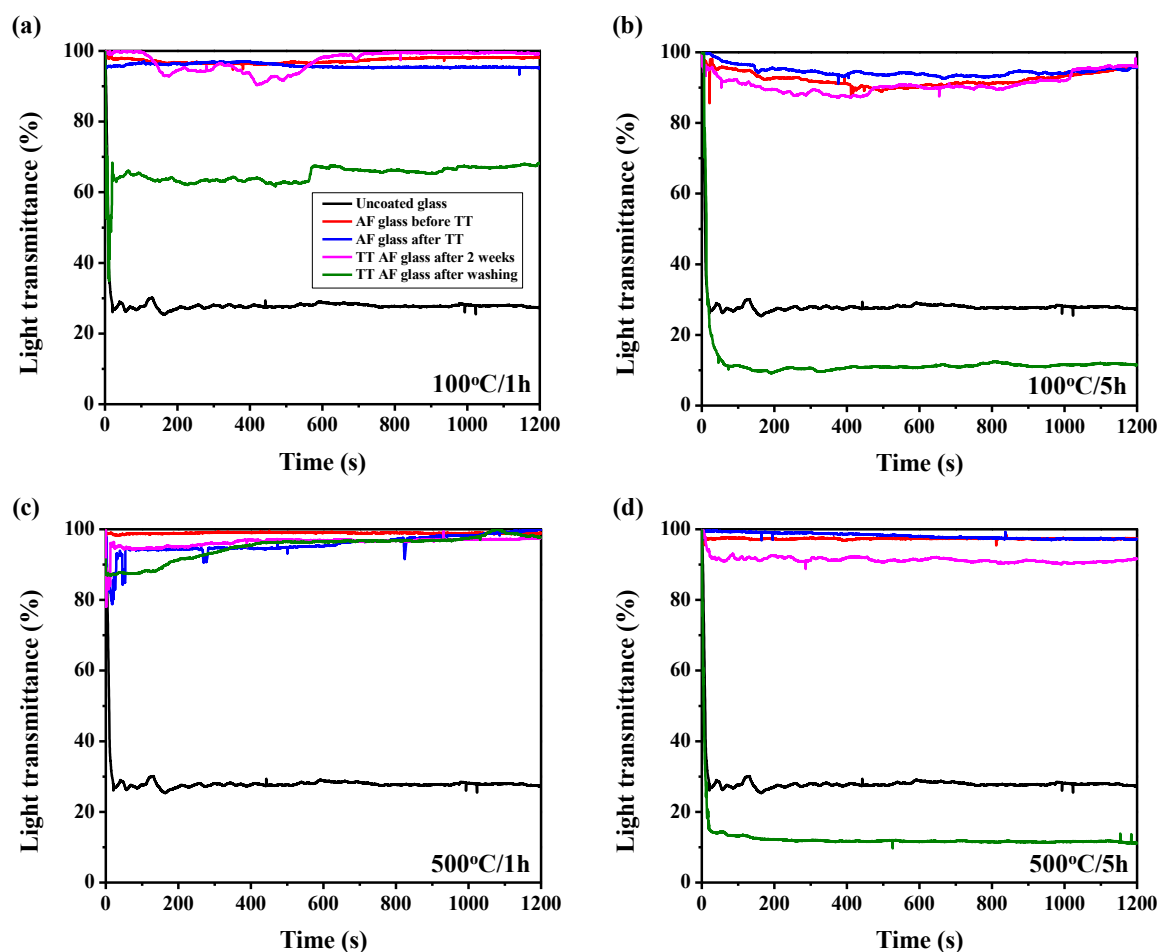
Figure 6.12: *Percentage of light transmitted as a function of time through the TMCTS-coated glasses treated at (a) 100 °C for 1 h, (b) 100 °C for 5 h, (c) 500 °C for 1 h, and (d) 500 °C for 5 h, under an Ar/O_2 (2% v/v) atmosphere.*

The ASTM F659-06 protocol evidenced superior anti-fogging performance (Transmittance > 80%) in coated glasses before and after two weeks of exposure to (non-

controlled) room conditions, and following thermal treatment (compare red, pink and blue lines, respectively in **Figure 6.12**). As in the previous case, the duration and temperature of the thermal treatment barely alter the anti-fogging performance of the TMCTS-coated glasses. Unlike the thermal treatment in pure Ar, an increase in the temperature in combination with an increase in the treatment time did not result in coated glasses with a better anti-fogging performance after being subjected to a washing treatment (compare green lines in **Figures 6.12a** and **6.12d**). An increase in the duration of the thermal treatment from 1 to 5 h caused no noticeable effect on the anti-fogging capacity (compare green lines in **Figures 6.12a** and **6.12b**). In contrast, an increase in the temperature resulted in coatings with enhanced anti-fogging performance if the thermal treatment lasts 1 h (compare green lines in **Figures 6.12a** and **6.12c**). The best anti-fogging performance, which was attained in coated glasses treated at 500°C for 1 h, is most likely due to an enhancement of the coating's robustness and a better coating/substrate adhesion.

6.6 Conclusions

In this study, it has been demonstrated the feasibility of conferring anti-fogging performance to glass substrates by plasma-assisted chemical vapor deposition at atmospheric pressure. Of all of the siloxane precursors used as coating materials, TMCTS was shown to be the most appropriate for that purpose. Due to their extreme wetting behavior (WCA < 5°), TMCTS-coated glasses remained optically clear when placed over an Erlenmeyer containing water at 80°C. In addition, the "see-through" property was preserved even after the TMCTS-coated glasses were brought back to ambient lab conditions. In contrast, OMCTS-, TMDSO-, and HMDSO-coated glasses lost their "see-through" property on exposure to hot water, because of their less hydrophilic nature (WCA ≈ 80°). After hot-fog testing, OMCTS-, TMDSO-, and HMDSO-coated glasses did not become clear, remaining severely fogged for a few seconds. Coupled with surface hydrophilic groups (e.g., Si-OH, C-OH, COOH), the relatively high surface roughness of TMCTS coatings (R_{rms} ≈ 19 nm), compared to that of OMCTS, TMDSO, and HMDSO-coated glasses (R_{rms} = 1.3–7 nm), was shown to endow glass samples with remarkable anti-fogging performance. These results lead us to believe that the cyclic

structure of TMCTS in conjunction with the high reactivity of Si-H bonds is behind the formation of these surface groups, the incorporation of nitrogen from the plasma phase, and the enhancement of surface roughness. By treating the coated glasses at high temperature, a better adhesion strength at the coating/glass interface can be imparted without compromising the anti-fogging property. Indeed, light transmittance measurements revealed that coated glasses treated for 1 h at 500°C under an Ar/O_2 (2% v/v) atmosphere featured excellent anti-fogging performance (> 80% transmittance) for at least 1200 s (20 min) after being subjected to vigorous washing. In conclusion, the use of AP-DBD under a controlled $TMCTS/N_2/N_2O$ atmosphere in combination with an appropriate thermal treatment is a winning strategy, with significant potential for integration into mass production, to prepare durable anti-fogging coatings on glass.

6.7 Acknowledgements

General discussion: Limitations and opportunities

Experimental results have demonstrated that both the hydrophilicity and surface roughness of the coatings are greatly influenced by the [N$_2$O]/[TMCTS] ratio, the power dissipated in the discharge, and the relative movement between the glass substrate and the plasma phase. Regardless of whether coating deposition is conducted or not in static or dynamic conditions, coatings were homogeneous and devoid of surface defects such as pinholes or cracks. In static conditions, coatings prepared under a [N$_2$O]/[TMCTS] ratio ≥ 30 or a dissipated power ≥ 0.25 W cm^{-2} endowed glass substrates with superior anti-fogging performance, as supported by the light transmission measurements (T$_{average}$ > 90%; **chapters 4** and **5**). The anti-fogging performance of the coatings correlated directly with a surface chemistry characterized by O/Si ratios ≥ 2.3 and values of the fogging parameter between 0 and 0.10. In other words, the presence of surface silanols (Si-OH) coupled with minor contributions due to hydroxyl (C-OH) carboxyl (COOH), or ester (COOR) groups is a necessary condition to prevent fogging. The results reported in **chapter 6** shows that the combination of the high reactivity of Si-H bonds with the cyclic structure of TMCTS is behind the anti-fogging performance. In this case, coating deposition conducted in dynamic conditions resulted in coatings with enhanced roughness and—as in the case of static conditions—with abundant silanol groups.

Although experimental evidence indicates that the anti-fogging property is due, to a great extent, to silanol groups, explaining how and where these functionalities form during the deposition process remains a controversial issue.

Silanol groups: Where do they come from?

In a PECVD process with siloxane precursors, it is standard practice to incorporate oxidants, such as N$_2$O, O$_2$, or CO$_2$, into the discharge to fabricate high-quality SiO$_2$ coatings. Nevertheless, in the presence of oxidants in the discharge, the obtention of silanol-containing SiO$_x$C$_y$:H or SiO$_2$ coatings—silanol groups are regarded as structural defects—is more the

rule than the exception when using atmospheric pressure plasmas [565,566] (see **Table 2.2**). Although undesired in applications where high-quality SiO_2 coatings are required, silanol groups are crucial to providing coatings with the anti-fogging feature.

Given that TMCTS does not possess Si-OH groups, it can be argued that such functionalities form as a result of interactions between precursor molecules and plasma species. A reasonable reaction mechanism accounting for the formation of Si-OH groups may involve the following steps: (1) homolytic cleavage of Si-H, Si-C, and C-H bonds in the precursor on collision with the N_2 $(A^3\Sigma_u^+)$ species; (2) oxygen atoms, coming from the dissociation of N_2O, and hydrogen radicals recombine to yield •OH radicals; (3) the as-formed •OH radicals reacts with •Si-containing radicals to produce Si-OH functionalities. Although quite simple, as it does not consider other plasma species such as the electrons, two reasons lead us to believe in the feasibility of this mechanism. First, the average energy of the metastable N_2 $(A^3\Sigma_u^+)$ state (6.3 eV) is high enough to break the Si-H (3.1 eV), C-H (3.5 eV), and Si-C (4.7 eV) bonds, but not to break the Si-O bond, whose energy is estimated at 8.3 eV [412,567]. That said, the cleavage of the Si-O bond is not impossible, but less likely to occur. Second, in DBDs operated in N_2 at atmospheric pressure (i.e., Townsend discharges), the concentration of N_2 $(A^3\Sigma_u^+)$ molecules is almost 5 orders of magnitude greater than that of electrons [568], so that it can be assumed that these species are responsible for the "activation" of TMCTS in the plasma phase.

Zhang et al. [569] and Bogart et al. [570] elegantly demonstrated that the oxygen of the OH group comes from the oxidant. This finding leads us to believe that the origin of the oxygen of the Si-OH group can also be explained in this manner, given that the O/Si ratios are almost always greater than 2 (XPS results). Indeed, the addition of N_2O into the discharge provides an additional source of oxygen—apart from TMCTS (O/Si = 1)—since the dissociation of N_2O yields O atoms in various excited states, including the triplet, $O(^3P)$ and singlet, $O(^1D)$ states. The generation of these electronically excited species in N_2-O_2 and N_2O plasmas has been studied with great detail by Kossyi et al. [571] and by Kline et al. [539]. Atomic oxygen can abstract hydrogen from the Si-CH$_3$ and Si-H groups and thus produce •OH radicals.

These radicals can then generate Si-OH groups by recombination with •Si-containing radicals, without extensive decomposition of the precursor. Using *ab initio* molecular dynamics, Rimsza and colleagues [498] investigated the interaction of 2,4,6-Trimethylcyclotrisiloxane, a cyclic siloxane with Si-H and Si-CH$_3$ groups, with oxygen atoms in triplet, O(^{3}P) and singlet, O(^{1}D) states at different energies and collision angles. Simulation results revealed that collisions with singlet oxygen atoms led to the formation of Si-O-CH$_3$ and Si-OH groups, while collisions with triplet oxygen atoms led to the removal of H, CH$_3$, C$_2$OH and OH$^-$. The collision of oxygen atoms in singlet state with TMCTS must therefore be kept in mind to explain the presence of silanol groups in the coatings.

Whether in the plasma phase or at the surface of the coating, the formation of Si-OH groups cannot be predicted from the results reported here, although Fanelli and colleagues [497] suggest that these functionalities are generated in the plasma phase. These authors found a relatively high content of silanol-containing species in the gas leaving the plasma reactor, thus suggesting that silanol groups found in the PMDSO-based coatings (PMDSO = pentamethyldisiloxane, a SiO$_2$ precursor with one Si-H group and five Si-CH$_3$ groups per molecule) were generated in the plasma phase via collisions between the PMDSO molecules and the plasma species. In the case of coatings deposited from hexamethyldisiloxane (HDMSO), a siloxane with six Si-CH$_3$ groups per molecule, the incorporation of silanol-containing entities from the gas phase may be excluded, as their content in the leaving gas was much lower. In this case, the formation of Si-OH groups may occur through heterogeneous reactions between the plasma and the surface. Considering the foregoing, there are substantial grounds for believing that the formation of silanol groups in the plasma phase is linked to the presence of Si-H groups in the precursor.

Deposition mechanism of anti-fogging coatings

The necessary incorporation of silanol groups or silanol-containing species with very high sticking coefficients from the plasma phase to the glass substrate may justify the observed high deposition rates [562,570] (**chapters 4** and **6**). Regardless of the working pressure, the

deposition rate of TMCTS-based coatings is surprisingly high compared to those reported in coatings deposited from other siloxane precursors. For example, Massines et al. [485] and Petersen et al. [510] reported maximum growth rates of approximately 12 nm min^{-1} in SiO$_2$-like coatings deposited at atmospheric pressure from HMDSO/N$_2$/N$_2$O mixtures. Pai and collaborators [403,404] found that the deposition rate was four times greater with TMCTS than with tetraethoxysilane (TEOS) or with silane (SiH$_4$) (**Table 2.2**). This result was correlated with the number of silicon atoms and the vapor pressure of the siloxane precursor. The deposition rate was higher in TMCTS as it contains four silicon atoms per molecule (both TEOS and SiH$_4$ have one silicon atom per molecule) and its vapor pressure is four times greater than that of TEOS. On the other hand, Cui et al. [417] argued that the differences in deposition rates can be explained in terms of bond energies and the structure of the siloxane precursor. They found that the deposition rate of the coatings obtained from bis(triethoxysilyl)ethane (BTESE) and TMCTS were similar but greater than that of the coatings obtained from TEOS. These results were explained in terms of bond dissociation energies and molecular structure. BTESE and TMCTS are more reactive than TEOS because of the Si-C and Si-H bonds, which are easier to break than the Si-O bonds. In addition, it was suggested that the cyclic structure of TMCTS play a crucial role in the deposition process. During the deposition process, TMCTS molecules react with each other through the Si-H bonds, leading to the formation of polycyclic entities. Although mass transport limitations are more significant at atmospheric pressure than at low pressure, these polycyclic structures bond at the first contact point with the substrate owing to their high sticking coefficients. Diffusion is a relatively slow process compared to convection, as supported by the Péclet number largely exceeding unity at atmospheric pressure. The Péclet number is a dimensionless number, named after the French physicist Jean Claude Eugène Péclet, that represents the ratio of mass transfer by motion of a fluid (convection) to mass transfer by diffusion, that is:

$$Pe = \frac{v \cdot L}{D} \qquad (7.1)$$

where v is gas velocity (m s^{-1}), L is a characteristic dimension of the system (m), and D is the diffusion coefficient (m^2 s^{-1}).

A Péclet number exceeding unity means that diffusion limits the transport of radicals from the plasma phase to the substrate, so that only those remaining in the immediate vicinity of the surface (i.e., boundary layer) deposit on it. For example, in the case of HMDSO, radicals generated at 150 μm at most from the substrate contribute to the growth of the coating [572]. Given that the gas velocity is lower in the boundary layer than in the plasma (bulk), the gas stays longer in this zone. As a result, the dissociation of the precursor is more efficient, and therefore, the concentration of radicals here is greater than in the plasma. When the concentration of radicals in the boundary layer is depleted, the coating continues to grow more slowly because of the diffusion-limited incorporation of radicals from the plasma phase. For an inter-electrode distance of some millimeters, it is therefore clear that DBDs are not very effective in depositing thin layers, to the extent that a non-negligible amount of the siloxane precursor escapes the plasma phase by convection.

Ward et al. [401] also highlighted the role of the Si-H bond in the deposition process after observing that TMCTS deposited faster than octamethylcyclotetrasiloxane (OMCTS) did under the same experimental conditions. This behavior was attributed to the presence of Si-H bonds and the greater volatility of TMCTS. Bearing in mind the FTIR results and the above-mentioned arguments, it is reasonable to suppose that the formation of cyclic structures occur in the plasma phase. **Figure 7.1** illustrates some possible reaction pathways involved in the deposition of anti-fogging coatings.

Figure 7.1: *Possible reaction pathways involved in the deposition of anti-fogging coatings showing the formation of different structures in the plasma phase.*

surface silanols

Glass **(a)**

cyclic structures

"D3H" "D5H"

"chain-like" structures

"cage-like" structures

T6 T8 T7

"ladder-like" structures

Si₆ Si₈ **(e)**

N₂ (³A Σ⁺ᵤ)

Hydroxylation
N₂O/N₂/e⁻

"activated" TMCTS

cycle
rearrangement

cycle opening

n H₂O

Condensation
in plasma phase

(OH)D4H

(³P) (¹D)

Reactive
oxygen atoms

Condensation
on surface

n H₂O

OH OH OH OH

"activated" TMCTS
incorporation

H₂O

Water release

silanol
condensation (Si-OH)

surface
incorporation

OH OH OH

N₂ (³A Σ⁺ᵤ)

OH

Glass **(b)**

z
y
x

deposited
film

OH OH OH

Glass **(d)**

"activated" TMCTS
incorporation

silanol
condensation (Si-OH)

Water release

H₂O

"activated" TMCTS
incorporation

Si-O-Si bond
formation

silanol
condensation (Si-OH)

Water release

H₂O

N molecules

"activated" TMCTS
incorporation

Glass **(c)**

225

Because of the labile nature of the Si-H bond, most of the Si-H groups in the TMCTS undergo hydroxylation—they convert into Si-OH groups—as soon as the precursor enters the plasma. The TMCTS activation may occur in two ways. The first involves collisions between oxygen atoms (^{1}D) with TMCTS, as suggested by Rimzsa and colleagues [498]; and the second involves the homolytic cleavage of Si-X (where X = H, CH_3) and C-H bonds on collision with the N_2 ($A^3\Sigma_u^+$) molecules, followed by the formation of Si-OH groups on recombination of Si$^\bullet$ and $^\bullet$OH radicals in the plasma phase. Considering the high reactivity of silanol groups, it is likely that the condensation of activated TMCTS molecules occurs in the plasma phase, as supported by Fanelli et al. [497]. The resulting entities (e.g., cage-like, ladder-like, chain-like structures) then deposit on the substrate on reaction with the surface silanols (condensation reactions). The remaining CH_3 groups undergo hydroxylation to a greater or lesser extent depending on the N_2O/TMCTS ratio, thus explaining the decrease in the $A_{\delta CH3}/A_{\delta Si\text{-}OH}$ ratio (i.e., fogging ratio) with the concentration of N_2O in the discharge. The heterogeneous reactions (plasma-surface) should not be overlooked, as the formation of such structures may also occur on the surface.

Despite considerable efforts made thus far to understand the mechanisms controlling the deposition of SiO_xC_y:H coatings at atmospheric pressure, the nature of the involved reactions remains unclear. The problem is even more complex because of the different types of plasma used for coating deposition, each of them characterized by a density and energy of charged species. While most of the studies have focused on explaining the mechanism of HMDSO deposition; however, little or no attention has been given to fabrication of TMCTS-based coatings by AP-DBDs. For this reason, the mechanism shown in **Figure 7.1** is an attempt to shed light on how and where silanol groups are formed and their potential role in the deposition process. On the other hand, understanding the physical phenomena behind the deposition of anti-fogging coatings involves modeling by computer-aided design. The modeling of mass transfer between the plasma phase and the substrate to explain the deposition mechanism and the dominant transport phenomenon involved in the formation of anti-fogging coatings is undoubtedly a pending issue.

On the reliability of the anti-fogging performance

As far as the reliability of the anti-fogging performance is concerned, two aspects deserve to be mentioned, namely the loss of the anti-fogging performance over time and the adherence coating/substrate.

In general, (super)hydrophilic surfaces are "unstable" in air to the extent that, they tend to reduce the solid/air interfacial energy over time (surface aging). In the case of anti-fogging coatings with water-attracting features—such as those reported in this dissertation—surface aging basically occurs through the adsorption of airborne hydrocarbons. It has been shown that the higher the concentration of surface hydroxyl groups, the more polluted the surface is [573–576]. Hence, surfaces that are favorably wetted by water are also aggressively fouled by contaminants. This naturally occurring phenomenon, which is intrinsically linked to high energy surfaces, disables the anti-fogging performance long term, as the water drops no longer form a continuous layer but rather a discrete pattern that scatters light [134]. In addition to this, anti-fogging surfaces are exposed to mechanical wear caused by finger contact or rubbing during day-to-day use or by solvents when washed with household cleaning products. Both mechanical wear and exposure to chemical reagents degrade the anti-fogging performance and, in the worst-case scenario, ultimately detach coatings from the substrate.

To prevent these problems from occurring, anti-fogging coatings were subjected to several thermal treatments. In view of **Figure 7.2**, which illustrates the number of Si-OH on the SiO_2 surface as a function of the temperature, a dramatic decrease in the anti-fogging performance may be expected on application of high temperatures. Contrary to all expectations, the application of a thermal treatment at 500°C for 1 h under a controlled Ar/O_2 (2% v/v) atmosphere was found to impart a better adhesive coating/substrate without apparent damage to the anti-fogging performance. This highlights the fact that a fully hydroxylated coating ($\alpha_{OH} = 4.6$ OH nm^{-2}) is not a necessary condition to prevent fogging. The combination of coating deposition followed by this thermal treatment made it possible to fabricate robust

SiO$_x$C$_y$:H coatings with an anti-fogging performance lasting even after several washing steps (**section 6.5.5**).
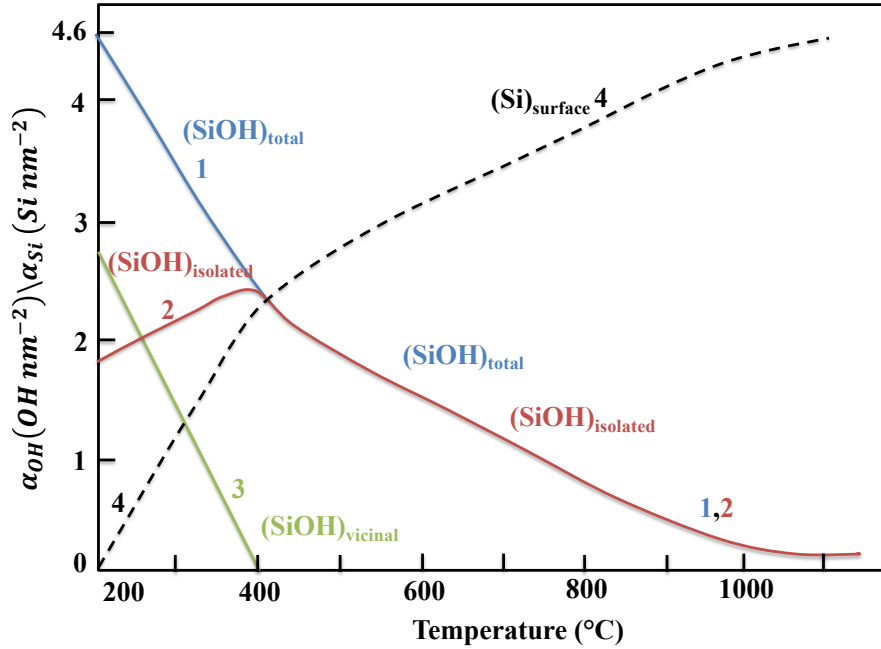
Figure 7.2: (a) Silanol type distribution as a function of the pretreatment temperature in vacuo in silica: curve 1, average concentration of the total OH groups; curve 2, average concentration of the free isolated OH groups; curve 3, average concentration of vicinal OH groups bound through the hydrogen bonds; and curve 4, average concentration of surface Si atoms that are part of the siloxane bridges and free of OH groups (Reproduced from ref. [402]).

Even though AP-DBD deposition followed by thermal treatment holds great promise for the manufacture of anti-fogging coatings, this procedure faces two major challenges. First, the requirement of thermal treatments makes this approach incompatible with polymeric substrates because of thermal degradation concerns and second, the fabrication of anti-fogging coatings can be particularly time-consuming. The exploration of alternative strategies is therefore crucial to broaden the range of application of anti-fogging coatings to thermally sensitive materials.

On the assessment of the anti-fogging performance

Regarding the assessment of the anti-fogging performance, there is not a wide variety of standardized testing methods available for that purpose. Indeed, standards used for testing the resistance to fogging in materials exposed to very humid conditions or sudden changes in temperature are few in number (e.g., CSA Z611-M86 [331] and ASTM F659-10/-06 [332,333] in North America and CEN EN 168 [334] in Europe) and restricted to very specific cases (e.g., protective eyeglasses). This limits the quantitative evaluation of the anti-fogging activity performed in this doctoral research, as it cannot be compared with the anti-fogging performance that could be evaluated by other standardized methods.

Future research: What's next?

I do believe that the future development of anti-fogging coatings prepared by atmospheric pressure Townsend discharges (APTD) will be built on four lines of research:

* The first one involves further research on the cyclic structure and the chemistry of the siloxane precursor to respond some unanswered questions: How does the number of Si-H groups affect the anti-fogging performance? Can be stated that the greater the number of Si-H groups in the precursor, the better the anti-fogging performance will be? How does the cycle size (i.e., number of O-Si-O units) affect the anti-fogging performance? Would it be possible to prepare anti-fogging coatings using mixtures of TMCTS with other siloxanes?

* The second one involves investigating the plasma phase to understand how TMCTS molecules react with the plasma species, and thus propose a mechanistic model to explain the growth rate of the coatings.

* The third line of research involves optimizing the optical properties (e.g., light transmitting capabilities in the absence of fogging) and the coating/substrate interface to

ensure anti-fogging coatings not detaching from the substrate when washed with household cleaning products.

- The fourth line of research pertains to the development of cost-effective AP-PECVD processes to fabricate anti-fogging coatings endowed with additional features. Compared to conventional deposition techniques, such as dip-coating, spin-coating, or layer-by-layer deposition, this manufacturing perspective would undoubtedly bring substantial environmental and economic savings

For example, anti-fogging coatings endowed with anti-reflective characteristics can be produced by injecting nanomaterials with high specific surface or high porosity into the discharge along with the liquid TMCTS. Here, the idea is to lower the refractive index of the anti-fogging coating as much as possible in a cost-effective manner, so as to meet the condition of "zero reflectance" [336]. Materials in a variety of sizes and morphologies such as solid silica nanoparticles (SSNPs), hollow mulberry-like silica nano-spheres, mesoporous silica nanoparticles (MPSNPs), or hollow silica nanospheres (HSNs) can be used for that purpose. These coatings can be integrated into the design of solar cells to enhance light harvesting and thus improve photovoltaic conversion efficiency of these devices [577]. In the same vein, anti-fogging coatings endowed with self-cleaning characteristics can be prepared by injecting nanomaterials along with the TMCTS. The catalytic properties of TiO_2, Bi_2O_3, or ZnO can be exploited in that regard. In this case, the surface of the anti-fogging coating is cleaned by combining two physical phenomena, namely the photocatalytic activity due to the formation of "reactive oxidizing species" (ROS) [463], and the "sweeping" effect of water layers resulting from the strong affinity between the water drops and the surface. Due to their anti-bacterial activity, these coatings show potential in applications dealing with fogging and bacterial growth, as in the medical practice (endoscopic surgery, surgical googles) and the food packaging industry. Anti-fogging coatings endowed with other interesting features may be also a reality. For example, with thermochromism by using VO_2 nanoparticles, with electrical/thermal conductivity by using reduced graphene oxide nanoparticles, or with scratch-resistance by using nanoparticles of cubic boron nitride (c-BN).

Conclusions

Throughout a systematic research work and an extensive review on the recent advances in anti-fogging technology, the potential applicability of coatings reported in this dissertation in scenarios dealing with fogging concerns has been established via the following original contributions:

- It has been demonstrated the feasibility of conferring anti-fogging performance to commercial glass substrates by coating deposition using atmospheric pressure DBDs.

- It has been found that the anti-fogging performance can be achieved by controlling the deposition parameters, namely the [N$_2$O]/[TMCTS] ratio and the power dissipated in the discharge.

- It has been provided evidence on the origin of the anti-fogging performance in terms of the chemistry and the structure of the siloxane precursor.

- It has been evidenced that certain "microscopic" parameters such as the O/Si ratio, the fogging parameter, and the surface roughness can be correlated with macroscopic ones such as the wetting behavior and the light transmitting capabilities under fogging conditions.

- It has been demonstrated that the application of a thermal treatment—under a controlled Ar/O$_2$ atmosphere—allows for the fabrication of robust anti-fogging coatings with enhanced adhesion to the glass substrate.

- It has been revealed a niche of opportunity for the manufacture of anti-fogging coatings using a Townsend discharge in nitrogen.

References

[1]   N. Agam, P.R. Berliner, Dew formation and water vapor adsorption in semi-arid environments - A review, J. Arid Environ. 65 (2006) 572–590. doi:10.1016/j.jaridenv.2005.09.004.

[2]   M.A. Fayazbakhsh, M. Bahrami, Analytical Modeling of Mist Condensation by Natural Convection over Inclined Flat Surfaces, ASME 2013 Summer Heat Transf. Conf. (2013) 1–7. doi:10.1115/HT2013-17219.

[3]   M. Gallaway, J. Aimino, M. Scheiman, The effect of protective sports eyewear on peripheral visual field and a peripheral visual performance task., J. Am. Optom. Assoc. 57 (1986) 304–310.

[4]   S.J. Dain, A.K. Hoskin, C. Winder, D.P. Dingsdag, Assessment of fogging resistance of anti-fog personal eye protection, Ophthalmic Physiol. Opt. 19 (1999) 357–361.

[5]   J. Crebolder, R. Sloan, Determining the effects of eyewear fogging on visual task performance, Appl. Ergon. 35 (2004) 371–381.

[6]   R. Sloan, J.M. Crebolder, R. Tyler, A foggy start: Determining the effect of eyewear fogging on visual task performance, Def. Civ. Inst Environ. Med. Downsview, ON,. (2000).

[7]   T.H. Margrain, C. Owen, The misting characteristics of spectacle lenses, Ophthalmic Physiol. Opt. 16 (1996) 108–114.

[8]   J. Hlavay, G.G. Guilbault, Applications of the piezoelectric crystal detector in analytical chemistry, Anal. Chem. 49 (1977) 1890–1898.

[9]   K. Oguri, N. Iwataka, A. Tonegawa, Y. Hirose, K. Takayama, Y. Nishi, Misting-free diamond surface created by sheet electron beam irradiation, J. Mater. Res. 16 (2001) 553–557. doi:10.1557/JMR.2001.0079.

[10]   G. Croce, P. D'Agaro, F. Della Mora, Numerical simulation of glass fogging and defogging, Int. J. Comut. Fluid Dyn. 19 (2005) 437–445.

[11]   M. San-Juan, Ó. Martín, B.J. Mirones, P. De Tiedra, Assessment of efficiency of windscreen demisting systems in electrical vehicles by using IR thermography, Appl. Therm. Eng. 104 (2016) 479–485.

[12]   K.M. Al-Khalil, T.G. Keith, K.J. De Witt, Modelling of surface water behaviour on ice protected aircraft components, Int. J. Numer. Methods Heat Fluid Flow. 2 (1992) 555–571. doi:10.1108/eb017511.

[13]   G.D. Herbage, Anti-fog and frost coatings, Aircr. Eng. Aerosp. Technol. 44 (1972) 49–50.

[14]   C. Nezhat, V. Morozov, A simple solution to lens fogging during robotic and laparoscopic surgery, J. Soc. Laparoendosc. Surg. 12 (2008) 431.

[15]   T. Ohdaira, H. Nagai, S. Kayano, H. Kazuhito, Antifogging effects of a socket-type device with the superhydrophilic, titanium dioxide–coated glass for the laparoscope, Surg. Endosc. 21 (2007) 333–338.

[16]   N. Lawrentschuk, N.E. Fleshner, D.M. Bolton, Laparoscopic lens fogging: A review of etiology and methods to maintain a clear visual field, J. Endourol. 24 (2010) 905–913.

[17]   A. Knauth, M. Weiss, M. Dave, A. Frotzler, T. Haas, Vergleich von Antibeschlagmethoden in der Endoskopie, Anaesthesist. 61 (2012) 1036–1044.

[18] P. Piromchai, P. Kasemsiri, S. Thanaviratananich, Alternative agents to prevent fogging in head and neck endoscopy, Clin. Med. Insights. Ear, Nose Throat. 4 (2011) 1–4.

[19] C. Wallace, T. Engelhardt, Videolaryngoscopes in paediatric anaesthesia, Curr. Treat. Options Pediatr. 1 (2015) 25–37.

[20] D. Hashimoto, M. Shouji, Development of a fogless scope and its analysis using infrared radiation pyrometer., Surg. Endosc. 11 (1997) 805–808.

[21] A. Jaffrin, S. Makhlouf, C. Scotto La Massese, A. Bettachini, R. Voisin, Effet de la mouillabilité d'un film polymère sur les températures et l'action nématicide obtenues en solarisation d'un sol de culture, Agronomie. 9 (1989) 729–741.

[22] B.J. Briscoe, K.P. Galvin, The effect of surface fog on the transmittance of light, Sol. Energy. 46 (1991) 191–197.

[23] Z. Fu, M. Liu, J. Xu, Q. Wang, Z. Fan, Surface Modification of Linear Low-Density Polyethylene Film by Amphiphilic Graft Copolymers Based on Poly (higher α-olefin)-graft-poly(ethylene glycol), J. Appl. Polym. Sci. 119 (2010) 1111–1121. doi:10.1002/app.

[24] M.-J. Cai, Synthesis, surface activity, and antifogging property of triethanolamine mono laureate ester, Chinese J. Chem. Phys. 28 (2015) 223–229.

[25] X.Y. Lu, Z. Wang, X.L. Yang, X. Xu, L. Zhang, N. Zhao, J. Xu, Antifogging and antireflective silica film and its application on solar modules, Surf. Coat. Technol. 206 (2011) 1490–1494. doi:10.1016/j.surfcoat.2011.09.031.

[26] J.T. Park, J.H. Kim, D. Lee, Excellent anti-fogging dye-sensitized solar cells based on superhydrophilic nanoparticle coatings, Nanoscale. 6 (2014) 7362–7368. doi:10.1039/c4nr00919c.

[27] L. Introzzi, J.M. Fuentes-Alventosa, C.A. Cozzolino, S. Trabattoni, S. Tavazzi, C.L. Bianchi, A. Schiraldi, L. Piergiovanni, S. Farris, "Wetting enhancer" pullulan coating for antifog packaging applications., ACS Appl. Mater. Interfaces. 4 (2012) 3692–700.

[28] M. Nie, P. Patel, K. Sun, D.D. Meng, Superhydrophilic anti-fog polyester film by oxygen plasma treatment, 4th IEEE Int. Conf. Nano/Micro Eng. Mol. Syst. NEMS. (2009) 1017–1020.

[29] P. Wagner, Anti-fog additives give clear advantage, Plast. Addit. Compd. 3 (2001) 18–21.

[30] V. Rizzo, G. Muratore, Effects of packaging on shelf life of fresh celery, J. Food Eng. 90 (2009) 124–128. doi:10.1016/j.jfoodeng.2008.06.011.

[31] A.L. Martikainen, Fog removal with a fog mesh—Mist eliminators and multiple mesh systems, Int. J. Mining, Reclam. Environ. 21 (2007) 85–197.

[32] A. Martikainen, Picaset, Fog removal in the declines of underground mines in sub-arctic regions, Helsinki University of Technology, 2007.

[33] H.-J. Kim, Y. Kim, J.-H. Jeong, J.-H. Choi, J. Lee, D.-G. Choi, A cupronickel-based micromesh film for use as a high-performance and low-voltage transparent heater, J. Mater. Chem. A. 3 (2015) 16621–16626.

[34] J.J. Bae, S.C. Lim, G.H. Han, Y.W. Jo, D.L. Doung, E.S. Kim, S.J. Chae, T.Q. Huy, N. Van Luan, Y.H. Lee, Heat dissipation of transparent graphene defoggers, Adv. Funct. Mater. 22 (2012) 4819–4826.

[35] P. D'Agaro, G. Croce, G. Cortella, Numerical simulation of glass doors fogging and defogging in refrigerated display cabinets, Appl. Therm. Eng. 26 (2006) 1927–1934.

[36] G. Zhang, H. Zou, F. Qin, Q. Xue, C. Tian, Investigation on an improved heat pump

AC system with the view of return air utilization and anti-fogging for electric vehicles, Appl. Therm. Eng. 115 (2017) 726–735.

[37] M. Bradford, T. Perrotta, Windshield temperature control system, USPat., 5496989A, 1996.

[38] A. Aroussi, A. Hassan, Y. Morsi, Numerical simulation of the airflow over and heat transfer through a vehicle windshield defrosting and demisting system, Heat Mass Transf. 39 (2003) 401–405.

[39] R. Cording, Anti-fog refrigeration door, USPat., 7891154, 2015.

[40] P. Wang, B. Singh, B. Ferian, T. Morgan, D. Welchel, M. Jackson, Electro-thermal antifog optical devices, USPat., 8398234B2, 2013.

[41] D. Sui, Y. Huang, L. Huang, J. Liang, Y. Ma, Y. Chen, Flexible and transparent electrothermal film heaters based on graphene materials, Small. 7 (2011) 3186–3192.

[42] L. Tan, M. Zeng, Q. Wu, L. Chen, J. Wang, T. Zhang, J. Eckert, M.H. Rümmeli, L. Fu, Direct growth of ultrafast transparent single-layer graphene defoggers, Small. 11 (2015) 1840–1846.

[43] X. Hu, Y. Yu, Y. Wang, Y. Wang, J. Zhou, L. Song, Highly transparent superhydrophilic graphene oxide coating for antifogging, Mater. Lett. 182 (2016) 372–375. doi:10.1016/j.matlet.2016.06.125.

[44] W. Sperbeck, Goggle defogging system with transparent indium-tin-oxide heating layer disposed on a lens, USPat. 5471036A, 1994.

[45] H.J. Kim, D.I. Kim, S.S. Kim, Y.Y. Kim, S.E. Park, G. Choi, D.W. Lee, Y. Kim, Observation of convection phenomenon by high-performance transparent heater based on Pt-decorated Ni micromesh, AIP Adv. 7 (2017) 025112. doi:10.1063/1.4977021.

[46] B. You, B.-K. Ju, J.-W. Kim, Photoresist-assisted fabrication of thermally and mechanically stable silver nanowire-based transparent heaters, Sensors Actuators A Phys. 250 (2016) 123–128.

[47] D. Beysens, The formation of dew, Atmos. Res. 39 (1995) 215–237.

[48] D. Beysens, Dew nucleation and growth, Comptes Rendus Phys. 7 (2006) 1082–1100.

[49] J.G. Pieters, J.M. Deltour, M.J. Debruyckere, Light transmission through condensation on glass and polyethylene, Agric. For. Meteorol. 85 (1997) 51–62.

[50] J. Blaschke, T. Lapp, B. Hof, J. Vollmer, Breath figures: Nucleation, growth, coalescence, and the size distribution of droplets, Phys. Rev. Lett. 109 (2012) 068701.

[51] P. Meakin, Droplet deposition growth and coalescence, Reports Prog. Phys. 55 (1999) 157–240.

[52] D. Beysens, C. Knobler, Growth of Breath Figures, Phys. Rev. Lett. 57 (1986) 1433–1436. doi:10.1103/PhysRevLett.57.1433.

[53] J.R. Bessell, E. Flemming, W. Kunert, G. Buess, Maintenance of clear vision during laparoscopic surgery, Minim. Invasive Ther. Allied Technol. 5 (1996) 450–455.

[54] C. Lamnatou, D. Chemisana, Solar radiation manipulations and their role in greenhouse claddings: Fluorescent solar concentrators, photoselective, and other materials, Renew. Sustain. Energy Rev. 27 (2013) 175–190.

[55] B. Cemek, Y. Demir, Testing of the condensation characteristics and light transmissions of different plastic film covering materials, Polym. Test. 24 (2005) 284–289.

[56] L.C. Hall, Z.L. Carpenter, G.C. Smith, White-spot formation on packaged beef steaks, J. Food Sci. 44 (1979) 1455–1459.

[57] J.J. Bae, S.C. Lim, G.H. Han, Y.W. Jo, D.L. Doung, E.S. Kim, S.J. Chae, T.Q. Huy,

N. Van Luan, Y.H. Lee, Heat dissipation of transparent graphene defoggers, Adv. Funct. Mater. 22 (2012) 4819–4826. doi:10.1002/adfm.201201155.

[58] R. Schoofs, Adsorbent for use in double glazed windows, CAPat., 1056216A, 1976.

[59] S. Van Den Bergh, R. Hart, B.P. Jelle, A. Gustavsen, Window spacers and edge seals in insulating glass units: A state-of-the-art review and future perspectives, Energy Build. 58 (2013) 263–280.

[60] E. Cuce, P.M. Cuce, Vacuum glazing for highly insulating windows: Recent developments and future prospects, Renew. Sustain. Energy Rev. 54 (2016) 1345–1347.

[61] K.C. Park, H.J. Choi, C.H. Chang, R.E. Cohen, G.H. McKinley, G. Barbastathis, Nanotextured silica surfaces with robust superhydrophobicity and omnidirectional broadband supertransmissivity, ACS Nano. 6 (2012) 3789–3799.

[62] Z. He, X. Lan, F. Chen, K. Wang, H. Deng, Q. Zhang, Q. Fu, Effect of surface wettability on transparency in different water conditions, J. Coatings Technol. Res. 10 (2013) 641–647.

[63] E. Bormashenko, Progress in understanding wetting transitions on rough surfaces, Adv. Colloid Interface Sci. 222 (2015) 92–103.

[64] J. Drelich, E. Chibowski, D.D. Meng, K. Terpilowski, Hydrophilic and superhydrophilic surfaces and materials, Soft Matter. 7 (2011) 9804–9828.

[65] K.-Y. Law, Definitions for hydrophilicity, hydrophobicity, and superhydrophobicity: Getting the basics right, J. Phys. Chem. Lett. 5 (2014) 686–688.

[66] J. Drelich, E. Chibowski, Superhydrophilic and superwetting surfaces: Definition and mechanisms of control, Langmuir. 26 (2010) 18621–18623.

[67] G. Grosu, L. Andrzejewski, G. Veilleux, G.G. Ross, Relation between the size of fog droplets and their contact angles with CR39 surfaces, J. Phys. D. Appl. Phys. 37 (2004) 3350–3355.

[68] M. Nosonovsky, B. Bhushan, Superhydrophobic surfaces and emerging applications: Non-adhesion, energy, green engineering, Curr. Opin. Colloid Interface Sci. 14 (2009) 270–280.

[69] M. Nosonovsky, B. Bhushan, Lotus Versus Rose: Biomimetic Surface Effects, Green Energy Technol. 49 (2012) 25–40. doi:10.1007/978-3-642-23681-5_2.

[70] A. Ghosh, S. Beaini, B. Zhang, R. Ganguly, C. Megaridis, Enhancing dropwise condensation through bioinspired wettability patterning, Langmuir. 30 (2014) 13103–13115.

[71] G.. Davies, W. Mojtehedi, A.. Ponter, Measurement of contact angles under condensation conditions. The prediction of dropwise-filmwise transition, Int. J. Heat Mass Transf. 14 (1971) 709–713.

[72] K. Rykaczewski, Microdroplet growth mechanism during water condensation on superhydrophobic surfaces, Langmuir. 28 (2012) 7720–7729.

[73] T. Young, An essay on the cohesion of fluids, Philos. Trans. R. Soc. B. 95 (1805) 65–87.

[74] L. Gao, T.J. McCarthy, An attempt to correct the faulty intuition perpetuated by the wenzel and cassie "laws," Langmuir. 25 (2009) 7249–7255. doi:10.1021/la901416m.

[75] J. Bico, U. Thiele, D. Quéré, Wetting of textured surfaces, Colloids Surfaces A Physicochem. Eng. Asp. 206 (2002) 41–46.

[76] E. Bormashenko, Young, Boruvka–Neumann, Wenzel and Cassie–Baxter equations as the transversality conditions for the variational problem of wetting, Colloids

Surfaces A Physicochem. Eng. Asp. 345 (2009) 163–165.

[77] G. Whyman, E. Bormashenko, T. Stein, The rigirious derivation of Young, Cassie–Baxter, and Wenzel equations, and the analysis of the contact angle hysteresis phenomenon., Chem. Phys. Lett. 450 (2008) 355–359.

[78] P. Letellier, A. Mayaffre, M. Turmine, Drop size effect on contact angle explained by nonextensive thermodynamics. Young's equation revisited, J. Colloid Interface Sci. 314 (2007) 604–614.

[79] R.N. Wenzel, Surface roughness and contact angle, J. Phys. Colloid Chem. 53 (1949) 1466–1467.

[80] R.N. Wenzel, Resistance of solid surfaces to wetting by water, Ind. Eng. Chem. 28 (1936) 988–994.

[81] D. Quéré, A. Lafuma, J. Bico, Slippy and sticky microtextured solids, Nanotechnology. 14 (2003) 1109–1112.

[82] S. Chen, J. Wang, D. Chen, States of a water droplet on nanostructured surfaces, J. Phys. Chem. C. 118 (2014) 18529–18536.

[83] P.S. Brown, B. Bhushan, Durable, superoleophobic polymer-nanoparticle composite surfaces with re-entrant geometry via solvent-induced phase transformation, Sci. Rep. 6 (2016). doi:10.1038/srep21048.

[84] A.B.D. Cassie, S. Baxter, Wettability of porous surfaces, Trans. Faraday Soc. 40 (1944) 546–551.

[85] A.B.D. Cassie, Contact angles, Discuss. Faraday Soc. 3 (1948) 11–16.

[86] A. Marmur, Wetting on hydrophobic rough surfaces: To be heterogeneous or not to be?, Langmuir. 19 (2003) 8343–8348.

[87] A. Méndez-Vilas, A.B. Jódar-Reyes, M.L. González-Martín, Ultrasmall liquid droplets on solid surfaces: Production, imaging, and relevance for current wetting research, Small. 5 (2009) 1366–1390. doi:10.1002/smll.200800819.

[88] A. Amirfazli, A.W. Neumann, Status of the three-phase line tension: A review, Adv. Colloid Interface Sci. 110 (2004) 121–141.

[89] J. Drelich, The significance and magnitude of the line tension in three-phase (solid-liquid-fluid) systems, Colloids Surfaces A Physicochem. Eng. Asp. 116 (1996) 43–54. doi:10.1016/0927-7757(96)03651-5.

[90] E. Bormashenko, General equation describing wetting of rough surfaces, J. Colloid Interface Sci. 360 (2011) 317–319.

[91] E. Bormashenko, Wetting of real solid surfaces: New glance on well-known problems, Colloid Polym. Sci. 291 (2013) 339–342.

[92] M. Ramiasa, J. Ralston, R. Fetzer, R. Sedev, The influence of topography on dynamic wetting, Adv. Colloid Interface Sci. 206 (2014) 275–293.

[93] C.W. Extrand, Y. Kumagai, An experimental study of contracted angle hysteresis, J. Colloid Interface Sci. 191 (1997) 378–383. doi:10.1006/jcis.1997.4935.

[94] E. Bormashenko, A. Musin, M. Zinigrad, Evaporation of droplets on strongly and weakly pinning surfaces and dynamics of the triple line, Colloids Surfaces A Physicochem. Eng. Asp. 385 (2011) 235–240. doi:10.1016/j.colsurfa.2011.06.016.

[95] H. Murase, T. Fujibayashi, Characterization of molecular interfaces in hydrophobic systems, Prog. Org. Coatings. 31 (1997) 97–104.

[96] T. Watanabe, A. Nakajima, R. Wang, M. Minabe, S. Koizumi, A. Fujishima, K. Hashimoto, Photocatalytic activity and photoinduced hydrophilicity of titanium dioxide coated glass, Thin Solid Films. 351 (1999) 260–263.

[97]   M. Miyauchi, A. Nakajima, K. Hashimoto, T. Watanabe, A highly hydrophilic thin film under 1 $\mu W/cm^2$ UV illumination, Adv. Mater. 12 (2000) 1923–1927.

[98]   A.O.T. Patrocinio, L.F. Paula, R.M. Paniago, J. Freitag, D.W. Bahnemann, Layer-by-Layer TiO_2/WO_3 thin films as efficient photocatalytic self-cleaning surfaces, ACS Appl. Mater. Interfaces. 6 (2014) 16859–16866.

[99]   Y. Chen, C. Zhang, W. Huang, C. Yang, T. Huang, Y. Situ, H. Huang, Synthesis of porous ZnO/TiO_2 thin films with superhydrophilicity and photocatalytic activity via a template-free sol–gel method, Surf. Coatings Technol. 258 (2014) 531–538. doi:10.1016/j.surfcoat.2014.08.042.

[100] S. Xu, H. Huang, C. Wang, Z. Huang, C. Wang, Synthesis, characterization and hydrophilic properties of $ZnFe_2O_4$–TiO_2 composite film, Mater. Res. Bull. 65 (2015) 210–215. doi:http://dx.doi.org/10.1016/j.materresbull.2015.01.051.

[101] J. Zhu, Y. Cao, J. He, Facile fabrication of transparent, broadband photoresponse, self-cleaning multifunctional graphene-TiO_2 hybrid films, J. Colloid Interface Sci. 420 (2014) 119–126.

[102] M. Machida, K. Norimoto, T. Watanabe, K. Hashimoto, A. Fujishima, The effect of SiO_2 addition in super-hydrophilic property of TiO_2 photocatalyst, J. Mater. Sci. 34 (1999) 2569–2574.

[103] U. Cernigoj, S. Lavrencic, Preparation of TiO_2/SiO_2 sols for deposition of self-cleaning anti-fogging coatings, USPat., 2010053459A1, 2010.

[104] S. Wang, K.K. Meng, L. Zhao, Q. Jiang, J.S. Lian, Superhydrophilic Cu-doped TiO_2 thin film for solar-driven photocatalysis, Ceram. Int. 40 (2014) 5107–5110.

[105] D. Dam Le, T.M. Dung Dang, V. Thang Chau, M. Chien Dang, H.M. R., The fabrication of visible light responsive Ag-SiO_2 co-doped TiO_2 thin films by the sol-gel method, Adv. Nat. Sci. Nanosci. Nanotechnol. 1 (2010) 015007.

[106] D.M. Chien, N.N. Viet, N.T.K. Van, N.T.P. Phong, Characteristics modification of TiO_2 thin films by doping with silica and alumina for self-cleaning application, J. Exp. Nanosci. 4 (2009) 221–232.

[107] J. Wang, D. Wang, J. Wang, W. Zhao, C. Wang, High transmittance and superhydrophilicity of porous TiO_2/SiO_2 bi-layer films without UV irradiation, Surf. Coatings Technol. 205 (2011) 3596–3599. doi:10.1016/j.surfcoat.2010.12.033.

[108] M. Faustini, L. Nicole, C. Boissière, P. Innocenzi, C. Sanchez, D. Grosso, Hydrophobic, antireflective, self-cleaning, and antifogging sol-gel coatings: An example of multifunctional nanostructured materials for photovoltaic cells, Chem. Mater. 22 (2010) 4406–4413.

[109] S.W. Lam, A. Soetanto, R. Amal, Self-cleaning performance of polycarbonate surfaces coated with titania nanoparticles, J. Nanoparticle Res. 11 (2009) 1971–1979. doi:10.1007/s11051-008-9555-0.

[110] V.A. Online, L. Xu, J. He, L. Yao, Fabrication of mechanically robust films with high transmittance and durable superhydrophilicity by treatment, J. Mater. Chem. A. 2 (2014) 402–409. doi:10.1039/c3ta13809g.

[111] Y. Wang, J. Wu, H. Wang, R. Chen, Effective balance of antireflection and self-cleaning properties via hollow silica nanospheres-based surface coated with scattered titania nanoparticles, Sol. Energy. 122 (2015) 763–772. doi:10.1016/j.solener.2015.10.003.

[112] D. Lee, M.F. Rubner, Robert E. Cohen, All-nanoparticle thin-film coatings, Nano Lett. 6 (2006) 2305–2312.

[113] X. Li, J. He, Synthesis of raspberry-like SiO_2–TiO_2 nanoparticles toward antireflective and self-cleaning coatings, ACS Appl. Mater. Interfaces. 5 (2013) 5282–5290.

[114] A. Matsuda, T. Matoda, T. Kogure, K. Tadanaga, T. Minami, M. Tatsumisago, Formation and characterization of titania nanosheet-precipitated coatings via sol-gel process with hot water treatment under vibration, Chem. Mater. 17 (2005) 749–757. doi:10.1021/cm048135h.

[115] A. Tricoli, M. Righettoni, S.E. Pratsinis, Anti-fogging nanofibrous SiO_2 and nanostructured SiO_2-TiO_2 films made by rapid flame deposition and in situ annealing, Langmuir. 25 (2009) 12578–12584. doi:10.1021/la901759p.

[116] W.S.Y. Wong, N. Nasiri, A.L. Rodriguez, D.R. Nisbet, A. Tricoli, Hierarchical amorphous nanofibers for transparent inherently super-hydrophilic coatings, J. Mater. Chem. A. 2 (2014) 15575–15581.

[117] Y. Chen, Y. Zhang, L. Shi, J. Li, Y. Xin, T. Yang, Z. Guo, Transparent superhydrophobic/superhydrophilic coatings for self-cleaning and anti-fogging, Appl. Phys. Lett. 101 (2012) 7420–7426. doi:10.1063/1.4737167.

[118] Y. Xiong, M. Lai, J. Li, H. Yong, H. Qian, C. Xu, K. Zhong, S. Xiao, Facile synthesis of ultra-smooth and transparent TiO_2 thin films with superhydrophilicity, Surf. Coatings Technol. 265 (2015) 78–82. doi:10.1016/j.surfcoat.2015.01.060.

[119] V. Zorba, X. Chen, S. Mao, Superhydrophilic TiO_2 surface without photocatalytic activation, Appl. Phys. Lett. 96 (2010) 093702.

[120] W. Huang, Y. Chen, C. Yang, Y. Situ, H. Huang, pH-driven phase separation: Simple routes for fabricating porous TiO_2 film with superhydrophilic and anti-fog properties, Ceram. Int. 41 (2015) 7573–7581.

[121] J. Wang, J. Wang, Y.-L. Sun, C.-W. Wang, The preparation of superhydrophilic surface of TiO_2 coating without ultraviolet irradiation through annealing treatment, J. Sol-Gel Sci. Technol. 68 (2013) 75–80.

[122] B. Bharti, S. Kumar, R. Kumar, Superhydrophilic TiO_2 thin film by nanometer scale surface roughness and dangling bonds, Appl. Surf. Sci. 364 (2016) 51–60. doi:10.1016/j.apsusc.2015.12.108.

[123] Z. Sun, T. Liao, K. Liu, L. Jiang, J.H. Kim, S.X. Dou, Fly-eye inspired superhydrophobic anti-fogging inorganic nanostructures, Small. 10 (2014) 3001–3006.

[124] Q. Shang, Y. Zhou, Fabrication of transparent superhydrophobic porous silica coating for self-cleaning and anti-fogging, Ceram. Int. 42 (2016) 8706–8712.

[125] M. Zhang, L. Wang, S. Feng, Y. Zheng, A Strategy of Antifogging: Air-Trapped Hollow Microsphere Nanocomposites, Chem. Mater. 29 (2017) 2899–2905. doi:10.1021/acs.chemmater.6b05139.

[126] W. Shi, L. Wang, Z. Guo, Y. Zheng, Excellent anti-icing abilities of optimal micropillar arrays with nanohairs, Adv. Mater. Interfaces. 2 (2015) 1500352.

[127] H.K. Raut, S.S. Dinachali, Y.C. Loke, R. Ganesan, K.K. Ansah-Antwi, A. Góra, E.H. Khoo, V.A. Ganesh, M.S.M. Saifullah, S. Ramakrishna, Multiscale ommatidial arrays with broadband and omnidirectional antireflection and antifogging properties by sacrificial layer mediated nanoimprinting, ACS Nano. 9 (2015) 1305–1314.

[128] X. Gao, X. Yan, X. Yao, L. Xu, K. Zhang, J. Zhang, B. Yang, L. Jiang, The dry-style antifogging properties of mosquito compound eyes and artificial analogues prepared by soft lithography, Adv. Mater. 19 (2007) 2213–2217. doi:10.1002/adma.200601946.

[129] M. Wen, L. Wang, M. Zhang, L. Jiang, Y. Zheng, Antifogging and icing-delay

properties of composite micro- and nanostructured surfaces, ACS Appl. Mater. Interfaces. 6 (2014) 3963–3968.

[130] P.S. Brown, B. Bhushan, Bioinspired, roughness-induced, water and oil super-philic and super-phobic coatings prepared by adaptable layer-by-layer technique, Sci. Rep. 5 (2015) 14030. doi:10.1038/srep14030.

[131] P.S. Brown, B. Bhushan, Mechanically durable, superoleophobic coatings prepared by layer-by-layer technique for anti-smudge and oil-water separation, Sci. Rep. 5 (2015) 8701. doi:10.1038/srep08701.

[132] M. Ueno, Y. Ugajin, K. Horie, T. Nishimura, Antifogging effect of cellulose films by chemical modification of the surface using nonionic fluorocarbon surfactant, J. Appl. Polym. Sci. 39 (1990) 967–977. doi:10.1002/app.1990.070390415.

[133] J.A. Howarter, J.P. Youngblood, Self-cleaning and next generation anti-fog surfaces and coatings, Macromol. Rapid Commun. 29 (2008) 455–466.

[134] J.A. Howarter, J.P. Youngblood, Self-cleaning and anti-fog surfaces via stimuli-responsive polymer brushes, Adv. Mater. 19 (2007) 3838–3843.

[135] Y. Wang, Q. Dong, Y. Wang, H. Wang, G. Li, R. Bai, Investigation on RAFT polymerization of a y-shaped amphiphilic fluorinated monomer and anti-fog and oil-repellent properties of the polymers, Macromol. Rapid Commun. 31 (2010) 1816–1821. doi:10.1002/marc.201000243.

[136] P.S. Brown, O.D.L.A. Atkinson, J.P.S. Badyal, Ultrafast oleophobic–hydrophilic switching surfaces for sntifogging, self-cleaning, and oil–water separation, ACS Appl. Mater. Interfaces. 6 (2014) 7504–7511.

[137] J.A. Howarter, K.L. Genson, J.P. Youngblood, Wetting behavior of oleophobic polymer coatings synthesized from fluorosurfactant-macromers, ACS Appl. Mater. Interfaces. 3 (2011) 2022–30.

[138] Y. Wang, J. Knapp, A. Legere, J. Raney, L. Li, Effect of end-groups on simultaneous oleophobicity/hydrophilicity and anti-fogging performance of nanometer-thick perfluoropolyethers (PFPEs), RSC Adv. 5 (2015) 30570–30576.

[139] L. Li, Y. Wang, M. Dugan, B. Urbaniak, Y. Wang, M. Dugan, B. Urbaniak, L. Li, Fabricating nanometer-thick simultaneously oleophobic / hydrophilic polymer coatings via a photochemical approach coatings via a photochemical approach, Langmuir. 32 (2016) 6723–6729. doi:10.1021/acs.langmuir.6b00802.

[140] Y. Wang, X. Gong, Special oleophobic and hydrophilic surfaces: approaches, mechanisms, and applications, J. Mater. Chem. A. 5 (2017) 3759–3773. doi:10.1039/C6TA10474F.

[141] S. Grube, K. Siegmann, M. Hirayama, A moisture-absorbing and abrasion-resistant transparent coating on polystyrene, J. Coatings Technol. Res. 12 (2015) 669–680. doi:10.1007/s11998-015-9678-z.

[142] X. Zhang, J. He, One-step construction of antifogging and frost-resisting coatings on flexible substrates, Int. J. Nanosci. 14 (2015) 1460015. doi:10.1142/S0219581X14600151.

[143] X. Zhang, J. He, Hydrogen-bonding-supported self-healing antifogging thin films, Sci. Rep. 5 (2015) 9227.

[144] M.W. England, C. Urata, G.J. Dunderdale, A. Hozumi, Anti-Fogging/Self-Healing Properties of Clay-Containing Transparent Nanocomposite Thin Films, ACS Appl. Mater. Interfaces. 8 (2016) 4318–4322. doi:10.1021/acsami.5b11961.

[145] Y. Li, X. Fang, Y. Wang, B. Ma, J. Sun, Highly transparent and water-enabled

healable antifogging and frost-resisting films based on poly(vinyl alcohol)-Nafion complexes, Chem. Mater. 28 (2016) 6975–6984. doi:10.1021/acs.chemmater.6b02684.

[146] J. Yuhang, L.I. Yao, W. Xuesong, P. Linglan, S.H.I. Zuosen, C.U.I. Zhanchen, Fabrication of new transparent and hydrophilic hybrid anti-fog coating from silane coupler modified by polyethylene glycols, Chem. Res. Chinese Univ. 33 (2017) 150–154.

[147] E.F. Molina, C.R.N. Jesus, L.A. Chiavacci, S.H. Pulcinelli, V. Briois, C. V. Santilli, Ureasil–polyether hybrid blend with tuneable hydrophilic/hydrophobic features based on U-PEO1900 and U-PPO400 mixtures, J. Sol-Gel Sci. Technol. 70 (2014) 317–328.

[148] S. Park, S. Park, D.H. Jang, H.S. Lee, C.H. Park, Anti-fogging behavior of water-absorbing polymer films derived from isosorbide-based epoxy resin, Mater. Lett. 180 (2016) 81–84. doi:10.1016/j.matlet.2016.05.114.

[149] C. Li, X. Li, C. Tao, L. Ren, Y. Zhao, S. Bai, X. Yuan, Amphiphilic Antifogging/Anti-Icing Coatings Containing POSS-PDMAEMA-b-PSBMA, ACS Appl. Mater. Interfaces. 9 (2017) 22959–22969. doi:10.1021/acsami.7b05286.

[150] C. Tao, S. Bai, X. Li, C. Li, L. Ren, Y. Zhao, X. Yuan, Formation of zwitterionic coatings with an aqueous lubricating layer for antifogging/anti-icing applications, Prog. Org. Coatings. 115 (2018) 56–64. doi:10.1016/j.porgcoat.2017.11.002.

[151] B. Yao, H. Zhao, L. Wang, Y. Liu, C. Zheng, H. Li, C. Sun, Synthesis of acrylate-based UV/thermal dual-cure coatings for antifogging, J. Coatings Technol. Res. 15 (2017) 1–10.

[152] Y. Yuan, R. Liu, C. Wang, J. Luo, X. Liu, Synthesis of UV-curable acrylate polymer containing sulfonic groups for anti-fog coatings, Prog. Org. Coatings. 77 (2014) 785–789.

[153] M. Ezzat, C.J. Huang, Zwitterionic polymer brush coatings with excellent anti-fog and anti-frost properties, RSC Adv. 6 (2016) 61695–61702.

[154] K.-T. Huang, S.-B. Yeh, C.-J. Huang, Surface modification for superhydrophilicity and underwater superoleophobicity: Applications in antifog, underwater self-cleaning, and oil-Water separation, ACS Appl. Mater. Interfaces. 7 (2015) 21021–9.

[155] L. Li, G. Zhang, Z. Su, One-step assembly of phytic acid metal complexes for superhydrophilic coatings, Angew. Chemie. 55 (2016) 9093–9096.

[156] L. Wang, G. Li, Y. Lin, Z. Zhang, Z. Chen, S. Wu, A strategy for constructing anti-adhesion surfaces based on interfacial thiol-ene photoclick chemistry between DOPA derivatives with a catechol anchor group and zwitterionic betaine macromolecules, Polym. Chem. 7 (2016) 4964–4974.

[157] X. Zhang, J. He, B. Jin, In Situ Nanopressing: A General Approach to Robust Nanoparticles-Polymer Surface Structures, Sci. Rep. 6 (2016) 33494. doi:10.1038/srep33494.

[158] X. Zhang, J. He, Antifogging antireflective thin films: Does the antifogging layer have to be the outmost layer?, Chem. Commun. 51 (2015) 12661–12664.

[159] Y. Asthana, L.Y. Hong, D.P. Kim, T.S. Lee, Y.M. Sung, Formulation of thermally cured organic-inorganic superhydrophilic coating for antifogging optical application, Mol. Cryst. Liq. Cryst. 463 (2006) 117–129. doi:10.1080/15421400601027668.

[160] K.-C. Song, J.-K. Park, H.-U. Kang, S.-H. Kim, Synthesis of hydrophilic coating solution for polymer substrate using glycidoxypropyltrimethoxysilane, J. Sol-Gel Sci. Technol. 27 (2003) 53–59.

[161] S. Kim, I. In, S. Park, Study of photo-induced hydrophilicity and self-cleaning property of glass surfaces immobilized with TiO_2 nanoparticles using catechol chemistry, Surf. Coatings Technol. 294 (2016) 75–82.

[162] C.S. Thompson, R. a. Fleming, M. Zou, Transparent self-cleaning and antifogging silica nanoparticle films, Sol. Energy Mater. Sol. Cells. 115 (2013) 108–113.

[163] N. Mizoshita, H. Tanaka, Microporous and Mesoporous Materials Interface-assisted synthesis of mesoporous silica nanoparticles using neat tetraalkoxysilanes, Microporous Mesoporous Mater. 239 (2017) 1–8. doi:10.1016/j.micromeso.2016.09.025.

[164] X. Li, B. Shi, M. Li, L. Mao, Synthesis of highly ordered alkyl-functionalized mesoporous silica by co-condensation method and applications in surface coating with superhydrophilic/antifogging properties, J. Porous Mater. 22 (2015) 201–210.

[165] X. Zhang, P. Lan, Y. Lu, Ji. Li, H. Xu, J. Zhang, Y. Lee, Y.J. Rhee, K.-L. Choy, W. Song, Multifunctional Antire fl ection Coatings Based on Novel Hollow Silica − Silica Nanocomposites, Appl. Mater. Interfaces. 6 (2014) 1415–1423. doi:10.1021/am405258d.

[166] L. Yao, J. He, Z. Geng, T. Ren, Fabrication of mechanically robust, self-cleaning and optically high-performance hybrid thin films by SiO_2@TiO_2 double-shelled hollow nanospheres, Nanoscale. 7 (2015) 13125–13134.

[167] N. Saxena, T. Naik, S. Paria, Organization of SiO_2 and TiO_2 Nanoparticles into Fractal Patterns on Glass Surface for the Generation of Superhydrophilicity, J. Phys. Chem. C. 121 (2017) 2428–2436. doi:10.1021/acs.jpcc.6b09519.

[168] J.-H. You, B.-I. Lee, J. Lee, H. Kim, S.-H. Byeon, Superhydrophilic and antireflective La(OH)3/SiO2-nanorod/nanosphere films., J. Colloid Interface Sci. 354 (2011) 373–9.

[169] L. Cao, H. Hao, P.K. Dutta, Fabrication of high-performance antifogging and antireflective coatings using faujasitic nanozeolites, Microporous Mesoporous Mater. 263 (2018) 62–70.

[170] F. Liu, J. Shen, W. Zhou, S. Zhang, L. Wan, In situ growth of TiO_2/SiO_2 nanospheres on glass substrates via solution impregnation for antifogging, RSC Adv. 7 (2017) 15992–15996.

[171] L. Ye, Y. Zhang, C. Song, Y. Li, B. Jiang, A simple sol-gel method to prepare superhydrophilic silica coatings, Mater. Lett. 188 (2017) 316–318.

[172] W.S. Law, S.W. Lam, W.Y. Gan, J. Scott, R. Amal, Effect of film thickness and agglomerate size on the superwetting and fog-free characteristics of TiO_2 films, Thin Solid Films. 517 (2009) 5425–5430.

[173] W.Y. Gan, S.W. Lam, K. Chiang, R. Amal, H. Zhao, M.P. Brungs, Novel TiO_2 thin film with non-UV activated superwetting and antifogging behaviours, J. Mater. Chem. 17 (2007) 952–954.

[174] T. Li, J. He, L. Yao, Z. Geng, Robust antifogging antireflective coatings on polymer substrates by hydrochloric acid vapor treatment, J. Colloid Interface Sci. 444 (2015) 67–73.

[175] J. Zhao, A. Meyer, L. Ma, X. Wang, W. Ming, J. Zhao, A. Meyer, L. Ma, W. Ming, Terpolymer-based SIPN coating with excellent antifogging and frost-resisting properties, RSC Adv. 5 (2015) 102560–102566.

[176] F. Wang, X. Yang, L. Zhang, W. Xu, H. Liu, Novel Macromolecular Emulsifiers as Coatings with Water-Tolerant Antifogging Properties Based on Coumarin-Containing

Copolymeric Micelles, Macromol. Mater. Eng. 302 (2017) 1700173. doi:10.1002/mame.201700173.

[177] J. Zhao, L. Ma, W. Millians, T. Wu, W. Ming, Dual-Functional Antifogging/Antimicrobial Polymer Coating, ACS Appl. Mater. Interfaces. 8 (2016) 8737–8742. doi:10.1021/acsami.6b00748.

[178] E. Nam, E.H.H. Wong, S. Tan, Q. Fu, A. Blencowe, G.G. Qiao, Antifogging Surface Facilitated by Nanoscale Coatings with Controllable Hydrophobicity and Cross-Linking Density, Macromol. Mater. Eng. 302 (2017) 1600199. doi:10.1002/mame.201600199.

[179] H. Dong, P. Ye, M. Zhong, J. Pietrasik, R. Drumright, K. Matyjaszewski, Superhydrophilic surfaces via polymer-SiO$_2$ nanocomposites., Langmuir. 26 (2010) 15567–73.

[180] W. Zhang, L. Zhu, H. Ye, H. Liu, W. Li, Modifying a waterborne polyacrylate coating with a silica sol for enhancing anti-fogging performance, RSC Adv. 6 (2016) 92252–92258.

[181] C.-C. Chang, F.-H. Huang, H.-H. Chang, T.-M. Don, C.-C. Chen, L.-P. Cheng, Preparation of water-resistant antifog hard coatings on plastic substrate, Langmuir. 28 (2012) 17193–201.

[182] B. Peng, L. Tan, D. Chen, X. Meng, F. Tang, Programming surface morphology of TiO$_2$ hollow spheres and their superhydrophilic films, ACS Appl. Mater. Interfaces. 4 (2012) 96–101.

[183] W. Shan, Y. Hu, M. Zheng, C. Wei, The enhanced photocatalytic activity and self-cleaning properties of mesoporous SiO$_2$/coated Cu-Bi$_2$O$_3$ thin films, Dalt. Trans. 44 (2015) 7428–36. doi:10.1039/c5dt00381d.

[184] Z. Bai, Y. Hu, S. Yan, W. Shan, C. Wei, Preparation of mesoporous SiO$_2$/Bi$_2$O$_3$/TiO$_2$ superhydrophilic thin films and their surface self-cleaning properties, RSC Adv. 7 (2017) 1966–1974. doi:10.1039/C6RA26078K.

[185] D. Tristantini, R. Widuri, Modification of TiO$_2$ nanoparticle with PEG and SiO$_2$ for anti-fogging and self-cleaning application, Int. J. Eng. Technol. IJET-IJENS. 11 (2011) 73–77.

[186] P. Chen, Y. Hu, C. Wei, Preparation of superhydrophilic mesoporous SiO$_2$ thin films, Appl. Surf. Sci. 258 (2012) 4334–4338. doi:10.1016/j.apsusc.2011.12.109.

[187] H. Budunoglu, A. Yildirim, M. Bayindir, Flexible and mechanically stable antireflective coatings from nanoporous organically modified silica colloids, J. Mater. Chem. 22 (2012) 9671–9677.

[188] L. Zhang, C. Lü, Y. Li, Z. Lin, Z. Wang, H. Dong, T. Wang, X. Zhang, X. Li, J. Zhang, B. Yang, Fabrication of biomimetic high performance antireflective and antifogging film by spin-coating, J. Colloid Interface Sci. 374 (2012) 89–95. doi:10.1016/j.jcis.2012.01.051.

[189] Y. Chang, Y. Li, J. Wang, C.-W. Wang, Novel wettability of Cu$_3$SnS$_4$ (CTS) surface for superamphiphilic or hydrophobicity-superlipophilic, Mater. Lett. 187 (2017) 162–165.

[190] N. Nuraje, R. Asmatulu, R.E. Cohen, M.F. Rubner, Durable antifog films from layer-by-layer molecularly blended hydrophilic polysaccharides, Langmuir. 27 (2011) 782–91.

[191] K. Manabe, C. Tanaka, Y. Moriyama, M. Tenjimbayashi, C. Nakamura, Y. Tokura, T. Matsubayashi, K.H. Kyung, S. Shiratori, Chitin nanofibers extracted from crab

shells in broadband visible antireflection coatings with controlling layer-by-layer deposition and the application for durable antifog surfaces, ACS Appl. Mater. Interfaces. 8 (2016) 31951–31958. doi:10.1021/acsami.6b11786.

[192] M. Shibraen, H. Yagoub, X. Zhang, J. Xu, S. Yang, Anti-fogging and anti-frosting behaviors of layer-by-layer assembled cellulose derivative thin film, Appl. Surf. Sci. 370 (2016) 1–5.

[193] H. Lee, M.L. Alcaraz, M.F. Rubner, R.E. Cohen, Zwitter-wettability and antifogging coatings with frost-resisting capabilities, ACS Nano. 7 (2013) 2172–2185.

[194] Y. Wang, T. Li, S. Li, J. Sun, Antifogging and frost-resisting polyelectrolyte coatings capable of healing scratches and restoring transparency, Chem. Mater. 27 (2015) 8058–8065.

[195] P. Chevallier, S. Turgeon, C. Sarra-Bournet, R. Turcotte, G. Laroche, Characterization of multilayer anti-fog coatings, ACS Appl. Mater. Interfaces. 3 (2011) 750–758. doi:10.1021/am1010964.

[196] L. Maechler, C. Sarra-Bournet, P. Chevallier, N. Gherardi, G. Laroche, Anti-fog layer deposition onto polymer materials: A multi-step approach, Plasma Chem. Plasma Process. 31 (2010) 175–187.

[197] G. Laroche, C. Sarra-Bournet, P. Chevalier, N. Gherardi, L. Maechler, Anti-fog coating, USPat., 20120183786A1, 2012.

[198] M. Florea-Spiroiu, D. Achimescu, I. Stanculescu, M. Purica, R. Gavrila, S. Peretz, Anti-fog chitosan/sodium lauryl ether sulfate films, Polym. Bull. 70 (2013) 3305–3316.

[199] H. Lee, J.B. Gilbert, F.E. Angilè, R. Yang, D. Lee, M.F. Rubner, R.E. Cohen, Design and fabrication of zwitter-wettable nanostructured films., ACS Appl. Mater. Interfaces. 7 (2015) 1004–11.

[200] F. Xu, X. Li, Y. Li, J. Sun, Oil-Repellent antifogging films with water-enabled functional and structural healing ability, ACS Appl. Mater. Interfaces. 9 (2017) 27955–27963.

[201] K. Manabe, M. Matsuda, C. Nakamura, K. Takahashi, K.H. Kyung, S. Shiratori, Antifibrinogen, antireflective, antifogging surfaces with biocompatible nano-ordered hierarchical texture fabricated by Layer-by-Layer self-assembly, Chem. Mater. 29 (2017) 4745–4753.

[202] F.C. Cebeci, Z. Wu, L. Zhai, R.E. Cohen, M.F. Rubner, Nanoporosity-driven superhydrophilicity: a means to create multifunctional antifogging coatings., Langmuir. 22 (2006) 2856–62.

[203] W. Yuan, Z. Lu, C.M. Li, Self-assembling microsized materials to fabricate multifunctional hierarchical nanostructures on macroscale substrates, J. Mater. Chem. A. 1 (2013) 6416–6424.

[204] H. Zheng, M. Rubner, N. Nueraji, R. Cohen, Process for preparing articles having anti-fog layer by layer coating and coated articles having enhanced anti-fog and durability properties, USPat., 9011970B2, 2015.

[205] B.-I. Lee, H. Jeong, S.-H. Byeon, Layer-by-layer deposition of highly transparent multifunctional Gd_2O_3:RE/SiO_2 (RE = Eu and Tb) films, Eur. J. Inorg. Chem. 21 (2014) 3298–3304.

[206] B.-I. Lee, E.-S. Lee, S.-H. Byeon, Assembly of layered rare-earth hydroxide nanosheets and SiO_2 nanoparticles to fabricate multifunctional transparent films capable of combinatorial color generation, Adv. Funct. Mater. 22 (2012) 3562–3569.

[207] J. Zhu, L. Xu, J. He, Assembly of graphene nanosheets and SiO$_2$ nanoparticles towards transparent, antireflective, conductive, and superhydrophilic multifunctional hybrid films, Chem. - A Eur. J. 18 (2012) 16393–16401. doi:10.1002/chem.201202494.

[208] X. Liu, X. Du, J. He, Hierarchically structured porous films of silica hollow spheres via layer-by-layer assembly and their superhydrophilic and antifogging properties., Chemphyschem. 9 (2008) 305–9.

[209] X. Du, X. Liu, H. Chen, J. He, Facile fabrication of raspberry-like composite nanoparticles and their application as building blocks for constructing superhydrophilic coatings, J. Phys. Chem. C. 113 (2009) 9063–9070.

[210] Y. Chen, Y. Zhang, L. Shi, J. Li, Y. Xin, T. Yang, Z. Guo, Transparent superhydrophobic/superhydrophilic coatings for self-cleaning and anti-fogging, Appl. Phys. Lett. 101 (2012) 033701.

[211] X. Liu, J. He, Hierarchically structured superhydrophilic coatings fabricated by self-assembling raspberry-like silica nanospheres, J. Colloid Interface Sci. 314 (2007) 341–345.

[212] X. Li, J. He, In situ assembly of raspberry- and mulberry-like silica nanospheres toward antireflective and antifogging coatings, ACS Appl. Mater. Interfaces. 4 (2012) 2204–11.

[213] X. Du, J. He, Facile Fabrication of Hollow Mesoporous Silica Nanospheres for Superhydrophilic and Visible/Near-IR Antireflection Coatings, Chem. Eur. J. 17 (2011) 8165–8174. doi:10.1002/chem.201003272.

[214] P.S. Brown, B. Bhushan, Mechanically durable, superomniphobic coatings prepared by layer-by-layer technique for self-cleaning and anti-smudge, J. Colloid Interface Sci. 456 (2015) 210–218.

[215] F. Yang, P. Wang, X. Yang, Z. Cai, Antifogging and anti-frosting coatings by Dip-layer-by-layer self-assembly of just triple-layer oppositely charged nanoparticles, Thin Solid Films. 634 (2017) 85–95. doi:10.1016/j.tsf.2017.05.018.

[216] L. Zhang, Y. Li, J. Sun, J. Shen, Mechanically stable antireflection and antifogging coatings fabricated by the layer-by-layer deposition process and postcalcination, Langmuir. 24 (2008) 10851–10857.

[217] X. Li, X. Du, J. He, Self-cleaning antireflective coatings assembled from peculiar mesoporous silica nanoparticles, Langmuir. 26 (2010) 13528–13534.

[218] X. Du, Y. Xing, M. Zhou, X. Li, H. Huang, X.M. Meng, Y. Wen, X. Zhang, Broadband antireflective superhydrophilic antifogging nano-coatings based on three-layer system, Microporous Mesoporous Mater. 255 (2018) 84–93. doi:10.1016/j.micromeso.2017.07.017.

[219] X. Li, B. Shi, W. Chaikittisilp, M. Li, Y. Wang, Y. Liu, L. Gao, L. Mao, A general method to synthesize a family of mesoporous silica nanoparticles less than 100 nm and their applications in anti-reflective/fogging coating, J. Mater. Sci. 51 (2016) 6192–6206.

[220] G. Zhou, J. He, Antireflective Coatings on Fresnel Lenses by Spin-Coating of Solid Silica Nanoparticles, J. Nanosci. Nanotechnol. 13 (2013) 5534–5541. doi:10.1166/jnn.2013.7480.

[221] M. Choi, L. Xiangde, J. Park, D. Choi, J. Heo, M. Chang, C. Lee, J. Hong, Superhydrophilic coatings with intricate nanostructure based on biotic materials for antifogging and antibiofouling applications, Chem. Eng. J. 309 (2017) 463–470.

[222] L. Zhang, Z.-A. Qiao, M. Zheng, Q. Huo, J. Sun, Rapid and substrate-independent

layer-by-layer fabrication of antireflection- and antifogging-integrated coatings, J. Mater. Chem. 20 (2010) 6125–6130.

[223] H. Guo, P. Sun, Y. Liang, Y. Ma, Z. Qin, S. Cui, In-situ fabrication of polyelectrolyte-CSH superhydrophilic coatings via layer-by-layer assembly, Chem. Eng. J. 253 (2014) 198–206.

[224] M. Eita, L. Wågberg, M. Muhammed, Thin films of zinc oxide nanoparticles and poly(acrylic acid) fabricated by the Layer-by-Layer technique: A facile platform for outstanding properties, J. Phys. Chem. C. 116 (2012) 4621–4627.

[225] X. Li, J. Lv, D. Li, L. Wang, Rapid fabrication of TiO_2@carboxymethyl cellulose coatings capable of shielding UV, antifog and delaying support aging, Carbohydr. Polym. 169 (2017) 398–405.

[226] K. Takagi, T. Makimoto, H. Hiraiwa, T. Negishi, Photocatalytic, antifogging mirror, J. Vac. Sci. Technol. A Vacuum, Surfaces, Film. 19 (2001) 2931. doi:10.1116/1.1415357.

[227] P. Zeman, S. Takabayashi, Self-cleaning and antifogging effects of TiO_2 films prepared by radio frequency magnetron sputtering, J. Vac. Sci. Technol. A Vacuum, Surfaces, Film. 20 (2002) 388–393. doi:10.1116/1.1446445.

[228] G. Kwak, S. Jung, K. Yong, Multifunctional transparent ZnO nanorod films, Nanotechnology. 22 (2011) 115705. doi:10.1088/0957-4484/22/11/115705.

[229] H.K. Park, S.W. Yoon, W.W. Chung, B.K. Min, Y.R. Do, Fabrication and characterization of large-scale multifunctional transparent ITO nanorod films, J. Mater. Chem. A. 1 (2013) 5860–5867. doi:10.1039/c3ta10422b.

[230] J. Zheng, S. Bao, P. Jin, TiO_2(R)/VO_2(M)/TiO_2(A) multilayer film as smart window: Combination of energy-saving, antifogging and self-cleaning functions, Nano Energy. 11 (2015) 136–145. doi:10.1016/j.nanoen.2014.09.023.

[231] C. Loka, K.R. Park, K.S. Lee, Multi-functional TiO_2/Si/Ag(Cr)/TiN_x coatings for low-emissivity and hydrophilic applications, Appl. Surf. Sci. 363 (2016) 439–444. doi:10.1016/j.apsusc.2015.12.069.

[232] A. Eshaghi, A.A. Aghaei, H. Zabolian, M. Jannesari, A. Firoozifar, Transparent superhydrophilic SiO_2/TiO_2/SiO_2 tri-layer nanostructured antifogging thin film, Ceramics-Silikàty. 57 (2013) 210–214.

[233] C. Garlisi, G. Palmisano, Radiation-free superhydrophilic and antifogging properties of e-beam evaporated TiO_2 films on glass, Appl. Surf. Sci. 420 (2017) 83–93.

[234] J. Chen, L. Zhang, Z. Zeng, G. Wang, G. Liu, W. Zhao, T. Ren, Q. Xue, Facile fabrication of antifogging, antireflective, and self-cleaning transparent silica thin coatings, Colloids Surfaces A Physicochem. Eng. Asp. 509 (2016) 149–157. doi:10.1016/j.colsurfa.2016.08.037.

[235] A. Shoji, T. Fukushima, D.S. Kumar, K. Kashiwagi, Y. Yoshida, Surface modification of plasma polymerized silicon resin films produced at different gas atmospheres, J. Photopolym. Sci. Technol. 19 (2006) 241–244.

[236] G. Maino, D. Meroni, V. Pifferi, L. Falciola, G. Soliveri, G. Cappelletti, S. Ardizzone, Electrochemically assisted deposition of transparent, mechanically robust TiO_2 films for advanced applications, J. Nanoparticle Res. 15 (2013) 2087.

[237] P. Patel, C.K. Choi, D.D. Meng, Superhydrophilic surfaces for antifogging and antifouling microfluidic devices, J. Assoc. Lab. Autom. 15 (2010) 114–119.

[238] J.W. Rhim, Mechanical and water barrier properties of multicomponent (agar/carrageenan/konjac) hydrogel films, Ital. J. Food Sci. 24 (2012) 112–116.

[239] L.F. Wang, J.W. Rhim, Preparation and application of agar/alginate/collagen ternary blend functional food packaging films, Int. J. Biol. Macromol. 80 (2015) 460–468. doi:10.1016/j.ijbiomac.2015.07.007.

[240] R. Liu, J. Zheng, Z. Li, J. Liu, X. Liu, Preparation of surface self-concentration and contact-killing antibacterial coating through UV curing, RSC Adv. 5 (2015) 34199–34205.

[241] R. Tang, A. Muhammad, J. Yang, J. Nie, Preparation of antifog and antibacterial coatings by photopolymerization, Polym. Adv. Technol. 25 (2014) 651–656.

[242] F. Li, P. Biagioni, M. Bollani, A. Maccagnan, L. Piergiovanni, Multi-functional coating of cellulose nanocrystals for flexible packaging applications, Cellulose. 20 (2013) 2491–2504.

[243] M. Cai, Q. Li, X. Chen, Synthesis, surface activity, and antifogging property of triethanolamine monolaurate ester, Chinese J. Chem. Phys. 28 (2015) 223–229.

[244] S.-W. Lee, J.-G. Kang, Fabrication and characterization of superhydrophilic layer on PET film via silica nanocompositions, Bull. Korean Chem. Soc. 36 (2015) 1926–1928.

[245] C.-C. Chang, K.-C. Wang, C.-C. Chen, L.-P. Cheng, Preparation and characterization of silica/polymer antifogging coatings, Polym. Polym. Compos. 22 (2014) 39–44.

[246] T. Ogawa, N. Murata, S. Yamazaki, Development of anti-fogging mirror coated with SiO_2-ZrO_2-Colloidal SiO_2 film by the sol-gel process, J. Sol-Gel Sci. Technol. 27 (2003) 237–238.

[247] M. Rukosuyev, A. Esmaeilirad, S.A. Baqar, M.B.G. Jun, Uniform silver nanoparticles coating using dual regime spray deposition system for superhydrophilic and antifogging applications, J. Coatings Technol. Res. 14 (2017) 347–354.

[248] Y. Jia, G. Liu, X. Wu, H. Liu, R. Yue, Y. Chen, Anti-fogging and anti-reflective silica nanofibrous film fabricated by seedless flame method, Mater. Lett. 108 (2013) 200–203.

[249] S.S. Chae, K.H. Kim, J.H. Park, K.H. Lee, S.W. Han, J.Y. Oh, H.K. Baik, Y.S. Kim, Ultrathin Photo-Oxidized Siloxane Layer for Extreme Wettability: Anti-Fogging Layer for Spectacles, Adv. Mater. Interfaces. 3 (2016) 1500725. doi:10.1002/admi.201500725.

[250] Z. Hua, J. Yang, T. Wang, G. Liu, G. Zhang, Transparent surface with reversibly switchable wettability between superhydrophobicity and superhydrophilicity, Langmuir. 29 (2013) 10307–10312.

[251] X. Du, J. He, Structurally colored surfaces with antireflective, self-cleaning, and antifogging properties, J. Colloid Interface Sci. 381 (2012) 189–197.

[252] J. Xiong, S.N. Das, J.P. Kar, J.-H. Choi, J.-M. Myoung, A multifunctional nanoporous layer created on glass through a simple alkali corrosion process, J. Mater. Chem. 20 (2010) 10246–10252.

[253] T. Fujima, E. Futakuchi, T. Tomita, Y. Orai, T. Sunaoshi, Hierarchical nanoporous glass with antireflectivity and superhydrophilicity by one-pot etching, Langmuir. 30 (2014) 14494–14497.

[254] L. Yao, J. He, Multifunctional surfaces with outstanding mechanical stability on glass substrates by simple H_2SiF_6-based vapor etching, Langmuir. 29 (2013) 3089–3096.

[255] L. Yao, J. He, Broadband antireflective superhydrophilic thin films with outstanding mechanical stability on glass substrates, Chinese J. Chem. 32 (2014) 507–512.

[256] R. Di Mundo, R. D'Agostino, F. Palumbo, Long-lasting antifog plasma modification of transparent plastics, ACS Appl. Mater. Interfaces. 6 (2014) 17059–17066.

[257] S. Han, S. Ji, A. Abdullah, D. Kim, H. Lim, D. Lee, Superhydrophilic nanopillar-structured quartz surfaces for the prevention of biofilm formation in optical devices, Appl. Surf. Sci. 429 (2018) 244–252.

[258] Y.M. Song, G.C. Park, E.K. Kang, C. Il Yeo, Y.T. Lee, Antireflective grassy surface on glass substrates with self-masked dry etching, Nanoscale Res. Lett. 8 (2013) 505.

[259] H. Xu, L. Liu, F. Wu, D. Xu, N. Lu, Fabrication of biomimetic patterns for high transmission and antifogging property, RSC Adv. 5 (2015) 28014–28018.

[260] D. Tahk, T. Il Kim, H. Yoon, M. Choi, K. Shin, K.Y. Suh, Fabrication of antireflection and antifogging polymer sheet by partial photopolymerization and dry etching, Langmuir. 26 (2010) 2240–2243.

[261] D. Sim, M.-J. Choi, Y. Hur, B. Nam, G. Chae, J. Park, Y. Jung, Ultra-high optical transparency of robust, graded-index, and anti-fogging silica coating derived from Si-containing block copolymers, Adv. Opt. Mater. 1 (2013) 428–433.

[262] A. Mao, Y. Li, G. Wang, The fabrication of hydrophilic structure on lens via direct laser interference lithography, Opt. - Int. J. Light Electron Opt. 149 (2017) 90–94.

[263] J.G. Kim, H.J. Choi, K.C. Park, R.E. Cohen, G.H. McKinley, G. Barbastathis, Multifunctional inverted nanocone arrays for non-wetting, self-cleaning transparent surface with high mechanical robustness, Small. 10 (2014) 2487–2494. doi:10.1002/smll.201303051.

[264] Z. Duan, D. Luo, Z. Liu, Z. Zhao, M. Zhao, J. Zhang, G. Zhao, Patterning ZrO2 films surface: Superhydrophilic and superhydrophobic properties, Ceram. Int. 43 (2017) 5089–5094.

[265] Z. Han, H. Guan, Y. Cao, S. Niu, L. Ren, Antifogging properties and mechanism of micron structure in Ephemera pictiventris McLachlan compound eyes, Chinese Sci. Bull. 59 (2014) 2039–2044. doi:10.1007/s11434-014-0252-3.

[266] T. Mouterde, G. Lehoucq, S. Xavier, A. Checco, C.T. Black, A. Rahman, T. Midavaine, C. Clanet, D. Quéré, Antifogging abilities of model nanotextures, Nat. Mater. 16 (2017) 658–663.

[267] Q. Zhang, B. Jin, B. Wang, Y. Fu, X. Zhan, F. Chen, Fabrication of a Highly Stable Superhydrophobic Surface with Dual- Scale Structure and Its Antifrosting Properties, Ind. Eng. Chem. Res. 56 (2017) 2754–2763. doi:10.1021/acs.iecr.6b04650.

[268] J. Li, J. Zhu, X. Gao, Bio-inspired high-performance antireflection and antifogging polymer films, Small. 10 (2014) 2578–2582.

[269] Z. Han, Z. Mu, B. Li, Z. Wang, J. Zhang, S. Niu, L. Ren, Active Antifogging Property of Monolayer SiO_2 Film with Bioinspired Multiscale Hierarchical Pagoda Structures, ACS Nano. 10 (2016) 8591–8602. doi:10.1021/acsnano.6b03884.

[270] S. Utech, K. Bley, J. Aizenberg, N. Vogel, Tailoring re-entrant geometry in inverse colloidal monolayers to control surface wettability, J. Mater. Chem. A. 4 (2016) 6853–6859.

[271] M. Ozdemir, C. Yurteri, H. Sadikoglu, Physical polymer surface modification methods and applications in food packaging polymers, Crit. Rev. Food Sci. Nutr. 39 (1999) 457–477.

[272] L.-A. O'Hare, S. Leadley, B. Parbhoo, Surface physicochemistry of corona-discharge-treated polypropylene film, Surf. Interface Anal. 33 (2002) 335–342.

[273] K. Siow, L. Britcher, S. Kumar, H. Griesser, Plasma methods for the generation of chemically reactive surfaces for biomolecule immobilization and cell colonization-A review, Plasma Process. Polym. 3 (2006) 392–418.

[274] J. Lai, B. Sunderland, J. Xue, S. Yan, W. Zhao, M. Folkard, B.D. Michael, Y. Wang, Study on hydrophilicity of polymer surfaces improved by plasma treatment, Appl. Surf. Sci. 252 (2006) 3375–3379.

[275] P. Singh, S. Saengerlaub, A.A. Wani, H.C. Langowski, Role of plastics additives for food packaging, Pigment Resin Technol. 41 (2012) 368–379. doi:10.1108/03699421211274306.

[276] M. de Fátima Poças, T. Hogg, Exposure assessment of chemicals from packaging materials in foods: A review, Trends Food Sci. Technol. 18 (2007) 219–230.

[277] D. Tijunelis, Synergistic additive system for anti-fog vinyl film, USPat., 3712875A, 1973.

[278] T. Fackler, C. Schweitzer, W. Bernig, B. Dujardin, Transparent deep drawn anti-fog films, USPat., 20080113133A1, 2008.

[279] H. Kuriu, Anti-fogging, stretched, multilayer film excellent in quick-acting property, USPAt., 7014920B2, 2006.

[280] V. Plasman, T. Caulier, N. Boulos, Polyglycerol esters demonstrate superior antifogging properties for films, Plast. Addit. Compd. 7 (2005) 30–33.

[281] L.-J. Wei, F.-X. Yang, Y.-P. Du, J.-Y. Chen, H.-L. Wang, Fabrication and characterization of polyglycerol fatty acid esters/polyethylene antifogging film, J. Food Process Eng. 40 (2017) 12420.

[282] D. Devore, A. Gupta, J. Mcnamara, A. Zedda, Polyolefin film compositions with permanent antifog properties, USPat., 7037964, 2001.

[283] H. Niemann, Fog-resistant olefin polymer films, USPat., 4486552, 1985.

[284] L. Irusta, A. González, M.J. Fernández-Berridi, J.J. Iruin, J.M. Asúa, I. Albizu, A. Ibarzabal, A. Salmerón, E. Espi, A. Fontecha, Y. García, A.I. Real, Migration of antifog additives in agricultural films of low-density polyethylene and ethylene-vinyl acetate copolymers, J. Appl. Polym. Sci. 111 (2009) 2299–2307.

[285] E. Espí, A. Salmerón, A. Fontecha, Y. García, A.I. Real, Plastic films for agricultural applications, J. Plast. Film Sheeting. 22 (2006) 85–102.

[286] R. Zhang, J. Yang, Nanoengineered composite defog coating, USPat., 8367209B2, 2013.

[287] J. Rosen-Kligvasser, R.Y. Suckeveriene, R. Tchoudakov, M. Narkis, A novel methodology for controlled migration of antifog from thin polyolefin films, Polym. Eng. Sci. 54 (2014) 2023–2028.

[288] K. Shlosman, J. Rosen-Kligvasser, R. Suckeveriene, R. Tchoudakov, M. Narkis, Novel antifog modification for controlled migration and prolonged wetting of LLDPE thin films, Eur. Polym. J. 90 (2017) 220–230.

[289] K. Shlosman, R.Y. Suckeveriene, J. Rosen-Kligvasser, R. Tchoudakov, E. Zelikman, R. Semiat, M. Narkis, Controlled migration of antifog additives from LLDPE compatibilized with LLDPE grafted maleic anhydride, Polym. Adv. Technol. 25 (2014) 1484–1491.

[290] A. Bhattacharya, B.N. Misra, Grafting: A versatile means to modify polymers: Techniques, factors, and applications, Prog. Polym. Sci. 29 (2004) 767–814.

[291] Z. Yao, J. Yin, Y. Song, G. Jiang, Y. Song, Preparation and properties of a reactive type nonionic surfactant grafted linear low density polyethylene, Polym. Bull. 59 (2007) 135–144.

[292] W. Li, Z. Yao, Y. Yuan, Y. Meng, L. Xie, Synthesis and characterization of linear low density polyethylene grafted glycerol monolauric acid monoitaconic acid diester,

Polym. Plast. Technol. Eng. 51 (2012) 620–625.

[293] Y.C. Han, S. Lee, B.H. Ahn, S.W. Oh, Y.S. Kang, Preparation of anti-fogging low density polyethylene film by using γ-irradiation, Sensors Actuators B Chem. 126 (2007) 266–270.

[294] S. Sanchez-Valdés, C.J. Picazo-Rada, M.L. López-Quintanilla, Polyethylene grafted maleic anhydride to improve wettability of liquid on polyethylene films, J. Appl. Polym. Sci. 79 (2001) 1802–1808.

[295] W. Li, Z. Yao, R. Yao, S. Liu, Polyethylene grafted polyether pentaerythritol mono-maleate to improve wettability of liquid on polyethylene films, Polym. Plast. Technol. Eng. 52 (2013) 603–606.

[296] J.G. Pieters, J.M. Deltour, M.J. Debruyckere, Experimental determination of the geometry of real drops on transparent materials, J. Phys. III. 6 (1996) 975–989.

[297] S. Pearson, A.E. Wheldon, P. Hadley, Radiation transmission anf fluorescence of nine greenhouse cladding materials, Agric. Eng. 62 (1995) 61–70.

[298] F. Geoola, U.M. Pieper, Outdoor testing of the condensation characteristics of plastic film covering materials using a model greenhouse, J. Agric. Eng. Res. 57 (1994) 167–172.

[299] Techmer PM introduces new viscosity modifier, unique PP antifog agent, Addit. Polym. (2006).

[300] Croda Polymer Additives introduces antifogging concentrate for polypropylene food packaging, Addit. Polym. (2012).

[301] Danisco introduces two anti-fog solutions for polypropylene food packaging, Addit. Polym. (2011) 2–3.

[302] Tosaf enhances anti-fog masterbatch range for packaging applications, Addit. Polym. (2014).

[303] Dyneon develops anti-dripping additive, Addit. Polym. (2007).

[304] Anti-fogging concentrate for blown film, Addit. Polym. (1996).

[305] T. Miyake, T. Yamamoto, Y. Kurihara, Bactericidal antifogging agents useful for coatings on food-packaging materials, Zeolites. 11 (1991) 300.

[306] PolyOne introduces new additives for biopolymers, Addit. Polym. (2008).

[307] A. Mohammad Bagher, Types of Solar Cells and Application, Am. J. Opt. Photonics. 3 (2015) 94. doi:10.11648/j.ajop.20150305.17.

[308] M.R. Maghami, H. Hizam, C. Gomes, M.A. Radzi, M.I. Rezadad, S. Hajighorbani, Power loss due to soiling on solar panel: A review, Renew. Sustain. Energy Rev. 59 (2016) 1307–1316. doi:10.1016/j.rser.2016.01.044.

[309] J. Wan, Y. Lei, Y. Zhang, Y. Leng, J. Liu, Study on TiO_2 photoelectrode to improve the overall performance of dye-sensitized solar cells, Electrochim. Acta. 59 (2012) 75–80. doi:10.1016/j.electacta.2011.10.040.

[310] J. Li, Y. Lu, P. Lan, X. Zhang, W. Xu, R. Tan, W. Song, K. Choy, Design, preparation, and durability of TiO_2/SiO_2 and ZrO_2/SiO_2 double-layer antireflective coatings in crystalline silicon solar modules, Sol. Energy. 89 (2013) 134–142.

[311] Y. Akila, N. Muthukumarasamy, S. Agilan, T. Mallick, S. Senthilarasu, D. Velauthapillai, Enhanced performance of natural dye sensitised solar cells fabricated using rutile TiO_2 nanorods, Opt. Mater. (Amst). 58 (2016) 76–83.

[312] S. Sunny, G. Cheng, D. Daniel, P. Lo, S. Ochoa, C. Howell, N. Vogel, A. Majid, J. Aizenberg, Transparent antifouling material for improved operative field visibility in endoscopy, Proc. Natl. Acad. Sci. 113 (2016) 11676–11681.

doi:10.1073/pnas.1605272113.

[313] D. Abbitt, B. Ben Khallouq, J. Redan, Quantifying intraoperative laparoscopic visual field opacity, JSLS J. Soc. Laparoendosc. Surg. 21 (2017) e2017.00004.

[314] A. Macario, What does one minute of operating room time cost?, J. Clin. Anesth. 22 (2010) 233–236.

[315] A.J. Runia, J.F. Zengerink, G.H.H. Mannaerts, Easy cleaning of the scope's lens in a syringe to prevent condensation during laparoscopic surgery, Surg. Endosc. 23 (2009) 2849–2850.

[316] B. Mohammadhosseini, Povidone-iodine surgical scrub solution prevents fogging of the scope's lens during laparoscopic surgery, Surg. Endosc. 24 (2010) 1498–1499.

[317] L. Fraser, S. Gunasekaran, H. Cruickshank, Patient saliva: A useful anti-fog agent for the fibre-optic nasolaryngoscope, Int. J. Clin. Pract. 63 (2009) 1668.

[318] P. Jategaonkar, S. Jategaonkar, S. Yadav, Simple, rapid and effective technique for intracorporeal defogging of laparoscopic lens, Hell. J. Surg. 88 (2016) 214–216.

[319] Y. Yavuz, J.G. Skogas, M.G. Gulluoglu, T. Lango, R. Marvik, Are cold light sources really cold?, Surg. Laparosc. Endosc. Percutan. Tech. 16 (2006) 370–376.

[320] T. Ohdaira, K. Endo, N. Abe, Y. Yasuda, Usefulness in notes of an intra-abdominal antifogging wireless charge-coupled device (CCD) camera with pantograph-type needle unit for placement to the intra-abdominal wall, Surg. Endosc. 24 (2010) 198–209.

[321] D.A. Lombardi, S.K. Verma, M.J. Brennan, M.J. Perry, Factors influencing worker use of personal protective eyewear, Accid. Anal. Prev. 41 (2009) 755–62.

[322] F. Akbar-Khanzadeh, M. Bisesi, R. Rivas, Comfort of personal protective equipment, Appl. Ergon. 26 (1995) 195–8.

[323] S.J. Chong, C. Smith, A. Bialostocki, C.N. McEwan, Do modern spectacles endanger surgeons? The Waikato eye protection study, Ann. Surg. 245 (2007) 495–501. doi:10.1097/01.sla.0000252406.94464.16.

[324] A. Brackeen, J. Smith, J.M. Crebolder, R.B. Solan, Surgical pearl: Antifog solution for surgery goggles, J. Am. Acad. Dermatol. 55 (2006) 694–695.

[325] M. Komatsu, Toru.; Kobayashi, Colored anti-fog mirror, USPat., 6425670B1, 2002.

[326] H. Kikuchi, M. Nakamura, Colored anti-fog mirror, USPat., 20070247713A1, 2007.

[327] H. Kikuchi, T. Mochizuka, M. Koabayashi, Anti-fog mirror, USPat., 20060077549A1, 2006.

[328] S. Hata, Y. Kai, I. Yamanaka, H. Oosaki, Kazuo Hirota, S. Yamazaki, Development of hydrophilic outside mirror coated with titania photocatalyst, JSAE Rev. 21 (2000) 97–102. doi:10.1016/S0389-4304(99)00075-2.

[329] A. Yahiaoui, R. Quincy, J. McDonald, E. Steindorf, J. Brostin, Facemasks containing an anti-fog / anti-glare composition, USPat., 20050133035A1, 2005.

[330] N. Herbots, C. Watson, J. Culberston, P. Thilmany, M. Gupta, S. Sinha, Permanent anti-fog coatings and delivery devices for direct application of wet or dry temporary, semi-permanent & permanent anti-fog coatings on lenses, surfaces & medical devices, USPat., 20160251525, 2016.

[331] CSA. Z611-M86 Test for fogging of visors. Toronto, Canada: Canadian Standards Association, 1986.

[332] ASTM International. F659-10 Standard specification for ski and snowboard goggles. West Conshohocken PA: ASTM International, 2010.

[333] ASTM International. F659-06 Standard specification for skier goggles and

faceshields-Annex A1. Test method for fogging propeties. West Conshohocken, PA: ASTM International, 2004.

[334] CEN. EN 168 Personal eye protection, non-optical test methods. Brussels: Comité Européen de Normalisation (CEN), 2001.

[335] S. Chattopadhyay, Y.F. Huang, Y.J. Jen, A. Ganguly, K.H. Chen, L.C. Chen, Anti-reflecting and photonic nanostructures, Mater. Sci. Eng. R Reports. 69 (2010) 1–35.

[336] H.K. Raut, V.A. Ganesh, A.S. Nair, S. Ramakrishna, Anti-reflective coatings: A critical, in-depth review, Energy Environ. Sci. 4 (2011) 3779–3804.

[337] R. Kim, C. Park, A. Lee, J. Moon, Development of the noncontact temperature sensor using the infrared optical fiber coated with antifog solution, Sci. Technol. Nucl. Install. 2015 (2015) 1–4.

[338] J.A. Bittencourt, Fundamentals of Plasma Physics, 2013. doi:10.1007/978-1-4757-4030-1.

[339] M. Moisan, J. Pelletier, Plasmas collisionnels-Physique des décharges RF et micro-onde 2e édition. EDP Sciences, (2014).

[340] A. Grill, Cold Plasma Materials Fabrication: From fundamentals to applications. IEES PRESS, 1994. doi:10.1109/9780470544273.

[341] S. Lovascio, Cold plasma deposition of organosilicon films with different monomers in a dielectric barrier discharge, 2010.

[342] J. Shul, S.L.P. (eds), Handbook of Advanced Plasma Processing Techniques, 2002. doi:10.1088/0741-3335/43/3/703.

[343] A. Schutze, J.Y. Jeong, S.E. Babayan, G.S. Selwyn, R.F. Hicks, The atmospheric-pressure plasma jet: A review and comparison to other plasma sources, IEEE Trans. Plasma Sci. 26 (1998) 1685–1694.

[344] G.P. Canal, H. Luna, R.M.O. Galṽo, R. Castell, An approach to a non-LTE Saha equation based on the Druyvesteyn energy distribution function: A comparison between the electron temperature obtained from OES and the Langmuir probe analysis, J. Phys. D. Appl. Phys. 42 (2009). doi:10.1088/0022-3727/42/13/135202.

[345] D. Boonyawan, Atmospheric Pressure Plasma Jet Induced Graft-Polymerization for Flame Retardant Silk, in: Adv. Plasma Spray Appl., 2012. doi:10.5772/28047.

[346] A. Piel, A. Piel, Definition of the Plasma State, in: Plasma Phys., 2010: pp. 29–43. doi:10.1007/978-3-642-10491-6_2.

[347] G.S. Selwyn, H.W. Herrmann, J. Park, I. Henins, Materials processing using an atmospheric pressure, RF-generated plasma source, Contrib. to Plasma Phys. 41 (2001) 610–619. doi:10.1002/1521-3986.

[348] F. Taccogna, G. Dilecce, Non-equilibrium in low-temperature plasmas, Eur. Phys. J. D. 70 (2016). doi:10.1140/epjd/e2016-70474-0.

[349] L. Martinu, O. Zabeida, J.E. Klemberg-Sapieha, Plasma-Enhanced Chemical Vapor Deposition of Functional Coatings, in: Handb. Depos. Technol. Film. Coatings, 2010: pp. 392–465. doi:10.1016/B978-0-8155-2031-3.00009-0.

[350] S.E. Alexandrov, M.L. Hitchman, Chemical vapor deposition enhanced by atmospheric pressure non-thermal non-equilibrium plasmas, Chem. Vap. Depos. 11 (2005) 457–468. doi:10.1002/cvde.200500026.

[351] N. Naudé, Etude électrique de la physique d'une décharge de Townsend à la pression atmosphérique et de son interaction avec un générateur : Modèle et Expérience, Université Paul Sabatier - Toulouse III, 2005.

[352] S. Muhl, A. Pérez, The use of hollow cathodes in deposition processes: A critical

review, Thin Solid Films. 579 (2015) 174–198. doi:10.1016/j.tsf.2015.02.066.

[353] K.H. Schoenbach, A. El-Habachi, W. Shi, M. Ciocca, High-pressure hollow cathode discharges, Plasma Sources Sci. Technol. 6 (1997) 468–477. doi:10.1088/0963-0252/6/4/003.

[354] J.-S. Chang, P.A. Lawless, T. Yamamoto, Corona discharge processes, IEEE Trans. Plasma Sci. 19 (1991) 1152–1166.

[355] R. Siliprandi, Atmospheric Pressure Plasmas for Surface Modifications, 2007.

[356] A. Sublet, Caractérisation de décharges à barrières diélectriques atmosphériques et sub-atmosphériques et application à la déposition de couches d'oxyde de silicium, 2007.

[357] A. Bogaerts, E. Neyts, R. Gijbels, J. Van der Mullen, Gas discharge plasmas and their applications, Spectrochim. Acta - Part B At. Spectrosc. 57 (2002) 609–658. doi:10.1016/S0584-8547(01)00406-2.

[358] S. Nijdam, E. van Veldhuizen, P. Bruggeman, U. Ebert, An Introduction to Nonequilibrium Plasmas at Atmospheric Pressure, in: Plasma Chem. Catal. Gases Liq., 2012: pp. 1–44. doi:10.1002/9783527649525.ch1.

[359] A. Mahrle, S. Rose, M. Schnick, E. Beyer, U. Füssel, Laser-assisted plasma arc welding of stainless steel, J. Laser Appl. 25 (2013) 032006. doi:10.2351/1.4798338.

[360] D.R. Mac Rae, Plasma arc process systems, reactors, and applications, Plasma Chem. Plasma Process. 9 (1989). doi:10.1007/BF01015875.

[361] A.R. Hoskinson, Measurements and Simulations of Surface Dielectric Barrier Discharges Used as Plasma Actuators, NASA Tech. Rep. NASA/CR. 217628 (2012) 239. doi:20120014222.

[362] F. Massines, N. Gherardi, N. Naudé, P. Ségur, Recent advances in the understanding of homogeneous dielectric barrier discharges, Eur. Phys. J. Appl. Phys. 47 (2009) 22805. doi:10.1051/epjap/2009064.

[363] A. Fridman, Plasma Physics and Engineering, 4th edition, Elsevier (2011).

[364] A.H. Qureshi, J.A. Dayton, Insulation Requirements of High-Voltage Power Systems in Future Spacecraft, 1995.

[365] J.K. E. Kuffel, W. S. Zaengl, High Voltage Engineering : Fundamentals, 2000. doi:10.1017/CBO9781107415324.004.

[366] I.S. Marshak, Electric breakdown of gases at pressures close to atmospheric pressure, Uspekhi Fiz. Nauk. 71 (2014) 631–675. doi:10.3367/ufnr.0071.196008c.0631.

[367] R.S. Berry, The Theory of Penning Ionization, Radiat. Res. 59 (2006) 367. doi:10.2307/3573984.

[368] V.I. Gushenets, E.M. Oks, G.Y. Yushkov, N.G. Rempe, Current status of plasma emission electronics: I. Basic physical processes, Laser Part. Beams. 21 (2003) 123–138. doi:10.1017/S0263034603212027.

[369] J.S. Townsend, Electricity in Gases, J. Röntgen Soc. 11 (2015) 87–87. doi:10.1259/jrs.1915.0049.

[370] K.A. Ghosh, On the pressure dependence of Townsend's second coefficient at constant E/p, Can. J. Phys. 43 (1965).

[371] W.E. Bowls, The effect of cathode material on the second townsend coefficient for ionization by collision in pure and contaminated N_2 Gas, Phys. Rev. 53 (1938) 293–301. doi:10.1103/PhysRev.53.293.

[372] L. Babich, T. V. Loiko, Generalized Paschen's Law for Overvoltage Conditions, IEEE Trans. Plasma Sci. 44 (2016) 3243–3248. doi:10.1109/TPS.2016.2629022.

[373] A. Fridman, A. Chirokov, A. Gutsol, Non-thermal atmospheric pressure discharges, J. Phys. D. Appl. Phys. 38 (2005). doi:10.1088/0022-3727/38/2/R01.

[374] A. Anders, The physics of cathode processes, in: Cathodic Arcs. Springer Sci., 2008: pp. 75–174. doi:10.1007/978-0-387-79108-1.

[375] A. Pedersen, On the Electrical Breakdown of Gaseous Dielectrics: An Engineering Approach, IEEE Trans. Electr. Insul. 24 (1989) 721–739. doi:10.1109/14.42156.

[376] B. Eliasson, U. Kogelschatz, Modeling and Applications of Silent Discharge Plasmas, IEEE Trans. Plasma Sci. 19 (1991) 309–323. doi:10.1109/27.106829.

[377] H. Raether, Electron avalanches and breakdown in gases. Washington, D.C., Butterworth Co., 1964.

[378] U. Kogelschatz, Dielectric-barrier discharges: Their history, discharge physics, and industrial applications, Plasma Chem. Plasma Process. 23 (2003) 1–46.

[379] R. Brandenburg, Dielectric barrier discharges: Progress on plasma sources and on the understanding of regimes and single filaments, Plasma Sources Sci. Technol. 26 (2017). doi:10.1088/1361-6595/aa6426.

[380] A. Chirokov, A. Gutsol, A. Fridman, Atmospheric pressure plasma of dielectric barrier discharges, Pure Appl. Chem. 77 (2005) 487–495. doi:10.1351/pac200577020487.

[381] S. Veerapandian, C. Leys, N. De Geyter, R. Morent, Abatement of VOCs Using Packed Bed Non-Thermal Plasma Reactors: A Review, Catalysts. 7 (2017) 113. doi:10.3390/catal7040113.

[382] U. Kogelschatz, Filamentary, patterned, and diffuse barrier discharges, IEEE Trans. Plasma Sci. 30 (2002) 1400–1408. doi:10.1109/TPS.2002.804201.

[383] F. Massines, C. Sarra-Bournet, F. Fanelli, N. Naudé, N. Gherardi, Atmospheric pressure low temperature direct plasma technology: Status and challenges for thin film deposition, Plasma Process. Polym. 9 (2012) 1041–1073.

[384] R. Brandenburg, V.A. Maiorov, Y.B. Golubovskii, H.E. Wagner, J. Behnke, J.F. Behnke, Diffuse barrier discharges in nitrogen with small admixtures of oxygen: Discharge mechanism and transition to the filamentary regime, J. Phys. D. Appl. Phys. 38 (2005) 2187–2197. doi:10.1088/0022-3727/38/13/017.

[385] T. Shirafuji, T. Kitagawa, T. Wakai, K. Tachibana, Observation of self-organized filaments in a dielectric barrier discharge of Ar gas, Appl. Phys. Lett. 83 (2003) 2309–2311. doi:10.1063/1.1613796.

[386] H. Itoh, K. Kobayashi, K. Teranishi, N. Shimomura, S. Suzuki, Time-resolved observation of self-organized filaments formed in a helium-dielectric barrier discharge, IEEE Trans. Plasma Sci. 39 (2011) 2204–2205. doi:10.1109/TPS.2011.2160568.

[387] N. Gherardi, G. Gouda, E. Gat, A. Ricard, F. Massines, Transition from glow silent discharge to micro-discharges in nitrogen gas, Plasma Sources Sci. Technol. 9 (2000) 340–346. doi:10.1088/0963-0252/9/3/312.

[388] F. Massines, N. Gherardi, N. Naudé, P. Ségur, Glow and townsend dielectric barrier discharge in various atmosphere, Plasma Phys. Control. Fusion. 47 (2005) 577–588.

[389] X. Bonnin, H. Piquet, N. Naudé, M. Chérif Bouzidi, N. Gherardi, J.-M. Blaquière, Design of a current converter to maximize the power into homogeneous dielectric barrier discharge (DBD) devices, Eur. Phys. J. Appl. Phys. 64 (2013) 10901. doi:10.1051/epjap/2013130080.

[390] C. Tyl, X. Lin, M.C. Bouzidi, S. Dap, H. Caquineau, P. Ségur, N. Gherardi, N. Naudé, Investigation of memory effect in atmospheric pressure dielectric barrier discharge in

nitrogen with small oxygen or nitric oxide addition, J. Phys. D. Appl. Phys. 51 (2018). doi:10.1088/1361-6463/aad472.

[391] M.J. Shaw, Penning ionization, Contemp. Phys. 15 (1974) 445–464. doi:10.1080/00107517408210804.

[392] G. Instrumentation, Chemical Ionization Potential (eV) and 10.6 eV PID Correction Factors (CF), (2019) 2–4.

[393] A. Bogaerts, The glow discharge: An exciting plasma!, J. Anal. At. Spectrom. 14 (1999) 1375–1384. doi:10.1039/a900772e.

[394] Y.B. Golubovskii, V.A. Maiorov, P. Li, M. Lindmayer, Effect of the barrier material in a Townsend barrier discharge in nitrogen at atmospheric pressure, J. Phys. D. Appl. Phys. 39 (2006) 1574–1583. doi:10.1088/0022-3727/39/8/016.

[395] S.F. Miralai, E. Monette, R. Bartnikas, G. Czeremuszkin, M. Latreèche, M.R. Wertheimer, Electrical and optical diagnostics of dielectric barrier discharges (DBD) in He and N_2 for polymer treatment, Plasmas Polym. 5 (2000) 63–77. doi:10.1023/A:1009531831404.

[396] K. V. Kozlov, R. Brandenburg, H.E. Wagner, A.M. Morozov, P. Michel, Investigation of the filamentary and diffuse mode of barrier discharges in N_2/O_2 mixtures at atmospheric pressure by cross-correlation spectroscopy, J. Phys. D. Appl. Phys. 38 (2005) 518–529. doi:10.1088/0022-3727/38/4/003.

[397] C. Sarra-Bournet, N. Gherardi, S. Turgeon, G. Laroche, F. Massines, Deposition of functional hydrogenated amorphous carbon-nitride film (a-CN:H) using C_2H_4/N_2 townsend dielectric barrier discharge, Eur. Phys. J. Appl. Phys. 47 (2009) 22820. doi:10.1051/epjap/2009079.

[398] N.S.J. Braithwaite, Introduction to gas discharges, Plasma Sources Sci. Technol. 9 (2000) 517–527. doi:10.1088/0963-0252/9/4/307.

[399] K.L. Choy, Chemical vapour deposition of coatings, Prog. Mater. Sci. 48 (2003) 57–170. doi:10.1016/S0079-6425(01)00009-3.

[400] C. Sarra-Bournet, Fonctionnalisation de surface de polymères par plasma à la pression atmosphérique, 2009.

[401] L.J. Ward, W.C.E. Schofield, J.P.S. Badyal, A.J. Goodwin, P.J. Merlin, Atmospheric pressure glow discharge deposition of polysiloxane and SiO_x films, Langmuir. 19 (2003) 2110–2114.

[402] I.R. Durán, G. Laroche, Current trends, challenges, and perspectives of anti-fogging technology: Surface and material design, fabrication strategies, and beyond, Prog. Mater. Sci. 99 (2019) 106–186. doi:10.1016/j.pmatsci.2018.09.001.

[403] C.S. Pai, J.F. Miner, P.D. Foo, Biased ECR CVD oxide deposition using TEOS and TMCTS, in: 1991 Proc. Eighth Int. IEEE VLSI Multilevel Interconnect. Conf., IEEE, 1991: pp. 442–444.

[404] C.S. Pai, J.F. Miner, P.D. Foo, Electron cyclotron resonance microwave discharge for oxide deposition using tetramethylcyclotetrasiloxane, J. Appl. Phys. 73 (1993) 3531–3538.

[405] M. Tabasky, Investigation of thick, low-temperature plasma deposited silica films for waveguide fabrication, J. Vac. Sci. Technol. A Vacuum, Surfaces, Film. 12 (1994) 1244.

[406] A. Grill, V. Patel, Ultralow dielectric constant pSiCOH films prepared with tetramethylcyclotetrasiloxane as skeleton precursor, J. Appl. Phys. 104 (2008) 024113.

[407] Y. Qi, Z.G. Xiao, T.D. Mantei, Comparison of silicon dioxide layers grown from three polymethylsiloxane precursors in a high-density oxygen plasma, J. Vac. Sci. Technol. A Vacuum, Surfaces, Film. 21 (2003) 1064.

[408] J. Widodo, W. Lu, S.G. Mhaisalkar, L.C. Hsia, P.Y. Tan, L. Shen, K.Y. Zeng, Characterization of tetra methyl cyclo tetra siloxanes-based low-k dielectric film, Thin Solid Films. 462–463 (2004) 213–218.

[409] J. Widodo, L.N. Goh, W. Lu, S.G. Mhaisalkar, K.Y. Zeng, L.C. Hsia, Comparative Study of Trimethyl Silane and Tetramethylcyclotetrasiloxane-Based Low- k Films, J. Electrochem. Soc. 152 (2005) G246–G251. doi:10.1149/1.1861176.

[410] J. Widodo, W. Lu, S.G. Mhaisalkar, J.L. Sudijono, L.C. Hsia, L. Shen, K.Y. Zeng, Effects of CO_2 and O_2 on the property of tetra methyl tetra cyclo siloxanes based low-k film, Thin Solid Films. 472 (2005) 195–202.

[411] J. Zhang, D.S. Wavhal, E.R. Fisher, Mechanisms of SiO_2 film deposition from tetramethylcyclotetrasiloxane, dimethyldimethoxysilane, and trimethylsilane plasmas, J. Vac. Sci. Technol. A Vacuum, Surfaces, Film. 22 (2004) 201.

[412] A. Grill, D.A. Neumayer, Structure of low dielectric constant to extreme low dielectric constant SiCOH films: Fourier transform infrared spectroscopy characterization, J. Appl. Phys. 94 (2003) 6697.

[413] S. Osaki, M. Chen, P.O. Zamora, Controlled drug release through a plasma polymerized tetramethylcyclo-tetrasiloxane coating barrier., J. Biomater. Sci. Polym. Ed. 23 (2012) 483–96.

[414] K. Fujino, Y. Nishimoto, N. Tokumasu, K. Maeda, Low-yemperature atmospheric-pressure chemical vapor deposition using 2, 4, 6, 8-tetramethylcyclotetrasiloxane and ozone, Jpn. J. Appl. Phys. 33 (1994) 2019–2024.

[415] G.R. Nowling, M. Yajima, S.E. Babayan, M. Moravej, X. Yang, W. Hoffman, R.F. Hicks, Chamberless plasma deposition of glass coatings on plastic, Plasma Sources Sci. Technol. 14 (2005) 477–484.

[416] M.D. Barankin, T.S. Williams, E. Gonzalez, R.F. Hicks, Properties of fluorinated silica glass deposited at low temperature by atmospheric plasma-enhanced chemical vapor deposition, Thin Solid Films. 519 (2010) 1307–1313.

[417] L. Cui, A.N. Ranade, M.A. Matos, L.S. Pingree, T.J. Frot, G. Dubois, R.H. Dauskardt, Atmospheric plasma deposited dense silica coatings on plastics, ACS Appl. Mater. Interfaces. 4 (2012) 6587–98.

[418] S.E. Glassford, B. Byrne, S.G. Kazarian, Recent applications of ATR FTIR spectroscopy and imaging to proteins, Biochim. Biophys. Acta - Proteins Proteomics. 1834 (2013) 2849–2858. doi:10.1016/j.bbapap.2013.07.015.

[419] R. Bauer, H. Nieuwoudt, F.F. Bauer, J. Kossmann, K.R. Koch, K.H. Esbensen, FTIR spectroscopy for grape and wine analysis, Anal. Chem. 80 (2008) 1371–1379. doi:10.1021/ac086051c.

[420] L. Raphael, Application of FTIR Spectroscopy to Agricultural Soils Analysis, Fourier Transform. - New Anal. Approaches FTIR Strateg. (2011) 385–404. doi:10.5772/15732.

[421] L.E. Rodriguez-Saona, M.E. Allendorf, Use of FTIR for Rapid Authentication and Detection of Adulteration of Food, Annu. Rev. Food Sci. Technol. 2 (2011) 467–483. doi:10.1146/annurev-food-022510-133750.

[422] J. Coates, Interpretation of Infrared Spectra, A Practical Approach, in: Encycl. Anal. Chem., John Wiley & Sons, Ltd, 2006. doi:10.1002/9780470027318.a5606.

[423] S. Mukhopadhyay, FTIR spectroscopy - principles and applications, J. Text. Assoc. 64 (2003) 187–192. doi:10.1007/978-3-662-09280-4.

[424] M. Milosevic, Fresnel equations, Intern. Reflect. ATR Spectrosc. (2012) 39–54.

[425] H.M. Lai, F.C. Cheng, W.K. Tang, Goos–Hänchen effect around and off the critical angle, J. Opt. Soc. Am. A. 3 (2008) 550. doi:10.1364/josaa.3.000550.

[426] M. Milosevic, Internal reflection and ATR spectroscopy, Appl. Spectrosc. Rev. 39 (2004) 365–384.

[427] G. Laroche, J. Fitremann, N. Gherardi, FTIR-ATR spectroscopy in thin film studies: The importance of sampling depth and deposition substrate, Appl. Surf. Sci. 273 (2013) 632–637. doi:10.1016/j.apsusc.2013.02.095.

[428] C.J. Attridge, Correlation of Si-H infrared stretching frequencies, J. Organomet. Chem. 13 (1968) 259–262.

[429] I.A. Mudunkotuwa, A. Al Minshid, V.H. Grassian, ATR-FTIR spectroscopy as a tool to probe surface adsorption on nanoparticles at the liquid-solid interface in environmentally and biologically relevant media, Analyst. 139 (2014) 870–881. doi:10.1039/c3an01684f.

[430] Z.M. Khoshhesab, Reflectance IR Spectroscopy, Infrared Spectrosc. - Mater. Sci. Eng. Technol. (2012). doi:10.5772/37180.

[431] C. Vigano, J.M. Ruysschaert, E. Goormaghtigh, Sensor applications of attenuated total reflection infrared spectroscopy, Talanta. 65 (2005) 1132–1142. doi:10.1016/j.talanta.2004.07.052.

[432] R.T. Haasch, X-Ray photoelectron spectroscopy (XPS) and auger electron spectroscopy (AES), in: Pract. Mater. Charact., 2014: pp. 93–132. doi:10.1007/978-1-4614-9281-8_3.

[433] J.C. Vickerman, I.S. Gilmore, Surface Analysis– The Principal Techniques, 2009. doi:10.1002/9780470721582.

[434] C.N. Berglund, W.E. Spicer, Photoemission studies of copper and silver: Theory, Phys. Rev. 136 (1964) 1030–1044.

[435] M. Jacquemin, M.J. Genet, E.M. Gaigneaux, D.P. Debecker, Calibration of the X-ray photoelectron spectroscopy binding energy scale for the characterization of heterogeneous catalysts: Is everything really under control?, ChemPhysChem. 14 (2013) 3618–3626. doi:10.1002/cphc.201300411.

[436] C.J. Powell, Summary of the American society for testing and materials practice E 2108-00 for calibration of the electron binding-energy scale of an x-ray photoelectron spectrometer, J. Vac. Sci. Technol. A Vacuum, Surfaces, Film. 19 (2001) 2689.

[437] P.S. Bagus, F. Illas, G. Pacchioni, F. Parmigiani, Mechanisms responsible for chemical shifts of core-level binding energies and their relationship to chemical bonding, J. Electron Spectros. Relat. Phenomena. 100 (1999) 215–236.

[438] A. Cros, Charging effects in X-ray photoelectron spectroscopy, J. Electron Spectros. Relat. Phenomena. 59 (1992) 1–14. doi:10.1016/0368-2048(92)85008-U.

[439] C.J. Powell, A. Jablonski, Progress in quantitative surface analysis by X-ray photoelectron spectroscopy: Current status and perspectives, J. Electron Spectros. Relat. Phenomena. 178–179 (2010) 331–346.

[440] D. McMullan, Scanning electron microscopy 1928–1965, Scanning. 17 (1995) 175–185. doi:10.1002/sca.4950170309.

[441] D. Johnson, N. Hilal, W.R. Bowen, Basic principles of atomic force microscopy, in: At. Force Microsc. Process Eng., 2009: pp. 1–30. doi:10.1016/B978-1-85617-517-

3.00001-8.

[442] A. Vilalta-Clemente, K. Gloystein, N. Frangis, Principles of Atomic Force Microscopy (AFM), Phys. Adv. Mater. Winter Sch. 2008. (2008) 1–10.

[443] F.J. Giessibl, Advances in atomic force microscopy, Rev. Mod. Phys. 75 (2003) 949–983. doi:10.1103/RevModPhys.75.949.

[444] B. Cappella, G. Dietler, Force-distance curves by atomic force microscopy, Surf. Sci. Rep. 34 (1999) 1–3. doi:10.1016/S0167-5729(99)00003-5.

[445] B. Bhushan, Surface Roughness Analysis and Measurement Techniques, in: 2010. doi:10.1201/9780849377877.ch2.

[446] E.S. Gadelmawla, M.M. Koura, T.M.A. Maksoud, I.M. Elewa, H.H. Soliman, Roughness parameters, J. Mater. Process. Technol. 123 (2002) 133–145.

[447] A. Duparré, J. Ferre-Borrull, S. Gliech, G. Notni, J. Steinert, J.M. Bennett, Surface characterization techniques for determining the root-mean-square roughness and power spectral densities of optical components, Appl. Opt. 41 (2007) 154. doi:10.1364/ao.41.000154.

[448] J.W. Haus, Nanocharacterization, in: Fundam. Appl. Nanophotonics, 2016: pp. 185–210. doi:10.1016/B978-1-78242-464-2.00006-3.

[449] L. Yuan, T. Randall, Contact angle and Wetting properties, in: Surf. Sci. Tech. Springer-Verlag VErling Heidelb., 2013: pp. 1–34. doi:10.1007/978-3-642-34243-1_1,.

[450] T. Huhtamäki, X. Tian, J.T. Korhonen, R.H.A. Ras, Surface-wetting characterization using contact-angle measurements, Nat. Protoc. 13 (2018) 1521–1538. doi:10.1038/s41596-018-0003-z.

[451] J. Drelich, Guidelines to measurements of reproducible contact angles using a sessile-drop technique, Surf. Innov. 1 (2013) 248–254. doi:10.1680/si.13.00010.

[452] H. Eral, F. Mannetje, J. Oh, Contact angle hysteresis: A review of fundamentals and applications, Colloid Polym. Sci. 2 (2013) 247–260. doi:http://dx.doi.org/10.1007/s00396-012-2796-6.

[453] Kruss, Comparison of Wilhelmy and Sessile Drop Technique, 1996.

[454] J. Shang, M. Flury, J.B. Harsh, R.L. Zollars, Comparison of different methods to measure contact angles of soil colloids, J. Colloid Interface Sci. 328 (2008) 299–307. doi:10.1016/j.jcis.2008.09.039.

[455] P. Pretto, J.P. Bresciani, G. Rainer, H.H. Bülthoff, Foggy perception slows us down, Elife. 2012 (2012) 1–12.

[456] P.M. Biddell, Anti-fogging device and anti-fogging viewing member, USPat., 20080290081A1, 2008. http://www.google.com/patents/US8399805 (accessed March 29, 2016).

[457] S. Kaufmann, Y. Loretz, K. Hilfiker, Prevention of fog in a condenser by simultaneous heating and cooling, Heat Mass Transf. Und Stoffuebertragung. 32 (1997) 403–410. doi:10.1007/s002310050138.

[458] S.M. With, C.R. FIAT, Windshield fogging prevention by means of mean radiant temperature sensor, in: J. Valldorf, W. Gessner (Eds.), Springer Berlin Heidelberg, Berlin, Heidelberg, 2004.

[459] J. Jacques, M. Mage, Fog-resistant sunglasses incorporating ventilation channels, USPat., 6050684A, 2000.

[460] M.A. McNeilly, Sport sunglasses resistant to fogging, USPat., 4150443A, 1979.

[461] G. Reitz, Dental mirror incorporating air flow, USPat., 5449290A, (1995).

[462] H. Toida, T. Kozai, K. Ohyama, Enhancing fog evaporation rate using an upward air stream to improve greenhouse cooling performance, Biosyst. Eng. 93 (2006) 205–211.

[463] A. Fujishima, X. Zhang, D.A. Tryk, TiO_2 photocatalysis and related surface phenomena, Surf. Sci. Rep. 63 (2008) 515–582.

[464] L. Xu, J. He, Antifogging and antireflection coatings fabricated by integrating solid and mesoporous silica nanoparticles without any post-treatments, ACS Appl. Mater. Interfaces. 4 (2012) 3293–3299.

[465] A. Kuzminova, A. Shelemin, O. Kylian, M. Petr, J. Kratochvil, P. Sola, H. Biederman, From super-hydrophilic to super-hydrophobic surfaces using plasma polymerization combined with gas aggregation source of nanoparticles, Vacuum. 110 (2014) 58–61.

[466] L. Chen, G. Henein, J.A. Liddle, Super-hydrophobic and/or super-hydrophilic surfaces made by plasma process, in: Tech. Proc. 2009 NSTI Nanotechnol. Conf. Expo NSTINanotech 2009, 2009: pp. 194–197. doi:901919.

[467] I. Enache, H. Caquineau, N. Gherardi, T. Paulmier, L. Maechler, F. Massines, Transport Phenomena in an Atmospheric-Pressure Townsend Discharge Fed by N_2/ N_2O/HMDSO Mixtures, Transport. 4 (2007) 806–814. doi:10.1002/ppap.200700073.

[468] P.A. Premkumar, S.A. Starostin, H. De Vries, R.M.J. Paffen, M. Creatore, T.J. Eijkemans, P.M. Koenraad, M.C.M. Van De Sanden, High quality SiO_2-like layers by large area atmospheric pressure plasma enhanced CVD: Deposition process studies by surface analysis, Plasma Process. Polym. 6 (2009) 693–702. doi:10.1002/ppap.200900033.

[469] T. Alvik, J. Dale, Infrared and raman spectra of cyclic dimethylsiloxane oligomers, Acta Chem. Scand. 25 (1971) 2142–2148.

[470] H.G.P. Lewis, T.B. Casserly, K.K. Gleason, Hot-filament chemical vapor deposition of organosilicon thin films from hexamethylcyclotrisiloxane and octamethylcyclotetrasiloxane, J. Electrochem. Soc. 148 (2001) 212–220.

[471] C. Rau, W. Kulisch, Mechanisms of plasma polymerization of various silico-organic monomers, Thin Solid Films. 249 (1994) 28–37.

[472] A. Nyczyk, C. Paluszkiewicz, M. Hasik, M. Cypryk, P. Pospiech, Cross-linking of linear vinylpolysiloxanes by hydrosilylation – FTIR spectroscopic studies, Vib. Spectrosc. 59 (2012) 1–8.

[473] C.H. Lo, M.H. Lin, K.S. Liao, M. De Guzman, H.A. Tsai, V. Rouessac, T.C. Wei, K.R. Lee, J.Y. Lai, Control of pore structure and characterization of plasma-polymerized SiOCH films deposited from octamethylcyclotetrasiloxane (OMCTS), J. Memb. Sci. 365 (2010) 418–425. doi:10.1016/j.memsci.2010.09.042.

[474] L. Favennec, V. Jousseaume, G. Gerbaud, A. Zenasni, G. Passemard, Ultralow k using a plasma enhanced chemical vapor deposition porogen approach: Matrix structure and porogen loading influences, J. Appl. Phys. 102 (2007) 064107.

[475] D. Burkey, K. Gleason, Structure and mechanical properties of thin films deposited from 1,3,5-trimethyl-1,3,5-trivinylcyclotrisiloxane and water, J. Appl. Phys. 93 (2003) 5143–5150.

[476] A.L. Smith, D.R. Anderson, VIBRATIONAL SPECTRA OF Me_2SiCl_2, Me_3SiCl, $Me_3SiOSiMe_3$, $(Me_2SiO)_3$, $(Me_2SiO)_4$, $(Me_2SiO)_x$, AND THEIR DEUTERATED ANALOGS., Appl. Spectrosc. 38 (1984) 822–834. doi:10.1366/0003702844554549.

[477] R.E. Richards, H.W. Thompson, Infra-red spectra of compounds of high molecular weight. Part IV. Silicones and related compounds, J. Chem. Soc. (1949) 124–132. doi:10.1039/jr9490000124.

[478] N. Wright, M.J. Hunter, Organosilicon polymers. III. infrared spectra of the methylpolysiloxanes, J. Am. Chem. Soc. 69 (1947) 803–809.

[479] C.W. Young, P.C. Servais, C.C. Currie, M.J. Hunter, Organosilicon polymers. IV. Infrared studies on cyclic disubstituted siloxanes, J. Am. Chem. Soc. 70 (1948) 3758–3764.

[480] Y. Abe and T. Gunji, Oligo- and polysiloxanes, Prog. Polym. Sci. 29 (2004) 149–182.

[481] A.L. Smith, N.C. Angelotti, Correlation of the SiH stretching frequency with molecular structure, Spectrochim. Acta. 15 (1959) 412–420.

[482] G. Lucovsky, Chemical effects on the frequencies of Si-H vibrations in amorphous solids, Solid State Commun. 29 (1979) 571–576.

[483] N. Majoul, S. Aouida, B. Bessaïs, Progress of porous silicon APTES-functionalization by FTIR investigations, Appl. Surf. Sci. 331 (2015) 388–391.

[484] B. a. Morrow, A.J. McFarlan, Chemical reactions at silica surfaces, J. Non. Cryst. Solids. 120 (1990) 61–71.

[485] F. Massines, N. Gherardi, A. Fornelli, S. Martin, Atmospheric pressure plasma deposition of thin films by Townsend dielectric barrier discharge, Surf. Coatings Technol. 200 (2005) 1855–1861.

[486] S. Lee, J. Yang, S. Yeo, J. Lee, D. Jung, J. Boo, H. Kim, H. Chae, Effect of Annealing Temperature on Dielectric Constant and Bonding Structure of Low- k SiCOH Thin Films Deposited by Plasma Enhanced Chemical Vapor Deposition, Jpn. J. Appl. Phys. 46 (2007) 536–541. doi:10.1143/JJAP.46.536.

[487] A.M. Coclite, A. Milella, R. D'Agostino, F. Palumbo, On the relationship between the structure and the barrier performance of plasma deposited silicon dioxide-like films, Surf. Coatings Technol. 204 (2010) 4012–4017.

[488] J. Schäfer, R. Foest, A. Quade, A. Ohl, K.-D. Weltmann, Chemical Composition of SiO_x Films Deposited by an Atmospheric Pressure Plasma Jet (APPJ), Plasma Process. Polym. 6 (2009) S519–S524. doi:10.1002/ppap.200931103.

[489] C.T. Kirk, Quantitative analysis of the effect of disorder-induced mode copling on infrared absorption in silica, Phys. Rev. B. 38 (1988) 1255–1273.

[490] D. Rouchon, N. Rochat, F. Gustavo, A. Chabli, O. Renault, P. Besson, Study of ultrathin silicon oxide films by FTIR-ATR and ARXPS after wet chemical cleaning processes, Surf. Interface Anal. 34 (2002) 445–450. doi:10.1002/sia.1335.

[491] P. Supiot, C. Vivien, A. Granier, A. Bousquet, A. Mackova, D. Escaich, R. Clergereaux, P. Raynaud, Z. Stryhal, J. Pavlik, Growth and modification of organosilicon films in PECVD and remote afterglow reactors, Plasma Process. Polym. 3 (2006) 100–109.

[492] R. Clergereaux, M. Calafat, F. Benitez, D. Escaich, I. Savin de Larclause, P. Raynaud, J. Esteve, Comparison between continuous and microwave oxygen plasma post-treatment on organosilicon plasma deposited layers: effects on structure and properties, Thin Solid Films. 515 (2007) 3452–3460. doi:10.1016/j.tsf.2006.10.076.

[493] V. Raballand, J. Benedikt, S. Hoffmann, M. Zimmermann, A. von Keudell, Deposition of silicon dioxide films using an atmospheric pressure microplasma jet, J. Appl. Phys. 105 (2009) 083304.

[494] A. Matilainen, N. Britun, J.S. Bong, J.G. Han, Optical emission spectra of OMCTS/O_2 fed plasmas used for thin film deposition, Surf. Coatings Technol. 205 (2010) 300–304.

[495] P. González, D. Fernández, J. Pou, E. García, J. Serra, B. León, M. Pérez-Amor, T.

Szörényi, Study of the gas-phase parameters affecting the silicon-oxide film deposition induced by an ArF laser, Appl. Phys. A Solids Surfaces. 57 (1993) 181–185. doi:10.1007/BF00331442.

[496] F. Massines, P. Ségur, N. Gherardi, C. Khamphan, A. Ricard, Physics and chemistry in a glow dielectric barrier discharge at atmospheric pressure: Diagnostics and modelling, Surf. Coatings Technol. 174–175 (2003) 8–14. doi:10.1016/S0257-8972(03)00540-1.

[497] F. Fanelli, S. Lovascio, R. Agostino, F. Fracassi, Insights into the Atmospheric Pressure Plasma- Enhanced Chemical Vapor Deposition of Thin Films from Methyldisiloxane Precursors, Plasma Process. Polym. 9 (2012) 1132–1143. doi:10.1002/ppap.201100157.

[498] J.M. Rimsza, J.A. Kelber, J. Du, Mechanisms of oxygen plasma damage of amine and methyl terminated organosilicate low- k dielectrics from *ab initio* molecular dynamics simulations, J. Phys. D. Appl. Phys. 47 (2014) 335204. doi:10.1088/0022-3727/47/33/335204.

[499] N. Gherardi, L. Maechler, N. Naudé, F. Massines, APGD and APTD for the deposition of silicon based thin films from N_2O/HMDSO mixtures : application to gas-barrier layers, in: Ispc_19, 2009: pp. 1–4.

[500] G. Borcia, N. Brown, Hydrophobic coatings on selected polymers in an atmospheric pressure dielectric barrier discharge, J. Phys. D. Appl. Phys. 40 (2007) 1927.

[501] H. Hamze, M. Jimenez, D. Deresmes, A. Beaurain, N. Nuns, M. Traisnel, Influence of processing gases on the properties of cold atmospheric plasma SiO_xC_y coatings, Appl. Surf. Sci. 315 (2014) 531–537.

[502] L.A. O'Hare, B. Parbhoo, S.R. Leadley, Development of a methodology for XPS curve-fitting of the Si 2p core level of siloxane materials, Surf. Interface Anal. 36 (2004) 1427–1434. doi:10.1002/sia.1917.

[503] M.R. Alexander, R.D. Short, F.R. Jones, W. Michaeli, C.J. Blomfield, A study of $HMDSO/O_2$ plasma deposits using a high-sensitivity and energy resolution XPS instrument: Curve fitting of the Si 2p core level, Appl. Surf. Sci. 137 (1999) 179–183.

[504] H. Ibach, Nucleation and Growth, Phys. Surfaces Interfaces. 13 (2006) 555–612. doi:10.1351/goldbook.N04244.

[505] K.R. Jensen, P. Fojan, R.L. Jensen, L. Gurevich, Water Condensation: A Multiscale Phenomenon, J. Nanosci. Nanotechnol. 14 (2014) 1859–1871. doi:10.1166/jnn.2014.9108.

[506] V.S. Nikolayev, P. Sibille, D.A. Beysens, Coherent light transmission by a dew pattern, Opt. Commun. 150 (1998) 263–269. doi:10.1016/S0030-4018(98)00051-0.

[507] I.R. Durán, G. Laroche, Water drop-surface interactions as the basis for the design of anti-fogging surfaces: Theory, practice, and applications trends, Adv. Colloid Interface Sci. 263 (2018) 68–94. doi:S0001868618302422.

[508] C.G. Jothi Prakash, C. Clement Raj, R. Prasanth, Fabrication of zero contact angle ultra-super hydrophilic surfaces, J. Colloid Interface Sci. 496 (2017) 300–310. doi:10.1016/j.jcis.2017.01.007.

[509] X. Wang, G. Wu, J. Zou, Y. Ou, Photoinduced hydrophilicity and antifogging ability on ZnO thin film., Nanchang Daxue Xuebao, Likeban. 35 (2011) 450–452.

[510] N. Petersen, J., Bardon, J., Dinia, A., Ruch, D., Gherardi, Organosilicon coatings deposited in atmospheric pressure Townsend discharge for gas barrier purpose : Effect of substrate temperature on structure and properties, ACS Appl. Mater. Interfaces. 4

(2012) 5872–82.

[511] B. Verheyde, D. Havermans, A. Vanhulsel, Characterization and tribological behaviour of siloxane-based plasma coatings on HNBR rubber, Plasma Process. Polym. 8 (2011) 755–762.

[512] L. Zhou, G.-H. Lv, C. Ji, S.-Z. Yang, Application of plasma polymerized siloxane films for the corrosion protection of titanium alloy, Thin Solid Films. 520 (2012) 2505–2509.

[513] B.C. Chakoumakos, R.J. Hill, G. V. Gibbs, A molecular orbital study of rings in silicates and siloxane, Am. Miner. 66 (1981) 1237.

[514] E. Todd Ryan, S.M. Gates, S.A. Cohen, Y. Ostrovski, E. Adams, K. Virwani, A. Grill, Effect of low-frequency radio frequency on plasma-enhanced chemical vapor deposited ultra low-κ dielectric films for very large-scale integrated interconnects, J. Appl. Phys. 115 (2014). doi:10.1063/1.4870453.

[515] C. Nwankire, G. Favaro, Q.-H. Duong, D. Dowling, Enhancing the mechanical properties of superhydrophobic atmospheric pressure plasma deposited siloxane coatings, Plasma Process. Polym. 8 (2011) 305–315.

[516] B.C. Trasferetti, C.U. Davanzo, M.A.B. de Moraes, Infrared and raman studies on films of organosiloxane networks produced by PECVD, Macromolecules. 37 (2004) 459–466.

[517] R. Reuter, N. Gherardi, J. Benedikt, Effect of N_2 dielectric barrier discharge treatment on the composition of very thin SiO_2-like films deposited from hexamethyldisiloxane at atmospheric pressure, Appl. Phys. Lett. 101 (2012) 194104.

[518] M. Wilamowska-Zawlocka, P. Puczkarski, Z. Grabowska, J. Kaspar, M. Graczyk-Zajac, R. Riedel, G.D. Sorarù, Silicon oxycarbide ceramics as anodes for lithium ion batteries: Influence of carbon content on lithium storage capacity, RSC Adv. 6 (2016) 104597–104607. doi:10.1039/c6ra24539k.

[519] A. Fidalgo, L. Ilharco, Chemical tailoring of porous silica xerogels: Local structure by vibrational spectroscopy, Chem. - A Eur. J. 10 (2004) 392–398.

[520] S. Starostine, E. Aldea, H. de Vries, M. Creatore, M.C.M. Van de Sanden, Atmospheric pressure barrier discharge deposition of silica-like films on polymeric substrates, Plasma Process. Polym. 4 (2007) 440–444.

[521] N. Boscher, P. Choquet, D. Duday, S. Verdier, Advantages of a pulsed electrical excitation mode on the corrosion performance of organosilicon thin films deposited on aluminium foil by atmospheric pressure dielectric barrier discharge, Plasma Process. Polym. 7 (2009) 163–171.

[522] A. Coclite, A. Milella, F. Palumbo, F. Fracassi, R. D'Agostino, Chemical and morphological characterization of low-k dielectric films deposited from hexamethyldisiloxane and ethylene RF glow discharges, Plasma Process. Polym. 7 (2010) 1022–1029.

[523] N. Boscher, P. Choquet, D. Duday, S. Verdier, Chemical compositions of organosilicon thin films deposited on aluminium foil by atmospheric pressure dielectric barrier discharge and their electrochemical behaviour, Surf. Coatings Technol. 205 (2010) 2438–2448.

[524] J. Petersen, R. Bechara, J. Bardon, T. Fouquet, F. Ziarelli, L. Daheron, V. Ball, V. Toniazzo, M. Michel, A. Dinia, D. Ruch, Atmospheric plasma deposition process: A versatile tool for the design of tunable siloxanes-based plasma polymer films, Plasma Process. Polym. 8 (2011) 895–903.

[525] P.F. McMillan, R.L. Remmele, Hydroxyl sites in SiO_2, glass: A note on infrared and raman spectra, Am. Mineral. 71 (1986) 772–778.

[526] R. McDonald, Surface functionality of amorphous silica by infrared spectroscopy, J. Phys. Chem. 62 (1958) 1168–1178.

[527] A. Grill, V. Patel, K.P. Rodbell, E. Huang, M.R. Baklanov, K.P. Mogilnikov, M. Toney, H.-C. Kim, Porosity in plasma enhanced chemical vapor deposited SiCOH dielectrics: A comparative study, J. Appl. Phys. 94 (2003) 3427.

[528] A. Grill, Plasma enhanced chemical vapor deposited SiCOH dielectrics: From low-k to extreme low-k interconnect materials, J. Appl. Phys. 93 (2003) 1785.

[529] D.D. Burkey, K.K. Gleason, Temperature-resolved Fourier transform infrared study of condensation reactions and porogen decomposition in hybrid organosilicon-porogen films, J. Vac. Sci. Technol. A Vacuum, Surfaces, Film. 22 (2004) 61–70. doi:10.1116/1.1627766.

[530] C.Y. Wang, Z.X. Shen, J.Z. Zheng, High-temperature properties of a low dielectric constant organic spin-on glass for multilevel interconnects, Appl. Spectrosc. 55 (2001) 1347–1351. doi:10.1366/0003702011953469.

[531] C.Y. Wang, Z.X. Shen, J.Z. Zheng, Thermal cure study of a low-k methyl silsesquioxane for intermetal dielectric application by FT-IR spectroscopy, Appl. Spectrosc. 54 (2000) 209–213.

[532] J.S. Chou, S.C. Lee, Effect of porosity on IR spectra of SiO_x, J. Appl. Phys. 77 (1995) 1805.

[533] K.T. Queeney, M.K. Weldon, J.P. Chang, Y.J. Chabal, A.B. Gurevich, J. Sapjeta, R.L. Opila, Infrared spectroscopic analysis of the Si/SiO_2 interface structure of thermally oxidized silicon, J. Appl. Phys. 87 (2000) 1322–1330. doi:10.1063/1.372017.

[534] P.N. Sen, M.F. Thorpe, Phonons in AX_2 glasses: From molecular to band-like modes, Phys. Rev. B. 15 (1977) 4030–4038. doi:10.1103/PhysRevB.15.4030.

[535] F.L. Galeener, Band limits and the vibrational spectra of tetrahedral glasses, Phys. Rev. B. 19 (1979) 4292–4297. doi:10.1103/PhysRevB.19.4292.

[536] Y.-H. Kim, M.S. Hwang, H.J. Kim, J.Y. Kim, Y. Lee, Infrared spectroscopy study of low-dielectric-constant fluorine-incorporated and carbon-incorporated silicon oxide films, J. Appl. Phys. 90 (2001) 3367.

[537] X. Fan, S. Kang, J. Li, T. Zhu, Conversion of dilute nitrous oxide (N_2O) in N_2 and N_2-O_2 mixtures by plasma and plasma-catalytic processes, RSC Adv. 8 (2018) 26998–27007. doi:10.1039/c8ra05607b.

[538] Q.H. Trinh, S.H. Kim, Y.S. Mok, Removal of dilute nitrous oxide from gas streams using a cyclic zeolite adsorption-plasma decomposition process, Chem. Eng. J. 302 (2016) 12–22. doi:10.1016/j.cej.2016.05.030.

[539] L.E. Kline, W.D. Partlow, R.M. Young, R. Mitchell, T. V. Congedo, Diagnostics and Modeling of RF Discharge Dissociation in N_2O, IEEE Trans. Plasma Sci. 19 (1991) 278–285. doi:10.1109/27.106825.

[540] L. Date, K. Radouane, H. Caquineau, B. Despax, J.P. Couderc, M. Yousfi, Analysis of the N_2O dissociation by r.f. discharges in a plasma reactor, Surf. Coatings Technol. 116–119 (1999) 1042–1048. doi:10.1016/S0257-8972(99)00287-X.

[541] B. Mutel, J. Grimblot, O. Dessaux, P. Goudmand, XPS investigations of nitrogen-plasma-treated polypropylene in a reactor coupled to the spectrometer, Surf. Interface Anal. 30 (2000) 401–406. doi:10.1002/1096-9918.

[542] M. Strobel, N. Sullivan, M.C. Branch, J. Park, M. Ulsh, R.S. Kapaun, B. Leys, Surface

modification of polypropylene film using N₂O-containing flames, J. Adhes. Sci. Technol. 14 (2000) 1243–1264. doi:10.1163/156856100742186.

[543] L. Zhou, G.H. Lv, H. Pang, G.P. Zhang, S.Z. Yang, Comparing deposition of organic and inorganic siloxane films by the atmospheric pressure glow discharge, Surf. Coatings Technol. 206 (2012) 2552–2557. doi:10.1016/j.surfcoat.2011.11.011.

[544] N. Shirtcliffe, P. Thiemann, M. Stratmann, G. Grundmeier, Chemical structure and morphology of thin, organo-silicon plasma-polymer films as a function of process parameters, Surf. Coatings Technol. 142–144 (2001) 1121–1128. doi:10.1016/S0257-8972(01)01226-9.

[545] G.K.H. Pang, K.Z. Baba-Kishi, A. Patel, Topographic and phase-contrast imaging in atomic force microscopy, Ultramicroscopy. 81 (2000) 35–40. doi:10.1016/S0304-3991(99)00164-3.

[546] R. Godehardt, W. Lebek, R. Adhikari, M. Rosenthal, C. Martin, S. Frangov, G.H. Michler, Optimum topographical and morphological information in AFM tapping mode investigation of multicomponent polyethylene, Eur. Polym. J. 40 (2004) 917–926. doi:10.1016/j.eurpolymj.2004.01.034.

[547] Z. Navrátil, D. Trunec, L. Zají ková, P. Stahel, V. Bur íková, J. Cech, Deposition of thin organosilicon polymer films in atmospheric pressure glow discharge, J. Phys. D. Appl. Phys. 37 (2004) 2112–2120. doi:10.1088/0022-3727/37/15/010.

[548] N. Gherardi, F. Massines, Mechanisms controlling the transition from glow silent discharge to streamer discharge in nitrogen, IEEE Trans. Plasma Sci. 29 (2001) 536–544. doi:10.1109/27.928953.

[549] D. Fritter, C.M. Knobler, D.A. Beysens, Experiments and Simulation of the Growth of Droplets on a Surface, Phys. Rev. A. 43 (1991) 2858–2870.

[550] R.T. Spurr, J.G. Butlin, Breath figures, Nature. 179 (1957) 1187. doi:10.1038/1791187b0.

[551] T.J. Baker, Breath figures, Philos. Mag. Ser. 6. 44 (1922) 752–765.

[552] C.M. Knobler, D. Beysens, Growth of breath figures on fluid surfaces, Epl. 6 (1988) 707–712. doi:10.1209/0295-5075/6/8/007.

[553] F. Geoola, Y. Kashti, A. Levi, R. Brickman, Quality evaluation of anti-drop properties of greenhouse cladding materials, Polym. Test. 23 (2004) 755–761.

[554] Z. Duan, D. Luo, Z. Liu, Z. Zhao, M. Zhao, J. Zhang, Patterning ZrO₂ films surface: Superhydrophilic and superhydrophobic properties, Ceram. Int. 43 (2017) 5089–5094.

[555] J. Han, Y. Dou, M. Wei, D.G. Evans, X. Duan, Antireflection/antifogging coatings based on nanoporous films derived from layered double hydroxide, Chem. Eng. J. 169 (2011) 371–378.

[556] E. Van Besien, A. Singh, Y. Barbarin, P. Verdonck, H.F.W. Dekkers, K. Vanstreels, J.F. De Marneffe, M.R. Baklanov, S. Van Elshocht, Low-k a-SiCO:H films as diffusion barriers for advanced interconnects, Microelectron. Eng. 120 (2014) 221–224. doi:10.1016/j.mee.2013.12.022.

[557] N.D. Boscher, P. Choquet, D. Duday, S. Verdier, Influence of cyclic organosilicon precursors on the corrosion of aluminium coated sheet by atmospheric pressure dielectric barrier discharge, Surf. Coatings Technol. 205 (2011) 5350–5357. doi:10.1016/j.surfcoat.2011.05.043.

[558] Y. Ding, S. Dong, J. Han, D. He, Z. Zhao, R.H. Dauskardt, Optically Transparent Protective Coating for Plastics Using Dual Spray and Atmospheric Plasma Deposition, Adv. Mater. Interfaces. 5 (2018). doi:10.1002/admi.201701433.

[559] M. Handke, B. Handke, A. Kowalewska, W. Jastrzebski, New polysilsesquioxane materials of ladder-like structure, J. Mol. Struct. 924–926 (2009) 254–263. doi:10.1016/j.molstruc.2008.11.039.

[560] A. Nyczyk, C. Paluszkiewicz, A. Pyda, M. Hasik, Preceramic polysiloxane networks obtained by hydrosilylation of 1,3,5,7-tetravinyl-1,3,5,7-tetramethylcyclotetrasiloxane, Spectrochim. Acta - Part A Mol. Biomol. Spectrosc. 79 (2011) 801–808. doi:10.1016/j.saa.2010.08.056.

[561] P. González, E. García, J. Pou, D. Fernández, B. León, M. Pérez-Amor, Excimer laser CVD of silicon oxide on GaAs: a comparison with deposition on c-Si, Appl. Surf. Sci. 54 (1992) 108–111. doi:10.1016/0169-4332(92)90027-U.

[562] K.H.A. Bogart, J.P. Cushing, E. Fisher, Effects of plasma processing parameters on the surface reactivity of OH ($X^2\Pi$) in tetraethoxysilane/O_2 plasmas during deposition of SiO_2, J. Phys. Chem. B. 101 (1997) 10016–10023.

[563] T. Mori, T. Masuko, A. Shirakura, T. Suzuki, Synthesis of SiOC(–H) Films by the Atmospheric Pressure Plasma Enhanced Chemical Vapor Deposition Method, E-Journal Surf. Sci. Nanotechnol. 13 (2015) 445–450. doi:10.1380/ejssnt.2015.445.

[564] J. Profili, O. Levasseur, N. Naudé, C. Chaneac, L. Stafford, N. Gherardi, Influence of the voltage waveform during nanocomposite layer deposition by aerosol-assisted atmospheric pressure Townsend discharge, J. Appl. Phys. 120 (2016). doi:10.1063/1.4959994.

[565] Y. Sawada, S. Ogawa, M. Kogoma, Synthesis of plasma-polymerized tetraethoxysilane and hexamethyldisiloxane films prepared by atmospheric pressure glow discharge, J. Phys. D. Appl. Phys. 28 (1995) 1661–1669. doi:10.1088/0022-3727/28/8/015.

[566] H. Kakiuchi, H. Ohmi, Y. Yamaguchi, K. Nakamura, K. Yasutake, Low refractive index silicon oxide coatings at room temperature using atmospheric-pressure very high-frequency plasma, Thin Solid Films. 519 (2010) 235–239.

[567] J.L. Jauberteau, I. Jauberteau, Comparison of hexamethyldisiloxane dissociation processes in plasma, J. Phys. Chem. A. 116 (2012) 8840–8850. doi:10.1021/jp304694z.

[568] P.S. Henderson, P.J. Kelly, R.D. Arnell, H. Backer, J.W. Bradley, Investigation into the properties of titanium based films deposited using pulsed magnetron sputtering, Surface. 174 (2003) 779–783. doi:10.1016/S0257-8972.

[569] J. Zhang, E.R. Fisher, Surface reactivity of OH molecules during deposition of SiO_2 from siloxane-based plasmas, J. Phys. Chem. B. 108 (2004) 9821–9828.

[570] K.H.A. Bogart, J.P. Cushing, E. Fisher, Surface reactivity measurements for OH radicals during deposition of SiO_2 from tetraethoxysilane/O_2 plasmas, Chem. Phys. Lett. 267 (1997) 377–383.

[571] I.A. Kossyi, A.Y. Kostinsky, A.A. Matveyev, V.P. Silakov, Kinetic scheme of the non-equilibrium discharge in nitrogen-oxygen mixtures, Plasma Sources Sci. Technol. 1 (1992) 207–220. doi:10.1088/0963-0252/1/3/011.

[572] I. Enache, Etude Expérimentale et Modélisation du Transfert de Matière dans des Décharges de Townsend à Pression Atmosphérique en Mélange HMDSO-N_2O-N_2 et SIH$_4$-N_2O-N_2. Université Toulouse III. Paul Sabatier, 2007.

[573] S. Takeda, M. Fukawa, A.G. Company, Surface (OH) Groups Governing Surface Chemical Properties of Metal Oxide Films, Thin Solid Films. 339 (1999) 7188.

[574] S. Takeda, K. Yamamoto, Y. Hayasaka, K. Matsumoto, Surface OH group governing

wettability of commercial glasses, J. Non. Cryst. Solids. 249 (1999) 41–46.

[575] S. Takeda, M. Fukawa, Role of surface OH groups in surface chemical properties of metal oxide films, Mater. Sci. Eng. B. 119 (2005) 265–267.

[576] S. Takeda, M. Fukawa, Surface OH groups governing surface chemical properties of SiO2 thin films deposited by RF magnetron sputtering, Thin Solid Films. 444 (2003) 153–157. doi:10.1016/S0040-6090(03)01094-0.

[577] G. He, C. Zhou, Z. Li, Review of self-cleaning method for solar cell array, Procedia Eng. 16 (2011) 640–645.